SORBONNE UNIVERSITÉ
CRÉATEURS DE FUTURS DEPUIS 1257

SYRTE l'Observatoire de Paris | PSL
SYstèmes de Référence Temps-Espace

UAM UNIVERSIDAD AUTONOMA DE MADRID

THÈSE DE DOCTORAT DE SORBONNE UNIVERSITÉ

Spécialité : Physique

École doctorale : Physique en Île-de-France (ED 564)

réalisée

au laboratoire de SYstèmes de Référence Temps-Espace

présentée par

Héctor ÁLVAREZ MARTÍNEZ

pour obtenir le grade de :

DOCTEUR DE SORBONNE UNIVERSITÉ

Sujet de la thèse :

Caractérisation des mesures par peigne de fréquences optiques et transfert de pureté spectrale à des horloges atomiques optiques

Characterization of optical frequency comb based measurements and spectral purity transfer for optical atomic clocks

soutenue le 15 mars 2021

devant le jury composé de :

M.	Pierre LEMONDE	Rapporteur
M.	Yann KERSALÉ	Rapporteur
Mme.	Saïda GUELLATI	Examinatrice
M.	Ginés LIFANTE PEDROLA	Examinateur
Mme.	Lucile RUTKOWSKI	Examinatrice
M.	Yann LE COQ	Directeur de thèse
M.	Pedro CORREDERA GUILLÉN	Co-directeur de thèse
M.	Rodolphe LE TARGAT	Co-encadrant

Héctor ÁLVAREZ MARTÍNEZ **15 mars 2021**

Sujet : Caractérisation des mesures par peigne de fréquences optiques et transfert de pureté spectrale à des horloges atomiques optiques

Résumé : Cette thèse présente les avancées de la chaîne de fréquence opérationnelle du SYRTE, emsemble de différentes oscillateurs ultrastables et peignes de fréquence. Le travail de recherche porte sur l'analyse du bruit des éléments critiques, afin de déterminer les limites pratiques de stabilité et d'exactitude de cette architecture métrologique. Les performances sont mesurées par comparaisons simultanées de paires d'oscillateurs avec 3 chaînes entièrement indépendantes. Les résolutions relatives obtenues, en deçà de $1 \cdot 10^{-16}$ dans le domaine micro-onde et $1 \cdot 10^{-18}$ dans le domaine optique, démontrent que ces moyens de mesures ne sont pas limitants, même avec les horloges à l'état-de-l'art. Un élément clé des horloges optiques est la lumière sondant la transition métrologique. Si les meilleurs lasers ultrastables sont conçus dans l'infrarouge, la technique du transfert de pureté spectrale permet de transmettre leur niveau de performance aux longueurs d'onde visibles cibles (698 nm et 1062 nm) via un peigne de fréquence. Ce travail décrit ainsi un transfert hors boucle de résolution meilleure que $5 \cdot 10^{-18}$ à 1 s, utilisé pour l'interrogation synchronisées des horloges strontium et mercure du laboratoire lorsque leurs lasers d'horloge respectifs bénéficient du transfert d'un unique maître à 1542 nm. Ceci a déjà permis un gain d'un facteur 2 de la stabilité dans la mesure du rapport mercure/strontium.

Mots clés : chaîne de fréquences, horloges optiques, lasers ultrastables, métrologie de fréquence, peignes de fréquences optiques, transfert de pureté spectrale

Tema: Caracterización de medidas mediante peine de frecuencias ópticas y transferencia de pureza espectral para relojes atómicos ópticos

Resumen:
Esta tesis doctoral presenta los últimos avances de la cadena de frecuencias operacional del SYRTE, conjunto de diferentes osciladores ultra-estables y peines de frecuencia. Este trabajo de investigación se centra en el análisis del ruido de sus elementos más críticos con el fin de determinar los límites de estabilidad y exactitud de esta arquitectura metrológica. El rendimiento de estas capacidades fue medido mediante comparaciones simultáneas de pares de osciladores con 3 cadenas totalmente independientes. Las resoluciones relativas obtenidas, por debajo de 10^{-16} en el dominio de las microondas y de 10^{-18} en el óptico, demuestran que estos medios de medida no son un factor limitante, incluso con relojes de tecnología punta. Un elemento clave de los relojes ópticos es la luz que sondea la estrecha transición atómica. Mientras que en la práctica estos láseres son construidos en el rango infrarrojo, la técnica de transferencia de pureza espectral permite transmitir sus prestaciones hacia las longitudes de onda visibles de interés (698 nm y 1062 nm) por medio de un peine de frecuencias. Este trabajo demuestra una transferencia fuera de lazo mejor que $5 \cdot 10^{-18}$ a 1 s, utilizada para la interrogación sincronizada entre los relojes de estroncio y mercurio del laboratorio cuando sus respectivos láseres reloj se benefician de la transferencia de un único laser maestro a 1542 nm. Esto ha permitido la mejora en un factor de 2 de la estabilidad de la medida del ratio mercurio/estroncio.

Palabras clave: cadena de frecuencias, láseres ultra-estables, metrología de frecuencias, peines de frecuencias ópticas, relojes ópticos, transferencia de pureza espectral

Subject: Characterization of optical frequency comb based measurements and spectral purity transfer for optical atomic clocks

Abstract: This PhD thesis presents the latest advances in SYRTE operational frequency chain, based on ultrastable oscillators at different wavelengths and frequency comb technologies. After describing this metrological architecture, the work focuses on the noise analysis of its critical elements so as to determine its stability and accuracy limits. The performance of these capabilities was measured by performing simultaneous comparisons of oscillators pairs with 3 fully independent chains. The relative resolutions obtained, below 10^{-16} in the microwave and 10^{-18} in the optical domains, demonstrate that these means of measurement are not a limiting factor, even with state-of-the-art clocks. A key element of optical clocks is the light probing the narrow atomic transition. While in practice ultrahigh stability lasers are built in the infrared range, the technique known as transfer of spectral purity makes use of a frequency comb to transmit its level of performance to target visible wavelengths (698 nm and 1062 nm in the SYRTE case). This work demonstrates an out-of-loop transfer reaching a resolution better than $5 \cdot 10^{-18}$ at 1 s. This lead to the first synchronized interrogation between the SYRTE strontium and mercury clocks when their respective clock lasers benefit from the transfer of a single master at 1542 nm, resulting in a 2-fold improvement of their stability ratio measurement.

Keywords: frequency chain, frequency metrology, optical clocks, optical frequency combs, spectral purity transfer, ultrastable lasers

Never measure anything but frequency.
Arthur Leonard Schawlow

Acknowledgments

It looks like yesterday when I look back and I remember when I first landed in Paris on my way to the department of Systemes de Référence Temps-Espace (SYRTE), in the prestigious and worldwide-known Observatoire de Paris.

All started with the initiative of Francisco Javier Galindo Mendoza, the director of the Real Instituto y Observatorio de la Armada (ROA), on developing an optical frequency standard in the coming future in Spain, for which he bet for the proper training of the new personnel posted at ROA as the most fundamental step to accomplish first. Together with the support of Héctor Esteban Pinillos, head of the Sección de Hora of ROA, I was able to ask for one of the Research Mobility Grants attached to the OC18 Joint Research Project in the frame of the European Association of National Metrology Institutes. The one offered by Rodolphe Le Targat, as one of the OC18 Working Packages leaders, gave me the opportunity to work with the SYRTE Fréquences Optiques (FOP) group.

I would like to send my most sincere thanks to my supervisor Rodolphe Le Targat. Honestly, I have no words to describe the infinite time he has invested on my scientific training, his knowledge, his expertise and especially his patience! He integrated me in the team and assigned me tasks from the very beginning. He always made sure that I was understanding the experiments and he continuously motivated me to push them forward, improving them or finding new approaches. Apart from all the lab tricks he has taught me, he also introduced me to his colleagues and friends and made me feel like at home. I will be forever grateful for all he has done for me.

I express my gratitude to Yann Le Coq, my thesis director, for his guidance, proximity and accepting me as one of his new students. Despite having two other PhD students at the same time, he always found the time to follow my research and gave me precious advice.

Jérôme Lodewyck, with who I have shared office during my stay, for explaining me all little things that came to my mind spontaneously when reading papers about optical clocks and wondering "why" again and again. I will miss his short but concise explanations and his smart sense of humor.

Michel Abgrall, my "godfather" who has not only supported me along my PhD but also he has always replied to all my questions during his coffee breaks and with video

conferences during the confinements about Molly, masers and time scale generation.

Sébastien Bize, the head of the FOP group for his continuous interest on the different activities I was involved and his popular expression "*Ça roule ?*". It took me a long time to realize that he was simply asking about how everything was going, and not asking for someone called "Saúl".

I can not forget Arnaud Landragin, the director of SYRTE, Franck Pereira, my PhD tutor, Paul-Eric Pottie, Ouali Acef, Bess Fang, Stéphane Guerandel and all the other permanent members who I have interacted with and exchanged ideas, thoughts and jokes. All of you are part of the good atmosphere, on top of the high academic level, that makes of SYRTE the perfect place to work, beyond the excellence. I would like to mention the electronic workshop with Michel Lours and Jose Pinto for his help and availability every time we had to modify or fix our different kind of "lock boxes", as well as the administration department and the mechanical workshop.

My research stay would not have been the same without all the other students and postdocs from the strontium, mercury, fiber and spectral hole burning teams. But in particular I would like to mention to Christian Bærentsen, my former colleague in the comb lab, for all the time we spent together working in parallel in the same experiments, discussions and our after work dinners.

I would like to especial thank to Pedro Corredera Guillén, my thesis codirector, for his confidence and assistance. I will miss all those explanations at lunch time in Madrid. He has been the one who taught me for the very first time what an optical frequency comb is and let me operate it when doing my master thesis with him back in 2016. At that time I would have never imagined that I was going to have the opportunity and honor of being part of frequency comb based state-of-the-art metrology experiments at SYRTE.

I show the jury gratitude for taking their time to review the present dissertation adding value to it: Pierre Lemonde and Yann Kersalé as reviewers, and Saïda Guellati, Ginés Lifante Pedrola and Lucile Rutkowski and as examiners.

Finally, I would like to thank and to dedicate this manuscript to my parents for their unconditional support and for always encourage me to do my best along all these years.

Contents

Acknowledgments iii

Acronyms vii

List of Figures ix

List of Tables 1

Introduction 3

1 Context and motivation 7
1.1 Atomic clocks . . . 7
1.1.1 Microwave clocks . . . 8
1.1.2 Optical clocks . . . 9
1.1.3 Dick effect . . . 11
1.2 Narrow-linewidth lasers . . . 13
1.2.1 Ultrastable cavities . . . 13
1.2.2 Exploratory sources . . . 15
1.3 Optical frequency combs . . . 16
1.3.1 Mode-locked lasers . . . 17
1.3.2 The two degrees of freedom . . . 19
1.3.3 Different comb technologies available . . . 23
1.3.4 Combs for frequency metrology . . . 24
1.4 Overview of the SYRTE frequency chain . . . 25

2 SYRTE frequency chain: techniques and noise analysis 29
2.1 The operational frequency chain . . . 29
2.1.1 The Er:fiber and Ti:sa comb main oscillators . . . 29
2.1.2 Frequency combs in the narrow linewidth regime . . . 31
2.1.3 Outputs of the Er:fiber comb . . . 35
2.2 Counting the signals . . . 37

2.2.1 The phase/frequency counter . . . 37
2.2.2 Noise floor of microwave measurements . . . 40
2.2.3 Noise floor of optical measurements . . . 46
2.3 Multi-branch topology: technical noise added . . . 50
2.4 Conclusion . . . 53

3 Accuracy and stability of the SYRTE frequency chain 55
3.1 Comparing clocks and oscillators . . . 55
3.1.1 Expression of absolute optical frequencies . . . 56
3.1.2 Expression of optical frequency ratios . . . 57
3.1.3 Examples of comparisons in the microwave domain . . . 59
3.1.4 Examples of comparisons in the optical domain . . . 68
3.2 Comparison setups . . . 71
3.2.1 Optical to microwave comparisons . . . 75
3.2.2 Optical to optical comparisons . . . 79
3.3 Conclusion . . . 84

4 Spectral purity transfer 87
4.1 The transfer oscillator technique . . . 88
4.1.1 Transfer and readout . . . 88
4.1.2 Limits of the implementation . . . 93
4.2 Multi-branch configuration . . . 96
4.2.1 Optical setup . . . 96
4.2.2 Noise limit for 1062 nm - 698 nm transfer . . . 97
4.3 Single-branch configuration . . . 99
4.3.1 Transfer from 1542 nm to 1062 nm . . . 100
4.3.2 Transfer from 1542 nm to 698 nm . . . 103
4.3.3 Double single-branch: from 1062 nm to 698 nm . . . 107
4.4 Direct application to optical lattice clocks . . . 109
4.5 Conclusion . . . 110

Conclusion 113

A Photodetection of an optical beatnote 125

B Deriving the comb mode index and its uncertainty 129

C Fiber noise characterization 133

D OFC auto-relock implementation 139

Bibliography 147

Acronyms

AF atomic fountain

AOM acousto-optic modulator

BIPM Bureau International des Poids et Mesures

CEO carrier envelope offset

CGPM Conférence Générale des Poids et Mesures

CSO cryogenic sapphire oscillator

DDS direct digital synthesizer

EDFA erbium doped fiber amplifier

EOM electro-optic modulator

FBG fiber Bragg grating

HLPD highly linear photodiode

HNLF highly non linear fiber

InGaAs indium gallium arsenide

IRef infrared reference

ITU International Telecommunications Union

LO local oscillator

MLL mode-locked laser

MSF micro-structured optical fiber

OADM optical add and drop multiplexer

OC optical clock

OFC optical frequency comb

OLC optical lattice clock

PBS polarized beam splitter

PD photodetector

PDH Pound-Drever-Hall

PFS primary frequency standard

PLL phase lock loop

PPLN periodically-poled lithium niobate

PSFSs primary and secondary frequency standards

PZT piezo-electric

QPN quantum projection noise

REFIMEVE+ Réseau Fibré Métrologique à Vocation Européenne

ROA Real Instituto y Observatorio de la Armada

SHB spectral hole burning

SI Système International d'Unités

SNR signal to noise ratio

SYRTE Systèmes de Référence Temps-Espace

TAI Temps Atomique International

UMR ultrastabe microwave reference

USL ultrastable laser

VCO voltage control oscillator

List of Figures

1.1 Time and frequency domains of a mode-locked laser output 18
1.2 Connection between the optical and microwave spectra of an OFC . . . 20
1.3 f-$2f$ interferometer used for the f_0 detection. 22
1.4 Overview of the SYRTE operational frequency chain and its connections 27

2.1 Phase lock of the Er:fiber comb to an ultrastable cw laser ν_{IRef} at 1542 nm 33
2.2 Phase lock of the Ti:sa comb to an ultrastable cw laser at 1062.5 nm . . 35
2.3 Simplified scheme of the different operational OFC optical outputs . . . 36
2.4 UMR down-converted RF frequencies measured by the counter 39
2.5 Counter resolution vs noise signal 41
2.6 Comparison of the 36$^{\mathrm{th}}$ comb harmonic against the UMR 42
2.7 Scheme used to model the noise introduced by the $\times$200 box 43
2.8 Stability curves obtained from the $\times$200 noise model 45
2.9 Optical beatnote detection and real-time f_0 demodulation 45
2.10 Setup used to measure the phase response of the 1 kHz filter 48
2.11 Dephasing induced by the 1 kHz narrow band-pass filter (top plot), and maximum fractional frequency bias for a given optical frequency and its corresponding fractional drift rate (bottom plot) 49
2.12 Averaged fractional values and fractional stabilities after the Er:fiber 1 comb optical amplifiers 52
2.13 Averaged fractional values and fractional stabilities after the Er:fiber 2 comb optical amplifiers 52

3.1 Fractional frequency stability of the frequency ratio between the SrB OLC and the atomic fountain FO2-Cs (orange), and the Hg OLC (green) 60
3.2 Ultrastable microwave reference: oscillators and links' stabilities 61
3.3 Principle of work of the 200-multiplier box and the scheme used to characterize the different microwave references 62
3.4 1 GHz microwave reference signal stability 63
3.5 Stabilities of all microwave references available 64
3.6 Comparison of UMR against the IRef laser and dedrift implementation . 67

3.7 Optical ultrastable oscillators comparison . . . 70
3.8 Hg and Sr USLs comparison in the Er:fiber 1 and Ti:sa combs . . . 71
3.9 Simplified scheme of the three independent RF chains adapted to their respective combs for the measurement capacity evaluation of the operational frequency chain . . . 72
3.10 Optical to optical frequency chain evaluation . . . 73
3.11 Optical to microwave stability comparison . . . 78
3.12 Overall comb's comparison agreements in the microwave domain . . . 79
3.13 Multi-branch optical comparison between the two fiber combs and single-branch direct cycle slip detection . . . 81
3.14 Optical to optical stability comparison . . . 83
3.15 Overall comb's comparison agreements in the optical domain . . . 84

4.1 Principle of the transfer of spectral purity . . . 90
4.2 Out-of-loop assessment of the spectral purity transfer . . . 93
4.3 Multi-branch transfer scheme . . . 97
4.4 Multi-branch spectral purity transfer stability . . . 99
4.5 Single-branch and double single-branch schemes . . . 100
4.6 Optical setup for the 1542 nm $\rightarrow$ 1062 nm transfer . . . 101
4.7 Single-branch spectral purity transfer stability from ν_{IRef} to ν_{HgL} . . . 103
4.8 PPLN doubling crystal spectrum vs temperature for EDFA 2 of Er:fiber 2 104
4.9 Optical setup picture for the ν_{IRef} to ν_{SrL} spectral purity transfer . . . 104
4.10 Optical setup for the 1542 nm $\rightarrow$ 698 nm transfer . . . 105
4.11 Single-branch spectral purity transfer stability from ν_{IRef} to ν_{SrL} . . . 106
4.12 Dual single-branch spectral purity transfer stability from ν_{HgL} to ν_{SrL} . 108
4.13 Normalized optical ratio $\nu_{\mathrm{Hg}}/\nu_{\mathrm{Sr}}$ between the Hg and Sr OLCs . . . 110

C.1 Typical optical setup for fiber noise compensation . . . 134
C.2 Fiber noise characterization optical setup . . . 136
C.3 Fiber noise results . . . 137

D.1 Auto-relocking system design and main connections . . . 141
D.2 Auto-relocking software's decision tree . . . 145

List of Tables

2.1 Intra-cavity actuators of the Er:fiber and Ti:sa combs 30
2.2 DDS absolute noises vs frequency counter resolutions 39
2.3 Frequency agreements of the Er:fiber combs EDFAs 53

3.1 Corresponding values for repetition rates (f_{rep}) and their harmonics (n), offset frequencies (f_{offset}) and DDS frequencies (f_{DDS}) used for the OFCs accuracy and noise assessment 74
3.2 Comb mode N numbers with their signs and frequency shifts 74
3.3 optical to microwave averaged frequency differences and measurement resolutions 78
3.4 optical to optical averaged frequency differences and measurement resolutions 83

4.1 Noise components in a transfer oscillator scheme 95

Introduction

There is no doubt that time and its reciprocal quantity, frequency, constitutes one of the most quotidian physical quantities, alongside length and mass. Scientists and technicians have always tried to understand, define and measure it as precisely as possible with the instruments of their respective technological ages. To do so meant first finding a basis for comparison. The search in nature for a reference, i.e. a physical periodic phenomenon, was based since the ancient Egypt in the motion of the stars. Thus, various time-measurement artifacts or clocks began to appear: sundials, clepsydras, hourglasses, mechanical clocks and, in 1927, quartz clocks. All of these timekeeping technologies were based on the observable apparent movement of the Sun, to define the most basic unit of time, the second, as $1/86\,400$ of the Mean Solar Day. In other words, time has been connected to, until relatively recently, the rotation of the Earth, with astronomers in charge of its determination.

In 1875, representatives from several nations attended the *Convention du Mètre* in Paris with the task of standardizing the physical magnitude of the meter. The *Comité International des Poids et Mesures* was created under the decision-making body of the *Conférence Générale des Poids et Mesures* CGPM. At the beginning of the 20th century, with the advent of vacuum based pendulum clocks, astronomers confirmed the fluctuations in the rotation of the Earth due to tides, seasonal effects and geological phenomena. The fact that the velocity of Earth's rotation was decreasing did not surprise them as Newton had already predicted an apparent acceleration of the motion of the Moon. This is the reason why, in 1960, when the *Système International d'Unités* SI was created during the 11th CGPM, the definition of the second was once again redefined[1] in terms of the translation of the Earth as $1/31\,556\,925.975$ of the tropical year at 1900. This first definition of the SI second improved the long term stability but was not very practical for users other than astronomers.

The spectacular progress in the field of atomic physics and microwave spectroscopy revolutionized the art of "materializing" time with the invention of cesium (Cs) atomic clocks by locking a microwave source to an atomic resonance, first demonstrated in England at the National Physical Laboratory by L. Essen and J. V. L. Parry [1]. Due

[1] The International Astronomical Union in its General Assembly in 1952 had already redefined the second only in terms of the translation of the Earth, i.e. based on the sidereal year.

to the performance and accessibility of the output frequencies of these clocks, the SI second was redefined[2] in the 13th CGPM (1967) as "the duration of 9 192 631 770 periods of the radiation corresponding to the transition between the two hyperfine levels of the ground state of the caesium 133 atom" [3]. Contrary to the rotation of the Earth, no effect leading to a change of the fundamental frequency of the atoms is known, even now. It is therefore a reference much more "convenient" since it is steady. Since then, continuous refinements have improved the early relative accuracies of 10^{-10}, at a rate of approximately a factor 10 per decade, until the most advanced ones, the atomic fountains, which have reached their quasi fundamental limit in the low 10^{-16}.

Since the demonstration of the first laser by T. H. Maiman in 1960 [4], based on the idea of and previous work on masers by A. L. Schawlow and C. H. Townes [5], it was clear that the use of optical frequencies in metrology would provide much better clocks. The use of frequencies around five orders of magnitude higher than Cs clocks would allow an optical standard to reach a much better stability as it depends on the ratio of the clock transition to its linewidth. The advent of laser cooling techniques in 1980s made possible cold Cs atomic fountains, in the microwave domain, but few attempts were done in the optical domain. Optical frequency measurements relied on the those cumbersome multiplication frequency chains available in just a few institutions and that were dedicated to a specific optical transitions.

The development of optical clocks OCs was greatly stimulated by the advent of optical frequency combs (OFCs) which provided a grid of well known frequencies from the near IR to the near UV. This made it possible to measure and compare different optical frequencies, and even more importantly, to connect them to the microwave ones where the main time and frequency techniques and infrastructures exist. From that point on, the new generation of OCs, aimed at probing ultranarrow optical transitions (natural linewidth ≈ 1 mHz) has not only revolutionized precision timekeeping but also has stimulated interest in quantum physics, general relativity and geophysics.

In recent years, the performance of OCs have surpassed their counterparts in the microwave range which currently define the unit of time and the *Temps Atomique International* TAI. Systematic uncertainties below 10^{-18} have been demonstrated [6], raising the prospect of a new (third) redefinition of the SI second in the coming years. Despite of their performances, they have not reached their quasi fundamental quantum projection noise. The optical transition interrogation is still limited by a source of technical noise due to the sampling of the residual frequency noise of the interrogation laser known as the Dick effect. The development of even more stable lasers is therefore necessary to improve the clock stability. Nevertheless, these local oscillators operate in the visible at

[2]The SI second definition was modified in the 26th CGPM (2018) to be in agreement with the other base unit definitions (in terms of a fixed numerical value) and was effective from the 20th of May 2019 as follows: "The second, symbol s, is the SI unit of time. It is defined by taking the fixed numerical value of the caesium frequency $\Delta\nu_{Cs}$, the unperturbed ground-state hyperfine transition frequency of the caesium 133 atom, to be 9 192 631 770 when expressed in the unit Hz, which is equal to s^{-1}" [2].

specific metrological wavelengths to reach the desired clock transitions, while the best USLs have been built by locking them in ultrastable cavities in the infrared region. In consequence, the employment of an OFC is required to transfer the stability from the infrared domain to the target visible wavelengths.

Again, among all physical quantities, frequency (and time) is the most accurate quantity measured so far. Its accuracy is given by the precise counting of the zero crossings of a pure periodic physical signal. OFCs have enabled the high precision measurements required to implement and compare optical clocks. However, they must be carefully assessed and characterized both in terms of stability and accuracy to provide trustworthy and consistent frequency results together with their associated frequency chains, what has been the first objective of this PhD work. In parallel, these OFCs allow us to benefit from other USLs often built at very distant wavelengths than the ones required for the clocks by transferring their spectral purity. Moreover, the transfer of the same source to oscillators probing the respective atomic transition will lead to common mode noise and therefore to an improvement of the stability of the comparison between the two clocks, which has been the second objective pursued during this thesis. The present manuscript is organized as follows:

We will briefly review in the first chapter the evolution of the different type of atomic clocks available and we will notably show that OCs are now so advanced that they should soon become the reference clocks. We will outline the existing technologies and methods to built ultrastable lasers, focusing on high-finesse Fabry-Perot cavities as they provide the most stable lasers to date. Regardless of the chosen technology, the laser sources used as local oscillators will set the technical noise limit of the optical clock because of the Dick effect. The different atomic frequency standards at SYRTE will be shown and the architecture to measure and compare their output frequencies via OFCs will be described. The chain connects the optical standards to the microwave ones where the current time keeping infrastructure relies on, allowing the development and innovation of optical metrology techniques and systems.

The second chapter is dedicated to a detailed description of the two different technologies of metrological frequency combs used, their referencing to ultranarrow linewidth lasers that are locked to ultrastable cavities, and their comparison to a common microwave reference. We will see how the measuring process is carried out, which includes the noise characterization of the critical parts of the frequency chain.

We will show on the third chapter the equations used at SYRTE to compare optical clocks among them through frequency ratios and versus microwave clocks. When the last ones are the atomic fountains existing in the institution they will provide us with an absolute optical frequency, as they are in charge of realizing the SI second and steering the TAI. We take advantage of the availability of different OFCs to implement independent frequency chains so as to be able to study and evaluate the stability and accuracy limits imposed by our metrological architecture both in the microwave and

optical domains.

Finally, we explain the new approaches we have followed to transfer the spectral purity among four different metrological wavelengths along the fourth chapter. This method is of primary importance as OCs work in the visible domain but best USLs are usually built in the IR one. This is because lasers and optics are more developed in the IR domain thanks to the telecommunication industry and where better performances are achieved when using Fabry-Perot cavities to stabilize them, as the cavity fundamental thermal noise is better averaged. Thereby, their spectral purities must be transferred to the target visible ranges. Transferring the best source stability to several interrogation lasers improves the individual clock stability, minimizing the Dick effect. Furthermore, since the noise process leading to the Dick effect is in common mode, it is largely suppressed when clocks are probed synchronously by oscillators featuring the same spectral properties (the ones of the master laser), which helps to characterize faster their systematic effects.

Chapter 1

Context and motivation

1.1 Atomic clocks

At the beginning of the last century quantum physics uncovered the quantized energy levels of matter and the idea of clocks founded on discrete atomic transitions started to be considered. It is then when we stopped looking only at the stars in search of a frequency reference in nature and we started looking deep inside matter itself. The first demonstration of the idea came in 1949 with the implementation of an atomic clock based on the ammonia molecule [7, 8]. A few years later, in 1955, the first cesium-based atomic clock was realized [1].

Since then, a multitude of technical improvements have been instituted, leading to better performance with much higher accuracy and stability, which are the two properties that characterize any clock (atomic or not). On the one hand, the accuracy tells us how well the measured clock frequency $\nu(t)$ matches that of the reference used, in our case, the unperturbed atomic resonance ν_{at}. This variable represents the knowledge (and control) one has on systematics effects, i.e. the small energy shifts in the atomic transition itself caused by various internal perturbations such as interactions among atoms and external perturbations such as the Zeeman shift due to the coupling to an external magnetic field, which offset ν_{at}. On the other hand, stability is the repeatability of the measured $\nu(t)$ over time, expressed at a given time constant, which accounts for the noise introduced during measurement. In the case of an atomic clock limited by its quasi fundamental noise, i.e. the quantum projection noise of the atoms, stability over a given averaging time τ can be expressed as:

$$\sigma_y(\tau) \approx \frac{1}{Q_{\mathrm{at}}}\sqrt{\frac{T_{\mathrm{c}}}{\tau N}} \tag{1.1}$$

where τ/T_{c} is the number of measurements taken and N is the averaged number of probed atoms in the cycle time T_{c}. $Q_{\mathrm{at}} = \nu_{\mathrm{at}}/\Delta\nu_{\mathrm{exp}}$ is the experimental quality factor of

the clock transition for an experimental linewidth $\Delta\nu_{\text{exp}}$, which is limited either by the interaction time or by the coherence time of the source.

1.1.1 Microwave clocks

The first atomic clocks, based on Cs, were demonstrated in 1955 by L. Essen and J. V. L. Parry [1] and made the definition and adoption of the atomic time possible. These clocks use a thermal atomic Cs beam in a high vacuum chamber, where atoms are set in their minimum state of energy for the chosen transition. This is done by deflecting the atoms according to their magnetic moment by an inhomogeneous magnetic field. Once the atoms are in the desired (ground) state, they are sent to a microwave resonator that is fed by the radio frequency derived from a voltage controlled quartz crystal oscillator (VCXO). This last acts as the local oscillator (LO) and it is tuned to the frequency transition at 9.192 GHz. After leaving the resonator, a second magnetic field deflects the excited-state atoms into a detector, whose signal is used to deduce the frequency offset between the atomic transition and the LO, thereby providing an error signal suitable to derive the necessary correction to apply to the LO and keep it at resonance with the atoms. Consequently, a servo loop adjusts the oscillator's frequency in order to keep the received detector's current at a maximum.

Further improvement was made in these clocks regarding magnetic state selection, where only 1/16 of the atoms were set in the desired state. Preparation and detection was then performed by optical pumping [9], that allowed fractional stabilities of $3.5 \cdot 10^{-13}$ at 1 s, but performance was still limited by the quality factor of the thermal beam $Q \approx 10^8$.

Years later, in the 1980s, the progress in laser cooling and trapping techniques allowed for a new generation of microwave atomic clocks, the so-called atomic fountains (AFs) [10, 11]. In these clocks, the atomic samples are previously laser cooled by three pairs of counter-propagating laser beams, eventually leading to an increase of both the interaction time and the clock quality factor in two orders of magnitude. When the sample is ready, they are turned off and two vertical lasers throw the atoms upwards into a microwave-filled cavity. Due to gravity, they fall back down, passing through the cavity once more, resembling a fountain, hence the name. A final probe laser intercepts the sample after the round trip. Atoms in which the atomic states have been altered by the microwave cavity will emit light (fluorescence) which is then detected and used to tune the frequency's cavity.

The development of ultralow noise microwave sources, such as cryogenic sapphire oscillators (CSOs) [12, 13], has allowed the AFs to beat the Dick effect (sampling of the frequency noise of the source probing the metrological transition [14]) and reach the fundamental limit in the atomic transition interrogation given by the quantum projection noise (QPN). However, CSOs complexify the setup and require periodic maintenance due to the helium refill required to maintain the correct cryogenic temperature. To overcome this difficulty pulse-tube cryocoolers [15, 16], including commercial devices [17],

or a continuous flux of cold atoms [18] have been implemented.

Atomic fountains have reached short-term stabilities in the low 10^{-14} with accuracies around $1-2\cdot10^{-16}$ after a few days of averaging [19, 20, and references therein]. Their limited stability (around one day to reach a statistical resolution of 10^{-16}) imposes a hard practical limit of these clocks, preventing to push significantly further the control of their systematic effects and, thereby, improving their accuracy within a reasonable averaging time. Currently, they are the most accurate microwave clocks and are used to calibrate the atomic time scale, a function for which the Cs based ones received the name of primary frequency standards (PFSs).

1.1.2 Optical clocks

Since most systematic effects do not depend on the frequency of the clock, it was clear that operating clocks at higher frequencies would decrease drastically their fractional contribution, providing a much better resolution in time. This gave rise to a strong incentive toward the development of optical clocks, i.e. systems based on atomic frequency references lying on the optical domain. There were several technological difficulties that made them impractical. First, the need for spectrally ultranarrow lasers, at the relevant wavelengths, capable of probing the ultranarrow optical clock transitions (see subsection 1.2). Second, the lack of a tool capable of counting the light oscillations as electronics are not fast enough to follow them (see subsection 1.3). And third, whereas atomic microwave fountain clocks utilize a freely expanding cloud of atoms, it appears highly beneficiary, for realizing ultrahigh accuracy optical clocks, to use trapped atoms with a trapping mechanism that has a negligible impact on the atomic transition. For charged ions, this can be realized with carefully designed electromagnetic traps, as was pioneered several decades ago [21], but for neutral atoms, it was only in 2003 that a solution was proposed and implemented [22], as it will be discussed in the next paragraphs. Improvements in laser sources with narrower linewidths, and the advent of optical frequency combs brought the solution by not only providing a way to measure optical frequencies directly but also a coherent link between the optical and microwave regions of the electromagnetic spectrum. This resulted in a revolution in the field of optical frequencies' metrology and in the arrival of a new generation of clocks.

Optical clocks operate with frequencies that can be 10^5 times higher than their microwave counterparts. This, together with narrower atomic transitions, give them quality factors that could, in principle, exceed 10^{16} if laser sources become one day as narrow as the metrological transitions themselves (a few mHz wide). In contrast, the quality factor of atomic fountains is limited to 10^{10} because of the Fourier limit imposed on the experimental linewidth by the finite duration of the Ramsey spectroscopy (typically $\approx 0.5\,\mathrm{s}$). They consist of two different parts, a laser source (clock laser) and an atomic system that provides a reference frequency with which laser radiation can be compared and corrected. The laser source is a continuous wave (cw) ultrastable laser that functions

as the clock LO necessary for the clock transition interrogation. Once the clock laser is cyclically (typically every $0.5 - 1$ s) locked to the atomic transition, its frequency is measured by an OFC that allows to compare it to other clocks.

There are two types of OCs based on a radiative transition in the electron shell that are currently being investigated: ions and neutral atoms. Electrically charged particles like ions are easier to trap and confine than neutral atoms. In order to keep an ion confined in space, a combination of a quadrupole electric field and a magnetic field, Penning trap [23], or a time-varying electric field, Paul trap [24], is used. Once it is cooled and confined, it shows very long trapping lifetime, which benefits the clock transition interrogation and uptime. However, due to the strong interaction between ions that would be captured in the same trap, these clocks have so far mostly been restricted to just one particle, which limits their stability. To date, the major disadvantage is the long integration time needed to reach their limit because of their small signal-to-noise ratio (SNR), but still accuracies as low as $3 \cdot 10^{-18}$ in a $^{171}Yb^{+}$ single-ion clock [25] and $9.4 \cdot 10^{-19}$ in a $^{27}Al^{+}$ quantum logic clock [6] have been demonstrated. The use of a small number of ions is possible in linear quadrupole traps [26], and crystal-like structures with higher numbers of ions have been achieved in three-dimensional Paul traps, which could potentially increase the stability. The ongoing multiple-ion chain designs [27] are also good candidates to improve the short-term stability of ion clocks.

Neutral atom clocks, which came after the former ones, offer a higher SNR due to the large number of atoms used but where initially limited by the residual velocity of the absorbers when free expansion neutral atom OCs were implemented [28, 29]. Their weak atom-light interactions and the strong shifts induced on the internal atomic structure by these interactions involved a more complex trapping process than those used in ions. To date, they typically make use of a magneto-optical trap to initially cool the atoms and of an optical lattice to have them tightly confined by the dipole force. Hence, the atoms are in the Lamb-Dicke regime, where the length scale associated with their motion is much smaller than the wavelength of the laser probing the atoms, making them immune to a large extent to motional effects like Doppler and photon-recoil effects. But still, the trapping light induces unequal light shifts to the clock states. The solution to this issue was introduced by H. Katori when he imagined the strategy of confining atoms in an optical lattice at the so-called “magic wavelength”, where the frequency shift for the fundamental and excited states is the same to the first order [22]. Unlike ions, neutral atoms interact with each other in a much weaker way, and in the case of fermions, if strictly indistinguishable, they do not interact at all in the context of s-wave collisions. This makes it feasible to probe a large number (in the order of 10^4) simultaneously in the lattice, leading to a higher SNR and therefore to an increased stability. However, larger ensembles of atoms, combined with tight confinement, lead to higher densities, which might increase collisions, even in the case of fermions, contributing to the systematic inaccuracy. Optical lattice clocks (OLCs) have reached accuracies as

low as $1.4 \cdot 10^{-18}$ [30] for a ^{171}Yb or $2 \cdot 10^{-18}$ [31, 32] for ^{87}Sr and, more importantly, present better stabilities, considerably reducing the averaging time.

Even in the most advanced OCs, whether trapped ion or optical lattice, frequency shifts due to external electric or magnetic fields contribute significantly to the uncertainty budget and the number of absorbers interrogated are limited to $1-10$ for ion or to 10^4 for lattice traps. These limits can be increased with the novel concept of nuclear clocks, in which the local oscillator is frequency-stabilized to a nuclear γ-ray transition. These clocks are much less sensitive to the former systematic frequency shifts, resulting in enhanced accuracy, and the ability to interrogate more than 10^{10} absorbers (nuclei) thereby increasing stability. XUV or even X-ray transitions, can be also considered when suitable radiation sources become available. Even so, research on nuclear clocks is possible with existing laser technology, as demonstrated by the interrogation of a low level transition in the ^{229}Th [33, 34].

1.1.3 Dick effect

In any passive atomic frequency standard, the target is to measure the probability, P, of the atomic transition once it is interrogated by its local oscillator so that, after a servo loop, the frequency of the local oscillator can be tuned towards the accurate atomic frequency. Since the LO is not perfect, it will show some frequency fluctuations, $\delta\omega_{\mathrm{LO}}$, which will result in a probability change, δP.

The best atomic clocks, both microwave and optical, are probed (and corrected) with a process that is periodic and discontinuous. The frequency of the local oscillator is compared to the frequency of the atomic resonance of interest during a certain time period, i.e the spectroscopy time T_{sp}, of the clock cycle T_{c}. The rest of the time within the T_{c}, where the atoms do not see the frequency fluctuations of the LO, is the dead time. This time accounts for the state detection and restart of the cycle, including the loading and preparation of the atomic sample in the case of atomic fountains or OLCs. The transition probability change related to $\delta\omega_{\mathrm{LO}}$ integrated over the spectroscopy time is given by [35]:

$$\delta P = \frac{1}{2}\int_0^{T_{\mathrm{sp}}} g(t)\delta\omega_{\mathrm{LO}}(t)dt \tag{1.2}$$

where $g(t)$ is the sensitivity function that describes the atoms' sensitivity to frequency fluctuations of the LO during T_{sp}, being 0 when the atoms are not probed. The clock duty cycle is defined as $\eta = T_{\mathrm{sp}}/T_{\mathrm{c}}$ and depends on $g(t)$, which, in turn, depends on the type of interrogation performed (Rabi or Ramsey). The longer is η the better the frequency fluctuations of the interrogation oscillator are averaged out, determining the efficiency of the averaging process.

This stroboscopic probing leads to a frequency stability degradation of the oscillator, named the Dick effect, after G. J. Dick first derived it [14]. This effect is due to an alias-

ing of the harmonic Fourier frequencies of $1/T_c$ present on the LO residual frequency noise for $\delta\omega_{LO} > \delta\omega_{at}$. The contribution of the Dick effect to the Allan variance is given by [36]:

$$\sigma^2_{y,\mathrm{Dick}}(\tau) = \frac{1}{\tau g_0^2} \sum_{m=1}^{\infty} |g_m|^2 S_{y,\mathrm{LO}}\left(\frac{m}{T_c}\right)\Bigg(\tag{1.3}$$

where $S_{y,\mathrm{LO}}$ is the one-sided power spectral density of the relative frequency fluctuations of the free-running oscillator used for interrogation at Fourier frequencies m/T_c. The Fourier coefficients of $g(t)$ are given by:

$$g_m = \frac{1}{T_c}\int_0^{T_c} g(t)\mathrm{e}^{-2\pi i m t/T_c} dt \tag{1.4}$$

Because of the dead time, the frequency of the local oscillator is actually sampled by the cycle, so the noise that is measured on P is not only directly the noise of the oscillator but also its high frequency noise, at Fourier frequencies equal to m/T_c, which is folded back into the low frequencies. Once we close the feedback loop, this high frequency noise is imprinted on P, degrading therefore the final fractional stability.

Nowadays the clocks with the best short-term stabilities, the OLCs, are limited to the low 10^{-16} by the Dick effect. The noise introduced by this effect comes on top of other sources of technical noise, preventing clocks to reach the quasi[1] fundamental limit imposed by the QPN of the atoms involved in the spectroscopy process. There are four different approaches to reduce the contribution of the Dick effect and therefore to improve the clock stability:

1. To build a more stable clock laser, since the Dick effect comes directly from its frequency noise. Additionally, a narrower spectral linewidth laser will enhance Q_{at}, improving the fractional stability according to equation 1.1.

2. To optimize the time sequence in such a way that T_{sp} is directly increased or the dead time is decreased. One can reduce the loading time by refining the dynamics so that the preparation of the atomic sample is faster, carrying out non-destructive detection schemes in order to keep the atoms in the trap after detection [37, 38]. Hence, the atoms can be recycled (without being thrown out of the lattice trap) for subsequent clock state interrogations.

3. To implement zero-dead-time clocks, this way while one clock is being interrogated the other is preparing the sample and vice versa. This approach has led to a fractional instability as low as $6 \cdot 10^{-17}/\sqrt{\tau}$ for an averaging time τ in seconds [39] when compared to another dead-time clock.

[1] The use of squeezed atomic states could help to circumvent this limit.

4. To operate two optical clocks synchronously and probe each with the same clock laser. Since $g(t)$ and $S_y(f)$ are the same for the two clocks at the time of their comparison, the Dick effect cancels out, facilitating the characterization of the systematic effects. An unprecedented fractional stability of $3.5 \cdot 10^{-17}/\sqrt{\tau}$, dominated by the QPN, has been demonstrated recently [40] using this method. Thanks to the novel spectral purity transfer scheme implemented (see subsection 4.4), this method has been also performed between the strontium (Sr) and mercury (Hg) OLCs at SYRTE.

1.2 Narrow-linewidth lasers

Ultrastable lasers (USLs) are lasers featuring a spectrum where most of the power is contained in a narrow, sub-Hertz, window and low short-term instabilities. They play a fundamental role in applications which involve precision measurements like optical frequency standards [40], atom interferometry and gravitational wave detection [41], search of dark matter [42] or novel radar applications [43]. In particular, they are key elements for OCs where they allow the atomic ultranarrow (in the mHz range) "clock" transition interrogation, constituting their LOs, at the same time providing a measurable output. The coherence time (up to 10 s or more) of these prestabilized lasers sets the experimental linewidth and therefore the statistical resolution, that will determine the speed at which systematic effects can be determined. Nonetheless, the current limited laser's linewidth (not yet as narrow as the natural width of the atomic transition) and its associated Dick effect prevent the state-of-the-art OCs to reach the full stability that is, in principle, permitted by their clock transitions.

Accordingly, great effort has been put into their development. The traditional method is based on ultrastable (finesse of a few 10^5) Fabry-Perot cavities in well-controlled environments. This involves vibration isolation platforms, vacuum systems, temperature control and thermal and acoustic shielding to strictly control the thermo-mechanical length fluctuations. To date, the best USLs are stabilized to these reference cavities. However, even these state-of-the-art laser sources are still the limiting factor of the performance of OCs, preventing their stabilities from reaching their fundamental limit, the QPN.

In parallel, promising alternatives have been studied in the last ten years such as superradiant lasers and spectral hole burning techniques. These will be summarized in the next subsections.

1.2.1 Ultrastable cavities

Ultrastable cavities generally follow a Fabry-Perot design, consisting of two very high reflective mirrors, plane or concave, optically contacted to a spacer featuring a central

bore. The optical contacting is necessary to avoid the addition of a material (glue) that would have a different sensitivity to temperature and therefore would lead to unwanted stress on the mirrors. The laser is transmitted through the bore and its optical modes have a diameter at the mirror surface that is determined by the cavity geometry. Single frequency lasers are stabilized to one of the longitudinal modes of the cavity, usually one of the TEM00 modes[2], via the Pound-Drever-Hall (PDH) technique [44]. Thanks to the passive cavity, that acts as frequency discriminator, these stabilized lasers provide a well-defined frequency.

The different types of noise's sources from vibrations (mechanical, seismic or acoustic perturbations), pressure, and temperature fluctuations that are affecting the cavity induce a change of its total optical path length and degrades the frequency stability of any laser stabilized to it. In order to reduce temperature fluctuations to typically less than $1\,\mu$K and isolate it from vibrations, the cavity is placed in a vacuum enclosure outfitted with passive (thermal and acoustic shielding layers) and active (thermo-electric such as Peltier controllers) elements. The setup rests over an anti-vibration platform, that attenuates the vibration from the ground beyond Fourier frequencies of 1 Hz typically. It was demonstrated that the thermal noise plays a fundamental role for Fabry-Perot cavities and that the contribution of the spacer, the mirrors substrates and coatings could be calculated [45]. Classical 10-cm long Fabry-Perot cavities were limited to the mid 10^{-16}, which is why research groups started to investigate materials less exposed to thermal noise and alternative possibilities such as long and/or cryogenic cavities.

The Brownian motion, i.e. thermally excited local and random displacement of the masses of the cavity constituents, is the fundamental noise that ultimately limits the stability cavity performance. Since this noise scales as $1/\sqrt{L}$ in a spacer of length L, and scales with $1/w_0$ and $1/w_0^2$ for the mirror substrates and coatings respectively, where w_0 is the radius of the laser mode on the mirror, the following (and complementary) approaches are being implemented:

- Increasing the size mode on the mirror surfaces enhances the cavity stability since a bigger mirror surface will better average out the Brownian noise. One can do that by excitation of higher order TEM modes or operating the cavity close to instability conditions [46] (as the waist will diverge) at the expense of an increased alignment sensitivity that, in turn, results in a higher sensitivity to vibrations. Additionally, one can go for longer wavelengths since the beam waist scales with $\sqrt{\lambda}$ [47].

- Lengthening the cavity on the one hand reduces the fractional length fluctuations since they scale inversely with the total optical path length. On the other hand, longer cavities easily lead to a higher temperature gradient that fluctuates with the

[2] In some cases higher finesses are obtained with higher transversal modes due to likely local contamination on the mirror's coatings.

ambient temperature, which implies a better control of the resonator temperature and makes much more challenging to suppress the vibration noise. An instability of $8 \cdot 10^{-17}$ for an ultralow expansion (ULE) glass with fused silica mirror substrates 48-cm long cavity [48] has been demonstrated.

- Enclosing and operating the cavity under cryogenic condition reduces the thermal motion of the system [49, 50, 51]. However, cryostats make the operation more complex, add some extra vibration noise (because of the cooling mechanism), and require a periodic maintenance due to the cooling gas refill. Even so, an instability as low as $4 \cdot 10^{-17}$ for a crystalline silicon (Si) monocrystal (spacer and mirror substrates) has been achieved [49].

- Identifying materials showing both a high reflectivity and a low mechanical dissipation. Mirrors implementing high-reflectivity dielectric multilayer coatings on transparent substrates by ion beam sputtering (IBS) have been traditionally the best option available. A promising solution came in 2013 when substrate-transferred single-crystal semiconductor heterostructures appeared, also know as "crystalline coatings" [52, 53]. In comparison with their counterparts IBS coatings, they have demonstrated a lower Brownian noise, higher thermal conductivity and even a wider spectral coverage (including the mid-infrared range), representing nowadays the state-of-the-art-mirror's coatings.

1.2.2 Exploratory sources

Spectral hole burning

Despite the various approaches currently pursued to stabilize lasers in ultrastable cavities, an alternative strategy is to frequency lock the laser to narrow spectral features previously photo-imprinted in a rare-earth doped crystal by spectral hole burning [54].

Rare-earth elements such praseodymium (Pr) or europium (Eu) in crystalline matrices at cryogenic environments exhibit absorption lines of a few GHz linewidth (inhomogeneous broadening). One can imprint on them one or several narrow spectral patterns or "holes" by selectively pumping the resonant rare-earth atoms into a dark long-lived state. For the case of $Eu^{3+} : Y_2SiO_5$, they show homogeneous linewidths of 1 kHz and lifetimes from several hours up to several days at very low temperatures (< 4 K). This requires a pre-stabilized laser with a fractional stability of only 10^{-12} at $0.1 - 1$ s, according to the spectral width feature. Once the pattern is photo-inscribed, the same laser can be frequency locked to these spectral features, improving its former stability that typically comes from a commercial Fabry-Perot cavity.

Important progress for continuous operation of this technique, regardless of the degradation of the spectral hole [55] and improved cryostats setups, which better isolate the science chamber from the cooler, have been achieved. Moreover, a novel method

for generating the error signal is employed at SYRTE, where the optical phase is measured by the beat frequency against a single sideband, sufficiently frequency detuned to be only marginally influenced by the absorption spectrum [56]. This work was very recently improved by a double-heterodyne probing [57], which has reached a fractional stability of $1.7 \cdot 10^{-15}$ at 1 s, reducing substantially the former detection noise.

There are some challenges such as matrices and dopants with lower sensitivity to residual environmental perturbations, excessive vibrations due to the cooling cycles, highly temperature-stable and even lower cryogenic regimes that are under investigation. Still, fractional short-term stabilities as low as $6 \cdot 10^{-16}$ [58] and long-term extremely low frequency drifts [59] of a few mHz/s have been demonstrated.

Superradiant lasers

Great progress has taken place since superradiant lasers started to be considered for frequency standards' applications [60]. Superradiance takes place when the probability amplitudes in a spontaneous decay of several atoms interfere constructively [61]. Alkaline-earth-metal atoms, such as Sr or ytterbium (Yb), with longer excited lifetimes are currently under research.

Unlike passive optical clocks, in active references, the phase information needed to correct the local oscillator is collected directly from the clock transition emitted light. Thus, these lasers rely on the coherence of this light, maintained by an optical lattice that is trapping the atoms, rather than the coherence provided by the cavity standing wave (affected by length fluctuations due to the the thermal noise induced in the cavity mirrors). The collective emission of photons is achieved by operating the system in the "bad cavity" regime, as masers do in the microwave domain, where the linewidth of the atomic transition is narrower than the linewidth of the cavity.

A fractional stability of $7 \cdot 10^{-16}$ at 1 s has been shown recently [62] and promising investigations on ^{88}Sr [63] are currently rising interest on these highly stable laser sources. Active optical clocks might provide in the coming years a new way to reach the fundamental limits of optical frequency standards without the need of complex ultrastable cavity setups.

1.3 Optical frequency combs

Nowadays optical frequency combs are the fundamental key technology used in optical metrology as they work as precise rulers in frequency space that allow us to accurately measure optical frequencies. The pulsed aspect first appeared when the new technique of active mode-locking was demonstrated for pulse generation in a He-Ne laser back in 1964 [64]. Their use in precision spectroscopy became of big interest and began to sprout in the following years [65]. However, most of those experiments were relying on

optical wavelengths measurements via interferometers whose accuracies are limited to a few parts in 10^{10} due to unavoidable distortions in the wavefronts. Since time is the most accurate physical quantity measured, counting the number of cycles per second will provide us with a frequency f instead of a wavelength λ. In 1983 the speed of light was defined as a constant $c = 299\ 792\ 458$ m/s, which guaranteed a frequency to wavelength direct conversion with no loss of accuracy. But when referring to optical frequencies[3], ν, rather than radio or microwave ones, f, we are limited by the existing technology. The electronics are not able to follow the rapid optical oscillations and this is the reason why frequency counters and photodetectors (PDs) are limited up to the GHz range.

To overcome this limitation, a few national metrology institutes started to build up the frequency chains, which started from a Cs clock realizing the SI second. After a large number of steps involving non linear devices of different technologies and phase-lock transfer oscillators, only a single optical frequency was reached at the top end chain. The complexity, low flexibility (it had to be reconfigured for each different targeted frequency) and considerable investment in terms of cost, man-power and space, made these frequency chains impractical. For this reason, they were only built and operational in the most advanced laboratories [66, 67, 68].

The situation suddenly changed in 1999 when the first demonstrations of mode-locked femtosecond (fs) lasers for accurate frequency measurements took place [69]. The well-defined phase coherence across a broad spectrum of frequencies, together with novel techniques for non linear interaction, allowed to generate broad-bandwidth spectra of such fs lasers. This permitted to measure and control their offset frequency and gave birth to OFCs. Their impact on precision laser-based spectroscopy was recognized worldwide with half of the Nobel prize awarded jointly to T. W. Hänsch and J. L. Hall in 2005 [70]. They were the missing key technology that finally allowed the development of optical clocks among many other applications [71] and they were rapidly adopted by various communities all over the world.

1.3.1 Mode-locked lasers

Mode-locked lasers (MLLs) have a broadband gain medium to support a very large number of modes for a given cavity geometry. When a fixed phase relationship between all the lasing modes is implemented, they interfere constructively generating short optical pulses separated by $T_{\text{rep}} = L/c$, where L is the total optical length of the cavity. The frequency output is described by the formula $\nu_N = N \cdot f_{\text{rep}} + f_0$ where f_{rep} refers to the repetition rate of the MLL, f_0 is the carrier-envelope offset frequency, and N is the integer comb mode index, as shown in Fig. 1.1

[3] Optical frequencies will be intentionally written as ν to differentiate them from RF or microwave frequencies that will be denoted as f.

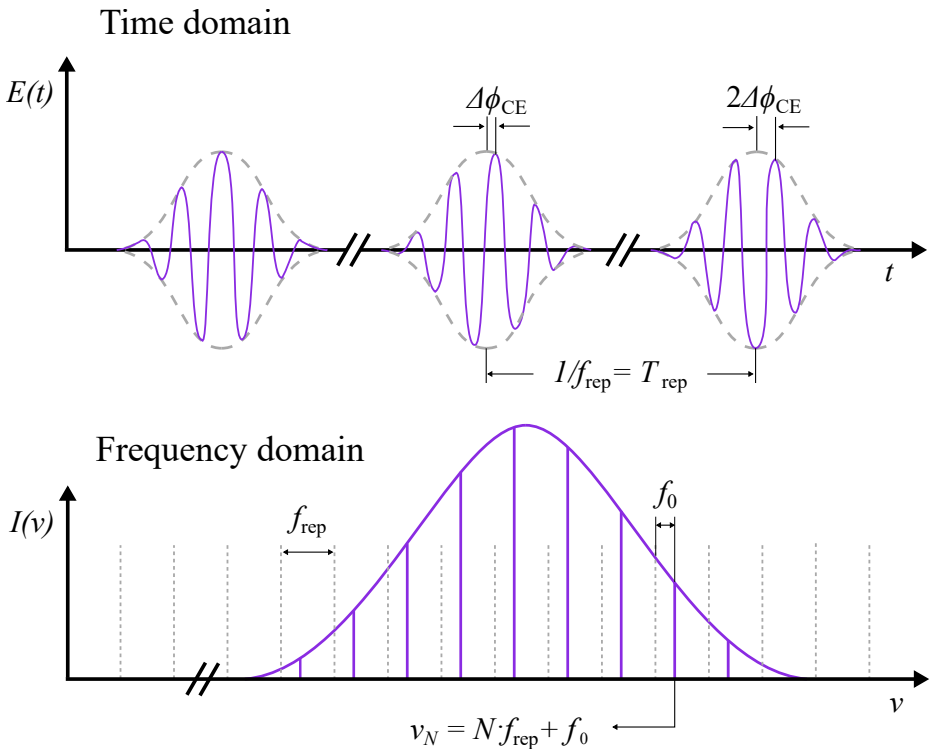

Figure 1.1: Time and frequency domains of a mode-locked laser output. The carrier wave (purple) shifts by $\Delta\phi_{CE}$ after each round trip with respect to the envelope (gray) due to their respective different phase and group velocities. The Fourier transfer of the train of pulses in time provides a comb of discrete modes whose frequency spacing is f_{rep} and whose origin is given by $f_0 = \Delta\phi_{\text{CE}}/T_{\text{rep}}$.

The mode-locked regime can be achieved either with active elements that are able to modulate the light inside the cavity or with passive techniques. These last ones can make use of saturate absorber materials (dye or semiconductors) or act as artificial absorbers implementing non-linear effects such as Kerr lens [72], polarization rotation [73] or fiber loop mirrors [74].

In order to ensure that short pulses are preserved, it is necessary to control the intra-cavity dispersion by interleaving prism pairs or chirped mirrors, for free-space cavities, or dispersion shifted (opposite signed) fibers. The ultimate pulse length duration will be given by the combination of the mode-locking mechanism, the net gain and the group velocity dispersion.

1.3.2 The two degrees of freedom

To understand a MLL longitudinal-mode structure and how frequency-domain methods can be used for its stabilization, we must have a close look at the two parameters describing the mode structure: f_{rep} and f_0. The first one has been measured and controlled early on, while the second one had to wait until the sources and nonlinear fiber optics facilitate spectral broadening [75] over twenty years ago now. This was precisely the key requirement in order to fully control the comb structure of a MLL, converting it into an OFC.

The repetition rate

To detect the repetition rate, f_{rep}, of the OFC we simply need to send the periodic bursts of light at the output of a MLL towards a PD. Since the PD detects the power of the incoming electric field, cross terms provide us with beatnotes corresponding to the different spectral components interfering together.

In the time domain, $T_{rep} = 1/f_{rep}$ is the time interval between two constructive interferences between all the circulating modes, while in the frequency domain f_{rep} is the frequency difference between two adjacent modes.

To illustrate where the spectrum comes from, let us assume a MLL with no intracavity dispersion, i.e. the carrier envelope phase does not change between two consecutive pulses ($f_0 = 0$). This train of identical pulses $E(t)$ can be represented as:

$$E(t) = \sum_{n=-\infty}^{\infty} E_p\left(t - nT_{rep}\right) \tag{1.5}$$

where T_{rep} is the time between pulses and n is an integer number that indicates the number of the pulse.

Since $E(t)$ is a periodic function, we can express equation 1.5 as a Fourier series, using a Poisson summation [76]:

$$\begin{aligned} E(t) &= \sum_{N=-\infty}^{\infty} \frac{1}{T_{rep}} \tilde{E}_p\left(N/T_{rep}\right) \exp\left(j2\pi Nt/T_{rep}\right) \\ &= \sum_{N=-\infty}^{\infty} f_{rep} \tilde{E}_p\left(Nf_{rep}\right) \exp\left(j2\pi Nf_{rep}t\right) \end{aligned} \tag{1.6}$$

where $\tilde{E}_p$ is the Fourier transform of E_p and N is the index of the frequency or comb mode number. Each term of the sum (longitudinal modes) composing the comb has an amplitude given by the Fourier transform of the function defining an isolated pulse, this is, $\tilde{E}_p$.

The output of the PD yields:

$$I(t) = \alpha \left|E\left(t\right)\right|^2 = \sum^{N} E_N\left(t\right) \cdot \sum^{N} E_N\left(t\right)^* \tag{1.7}$$

Developing equation 1.7 until $N = 6$, one finds the corresponding first four f_{rep} harmonics detected:

$$\begin{aligned} I(t) = \alpha \big[& \ldots + \tilde{E}_{p2}\tilde{E}^*_{p1} \exp\left(j\omega_{\text{rep}}t\right) + \ldots \\ & + \tilde{E}_{p3}\tilde{E}^*_{p1} \exp\left(j2\omega_{\text{rep}}t\right) + \tilde{E}_{p3}\tilde{E}^*_{p2} \exp\left(j\omega_{\text{rep}}t\right) + \ldots \\ & + \tilde{E}_{p4}\tilde{E}^*_{p1} \exp\left(j3\omega_{\text{rep}}t\right) + \tilde{E}_{p4}\tilde{E}^*_{p2} \exp\left(j2\omega_{\text{rep}}t\right) + \tilde{E}_{p4}\tilde{E}^*_{p3} \exp\left(j\omega_{\text{rep}}t\right) + \ldots \\ & + \tilde{E}_{p5}\tilde{E}^*_{p1} \exp\left(j4\omega_{\text{rep}}t\right) + \tilde{E}_{p5}\tilde{E}^*_{p2} \exp\left(j3\omega_{\text{rep}}t\right) + \tilde{E}_{p5}\tilde{E}^*_{p3} \exp\left(j2\omega_{\text{rep}}t\right) + \ldots \\ & + \tilde{E}_{p5}\tilde{E}^*_{p4} \exp\left(j\omega_{\text{rep}}t\right) + \ldots \big] \end{aligned} \tag{1.8}$$

where $\omega_{\text{rep}} = 2\pi f_{\text{rep}}$ and $\tilde{E}_{pN} = f_{\text{rep}}\tilde{E}_p\left(Nf_{\text{rep}}\right)$.

We see the spectral components appearing, harmonics of f_{rep}, and that each term is the constructive interference of many contributions. In practice, the summation in N does not extend on an infinite number of modes due to the limited gain of the laser medium. For instance, a spectrum between 1515 nm and 1595 nm and a $f_{\text{rep}} = 250\,\text{MHz}$, would let us observe typically around 40 300 modes.

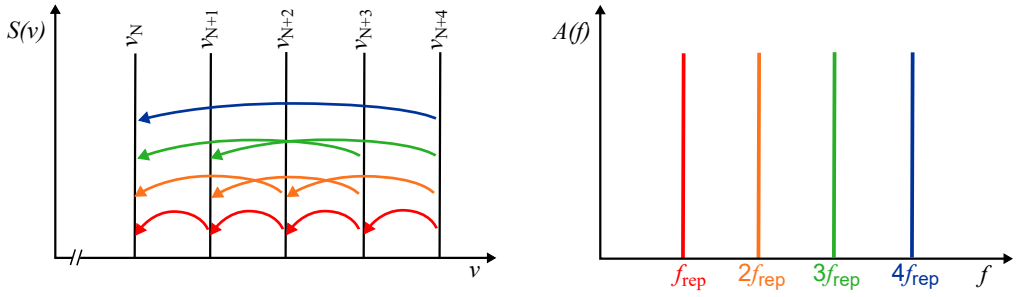

Figure 1.2: Connection between the optical spectrum and the microwave spectrum provided by the PD thus yielding the f_{rep} harmonics detection.

The carrier envelope offset frequency

To really understand the spectrum of an OFC it is necessary to explain the carrier envelope (CE) phase, ϕ_{CE}, determined by the phase difference between the envelope peak and the maximum peak amplitude of the carrier wave. Taking into account ϕ_{CE}, equation 1.6 becomes:

$$E(t) = \sum_{N=-\infty}^{\infty} f_{\text{rep}}\tilde{E}_p\left(Nf_{\text{rep}}\right) \exp\left[j\left(2\pi N f_{\text{rep}}t + \phi_{\text{CE}}\right)\right] \tag{1.9}$$

If we consider the decomposition of each electromagnetic pulse n in an envelope and a sinusoidal carrier wave (see top plot in Fig. 1.1), we are now able to define for each of the two waves a medium propagation velocity: the phase velocity of the carrier wave, v_p, and the group velocity of the envelope, v_g. In a laser medium (dispersive), where the index of refraction is dependent of the wavelength, these different velocities provoke a dephasing between the carrier and the envelope from one pulse to the next. After one round trip, the $\Delta\phi_{\text{CE}}$ is given as a function of the phase and group velocities by [77]:

$$\Delta\phi_{\text{CE}} = \left(\frac{1}{v_g} - \frac{1}{v_p}\right) L\omega_c \tag{1.10}$$

where L is the round-trip length of the cavity.

If we include a pulse-to-pulse shift, $\Delta\phi_{\text{CE}}$, means the pulses are not all identical, and the spectrum of the comb is no longer the simple Fourier series from equation 1.6. Assuming that v_g and v_p are constant, i.e. $\Delta\phi_{\text{CE}}$ is a fixed value, we can express the CE phase of a pulse n as $\phi_{\text{CE}} = n\Delta\phi_{\text{CE}} + \phi_0$. Inserting ϕ_{CE} in equation 1.9 and taking the Fourier transform, according to [78], we get:

$$E(\omega) = \exp(j\phi_0)\tilde{E}_e(\omega - \omega_c) \sum_{M=-\infty}^{\infty} \delta\left(\Delta\phi_{CE} - \omega T_{\text{rep}} - 2\pi M\right) \tag{1.11}$$

Equation 1.11 finally express the real spectrum of an OFC, comprised by a set of discrete modes, whose frequencies are given by the comb of Dirac deltas as:

$$\omega_M = M\frac{2\pi}{T_{\text{rep}}} - \frac{\Delta\phi_{CE}}{T_{\text{rep}}} \tag{1.12}$$

or, in terms of frequency:

$$\nu_M = M \cdot f_{\text{rep}} - \frac{\Delta\phi_{CE} \cdot f_{\text{rep}}}{2\pi} = M \cdot f_{\text{rep}} + f_0 \tag{1.13}$$

where the offset frequency $f_0 = -\frac{\Delta\phi_{CE} \cdot f_{\text{rep}}}{2\pi}$ is the quantity we were looking for. Note that changing the sign in this expression would simply change the sign in the definition of $\Delta\phi_{CE}$. In Fig. 1.1 the connection between the time and frequency domains is illustrated.

To conclude, we have seen that dispersion of the medium produces jumps on the ϕ_{CE} from one pulse to another, changing f_0. The knowledge and/or control of f_0 is necessary to unequivocally define the electric field of the comb and, therefore, it allows us to perform phase/frequency comparisons across different parts of the electromagnetic radiation spectrum.

The $f - 2f$ interferometer

The most common and simplest way to measure f_0 is with the self-referencing technique which needs a spectrum broad enough to cover at least one octave, i.e. a ratio of the high

and low frequency 2:1. This explains the use of a micro-structured optical fiber (MSF) or an erbium doped fiber amplifier (EDFA) followed by a highly non linear fiber (HNLF) after the main oscillator output in the case of fiber-based OFCs so as to span the initial spectrum. The MSF or HNLF keeps the phase coherence condition between the modes involved in the consecutive four wave mixing processes [79, 80].

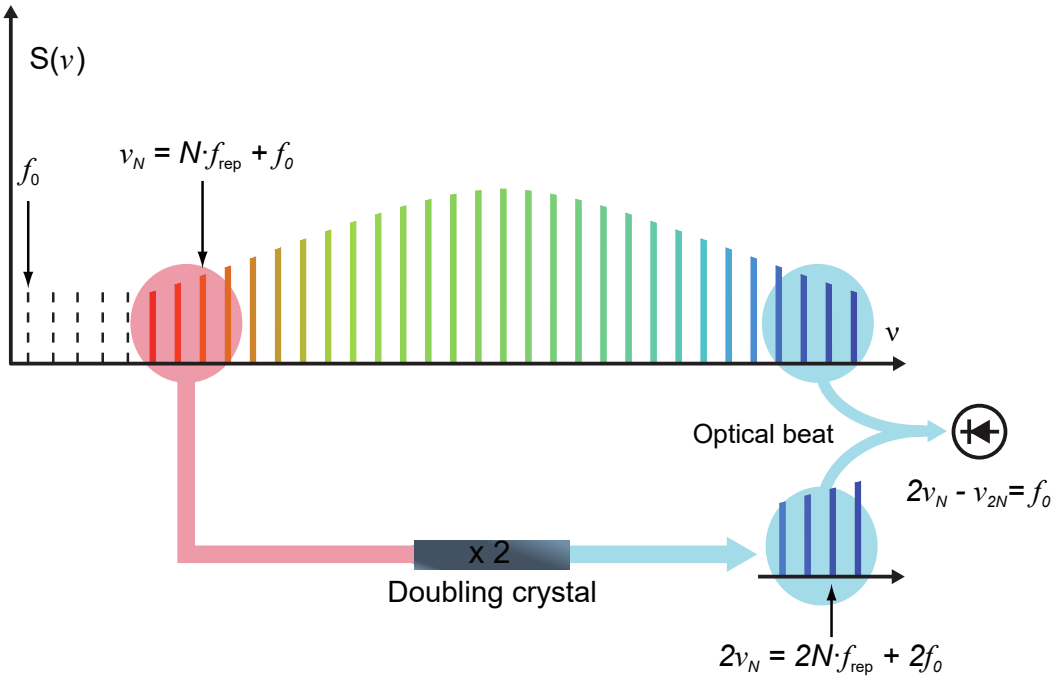

Figure 1.3: f-$2f$ interferometer used for the f_0 detection.

At the output of the MSF/HNLF, the modes from the low end of the gain profile of the OFC spectrum are frequency doubled in a nonlinear crystal, generally a periodically-poled lithium niobate (PPLN) or a lithium triborate (LBO), $2\nu_N = 2N \cdot f_{\text{rep}} + 2f_0$, and combined with modes from the high end of the gain profile at frequencies $\nu_{2N} = 2N \cdot f_{\text{rep}} + f_0$, as shown in Fig. 1.3. Thus, the second harmonic of the N^{th} mode (from the low-frequency wing) is beaten with the $2N^{\text{th}}$ mode (from the high-frequency wing) [81]. After photodetection, we end up with a beatnote that is precisely f_0 which results from the interference $|\nu_{2N} - 2\nu_N|$. The frequency doubling takes place for many pairs of modes which interfere coherently at the same time. The amplitude of the signal is increased and, more importantly, the signal-to-noise ratio when those pairs feature the same phase. One must have in mind that the optical power per pulse is in the order of hundreds of nW, so these pairs' modes coherent addition is critical for the f_0 detection.

It is important to remark the fact that all the pairs of modes contributing must be under phase-match condition. It is then necessary to control in the best possible way

the total dispersion of the optical system of the two arms of the $f-2f$ interferometer so that when they pass through the PPLN crystal they have identical phases.

This type of interferometer can be, for example, arranged in a Mach-Zehnder configuration although other approaches like Michelson, prism pair delay line or Wollaston prism-based interferometers are possible. Furthermore, other self-referencing schemes can be also performed by measuring any frequency difference between different harmonics of the same laser. The former octave span required can be reduced at the expense of using two or more nonlinear optical processes or additional lasers [81, 69].

1.3.3 Different comb technologies available

Traditionally fs solid state titanium ion-doped sapphire crystal (Ti:sa) combs have been extensively used in laboratories for many experiments. The recent progress on combs has expanded this technology to other interesting alternatives such as solid-state lasers like chromium-doped crystals (Cr:LiSAF or Cr:forsterite) and fiber ones like erbium or ytterbium doped fibers (Er:fiber, Yb:fiber, among others) [71].

In the same way fiber-based lasers boosted the research looking for reliable, cost-effective and transportable combs leaving behind their bulky counterparts. A new photonics breakthrough has arisen with the micro-cavity resonator based combs or micro-combs in the last ten years. These micro-combs stand out for their extremely low-power optical pump to enhance non linearities needed for the mode-locked pulsed operation [82]. This has permitted their integration in complementary metal-oxide semiconductor (CMOS) electronic circuits bringing ultra-compact, low-cost and energy-efficient solutions. Moreover, due to their small-size cavities they provide access to repetition rates ranging from 10 GHz to 1 THz which has become of great interest for microwave photonics [83] and telecommunication applications [84].

This manuscript is based on experiments involving the two comb technologies available at SYRTE, Ti:sa and Er:fiber, and their main differences are now briefly described in the next lines.

Ti:sa combs, as they pioneered this technology, are part of many laboratory setups and have been very well characterized but they are also commercially available. They are centered around 800 nm with a pulse length of $10-50$ fs. These short pulses together with the high intra-cavity power make them intrinsically less noisy [85] since they show less amplified spontaneous emission frequency noise, and they provide a high average output power at a single output. They can have repetitions rates up 10 GHz [86] and cover the spectral window $500-1100$ nm, which makes them an excellent choice for optical clocks (mostly in the visible) except for their limited uptimes due to the Kerr-lens mode-lock mechanism that is challenging to keep in a continuous long-term operation.

Er:fiber combs oscillate around 1550 nm with a wider pulse duration ($80-300$ fs). They present lower repetition rates (typically 100 MHz or 250 MHz) and they go from 1000 nm to 2000 nm, so doubling or spectral broadening is often required to access most

optical clock wavelengths. Nevertheless, their 24/7 mode-locked operation, robustness and low maintenance makes them a reliable choice for long and frequent measurements.

1.3.4 Combs for frequency metrology

The increased demand on OFCs has motivated the research of new fs laser sources to keep improving the high specifications needed for metrology-based applications such as optical frequency measurements, optical clocks, low-noise frequency synthesis, etc. In this context, there are several key properties that should be meticulously taken into account. In the first place is the repetition rate that typically goes from a few tens MHz up to a few GHz. The higher the repetition rate the more power per comb mode N we will have for a given average optical power, and the easier it will be to identify the comb modes. Having some tunability is also an advantage since it will facilitate the N index determination (see appendix B). Frequency and amplitude noise also plays a fundamental role. Unlike the noise arising from temperature or acoustics fluctuations, the one coming from pump lasers and spectral broadening in non-linear fibers can lead to unwanted decoherence in the spectrum that could limit the comb noise floor. The spectral range covered is also application-dependent, especially in optical clocks where many different lasers are at play. The spectral bandwidth provided by the OFC itself will determine the need for further spectral broadening to reach the octave typically required for self-referencing methods. Other features like size, weight and power should be also considered, in particular, for field-applications or transportable combs.

Principle of measurement with optical frequency combs

In the frequency domain, the optical teeth of an OFC can be described by its two degrees of freedom that we have presented in subsection 1.3.2: f_{rep} and f_0. The frequency of each of the longitudinal modes[4], ν_N, contained in its spectrum is given by:

$$\nu_N = N \cdot f_{\text{rep}} + f_0 \tag{1.14}$$

where f_{rep} is the repetition frequency, N is the corresponding index of the comb mode and f_0 the offset frequency, whose offset can be positive or negative.

In order to measure the frequency of an optical source like laser, ν_{L}, the approach is to photodetect the beatnote between the light from the comb and light from the source. Recalling equations A.6 and A.7 from appendix A and taking only the cross terms we

[4]The longitudinal modes are equally named peaks or teeth of the OFC.

are interested in:

$$
\begin{aligned}
I_{\mathrm{PD}}(t) &\propto \Big|\sum_N |E_N| \exp\big(2\pi j(N f_{\mathrm{rep}} + f_0)t\big) + |E_{\mathrm{L}}| \exp(2\pi j \nu_{\mathrm{L}} t)\Big|^2 \\
&= \sum_{N \neq M} 2E_N E_M^* \mathrm{Re}\{\underbrace{\exp\big(-2\pi j(N f_{\mathrm{rep}} - f_0 - M f_{\mathrm{rep}} - f_0)t\big)}_{\text{comb harmonics: } f_{\mathrm{comb},K}}\} \\
&+ \sum_N 2E_N E_{\mathrm{L}}^* \mathrm{Re}\{\underbrace{\exp\big(-2\pi j(\nu_{\mathrm{L}} - N f_{\mathrm{rep}} - f_0)t\big)}_{\text{beatnotes: } \tilde{f}_{\mathrm{L},N}}\} + \ldots
\end{aligned}
\tag{1.15}
$$

From equation 1.15 we see that there are several possible beatnotes, some of them corresponding to the beats between the laser and the different comb's teeth, $\tilde{f}_{\mathrm{L},N}$, and others to the f_{rep} harmonics detected, $f_{\mathrm{comb},K}$ (with $K = N - M$). The expected RF power of a single beatnote $\tilde{f}_{\mathrm{L}}$ is very small (usually in the order of hundreds of pW) compared to each of the $f_{\mathrm{comb},K}$, where lots of terms are contributing. It is necessary to filter out the part of the spectrum ranging from f_{rep} to the bandwidth of the PD to get rid of the unwanted comb harmonics in order to avoid the amplifier's detector suffering from saturation. Since we know that there is a beatnote in the segment $[0, f_{\mathrm{rep}}/2]$, the strategy is to low-pass filter the output of the photodetector at a cut-off frequency slightly higher than $f_{\mathrm{rep}}/2$. Doing that, we not only remove the undesirable f_{rep} harmonics but also we constrain the search to an optimized and unique beatnote (the one between the laser and the closest tooth), that is expressed as:

$$
\tilde{f}_{\mathrm{L}} = \mathrm{sign}_{\mathrm{L}}(\nu_{\mathrm{L}} - N_{\mathrm{L}} \cdot f_{\mathrm{rep}} - \mathrm{sign}_0 \cdot f_0) \tag{1.16}
$$

where $\tilde{f}_{\mathrm{L}}$ is the frequency of the optical beatnote and the tilde denotes its f_0 dependency. The signs of the beatnote and the offset frequency, $\mathrm{sign}_{\mathrm{L}}$ and sign_0, must be also taken into account since all frequencies are positive by definition.

1.4 Overview of the SYRTE frequency chain

The current state of the art of optical frequency standards have been possible thanks to the combination of the three types of systems we have described in this chapter. Optical clocks are composed of atomic ensembles probed by the respective necessary USL radiation, while the free-running USLs are compared one to the others by OFCs. In order to connect the various elements, we can not forget a fourth component that deserves its own attention: the frequency chain. At the end of the day, the frequency chain is necessary to link and precisely synchronize every single measurement taken (frequency conversions, comparisons, phase/frequency lock loops, etc.) so as to express meaningful results. Thus it forms the core, together with the OFCs, of a metrological architecture.

At SYRTE there are six different atomic clocks[5]. In the microwave domain, there are three AFs that are among the few operational primary and secondary frequency standards (PSFSs) nowadays steering the TAI, a uniform time scale computed and disseminated monthly through the *Bureau International des Poids et Mesures* (BIPM) *Circular T* from clock data provided by about 80 institutes. The FO1 and the FOM, are both based solely on Cs atoms, while the dual FO2 is operated simultaneously with Cs and rubidium (Rb) atoms. This added atomic specie (Rb) shows smaller collisional effects and it also allows for new tests of fundamental Physics inside the same apparatus. The FOM is a mobile fountain that can be transported in order to perform local absolute frequency measurements. Since 1999, three OLCs have been under development: Sr1 (since 1999), Hg (since 2005) and Sr2 (since 2006). Sr clocks are based on the narrow 429.2 THz $^1S_0$ – $^3P_0$ transition of the fermionic Sr isotope 87, while the Hg clock is based on the narrow 1 128.6 THz $^1S_0$ – $^3P_0$ transition of the fermionic Hg isotope 199 of their respective neutral atoms. In this optical domain, there are also two cell-based di-iodine (I_2) optical frequency standards based on molecular absorptions operated at 582.5 THz, and an ongoing experiment to realize spectral hole burning patterns based on the absorption $^7F_0$–$^5D_0$ transition in $Eu^{3+}Y_2SiO_5$ at 516.9 THz to post-stabilize a stable laser at 258.4 THz.

Along with all these clocks are the necessary ultrastable oscillators to interrogate their atomic or molecular metrological transitions. The three AFs operating in the microwave region are interrogated with a cryogenic sapphire oscillator (CSO) whose natural frequency is 11.932 GHz. In order to keep the crystal at a temperature of 6 K, it is kept in a bath of 250 liters dewar of liquid helium that must be refilled every 26 days [88]. The CSO short-term fractional stability of $2-3\cdot10^{-15}$ at 1 s allows the fountains to operate at the fundamental QPN limit, reducing considerably the integration time needed to perform their accuracy budget evaluation. Despite having an almost two orders of magnitude better stability than a hydrogen active maser (H maser), the CSO long-term stability starts degrading after 1000 s since it is a free-running oscillator. In order to benefit from both the CSO short-term stability and the H maser long-term one, the former is phase-locked to the latter with a time constant of 1000 s, constituting the ultrastabe microwave reference (UMR) of the laboratory. The final frequency at 11.98 GHz, it is subsequently rescaled to match eigen frequencies of Cs (9.192 GHz) and Rb (6.834 GHz) clocks, and to produce also a 1 GHz reference signal that is distributed to all the SYRTE experiments. The maser is needed for the local time scale realization UTC(OP) output which is periodically (three times per day) corrected by the AFs via a micro-phase stepper (MPS).

In the optical domain there are seven ultrastable cavities:

[5] We are not considering the five thermal beam commercial Cs clocks contribution to the free atomic time scale (*Echelle Atomique Libre, EAL,* in French) or the two compact Cs cell atomic frequency standards based on pulsed coherent population trapping in the Dicke regime [87] for GNSS applications' improvements.

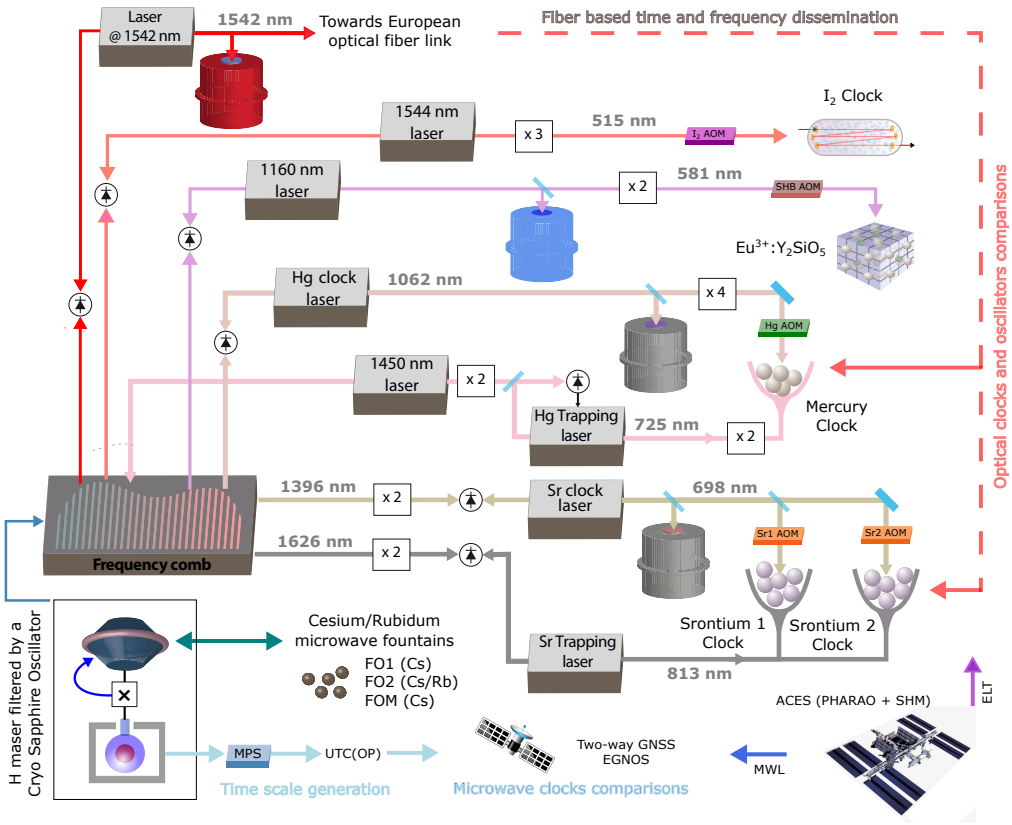

Figure 1.4: Overview of the SYRTE operational frequency chain and its connections. The operational OFC is based on an Er:fiber fs laser which is backed up by an almost identical second one.

- One IR cavity at 1542 nm is used to optical reference the two measurement Er:fiber OFCs. These two combs are transferring the cavity stability to and between other lasers, e.g. to 1542 nm and 1544 nm lasers used for the I_2 frequency standards (after frequency tripling) or the Hg trapping lattice laser at 1450 nm. This IR cavity is also stabilizing the seed laser in charge of the French metrological network REFIMEVE+ (*Réseau Fibré Métrologique à Vocation Européenne*) [89], which is connected to the other equivalent networks available in Europe to disseminate and compare optical frequency standards on a continental scale.

- There are two other auxiliary cavities also at the same wavelength used for novel time and frequency transfer techniques [90, 91], and for referencing other fiber based OFCs performing low phase noise microwave generation signals [92].

- A last IR cavity of 40-cm long, with crystalline mirror substrates and coatings, is under development and is expected to surpass the performance of the existing ones and become the operational IR cavity in the next years. This cavity and the former two IR ones are not represented in Fig. 1.4.

- There are two cavities that are directly connected to the three OLCs. One at 698 nm that is shared and used by the two Sr OLCs, and the second at 1062.5 nm is used for the Hg OLC (after frequency quadrupling). The lasers locked to these cavities have noise floors at 4 and $5 \cdot 10^{-16}$, respectively.

- The seventh cavity operates at 1160 nm and it is used to provide the pre-stabilized light needed at 580 nm (after frequency doubling) for the specific absorption spectral pattern photo-imprinted by SHB in the former Eu^{3+}-doped crystal.

The described oscillators must be connected on the one hand to the atomic or molecular transitions they aim at probing (Sr, Hg, I_2 or Eu^{+3}), and on the other hand to a frequency chain allowing to compare all of them together. Here the OFC becomes the masterpiece of this structural framework since it has enabled optical clocks metrology by measuring absolute optical frequencies and by intercomparing them. Thereby, the OFC and all the intermediate components interleaved all along the way are essential and must be well characterized. One of the central topics of this PhD work was therefore to measure the stability and the accuracy of all the elements of the architecture connecting the SYRTE frequency standards, and to ensure that no element limits the performance.

A crucial feature of the chain is its reliability, it must be robust and run continuously. For example for a comparison between the Sr and the Hg OLCs, to get a frequency measurement with a resolution at the 10^{-17}, considering that the stability is around $10^{-15}/\sqrt{\tau}$, we would need 10 000 points. But if we take into account the uptime of the two clocks together, in practice, this becomes typically in one day of integration. Automation is therefore fundamental, especially for large scale comparisons among multiple clocks [93] and for the coming European Space Agency mission Atomic Clock Ensemble in Space (ACES) [94, 95], scheduled to fly onboard the International Space Station in mid 2021. Ground stations will need to provide data continuously both for evaluation of the PHARAO[6] clock itself and ground atomic clocks' comparisons via its microwave link (MWL) with the possibility of optical time transfer thanks to its optical link (European Laser Timing, ELT) by exchanging laser pulses with the ground Satellite Laser stations.

[6] *Projet d'Horloge Atomique Par Refroidissement d'Atomes* in French. It is a microgravity Cs clock based on laser cooled atoms, similar to a ground-based atomic fountain, with an accuracy in the low 10^{-16}. PHARAO together with the Space Hydrogen Maser (SHM) constitutes the core of the ACES payload.

Chapter 2

SYRTE frequency chain: techniques and noise analysis

2.1 The operational frequency chain

After the general picture of the architecture of the SYRTE frequency chain previously introduced, in this section we focus on its critical parts. We describe in detail the operational erbium doped fiber (Er:fiber) and titanium ion-doped sapphire crystal (Ti:sa) combs that are making possible all connections between the different oscillators and clocks of the optical and of the microwave domains. We also describe the noise characterization of some particular components which play a fundamental role, and the technical noise added when using additional erbium doped fiber amplifiers (EDFAs) as it is the case for the Er:fiber OFCs.

2.1.1 The Er:fiber and Ti:sa comb main oscillators

In the OFC laboratory we count with three operational frequency combs of two different technologies. One Ti:sa comb that has been operating since 2000 and two commercial Er:fiber combs of different generations which have taken over as operational combs since 2009, due to their highly reliable mode-lock mechanism and easy-handling operation.

The Er:fiber comb is the output of a fiber fs laser mode-locked based on the nonlinear polarization effect [73], where a proper choice of orientation for the birefringent intra-cavity wave-plates strongly favors a pulsed mode operation. The active medium in the main fiber ring oscillator is Er^{3+}, and this oscillator is pumped by two high power diode lasers at 980 nm. Since the cavity has a few free-space centimeters, it is possible to place some actuators (intra-cavity electro-optic modulator (EOM) and glass wedges) to be able to control the two degrees of freedom of the comb, the repetition frequency (f_{rep})

Type of comb	Coarse tuning and dynamic range		Fine tuning and bandwidth		
			Slow actuator	Fast actuator	
	f_{rep}	f_0	f_{rep}		f_0
Er:fiber	Cavity end mirror mounted on a translation stage ≈ 2 MHz	2 glass wedges (motorized) ≈ 10 MHz	PZT < 5 kHz	EOM < 900 kHz > 5 kHz	DLs curr.
Ti:sa		1 glass wedge (motorized) ≈ 10 MHz	PZT 1 < 50 kHz PZT 2 < 1 kHz	AOM > 400 kHz	

Table 2.1: Intra-cavity elements and actuators used for the coarse and fine tuning necessary to fully control the two degrees of freedom of the Er:fiber and Ti:sa combs.

and the carrier envelope offset (CEO) frequency (f_0), while minimizing unavoidable cross-talks between them.

The Ti:sa comb mode-locked operation is carried out by the Kerr-lens effect [72] that takes place in the sapphire crystal itself, doped by Ti^{3+} ions that act as the active medium. The Ti:sa laser is pumped by a continuous wave (cw) frequency-double neodymium (Nd) YAG laser at 532 nm in a free-space resonant cavity.

At the output of the Er:fiber fs lasers we have pulses of 300 fs with a repetition rate of $f_{rep} \approx 250$ MHz ($T_{rep} = 4$ ns) covering an approximate spectrum of $1515-1595$ nm that will be later amplified by different EDFAs and broaden with HNLFs (see subsection 2.1.3). This leads to a spectrum covering $1050-2100$ nm roughly, what allows to reach both the octave spanning needed for the f_0 detection and all the metrological wavelengths targeted. For the Ti:sa output, the pulse length is typically 30 fs and $f_{rep} \approx 772$ MHz ($T_{rep} = 1.3$ ns). The output is directly broaden on a 20-cm non-linear photonic crystal (PC) which provides a spectral bandwidth of more than one octave around $520-1100$ nm. Note that here all the setup is in free-space and that by definition the continuum generated comes from the same oscillator, i.e. without any amplification stage needed, which leads to a comb less exposed to frequency noise compared to the fiber one [96].

Controlling f_{rep} and f_0

In order to fully exploit the comb we not only need to accurately detect f_{rep} and f_0 but also to control them in a stable way. All the control elements and their main features are summarized in table 2.1.

To act on f_{rep} in the fiber-based combs we modify the total optical path coarsely

with a step motor attached to one of the end mirror cavities and finely with a piezoelectric (PZT) ceramic acting on the same mirror, changing this way the geometrical cavity length. We fine tune it next with an intra-cavity EOM which acts on its round-trip group delay via a voltage controller. The EOM is DC-coupled to the PLL corrector and it is used to make fast adjustments of the refractive index of its crystal and therefore of the optical length of the fs cavity. Similarly, in the Ti:sa comb the f_{rep} is coarsely controlled by one mirror mounted on a translation stage and finely by two mirror-mounted PZT actuators, the first one has a single-stack bandwidth of 50 kHz, and the second one a multi-stack bandwidth of 1 kHz. The fine tuning is performed by an acousto-optic modulator (AOM), used in 0^{th} order, which acts on the optical power of a cw 8 W commercial diode-pumped solid state laser (Verdi) at 532 nm. This AOM has the downside that also affects the f_0 by modifying the dispersion together with the index of refraction.

For the f_0 control, in the case of the Er:fiber combs, a couple of motorized glass wedges are placed to deal coarsely with the intra-cavity dispersion by adding (or removing) a glass thickness in the laser cavity [97]. Hence, these wedges allow for arbitrary shifts of the CE phase from equation 1.10 while keeping dispersion in transmission nearly constant. We additionally act on the current of one of the two pump diode lasers of the main oscillator for a very fine adjustment when needed. On the contrary, in the Ti:sa comb there is only a single glass wedge at Brewster angle what causes a larger coupling of f_{rep}.

2.1.2 Frequency combs in the narrow linewidth regime

The main purpose of locking the OFC to an USL is to transfer the spectral purity of this latter to all the teeth contained in the spectrum covered by the comb, what is known as the "narrow linewidth regime". To do so, our strategy is to eliminate f_0 (by mixing it out from all the beatnotes so that we have a comb which is virtually f_0-free) and to transfer the USL fractional stability to the comb repetition rate.

Phase-lock of the Er:fiber combs to a 1542 nm cw laser

We choose to lock the combs to a 1542 nm USL because the fs main oscillator spectrum is centered close to this value and it is also the chosen wavelength for most European fiber links. To achieve this referencing, we detect a beatnote between the infrared reference (IRef) USL, ν_{IRef}, and the comb. Subsequently, we mix f_0 out and we phase lock the resulting quantity to a DDS.

As depicted on Fig. 2.1, the optical comb spectrum is reflected by an optical add and drop multiplexer (OADM)[1] in a window of 100 GHz around 1542.14 nm (channel 44 of

[1]The equivalent of a narrow band-pass interference filter, from the optical telecommunication technology, used for wavelength division multiplexing. The spectral region (or regions, in case of more than one output) of interest is reflected, i.e. filtered, while the rest is transmitted. Additionally, the device can

the International Telecommunication Union, ITU), and subsequently combined to light from the ν_{IRef}, while the rest of the comb spectrum is transmitted by the OADM.

In order to be less exposed to low frequency electronic noise, we decide to detect the beatnote at the high-range frequencies allowed by the PD which features a bandwidth of 1 GHz. We adjust the value of f_{rep} (tuning the length of the cavity) so as to detect a beatnote at 810 MHz. Thereby, we have:

$$\tilde{f}^{(0)}_{\mathrm{IRef}} = \mathrm{sign}^{(0)}_{\mathrm{IRef}} \left(\nu_{\mathrm{IRef}} + f^{(0)}_{\mathrm{s,IRef}} - N^{(0)}_{\mathrm{IRef}} \cdot f_{\mathrm{rep}} - \mathrm{sign}_0 \cdot f_0 \right) \Bigg(\tag{2.1}$$

where the superscript 0 stands for the main comb output, and being $f^{(0)}_{\mathrm{s,IRef}}$ a frequency shift of -69 MHz. The beatnote $\tilde{f}^{(0)}_{\mathrm{IRef}}$ can be either the beat with the 4$^{\mathrm{th}}$ tooth below $\nu^{(0)}_{\mathrm{IRef}}$ for $\mathrm{sign}^{(0)}_{\mathrm{IRef}} = +1$ or the 4$^{\mathrm{th}}$ tooth above for $\mathrm{sign}^{(0)}_{\mathrm{IRef}} = -1$, since we always keep f_{rep} close to 250 MHz. We target and filter in a narrow (40 MHz) RF band-pass filter centered at 810 MHz when scanning the offset voltage controller of the PZT for the locking of the comb.

Since we want to be in the narrow linewidth regime, where the stability of the optical source is transferred to the comb's teeth, we now proceed to mix f_0 out, so stabilizing only f_{rep} is sufficient as it is the only degree of freedom left. To do so, we demodulate $\tilde{f}^{(0)}_{\mathrm{IRef}}$ with the f_0 signal detected at the output of the $f-2f$ interferometer (see Fig. 2.1), centered around the arbitrary value of 70 MHz and band-pass filtered. Note that this f_0 signal results from the constructive interference of all the coherent pairs of modes generated after the doubling crystal as described in subsection 1.3.2 and it is also available at other combs outputs. For each of the two possible $N^{(0)}_{\mathrm{IRef}}$ numbers, the two available components at the output of the mixer are:

$$\mathrm{sign}_{\mathrm{IRef}} \left(\nu_{\mathrm{IRef}} + f^{(0)}_{\mathrm{s,IRef}} - N^{(0)}_{\mathrm{IRef}} \cdot f_{\mathrm{rep}} - \mathrm{sign}_0 \cdot f_0 \right) \Bigg(\pm f_0 \tag{2.2}$$

In one of these four quantities f_0 has been necessarily canceled out and the beatnote value is close to 880 MHz. We isolate this offset-free beatnote with the help of a tunable large band-pass filter centered at that frequency, getting:

$$f^{(0)}_{\mathrm{IRef}} = \mathrm{sign}^{(0)}_{\mathrm{IRef}} \left(\nu_{\mathrm{IRef}} + f^{(0)}_{\mathrm{s,IRef}} - N^{(0)}_{\mathrm{IRef}} \cdot f_{\mathrm{rep}} \right) \Bigg(\tag{2.3}$$

where $f^{(0)}_{\mathrm{IRef}} \approx 880$ MHz, and one of the two possibilities regarding the $\mathrm{sign}^{(0)}_{\mathrm{IRef}}$ will be f_0-free. It is worthy of remark that frequencies are always positive quantities, and the "sign" coefficient is necessary due to the fact that the frequency of the optical source might be larger ($\mathrm{sign}_{\mathrm{IRef}} = +1$) or smaller ($\mathrm{sign}_{\mathrm{IRef}} = -1$) than the comb's tooth of interest.

be used as a combiner.

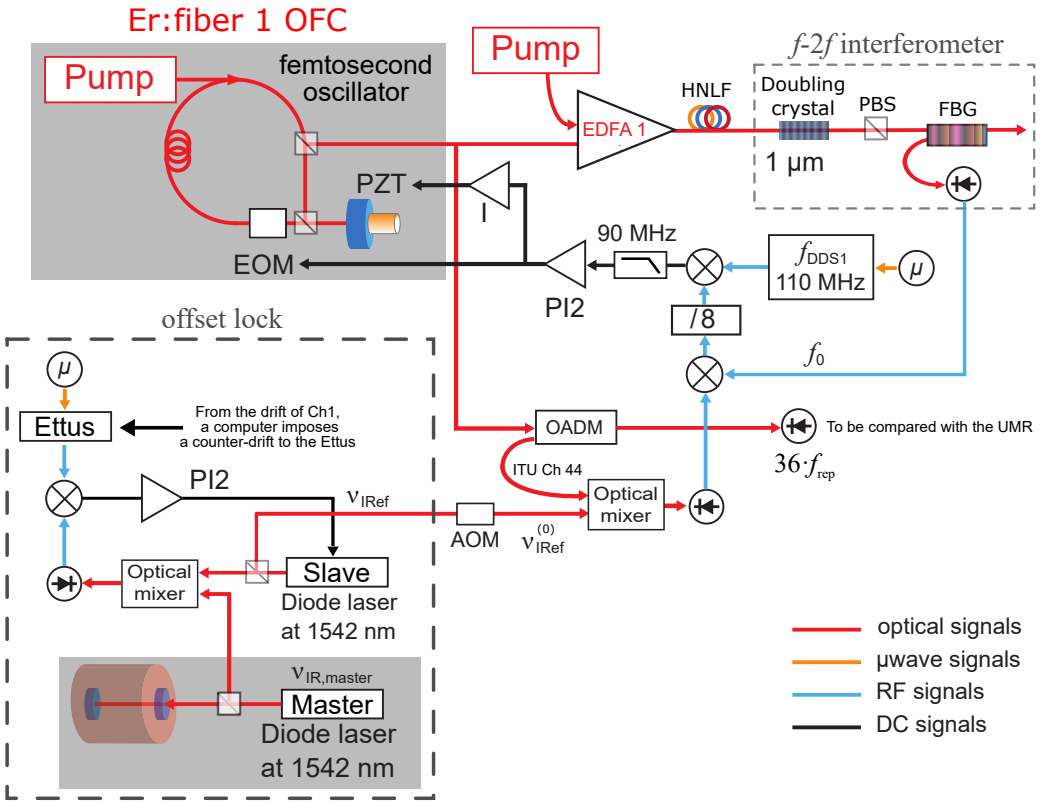

Figure 2.1: Phase lock of the Er:fiber comb to an ultrastable cw laser at ν_{IRef} 1542 nm. Bottom left plot (dash line): offset lock of the slave IR laser (ν_{IRef}) to the master IR laser ($\nu_{\mathrm{IR,master}}$) for the counter-drift of ν_{IRef} (see last example of subsection 3.1.3). AOM: acousto-optic modulator, EOM: electro-optic modulator, FBG: fiber Bragg grating, HNLF: highly non linear fiber, PBS: polarized beam splitter, and PZT: piezo-electric ceramic. The corresponding optical outputs are shown in Fig. 2.3.

We have established a direct one-to-one correspondence between $\nu^{(0)}_{\mathrm{IRef}}$ and f_{rep}. In order to reach the narrow linewidth regime, we divide by a factor $n = 8$ the phase corresponding to $f^{(0)}_{\mathrm{IRef}}$, $\Phi^{(0)}_{\mathrm{IRef}}$, so as to decrease typical phase excursions well below π, and we phase lock the result to a 48-bits DDS at $f_{\mathrm{DDS1}} = 110\,\mathrm{MHz}$. Thereby, the loop operates in the linear regime and avoids cycle slips. The resulting frequency lock is given by:

$$\frac{\mathrm{sign}^{(0)}_{\mathrm{IRef}}\left(\nu_{\mathrm{IRef}} + f^{(0)}_{\mathrm{s,IRef}} - N^{(0)}_{\mathrm{IRef}} \cdot f_{\mathrm{rep}}\right)}{8}\Bigg\rfloor = f_{\mathrm{DDS1}} \tag{2.4}$$

To close the PLL, we induce a feedback first on the intra-cavity EOM with a PI2 controller –a proportional (P) stage followed by a two-cascaded integrators (I2) stage– and second, on the PZT actuator with an independent integrator (I), in order to accurately

control the gains in the various ranges of the Fourier frequency space.

The intra-cavity EOM approach was invented to permit a very fast correction [98]. It has a very high bandwidth to convert voltage changes at the input into a change of the index of refraction, therefore it allows modifying the optical length of the fs cavity very quickly. Thanks to this feature, a bandwidth larger than 800 kHz have been obtained at SYRTE. The PZT actuator is used simply for a slow correction and keeping, at the same time, the correction sent to the EOM close to zero in average. It is complementary to the EOM in a bandwidth < 5 kHz and it allows for tuning the cavity length.

The part of the comb spectrum that is not reflected by the OADM (around 70 mW) is detected by a fast InGaAs highly linear photodiode (HLPD) (DSC40S, Discovery Semiconductors), with a bandwidth up to 16 GHz, which yields at its output RF and microwave components at the repetition rate and its harmonics.

Phase-lock of the Ti:sa comb to a 1062.5 nm cw laser

The optical reference lock for this comb is performed in a very similar way as for the fiber-based combs. We choose to reference this comb to the 1062.5 nm USL available at SYRTE that is used by the mercury clock. The achieved SNR of more than 60 dB in 1 kHz bandwidth is sufficient to performed the phase lock. The fact that the Ti:sa comb spectral range does not include the 1542 nm wavelength is actually a significant drawback since it does not allow a direct connection with the European fiber link used for the remote clock comparisons or optical reference dissemination.

Carrying out the same steps as before (beatnote derivation, f_0 demodulation, narrow band-pass filtering and RF division), and adapting in consequence the RF components, the lock equation is now defined by:

$$\frac{\mathrm{sign}_{\mathrm{HgL}}\left(\nu_{\mathrm{HgL}} + f_{\mathrm{s,HgL}} - N_{\mathrm{HgL}} \cdot f_{\mathrm{rep}}\right)}{16} \Bigg(= f_{\mathrm{DDS1}} \tag{2.5}$$

where the locking beatnote is divided by a factor $n = 16$, $f_{\mathrm{DDS1}} = 18.75\,\mathrm{MHz}$ and $f_{\mathrm{s,HgL}} = -52\,\mathrm{MHz}$.

The correction is performed by another PI2 controller and it is applied to the Ti:sa pump power yielded by the powerful 532 nm Verdi laser. The pump power is controlled via the 0^{th} of the AOM for high Fourier frequencies with a bandwidth $> 400\,\mathrm{kHz}$ (limited by its response time), which modifies the index of refraction seen by the fs laser in the Ti:sa crystal. In parallel, a slow correction is applied by an independent integrator (I) to the a PZT actuator acting on the physical length of the Ti:Sa cavity for the low Fourier frequencies (< 1 kHz), as shown in Fig. 2.2.

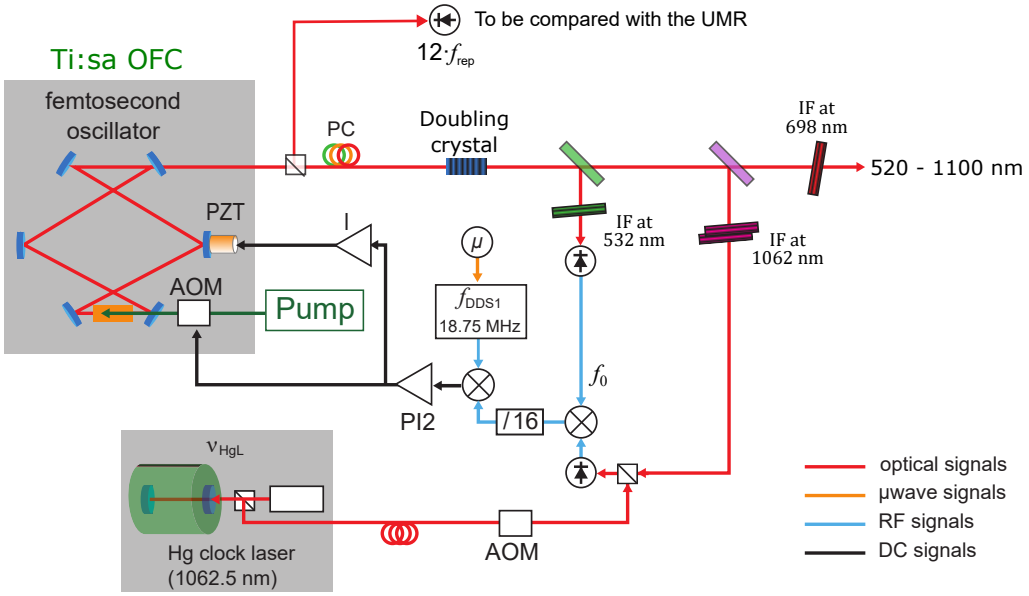

Figure 2.2: Phase lock of the Ti:sa comb to an ultrastable cw laser at 1062.5 nm and unique optical output. AOM: acousto-optic modulator, IF: interferometric filter (0.1 – 1 nm), PC: photonic crystal, and PZT: piezo-electric ceramic.

2.1.3 Outputs of the Er:fiber comb

The output of the fs laser (1515 – 1595 nm) is divided in four different branches, as depicted on Fig. 2.3.

The main output is sent to a two-channel OADM featuring three outputs. The first channel extracts the light around 1542.14 nm (ITU Ch 44) to beatnote it against IRef USL at 1542 nm ($\nu^{(0)}_{\mathrm{IRef}}$ after the frequency shift), as described before. The second channel extracts the light around 1543.73 nm (ITU Ch 42), to form a beatnote with a free running 1544 nm 2 kHz-linewidth diode laser in order to phase lock it to the comb itself locked to the IRef laser. This 1544 nm laser will therefore benefit from the spectral properties of the IR reference, within the bandwidth of the lock, and is used, after frequency tripling, for the spectroscopy of some of the best molecular transitions of di-iodine (I_2) cell-based optical frequency standard. The rest of this output is entirely used for the detection of the comb's repetition rate harmonics.

Three additional branches and less powerful branches are used to seed three independent EDFAs, each of them followed by a HNLF so as to broaden (after previous amplification) the spectral region of interest.

EDFA 1 amplifies the spectrum to enhance the four wave mixing occurring inside the HNLF that broadens it over more than one octave (1000 – 2100 nm). After the broadening, a PPLN non-linear crystal, in waveguide geometry, frequency double specifically

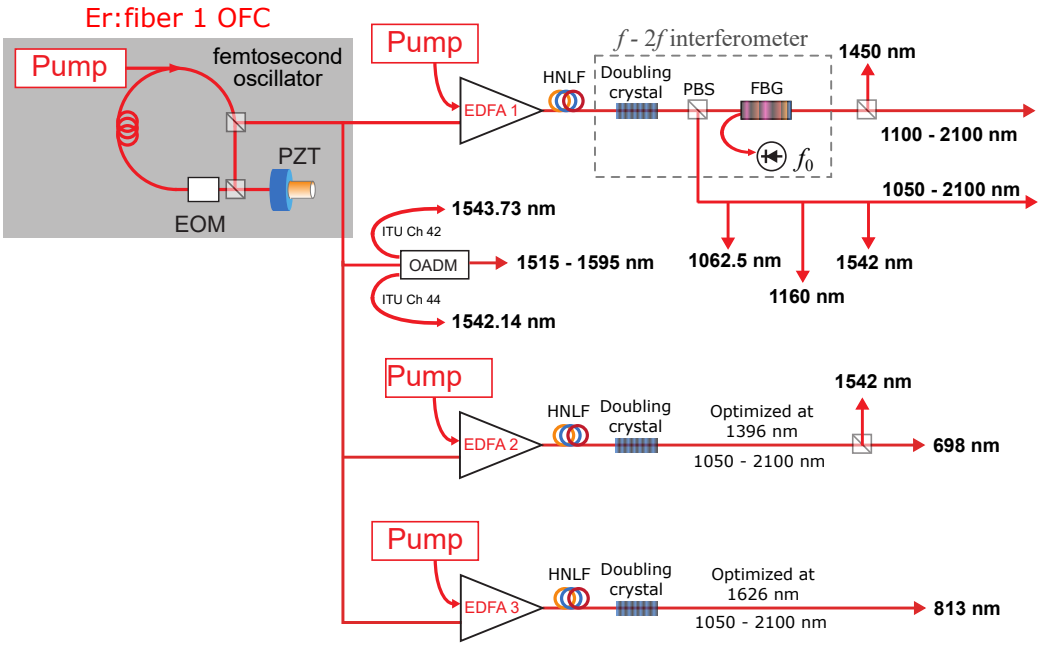

Figure 2.3: Simplified scheme of the different operational OFC optical outputs. On the very left is the only output that comes directly from the main oscillator which is is split, in an OADM, into 1542 nm (OFC lock), 1544 nm (I_2 laser lock) and $1515-1595$ nm (f_{rep} harmonics photodetection). On top the EDFA 1 is used for the f_0 detection, and to form the beatnotes with laser at 1450 nm (referencing of the Hg lattice laser), 1062.5 nm (counting/locking the Hg clock laser), 1160 nm (counting the SHB laser) and 1542 nm (auxiliary IR reference laser). At the bottom, the EDFA 2 is used for 698 nm (counting the Sr clock laser) and 1542 nm (a second auxiliary IR reference laser), and the EDFA 3 is for the 813 nm (counting/referencing Sr lattice laser lock).

the long wavelength side (2 μm doubled to 1 μm) of the spectrum, followed by a polarized beam splitter (PBS) yielding a first output featuring the whole spectrum (reflected port). This output is used to form beatnotes with several SYRTE USLs: 1062 nm (used to probe the metrological transition of the mercury clock, after frequency quadrupling to reach 265 nm), 1160 nm (for the SHB experiment after frequency doubling), and 1542 nm (an additional out-of-loop beatnote, used to assess and eliminate the noise of the EDFA, as it will be described further in section 4.3). In the PBS transmitted part, polarizations are matched, thus optimizing the detection of f_0 after selection of the two spectral components around 1 μm by a fiber Bragg grating (FBG). This leads to the beatnote described in subsection 1.3.2 to measure the quantity f_0. The part transmitted by the FBG can still be used to form beatnotes between 1100 nm and 2100 nm. This output is notably used to form a beatnote with a 1450 nm laser and lock it to the comb. In turn,

a small part of the 1450 nm laser light is frequency doubled to form a beatnote with a cw Ti:sa laser at 725 nm. The beatnote is digitally stabilized to phase-lock the Ti:sa laser to the 1450 nm one, and therefore to the comb. Lastly, the Ti:sa laser is frequency doubled in order to reach the magic wavelength around 362.5 nm to lattice trap Hg atoms. This last connection is used to establish a continuous frequency locking of the lattice laser, which allowed a clear progress of the stability of the Hg optical clock [99].

EDFA 2 and its HNLF amplify and optimize the light at 1396 nm before it reaches a PPLN crystal, after which it provides a 3-nm wide comb centered around 698 nm, with nearly 3 mW, required to form a beatnote with the Sr clock USL. Besides, an additional out-of-loop beatnote at 1542 nm after the doubling crystal is formed similarly to what is done with EDFA 1 output.

The last amplifier, EDFA 3, has the same configuration as the previous one, but being optimized at 1626 nm to be frequency doubled and to produce comb modes around 813 nm, that is the magic wavelength of the Sr lattice laser, in order to ensure its long-term frequency lock.

2.2 Counting the signals

Here we will focus on the three critical elements that allow us to characterize and measure the signals in an accurate and as stable as possible way according to our architecture, explaining the motivation, the implementation and the level of performance of our approach.

2.2.1 The phase/frequency counter

The final device that is going to detect, follow and count the phase oscillations of the signals we are interested in is a dead-free-time frequency counter (K+K FXE). Strictly speaking, it is a phase recorder (and not a frequency recorder) with a fixed sample rate of 1 kSample/s. This sample rate refers to phase readings, i.e the instantaneous readouts of a continuously growing quantity, the phase. The frequency measurements are actually calculated in an internal microprocessor or in the PC from successive phase readings according to: frequency = phase advance/gate time. The gate time, or report interval, is used to characterize the time between evaluations of one, or more, raw measurement/s towards the requested report mode, to be transmitted to the PC's DLLs. The report modes available are: non-averaged phase and frequency modes, averaged phase and frequency modes and difference phase mode. The first two modes are commonly known as Pi and Lambda modes (or Π-type and Λ-type [100]) due to the way of recording the raw phase measurements, for a given gate time, that recalls the "shape" of these two uppercase Greek letters, Π and Λ, respectively. The raw sampling rate is fixed at

1 kSample/s and what is changed, at the time of computing the frequencies, is the gate time and its mode.

To illustrate the Pi and Lambda concept, let us consider a frequency measurement with a gate time of 3 ms. Because of the fixed sample rate the phase will be counted every single ms as: $\phi_0, \phi_1, \phi_2, \phi_3, \phi_4, \phi_5 ...$ If we perform the non-averaged or Pi mode, the phase values are: $\phi_2, \phi_5, \phi_8, \phi_{11} ...$, i.e. only every three raw measurements we are taking a meaningful one, while the rest are ignored. Hence, from the former readings the Pi mode frequencies are:

$$\frac{\phi_5 - \phi_2}{3\,\text{ms}}, \frac{\phi_8 - \phi_5}{3\,\text{ms}}, \frac{\phi_{11} - \phi_8}{3\,\text{ms}} \ldots \tag{2.6}$$

If we perform instead the averaged or Lambda phase mode, the phase readings yield: $(\phi_0 + \phi_1 + \phi_2)/3$, $(\phi_3 + \phi_4 + \phi_5)/3$, $(\phi_6 + \phi_7 + \phi_8)/3$, $(\phi_9 + \phi_{10} + \phi_{11})/3 ...$, this is, every raw measurement is being taken into account. The corresponding Lambda mode first frequency now reads:

$$\begin{aligned} &\left(\frac{\phi_3 + \phi_4 + \phi_5}{3} - \frac{\phi_0 + \phi_1 + \phi_2}{3}\right) \Big/ 3\,\text{ms} \ldots = \\ &\left(\frac{\phi_3 - \phi_0}{3} + \frac{\phi_4 - \phi_1}{3} + \frac{\phi_5 - \phi_2}{3}\right) \Big/ 3\,\text{ms} \ldots = \\ &\left(\frac{\phi_3 - \phi_0}{3\,\text{ms}} + \frac{\phi_4 - \phi_1}{3\,\text{ms}} + \frac{\phi_5 - \phi_2}{3\,\text{ms}}\right) \Big/ 3 \ldots \end{aligned} \tag{2.7}$$

where every frequency in fact is an average over three frequencies, each of them with a 3 ms gate time and spaced apart 1 ms.

Resolution and noise of the counter

The resolution can be seen as the "granularity" of possible measurement results. For the FXE phase meter it is the period of the 80 MHz clock signal, phase locked to the 10 MHz external reference, that is used to count the length of the fractional portion of a input signal period, stretched by analog means by a factor of 1024. Hence the fixed phase (time) resolution is $1/80\,\text{MHz}/1024 = 12.2\,\text{ps}$ [101]. In principle, there is also a digital numerical resolution of reported results, which is significantly better than the hardware resolution so that it does not show up. This means that details finer than the resolution can not be detected. From equation 2.6 we see that the frequency resolution is $12.2\,\text{ps}/3\,\text{ms}$, i.e. there is a linear dependency with the gate time. Additionally, if we average like in equation 2.7, the resolution improves by $\sqrt{n}$ on top of the n factor proportional to the gate time, providing us with a resolution of $12.2\,\text{ps}/3\,\text{ms}/\sqrt{3}$.

The noise can be accounted for all the electronics components and circuitry that are to some degree temperature dependent. As a consequence, certain residual measurement errors vary with temperature, even though they are below the resolution of the counter.

When measuring the frequency (or the phase) of a signal with the K+K counter, we must be sure that both its noise and its resolution are lower than the noise of the signal under test. To this end, we have external referenced a 24-bit DDS (Rigol DG4162) with a 10 MHz from the UMR at 1 GHz (after down-conversion), so its fractional stability is kept at $3 \cdot 10^{-14}$ at 1 s (see red curve in Fig. 3.5), and generate different frequencies at 8 dBm within the range 10 kHz – 45 MHz. These frequencies are measured directly by the K+K counter in two different frequency modes Pi (non-averaged) and Lambda (averaged). In table 2.2 we show the DDS frequencies evaluated with their noises, and the corresponding counter resolutions for both modes.

	DDS frequencies at 8 dBm power						
	10 k	**100 k**	**1 M**	**10 M**	**15 M**	**20 M**	**45 M**
DDS noise	0.3 n	3 n	33 n	0.3 μ	0.45 μ	0.6 μ	1.4 μ
Count. res. Π	0.1 μ	1.2 μ	12.2 μ	0.12 m	0.18 m	0.24 m	0.5 m
Count. res. Λ	3.9 n	38.6 n	0.4 μ	3.9 μ	5.8 μ	7.7 μ	17.4 μ

Table 2.2: DDS absolute noises at 1 s and frequency counter resolutions in Pi and Lambda modes for the DDS frequencies generated from the 10 MHz UMR. All values in Hz units.

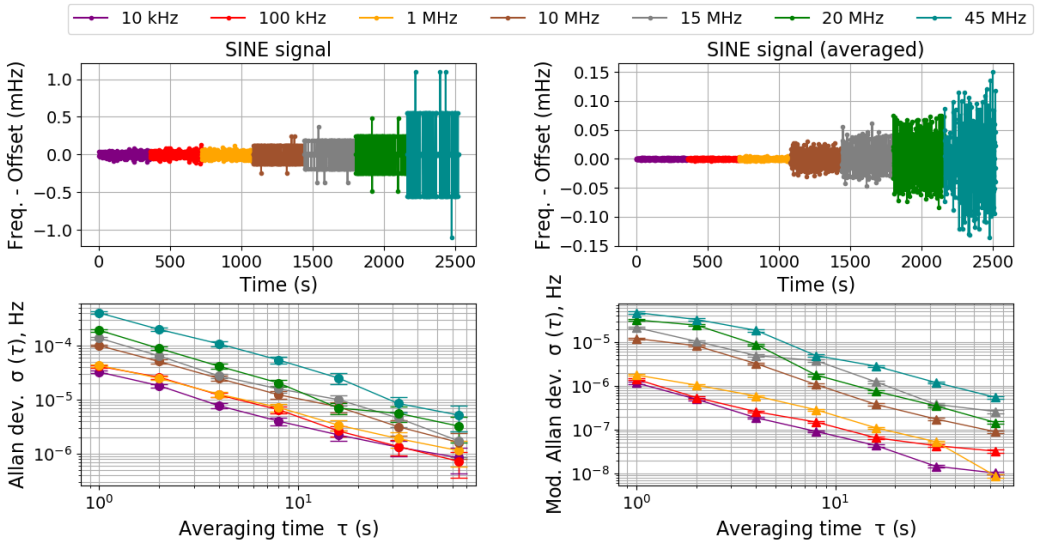

Figure 2.4: Different RF frequencies at 8 dBm from a 24-bit DDS external referenced to 10 MHz, down-converted from 1 GHz UMR ($\sigma_y \approx 3 \cdot 10^{-14}$ at 1 s) measured directly by the counter both in Pi (non-averaged) and Lambda (averaged) mode.

For the counter set in Pi mode with a gate time of 1 s the high frequency signals ($\geq$ 10 MHz) are limited by the resolution of the counter due to the very low noise signals, while for the low frequency ones the sine to square conversion at the frequency counter

input dominates as noise source, as shown in the left plot of Fig. 2.4. When the counter is operated in Lambda mode, its frequency resolution is divided by $\sqrt{1000} \approx 30$ for the same gate time. In this case the situation has not changed for the low frequencies where the absolute stabilities are a factor 30 lower. On the contrary, for the higher frequencies now the noise of the signals and the counter resolutions become closer, being difficult to distinguish what is the limiting factor, but in any case we can set un upper limit on the respective noises of these signals.

The signal we want to measure and to characterize its noise is the one from the mix of the $36 \cdot f_{\text{rep}}$ ($\approx 9\,\text{GHz}$) and the 8.985 GHz from the UMR, as we will explain in the next subsection. The dominant noise on the IF signal at the mixer's output at 15 MHz is the one from the UMR, whose fractional stability at 1 s is $6-7 \cdot 10^{-15}$ or $54-63\,\mu\text{Hz}$ in absolute terms.

On the other hand, the (fixed) non-average relative frequency resolution of the counter at 1 s is $12.2\,\text{ps}/1\,\text{s} = 1.22 \cdot 10^{-11}$, that for our 15 MHz corresponds to $183\,\mu\text{Hz}$. On the left side of Fig. 2.5 we have plotted both the counter resolution (black slope) and the UMR absolute noise (red slope) according to the counter frequency range available (up to 60 MHz). Since the resolution of the counter must be lower than the noise of the real signal we can multiply this last one. Doing this, we not only multiply the carrier frequency but also its noise, and we bring the signal to the high frequency range of the counter where the performance is better (less jitter phase noise). At this point, either we multiply the signal by at least a factor 3 or we demodulate it to a frequency value lower than the crossing point between the counter's resolution and the signal's noise, i.e 5.16 MHz for the present case (see Fig. 2.5 bottom left plot), although we would be at the low frequency range of the frequency counter.

Our approach solves both drawbacks at the same time, we first down-convert the signal to 275 kHz demodulating it with a DDS at 15.275 MHz and then we multiply it by a factor 200. After demodulation, the signal still preserves the original noise of the 15 MHz. Once the 275 kHz is multiplied, we end up with a carrier frequency at 55 MHz and, what it is even more important, with a noise of 12.6 mHz (see orange slope 55 MHz). This is more than a factor 20 above the corresponding counter's absolute frequency resolution at 1 s (0.67 mHz for the 55 MHz).

2.2.2 Noise floor of microwave measurements

To our laboratory arrive three frequency references: one from the master active H maser at 1 GHz, and other two from the CSO at 1 GHz and 8.985 GHz, all of them by independent links. These links are brought optically: the microwave signal is transmitted by AM over a $1.5\,\mu\text{m}$ optical carrier light. Only the 8.985 GHz signal link is compensated for propagation noise by detecting the phase after a round-trip and acting on a fiber stretcher, unlike the 1 GHz signal link, that is not compensated. This is because the last one is used to clock the DDSs and the 10 MHz CSO (after down-conversion) to

reference the synthesizers and counters involved in the different measurements. Thus, having fiber noise present on this link, has a negligible impact for this usage. In contrast, the 8.985 GHz link must be perfectly compensated since it will bring the signal to measure the f_{rep} of the comb and this comparison is what will set the limit of our system.

Towards this end, we take advantage of the availability of high bandwidth photodiodes at 1.5 μm (HLPD) to detect the 36$^{\text{th}}$ harmonic of the repetition rate and compared it to the UMR, i.e. to the CSO phase-locked to the maser (with a time constant of 1000 s), in order to filter its short-term noise. This hybrid system benefits therefore from the short-term ultra-low noise of the CSO and from the very predictable long-term behavior of the maser.

We have chosen this comb harmonic, $36 \cdot f_{\text{rep}} \approx 9\,\text{GHz}$, because once it is mixed with the f_{UMR} which is at a fixed 8.985 GHz, it gives a convenient RF frequency around 15 MHz, that is easy to handle by the electronics and RF components placed along the frequency chain. Besides, it provides a large lever arm to measure f_{rep} since the noise is multiplied by 36 as well. This frequency is additionally demodulated by a DDS at $f_{\text{DDS2}} \approx 15.275\,\text{MHz}$ such that it results in 275 kHz frequency after low-pass filtering the mixer's output. We finally multiply this frequency by a factor of 200 in order to beatnote the resolution of the counter and, at the same time, to have a final signal 55 MHz, as depicted in Fig. 2.6. This way we are closer to the upper frequency

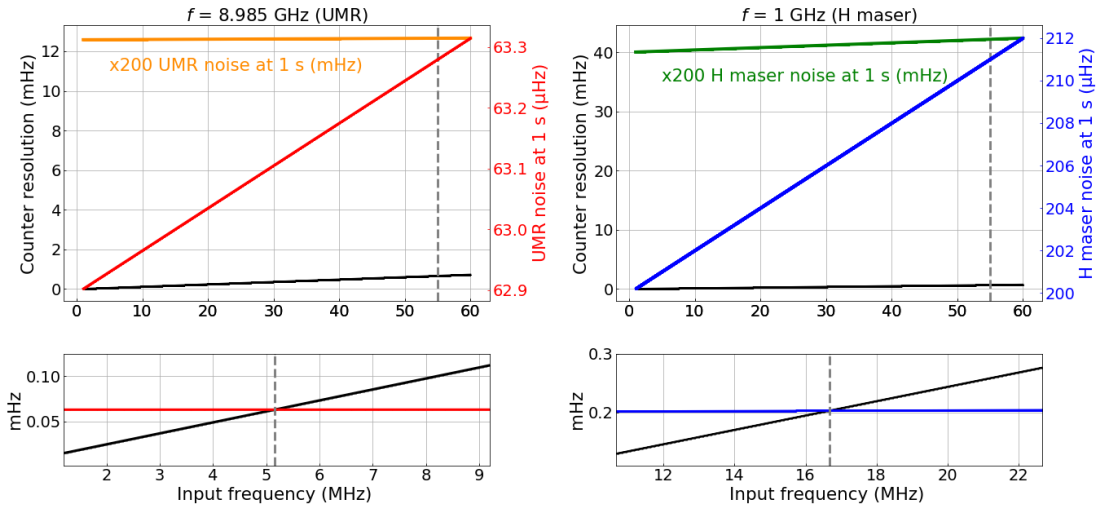

Figure 2.5: Resolution of the counter (black) vs the noise at 1 s of the ultrastable microwave reference (UMR) at 8.985 GHz (red, on the left) and H maser at 1 GHz (blue, on the right), both in Pi mode. In the bottom plots a zoom is made on the intersection points between the resolution and the noise's signals. Orange and green slopes are the resulting 200-multiplied noises for the UMR and the maser, respectively.

that the counter can deal with and we fully exploit its performance.

The f_{rep} is then deduced from the value of Ch1, given by the first channel of the counter, as:

$$\text{Ch1} = -200\left(36 \cdot f_{\text{rep}} - f_{\text{UMR}} - f_{\text{DDS2}}\right) \tag{2.8}$$

where Ch1 $\approx 55\,\text{MHz}$, and the negative sign is because $f_{\text{DDS2}} > 36 \cdot f_{\text{rep}} - f_{\text{UMR}}$.

It is very important to remark that the counter, the DDS and the UMR are referenced to the maser, so the final quantity measured is in terms of "maser Hertz". This unit is connected to the definition of the Hz by using the maser (filtered by the CSO) to probe cesium atoms in the three SYRTE microwave atomic fountains as it will be described in subsection 3.1.1.

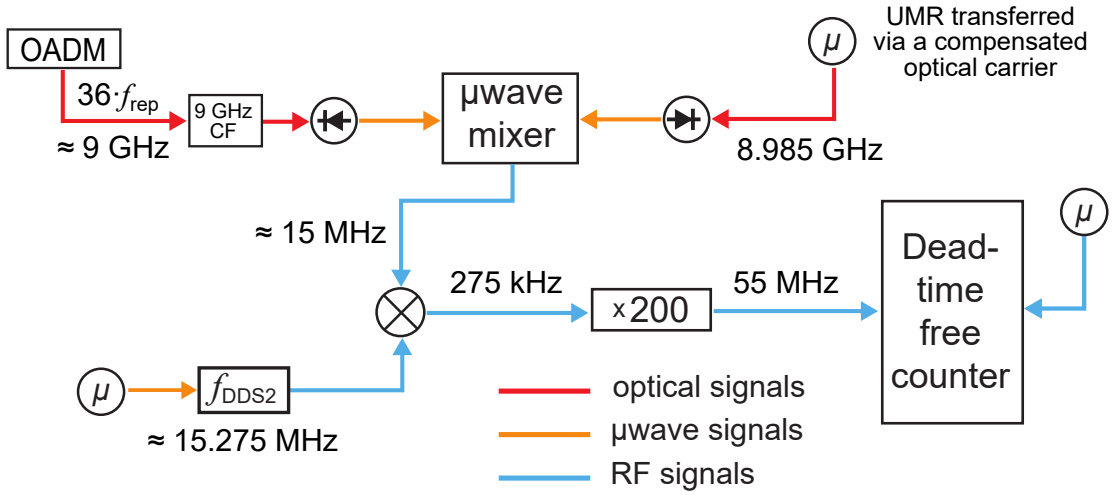

Figure 2.6: Comparison of the 36th comb harmonic against the microwave reference. UMR: ultrastable microwave reference, OADM: optical add and drop multiplexer, and CF: microwave cavity filter.

The goal of this subsection is to know the noise introduced by this 200-multiplier box that comes on top of the UMR and the $36 \cdot f_{\text{rep}}$ noises. A basic scheme of the 200-multiplier is shown in Fig. 3.3. We feedback a quartz oscillator (JCOS) set at 55 MHz with an error signal generated from the comparison of the $55\,\text{MHz}/200$ free-running oscillator against the input signal at 275 kHz that comes after the mixer on the left (microwave reference vs the comb harmonic).

Theoretical noise model

We have made a model that accounts for the noise introduced from a theoretical point of view and we have quantified it experimentally with the test setup shown in

Fig. 2.7. We split an ultrastable RF signal at 275 kHz, which has a negligible noise, in two branches. The upper one is split again, and each branch is sent to an independent $\times 200$ box and the resulting 55 MHz signals are counted by two channels of the K+K counter. The bottom branch goes directly to a third channel and is multiplied a posteri by 200. In order to model the noise, we introduce a multiplicative noise (ε_M) and an additive noise (ε_A). The reason for this approach is because it is not possible to make a difference between the two of them.

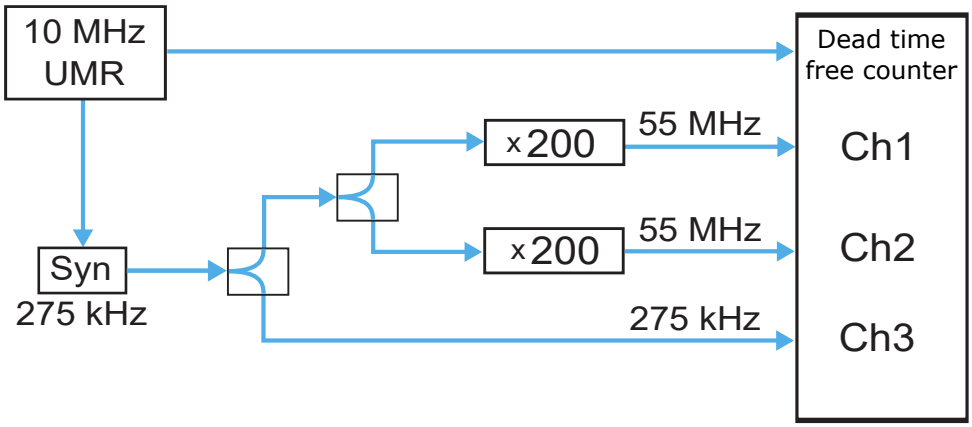

Figure 2.7: Scheme used to model and characterize the noise introduced by the $\times 200$ box depicted in Fig. 3.3.

The equations for the two single 200-multiplier boxes, with noise, yield:

$$\begin{aligned} \mathrm{Ch1} &= (200+\varepsilon_{M,1})\,(275\,\mathrm{k}+\varepsilon_{275\mathrm{k}})+\varepsilon_{A,1}+\varepsilon_{\mathrm{C},1} \\ \mathrm{Ch2} &= (200+\varepsilon_{M,2})\,(275\,\mathrm{k}+\varepsilon_{275\mathrm{k}})+\varepsilon_{A,2}+\varepsilon_{\mathrm{C},2} \end{aligned} \tag{2.9}$$

where $\varepsilon_{275\mathrm{k}}$ and ε_{C} account for the residual noises introduced by the synthesizer and the counter, respectively. The difference of these two equations therefore reads:

$$\begin{aligned} \mathrm{Ch1}-\mathrm{Ch2} = (\varepsilon_{M,1}-\varepsilon_{M,2})\,275\,\mathrm{k} &+ \left(\varepsilon_{A,1}-\varepsilon_{A,2}\right) \\ &+ \left(\varepsilon_{\mathrm{C},1}(55\,\mathrm{M})-\varepsilon_{\mathrm{C},2}(55\,\mathrm{M})\right) \end{aligned} \tag{2.10}$$

After uncertainty propagation and assuming that the various noise sources are uncorrelated, the variance of this two channels' difference is given by:

$$\begin{aligned} \sigma^2(\mathrm{Ch1}-\mathrm{Ch2}) = &\left(\sigma^2(\varepsilon_{M,1})+\sigma^2(\varepsilon_{M,2})\right)(275\,\mathrm{k})^2+\left(\sigma^2(\varepsilon_{A,1})+\sigma^2(\varepsilon_{A,2})\right) \\ &+\left[\sigma^2\left(\varepsilon_{\mathrm{C},1}(55\,\mathrm{M})\right)+\sigma^2\left(\varepsilon_{\mathrm{C},2}(55\,\mathrm{M})\right)\right] < (7\cdot 10^{-5}\ \mathrm{Hz})^2 \end{aligned} \tag{2.11}$$

which accounts for the combined contribution of the two boxes (orange curve in Fig. 2.8). Therefore, the instability contribution of one box would never be bigger than 70 μs at

1 s. Deriving the variance directly from one single box (equation 2.9), results in:

$$\begin{aligned}\sigma^2(\mathrm{Ch1}) = &\left(\sigma^2(\varepsilon_{275\mathrm{k}})\right)200^2 + \left(\sigma^2(\varepsilon_{M,1})\right)(275\,\mathrm{k})^2 \\ &+ \left(\sigma^2(\varepsilon_{A,1})\right) + \left[\sigma^2\left(\varepsilon_{\mathrm{C},1}(55\,\mathrm{M})\right)\right] \approx (8\cdot 10^{-4}\ \mathrm{Hz})^2\end{aligned} \tag{2.12}$$

where the term $\left(\sigma^2(\varepsilon_{275\mathrm{k}})\right)200^2$ is the predominating as it is the only one not present in equation 2.11, see green curve in Fig. 2.8.

In the same way, the noise equation for the last branch reads:

$$\mathrm{Ch3} = (275\,\mathrm{k} + \varepsilon_{275\mathrm{k}}) + \varepsilon_{\mathrm{C},3} \tag{2.13}$$

and its variance, after multiplying by 200 (by post-processing), is given by:

$$\sigma^2(200\cdot\mathrm{Ch3}) = \left(\sigma^2(\varepsilon_{275\mathrm{k}})\right)200^2 + \left[\sigma^2\left(\varepsilon_{\mathrm{C},3}(275\mathrm{k})\right)\right]200^2 \approx (4\cdot 10^{-3}\ \mathrm{Hz})^2 \tag{2.14}$$

where the contribution is due to the second term (blue curve in Fig. 2.8) since from equation 2.12 we know that the instability of the first term is around 0.8 mHz at 1 s.

If we now derive the variance of the $\mathrm{Ch1} - 200\cdot\mathrm{Ch3}$, we obtain:

$$\begin{aligned}\sigma^2(\mathrm{Ch1} - 200\cdot\mathrm{Ch3}) = &\left(\sigma^2(\varepsilon_{M,1})\right)(275\,\mathrm{k})^2 + \left(\sigma^2(\varepsilon_{A,1})\right) + \left[\sigma^2\left(\varepsilon_{\mathrm{C},1}(55\,\mathrm{M})\right)\right] \\ &+ \left[\sigma^2\left(\varepsilon_{\mathrm{C},3}(275\mathrm{k})\right)\right]200^2 \approx (4\cdot 10^{-3}\ \mathrm{Hz})^2\end{aligned} \tag{2.15}$$

which is clearly dominated by the last term as the stability is the same as in equation 2.14, so the noise of the counter $\sigma\left(\varepsilon_{\mathrm{C},1}(275\,\mathrm{k})\right)$ is around $3.5\cdot 10^{-5}$ once we have removed the factor 200. From the combined contribution of two boxes (orange-underlined terms in equation 2.11), taking into account that the boxes are uncorrelated and assuming equal contribution, the variance only due to a single 200-multiplier box yields:

$$\sigma^2(\times 200) = \sigma^2(\varepsilon_{M,1})\right)(275\,\mathrm{k})^2 + \sigma^2(\varepsilon_{A,1}) \approx (5\cdot 10^{-5}\ \mathrm{Hz})^2 \tag{2.16}$$

To see the impact of the multiplication process on the real measurement for $f_{\mathrm{UMR}} = 8.985\,\mathrm{GHz}$, we derive the variance from equation 2.8 and we also take into account the variance of the multiplication box from equation 2.16:

$$\sigma^2(\mathrm{Ch1}) = \sigma^2(\times 200) + 200^2\left[\sigma^2(36\cdot f_{\mathrm{rep}}) + \sigma^2(f_{\mathrm{UMR}}) + \sigma^2(f_{\mathrm{DDS2}})\right] \tag{2.17}$$

where $\sigma(\times 200)/(200\cdot f_{\mathrm{UMR}}) < 3\cdot 10^{-17}$ at 1 s, which is about two orders of magnitude below the fractional stability of the UMR ($1-2\cdot 10^{-15}$ up to 1000 s, as it will be shown in Fig. 3.2). Moreover, the noise averages quickly with τ^{-1} going down well below the noise the microwave signal after a few seconds.

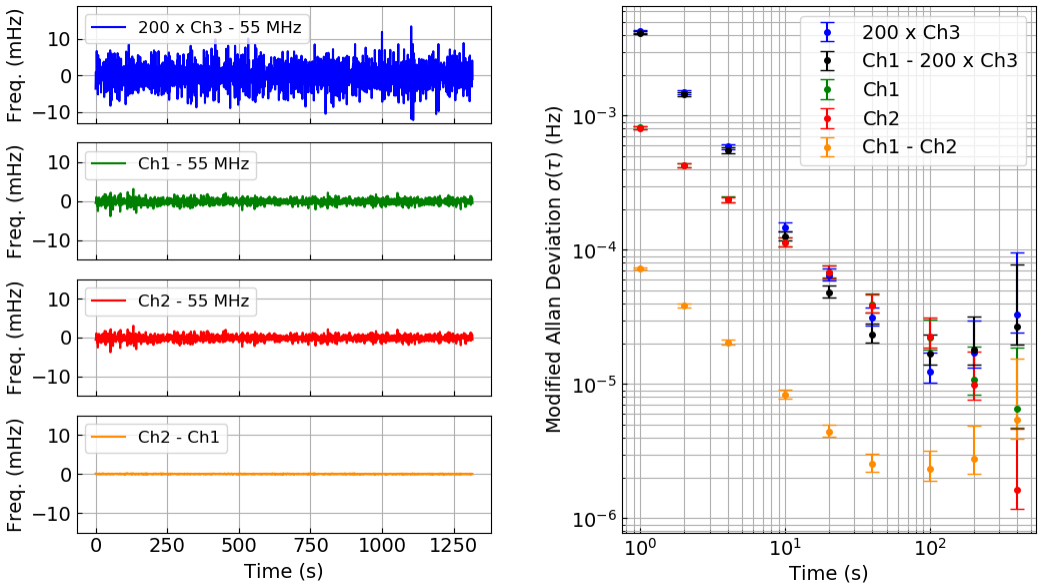

Figure 2.8: Stability curves obtained from the noise model of the scheme depicted in Fig. 2.7.

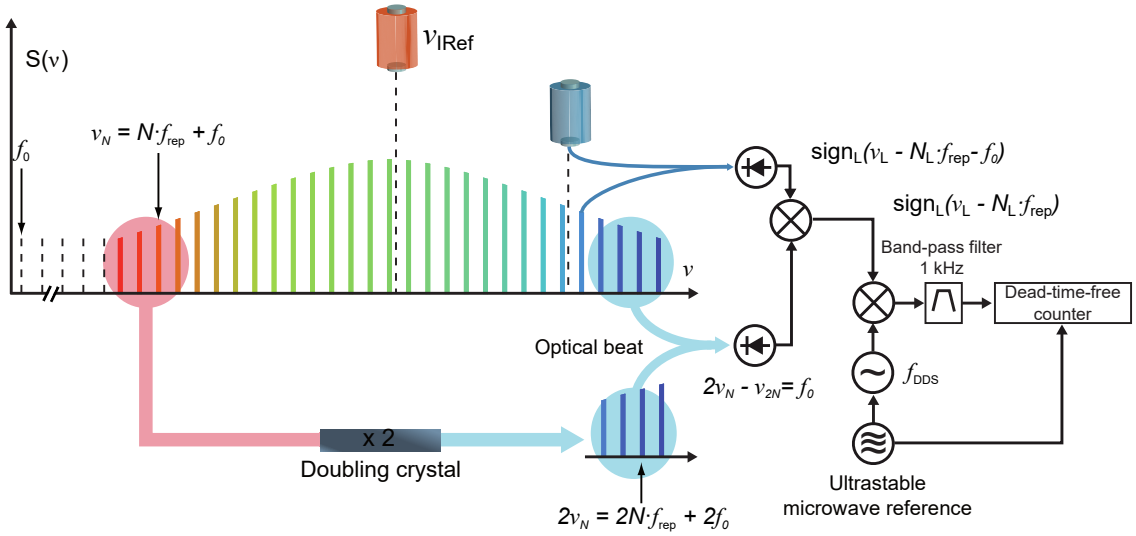

Figure 2.9: Optical beatnote detection and real-time f_0 demodulation. Red ultrastable cavity represents the USL, ν_{IRef}, to which the OFC is locked. Blue cavity is the USL to be measured once the beatnote has been photodetected, demodulated and filtered in the RF domain.

2.2.3 Noise floor of optical measurements

So far we have seen where the two degrees of freedom of the OFC (f_{rep} and f_0) come from and how to determine and count them. Let us retrieve equation 1.16 and mix the f_0 out in a mixer as depicted in Fig. 2.9. In the same way as we did for the OFC phase-lock to an optical reference, the f_0-free optical beatnote yields:

$$f_L = \text{sign}_L(\nu_L - N_L \cdot f_{rep}) \tag{2.18}$$

From equation 2.18 we can express any optical frequency (within the spectral bandwidth of the comb) in terms of the microwave one to which its f_{rep} is compared to (the UMR). To derive ν_L the only parameter we are still missing is the corresponding comb line N_L.

Comb mode index determination

There are different ways to derive the index N unequivocally, for a given optical frequency measurement, that depend on the laboratory capacities, i.e. on the independent oscillators the comb can be compared to, and/or to which reference the comb is locked to. These determinations are not only complementary but also it is recommended to double-check the N value with at least two of them, if possible. We can differentiate the four following cases:

1. The easiest and most straight forward approach is making use of a high performance wavemeter which will provide us with a frequency value that will depend on its accuracy and resolution, generally both at the MHz level.

2. Another way, along the same line as the former one, is based on a priori knowledge on the optical frequency to be measured ν_L, as long as it has a drift sufficiently small compared to f_{rep}, or if the change of frequency difference with respect to an atomic transition is known.

3. At SYRTE, since the OFC is locked to an optical reference, we can benefit from the optical phase-lock loop implemented. Following equation 2.3, we can induce a change in f_{rep}, while keeping the PLL closed, to calculate the N number after a couple of variations. In institutions where a stable oscillator to compare to is not available, with no possibility to implement the methods mentioned above, a measurement providing a bigger lever arm is necessary.

4. The last approach, and more general, is to lock the comb on two distant N numbers and to measure the corresponding change of f_{rep}.

In appendix B we have described in detail how to carry out all these procedures, giving some concrete examples and, more importantly, taking into account their associated uncertainties which will validate (or not) the final N number obtained for a given error margin assumed.

Narrow band-pass filters

Since most of the metrological lasers we work on are ultrastable ($\sigma_y(\tau) < 10^{-15}$ at 1 s), it is justified to place narrow band-pass filters to well isolate the optical beatnotes, between the OFC and the USLs, to be counted.

First, we demodulate all the beats, down to 10 kHz, by mixing them with and ultrastable RF source (DDS) whose noise is negligible compared to the noise of the beatnote under study. As a consequence, the frequency is too low to be counted correctly by the counter without adding extra noise (as seen in Fig. 2.4). This is because for low frequencies the slope of the voltage in the vicinity of zero crossing gets lower, and thus the same amount of (amplitude) noise transfers into larger phase noise. For this reason, once it is demodulated, we filter the beatnote in a 1 kHz band-pass filter (butterworth 4$^{\text{th}}$ order) and then we square[2] it. Thereby, the counter can track properly these (now steeper) zero crossings, and compare the phase internally against its local oscillator reference.

We want to check that this type of narrow filters do not induce any bias on the measurement. Any filter introduces a phase shift that depends on the frequency. Alternatively, if the beatnote frequency drifts –as it does, a few 10 mHz/s at most– this phase profile is explored, what results in a phase gradient, ergo a frequency bias. The goal of this study is to ensure that this fractional frequency bias is kept under $1 \cdot 10^{-18}$.

The electric fields of the optical beatnotes, $E_{f_{\text{L}}}$ (sent to the RF port of the mixer), and the RF ultrastable source used for demodulation, $E_{f_{\text{DDS}}}$ (LO port), are:

$$\begin{aligned} E_{f_{\text{L}}} &= E_{f_{\text{L}}} \exp\big(j(2\pi f_{\text{L}} t + \phi_{f_{\text{L}}})\big) = E_{f_{\text{L}}} \exp\big(j\Phi_{f_{\text{L}}}\big) \\ E_{f_{\text{DDS}}} &= E_{f_{\text{DDS}}} \exp\big(j(2\pi f_{\text{DDS}} t + \phi_{f_{\text{DDS}}})\big) = E_{f_{\text{DDS}}} \exp\big(j\Phi_{f_{\text{DDS}}}\big) \end{aligned} \tag{2.19}$$

After the mixer and the band-pass filter we will have:

$$E_{\text{OUT2}} = |E_{\text{OUT2}}| \exp\big(j(\Phi_{f_{\text{L}}} - \Phi_{f_{\text{DDS}}} + \phi_{f_{\text{filter}}})\big) \tag{2.20}$$

Since $\phi_{f_{\text{filter}}}$ depends on the frequency of the beatnote ($f_{\text{L}} - f_{\text{DDS}}$):

$$\frac{\Delta(f_{\text{L}} - f_{\text{DDS}})}{\Delta t} \neq 0 \Rightarrow \frac{\Delta\phi_{\text{filter}}}{\Delta t} \neq 0 \tag{2.21}$$

[2]The low frequency signal (10 kHz) goes trough two cascaded non-inverting operational amplifiers to increase the gain sufficiently. The resulting signal is then cut off between ± 3.3 v with a couple of clamp diodes.

Therefore, the real frequency at the output will be given by:

$$f_{\mathrm{OUT2}} = \frac{1}{2\pi}\frac{d\Phi_{\mathrm{OUT2}}}{dt} = \frac{1}{2\pi}\left[\frac{d(\Phi_{\mathrm{L}} - \Phi_{\mathrm{DDS}})}{dt} + \frac{d\phi_{\mathrm{filter}}}{dt}\right]\Bigg(\tag{2.22}$$

Measurement of the dephasing introduced by the filter

To characterize the last term of equation 2.22, we feed the two input ports of the mixer with two ultrastable signals coming from the same source in order to make the features of the filter appear. One signal simulates the real beatnote frequency, f_{RF}, while the other keeps acting as the demodulation frequency $f_{\mathrm{LO}} = f_{\mathrm{RF}} + 10\,\mathrm{kHz}$.

We split both signals and we send the first pair to the corresponding RF and LO ports of the mixer, and the second pair to two different channels of an oscilloscope, as shown in Fig. 2.10. Then, we make the product of these two signals internally in the scope and we select the frequency difference, $f_{\mathrm{dem,osc}}$. Doing this, we have simulated the demodulated beatnote frequency at the output of the mixer ("OUT ϕ 1", red sine wave represented in Fig. 2.10) without using a second mixer, which would have introduced additional noise. Finally, we start to change f_{RF1}, by steps (Δf) of 100 Hz, towards higher and lower frequencies. This way, we emulate the drift of the real beatnote and we explore the whole bandwidth of the filter and its response in phase. Thus, $\Delta\phi_{\mathrm{filter}}$ corresponds to the change of the phase difference between the phase at the output of the filter (ϕ_{filter}) and reference phase given by the scope ($\Phi_{\mathrm{dem,osc}}$). For this test, as the optical beats on the OFC are necessarily smaller than 125 MHz ($f_{\mathrm{rep}}/2$), we tried two different frequencies in this range: $f_{\mathrm{RF1}} = 10\,\mathrm{MHz}$ and $f_{\mathrm{RF1}} = 100\,\mathrm{MHz}$.

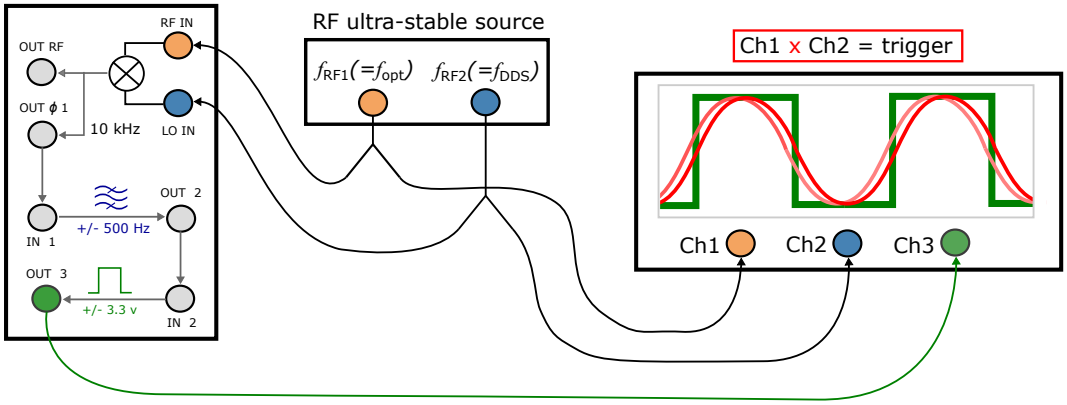

Figure 2.10: Setup used to measure the phase response of the 1 kHz filter. After 10 kHz down-conversion ("OUT ϕ 1"), 1 kHz band-pass filter ("OUT 2") and square wave conversion ("OUT 3"), the signal is sent to the scope (green). Next, it is triggered with a simulated demodulated signal $f_{\mathrm{dem,osc}}$ which results from multiplying internally Ch1 $\times$ Ch2 in the scope (red).

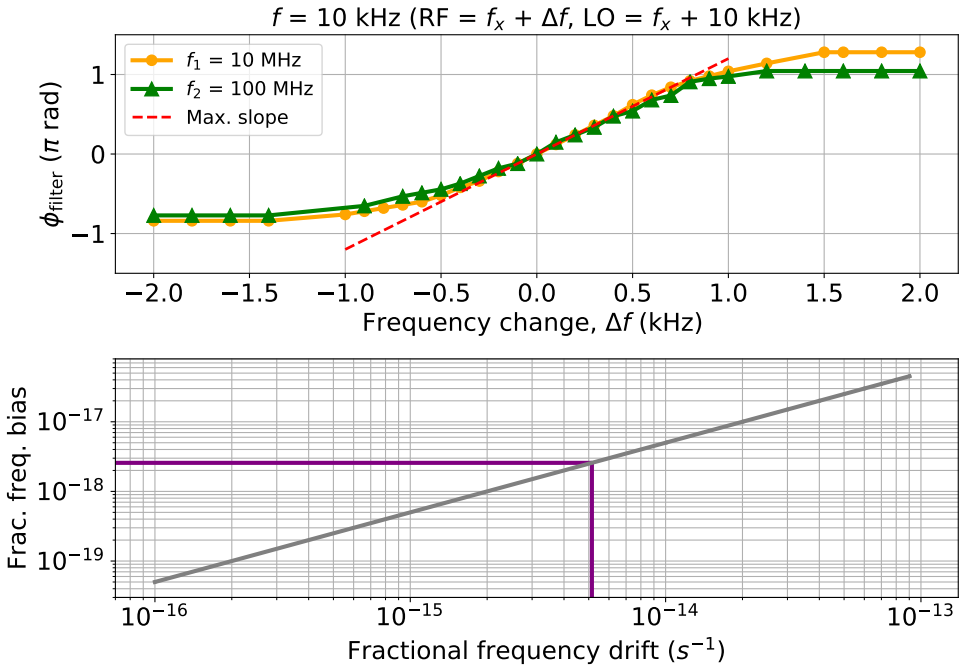

Figure 2.11: Top plot: dephasing induced by the 1 kHz narrow band-pass filter for the two frequencies simulating the beatnotes. Bottom plot: maximum fractional frequency bias for a given optical frequency and its corresponding fractional drift rate. The purple line shows equation 2.25 applied to a $\nu_L = \nu_{IRef}$, where for a drift of 1 Hz/s one would find a frequency bias of 0.5 mHz ($5.1 \cdot 10^{-15}\,s^{-1}$ and $2.6 \cdot 10^{-18}$, respectively, in relative units).

The result of this measurement, for the two different frequencies tested and shown in Fig. 2.11, corresponds to a maximum dephase of ≈ 2kHz where the maximal phase sensitivity, represented by the slope, is at the center of the filter:

$$\frac{d\phi_{\text{filter}}}{d(\Delta f)} = \frac{2\pi}{2\,\text{kHz}} \tag{2.23}$$

Therefore, the maximum frequency bias is given by:

$$f_{\text{bias,max}} = \frac{1}{2\pi}\frac{d\phi}{dt} = \frac{1}{2\pi}\frac{d\phi_{\text{filter}}}{d(\Delta f)}\frac{df}{dt} \tag{2.24}$$

Replacing equation 2.23 into 2.24, and normalizing by an optical frequency ν_L, the maximum fractional frequency bias would be:

$$\frac{f_{\text{bias,max}}}{\nu_L} = \frac{1}{\nu_L}\frac{1}{2\pi}\frac{\pi}{1\,\text{kHz}}\frac{df}{dt} \tag{2.25}$$

Since we want $f_{\text{bias,max}}/\nu_L$ to be smaller than 10^{-18}, then the maximum fractional drift of the beatnote must be $\frac{1}{\nu_L}\frac{df}{dt} < 2 \cdot 10^{-15}\ s^{-1}$.

2.3 Multi-branch topology: technical noise added

Due to the use of added and dedicated EDFAs (section 2.1.3) seeded by the main oscillator output of the Er:fiber 1 ($z = 1$) and Er:fiber 2 ($z = 2$) OFCs, we want to characterize, in particular, the comb outputs involved in the Hg and Sr OLCs measurements, this is, after EDFA 1 ($i = 1$) and EDFA 2 ($i = 2$). First, we will evaluate the intrinsic noise added, possibly degrading the spectral purity of the repetition rate. Second, we will check the accuracy of them to make sure that their central values present after each amplifier, $f_{\mathrm{rep}}^{(z,i)}$, are the same as the original $f_{\mathrm{rep}}^{(z)}$ coming from the principal oscillator, and it is only noise that is added.

To this end, we form additional out-of-loop beatnotes between each of the two EDFA outputs and the IRef laser, which is dispatched in independent fibers. The propagation noise is separately compensated for each fiber, which leads to a frequency shift $f_{\mathrm{s,IRef}}^{(z,i)}$ (see appendix C). Regardless of the wavelength for which the EDFA has been optimized (e.g. 1396 nm for EDFA 1), the amplifier always features enough power spectral density at 1542 nm to form a beatnote with a SNR sufficient to assess the noise introduced by the EDFA itself. According to equation 2.18, the beatnote is given by:

$$f_{\mathrm{IRef}}^{(z,i)} = \mathrm{sign}_{\mathrm{IRef}}^{(z,i)} \left(\nu_{\mathrm{IRef}}^{(z,i)} - N_{\mathrm{IRef}}^{(z,i)} \cdot f_{\mathrm{rep}}^{(z,i)} \right) \left(\right. \tag{2.26}$$

We assume that $f_{\mathrm{rep}}^{(z,i)}$ is in average equal to $f_{\mathrm{rep}}^{(z)}$ for which now we must account for the possible noise added $\varepsilon^{(z,0)}(\nu_{\mathrm{IRef}})$ by the few 10 cm of uncompensated paths in the arms locking the fs oscillators to ν_{IRef} or by possible PLL defaults (electronic noise or cycle slips). Hence, equation 2.4 becomes:

$$8 \cdot f_{\mathrm{DDS1}}^{(z)} = \mathrm{sign}_{\mathrm{IRef}}^{(z,0)} \left(\nu_{\mathrm{IRef}} + f_{\mathrm{s,IRef}}^{(z,0)} - N_{\mathrm{IRef}}^{(z,0)} \cdot f_{\mathrm{rep}}^{(z)} + \varepsilon^{(z,0)}(\nu_{\mathrm{IRef}}) \right) \left(\right. \tag{2.27}$$

We model the possible noise introduced by the respective EDFAs at 1542 nm and by the uncompensated propagation paths for the cw lasers to reach these specific outputs of the combs, that comes on top of $\varepsilon^{(z,0)}(\nu_{\mathrm{IRef}})$, adding a noise $\varepsilon^{(z,i)}$ that we will characterize. Thereby, we rewrite equation 2.26 as:

$$f_{\mathrm{IRef}}^{(z,i)} = \mathrm{sign}_{\mathrm{IRef}}^{(z,i)} \left(\nu_{\mathrm{IRef}} + f_{\mathrm{s,IRef}}^{(z,i)} - N_{\mathrm{IRef}}^{(z,i)} \cdot f_{\mathrm{rep}}^{(z,i)} + \varepsilon^{(z,i)}(\nu_{\mathrm{IRef}}) \right) \left(\right. \tag{2.28}$$

Deriving f_{rep} from equation 2.27 and replacing into 2.28, the final inaccuracy due to each of the EDFA outputs, yields:

$$\begin{aligned} \left\langle \varepsilon_{\mathrm{tot}}^{(z,i)}(\nu_{\mathrm{IRef}}) \right\rangle \left(\right. &= \mathrm{sign}_{\mathrm{IRef}}^{(z,i)} \left\langle f_{\mathrm{IRef}}^{(z,i)} \right\rangle \left(\right. - \langle \nu_{\mathrm{IRef}} \rangle \quad 1 - \frac{N_{\mathrm{IRef}}^{(z,i)}}{N_{\mathrm{IRef}}^{(z,0)}} \left. \right) \left(\right. \\ &\quad - f_{\mathrm{s,IRef}}^{(z,i)} + \frac{N_{\mathrm{IRef}}^{(z,i)}}{N_{\mathrm{IRef}}^{(z,0)}} \left(f_{\mathrm{s,IRef}}^{(z,0)} - 8 \cdot \mathrm{sign}_{\mathrm{IRef}}^{(z,0)} \cdot f_{\mathrm{DDS1}}^{(z)} \right) \left(\right. \end{aligned} \tag{2.29}$$

where $\varepsilon_{\mathrm{tot}}^{(z,i)}(\nu_{\mathrm{IRef}}) = \varepsilon^{(z,i)}(\nu_{\mathrm{IRef}}) - \frac{N_{\mathrm{IRef}}^{(z,i)}}{N_{\mathrm{IRef}}^{(z,0)}} \cdot \varepsilon^{(z,0)}(\nu_{\mathrm{IRef}})$.

The variance of the beatnote in the optical domain (normalized by ν_{IRef}), once we differentiate equation 2.29, is given by:

$$\left(\frac{\sigma(f_{\mathrm{IRef}}^{(z,i)})}{\nu_{\mathrm{IRef}}}\right)^2 = \underbrace{\left(\frac{\sigma(\nu_{\mathrm{IRef}})}{\nu_{\mathrm{IRef}}}\right)^2 \left(1 - \frac{N_{\mathrm{IRef}}^{(z,i)}}{N_{\mathrm{IRef}}^{(z,0)}}\right)^2}_{\sigma^2(1\,\mathrm{s}) \approx (<10^{-15})^2 (4\cdot 10^{-6})^2 \approx (4\cdot 10^{-21})^2} + \left(\frac{\sigma(\varepsilon_{\mathrm{tot}}^{(z,i)}(\nu_{\mathrm{IRef}}))}{\nu_{\mathrm{IRef}}}\right)^2 + \underbrace{\left(\frac{1}{\nu_{\mathrm{IRef}}}\right)^2 \left[\sigma(f_{\mathrm{s,IRef}}^{(z,i)}) + \frac{N_{\mathrm{IRef}}^{(z,i)}}{N_{\mathrm{IRef}}^{(z,0)}} \left(\sigma(f_{\mathrm{s,IRef}}^{(z,i)}) + 8\cdot\sigma(f_{\mathrm{DDS1}}^{(z)})\right)\right]^2}_{\sigma^2(1\,\mathrm{s}) \approx (5\cdot 10^{-15})^2 (<10^{-3})^2 \approx (5\cdot 10^{-18})^2} \tag{2.30}$$

In practice, $f_{\mathrm{IRef}}^{(z,i)}$ features a fractional stability between $5\cdot 10^{-17}$ and $2\cdot 10^{-16}$ at 1 s as shown in Fig. 2.12 and Fig. 2.13, which necessarily results from the term $\sigma(\varepsilon_{\mathrm{tot}}^{(z,i)}(\nu_{\mathrm{IRef}}))$ since the two other terms have a much better stability. The averaged fractional values derived from equation 2.29 and their statistical resolutions are compared in table 2.3.

For both combs, the resulting $\left\langle \varepsilon_{\mathrm{tot}}^{(z,i)}(\nu_{\mathrm{IRef}}) \right\rangle$ for EDFAs 1 and 2 are compatible with zero and negligible when compared to the limit imposed by the Cs atoms at the time of performing absolute frequency measurements (see section 3.1.1). The fractional stabilities $\sigma(\varepsilon_{\mathrm{tot}}^{(z,i)}(\nu_{\mathrm{IRef}}))$ of both outputs in the operational comb (Er:fiber 1) are between $5-6\cdot 10^{-17}$ at 1 s, reaching $1\cdot 10^{-16}$ after 10 s, while for the back-up comb (Er:fiber 2) start at $2\cdot 10^{-16}$ and reach a maximum of $4\cdot 10^{-16}$. For the two combs they are clearly below the flicker floor noise of the IRef USL to which the combs are locked to. The instabilities are negligible with respect to the stability of SYRTE clock lasers at any time scale. These limits must be however considered in order to be compatible with the expected stability of the ongoing work on new sources ($< 10^{-16}$ at 1 s). For this reason, to eliminate the noise of these EDFAs, we have developed the methods described in section 4.3 so that measurements of optical frequency ratios or stability transfer processes involving frequencies that are not beaten in the same comb output do not suffer from their limited performances.

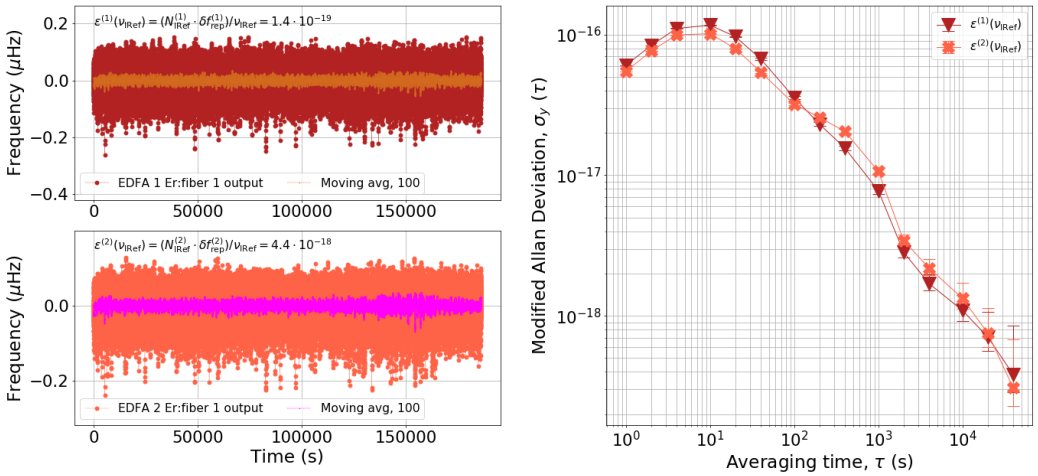

Figure 2.12: Averaged fractional values and fractional stabilities after the Er:fiber 1 comb optical amplifiers EDFA 1 and EDFA 2. The two outputs seem to present the same asymmetry and the cause has not been clearly identified yet, but it changes the respective averaged fractional values by a negligible amount. $N^{(1)}_{\mathrm{IRef}}$ and $N^{(2)}_{\mathrm{IRef}}$ are both equal to 777 602. Measurements in Lambda mode.

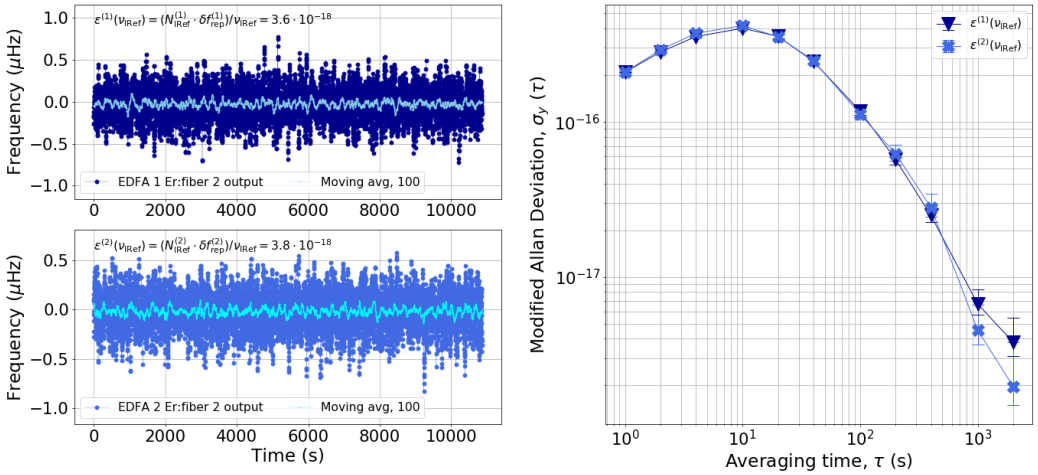

Figure 2.13: Averaged fractional values and fractional stabilities after the Er:fiber 2 comb optical amplifiers EDFA 1 and EDFA 2. $N^{(1)}_{\mathrm{IRef}}$ and $N^{(2)}_{\mathrm{IRef}}$ are equal to 777 289 and 777 290, respectively. Measurements in Lambda mode.

	Er:fiber 1	Er:fiber 2
EDFA 1 (a)	Avg: $3.5 \cdot 10^{-19}$	Avg: $3.6 \cdot 10^{-18}$
	Res: $3.8 \cdot 10^{-19}$	Res: $2.3 \cdot 10^{-18}$
EDFA 2 (b)	Avg: $2.6 \cdot 10^{-19}$	Avg: $3.8 \cdot 10^{-18}$
	Res: $3.1 \cdot 10^{-19}$	Res: $1.9 \cdot 10^{-18}$

Table 2.3: EDFAs frequency agreements in the optical domain after spectral broadening. Averaged values and resolution measurements in relative units respect to $\nu_{\mathrm{IRef}} = 194.4\,\mathrm{THz}$. (a) and (b) for measurement times of 185 996 s (51 h 39 m 56 s) and 10 859 s (3 h 00 m 59 s), respectively. The one order of magnitude difference is explained by a bit longer piece of uncompensated fiber in the IRef light locking the Er:fiber 2 together with the shorter measurement time performed.

2.4 Conclusion

We have presented the main characteristics of the different combs available and how they are referenced to ultrastable optical cavities. The fs intra-cavity elements and actuators provide us a precise and fine control of the two degrees of freedom of the comb in order to perform optical phase lock loops. Likewise, the RF components and the electronics play a fundamental role to achieve a robust lock, i.e. operating in a linear regime and with no phase lock-related cycle slips. The PLL bandwidth larger than 800 kHz ensures the transfer of spectral purity from the ultrastable optical source to all comb's teeth, reaching the comb the narrow linewidth regime. This is particularly important when comparing ultrastable lasers as it sets the stability floor of optical measurements, which is ultimately limited by the USL to which the comb is locked (as far as possible electronic/optical sources of noise are negligible or well compensated). On the other hand, an auto-relocking system has been implemented both to operate the comb remotely and to automatically rearm the comb's PLL when a sudden shock occur or simply when the PLL circuit is close to reach its finite dynamics. Thus permitting to operate the comb with nearly uninterrupted uptimes during months.

The frequency chain architecture attached to the combs is connecting the optical and microwave oscillators/references. We have evaluated the noise floor imposed by the critical elements interleaved in the chain, which have been designed and adapted according to the ultrastable microwave reference used in order to be able to quantify its intrinsic noise. The overall microwave noise floor of the chain has been derived when comparing the UMR versus the microwave photonic signals (f_{rep} and its harmonics) from the different combs. This limit of $6-7 \cdot 10^{-15}$ at 1 s has been proved to be a combination of the photodetection and amplification noises of the microwave signals together with the noise of the UMR itself and the residual propagation noise of its compensated link.

In the optical domain, narrow band-pass filters are used to isolate and enhance the

SNR of the optical beatnotes to be measured between the comb (in the narrow linewidth regimen) and the USLs. Despite rejecting significantly the white phase noise present on the optical signals they introduce a phase shift that depends on the frequency. The dephasing must be meticulously considered in case of a laser drift since it would translate in a frequency offset. Our system can tolerate a maximum fractional frequency drift of $2 \cdot 10^{-15}\,\mathrm{s}^{-1}$ so as to guarantee an accuracy lower than 10^{-18}. Additionally, the optical technical noise added by the Er:fiber comb outputs (a combined contribution of uncompensated fibers, residual propagation noise and possible noise added by the optical amplifiers) has been characterized, showing a performance of $5-6 \cdot 10^{-17}$ at 1 s for the operational comb. At the present stage, these outputs do not affect the comb narrow linewidth regimes but can lead to possible stability limitations for the new optical oscillators under research at SYRTE, which motivates the further comparisons and the techniques implemented followed in the next chapters in order to circumvent it.

Chapter 3

Accuracy and stability of the SYRTE frequency chain

In the previous chapter we have detailed the concept of an OFC, how it is linking the different oscillators and clocks via its frequency chain, and what are the limits imposed when counting signals. The objective of this chapter is to describe how OCs are compared to microwave clocks, in particular to the AFs, and to other OCs of different frequencies with an OFC. We will study how frequency combs enable the derivation of free-running oscillators' frequency ratios, and how the atomic corrections between the oscillators and the metrological atomic transitions are taken into account to derive clocks' frequency ratios. Since the SYRTE architecture is composed of several OFCs, this situation is utilized to assess the accuracy and the stability of the measurements. After reviewing the background necessary for frequency calculation, we will evaluate the practical stability limits of our frequency chain both in the microwave and optical domains.

3.1 Comparing clocks and oscillators

At the time of determining the frequency of an optical atomic standard, on the one hand, we measure the optical frequency from the clock laser with the OFC, given by equation 2.18, which can be rewritten as:

$$\nu_{\mathrm{L}} = N_{\mathrm{L}} \cdot f_{\mathrm{rep}} + \mathrm{sign}_{\mathrm{L}} \cdot f_{\mathrm{L}} + f_{\mathrm{s,L}} \tag{3.1}$$

where $f_{\mathrm{s,L}}$ accounts for all frequency's shifts along the setup due to the use of AOMs to compensate cavity's drifts and fiber noise from the laser source to the optical trap where the atoms are interrogated. Since there is no ambiguity in the sign of the added frequency shift we allow the sign to be positive or negative. On the other hand, the

optical atomic clock frequency, that is the clock laser frequency corrected by the atoms after interrogation, reads:

$$\nu_{at} = q \cdot \nu_L + f_{bridge} \tag{3.2}$$

where q is a conversion factor that might be needed for the atomic spectroscopy ($q = 2$ if the clock laser needs to be frequency doubled, for instance) and f_{bridge} is the frequency difference (positive or negative) between the initial ν_L and the real frequency provided by the atomic transition. This frequency is applied on top of a frequency shift made by the AOM in charge of driving the laser light to probe the atoms.

3.1.1 Expression of absolute optical frequencies

The "absolute" value of a physical quantity is no other than its relative value with respect to another one chosen as a reference. When referring to an absolute frequency measurement in fact we are implicitly talking about a frequency value that has been measured against the definition of the SI second, based on ^{133}Cs, which is set to be $f^0_{Cs} = 9.192\,631\,770\,\text{GHz}$. An ensemble of around 400 atomic clocks continuously operated (mainly commercial Cs clocks and H masers) spread worldwide constitute the EAL, which, in turn, is steered by the best PSFSs, such as Cs and Rb AFs and a few OCs, to provide the TAI. The continuous frequency comparison between TAI and the average of all the PSFSs available provides the SI second.

To perform an optical clock absolute measurement ν_{at} either one has access to a local realization of the SI second or one uses a satellite-based frequency linked to TAI [102, 103, 104, 105] to access to it. This last approach provides less resolution because TAI is computed at 5-day intervals via the *Circular T*[1] when the corresponding offset of that scale interval from the SI second is published as a monthly average, and long averaging times are needed to reduce the link uncertainty.

In the following we will focus on the case where PSFSs are directly available which is the case at SYRTE with its three AFs that provide an accuracy at the low parts in 10^{16} level after $2-3$ days. To derive the absolute frequency, for simplicity, we will omit the terms $f_{s,L}$ and q from equations 3.1 and 3.2 that must be added if exist. The final quantity targeted will be actually a ratio between the clock under evaluation ν_{at} and the Cs atoms from one of the Cs atomic fountains f_{Cs}. And this last, in turn, will be another ratio between the local Cs frequency and the mentioned above f^0_{Cs}.

Let us base the next equations on the frequency of an optical clock OC1 with respect to the SI second definition $\nu_{at,Cs}$. The frequency of the clock ν_{at} is measured against the H maser f_M used to reference all the counters and synthesizers, while this last in the meantime is measured against the Cs. Therefore, the absolute frequency we are looking

[1] The *Circular T* is a monthly publication from the BIPM Time Department which provides traceability to Coordinated Universal Time (UTC) for the local realizations UTC(k) through the values of the differences [UTC – UTC(k)] every five days.

for is:

$$\nu_{\mathrm{at,Cs}} = \frac{\nu_{\mathrm{at}}}{f_{\mathrm{Cs}}/f^0_{\mathrm{Cs}}} = \frac{\nu_{\mathrm{at}}}{f_{\mathrm{M}}/f^0_{\mathrm{M}}} \cdot \frac{f_{\mathrm{M}}/f^0_{\mathrm{M}}}{f_{\mathrm{Cs}}/f^0_{\mathrm{Cs}}} \tag{3.3}$$

where f^0_{M} is the 100 MHz frequency from the H maser. The first term of equation 3.3, $\frac{\nu_{\mathrm{at}}}{f_{\mathrm{M}}/f^0_{\mathrm{M}}}$, is derived after summing the respective ratios measured in the OFC laboratory and in the OC laboratory. Thus, according to equations 3.1 and 3.2:

$$\nu_{\mathrm{at,M}} = \frac{\nu_{\mathrm{at}}}{f_{\mathrm{M}}/f^0_{\mathrm{M}}} = \frac{\nu_{\mathrm{L}} + f_{\mathrm{bridge}}}{f_{\mathrm{M}}/f^0_{\mathrm{M}}} \tag{3.4}$$

To avoid large numbers, we express and publish all the quantities involved with reduced ratios η, i.e values with a small number of significant digits with respect to a reference number accepted by the community. To this end, from equation 3.4 we form the quantity:

$$\eta_{\mathrm{at,M}} = \frac{\nu_{\mathrm{at,M}}}{\nu^0_{\mathrm{at}}} - 1 \approx \frac{\nu_{\mathrm{at}}}{\nu^0_{\mathrm{at}}} - \frac{f_{\mathrm{M}}}{f^0_{\mathrm{M}}} \tag{3.5}$$

where ν^0_{at} it is a reference value for that optical frequency and must be the same in order to allow meaningful comparisons. In case of being listed among the Comité International des Poids et Mesures (CIPM) recommended frequency standard values [106], that is the agreed value to be used. Doing the same approach for the second term of equation 3.3 that is provided by the Cs fountain team, we have:

$$\eta_{\mathrm{M,Cs}} = \frac{f_{\mathrm{M}}/f^0_{\mathrm{M}}}{f_{\mathrm{Cs}}/f^0_{\mathrm{Cs}}} - 1 \approx \frac{f_{\mathrm{M}}}{f^0_{\mathrm{M}}} - \frac{f_{\mathrm{Cs}}}{f^0_{\mathrm{Cs}}} \tag{3.6}$$

From equations 3.5 and 3.6 we can get the expression:

$$\frac{\nu_{\mathrm{at,Cs}}}{\nu^0_{\mathrm{at}}} = (\eta_{\mathrm{at,M}} + 1)\,(\eta_{\mathrm{M,Cs}} + 1) \approx \eta_{\mathrm{at,M}} + \eta_{\mathrm{M,Cs}} + 1 \tag{3.7}$$

Finally, from this last equation we are able to retrieve the reduced ratio of the initial aimed value as:

$$\eta_{\mathrm{at,Cs}} \approx \eta_{\mathrm{at,M}} + \eta_{\mathrm{M,Cs}} \approx \frac{\nu_{\mathrm{at}}}{\nu^0_{\mathrm{at}}} - \frac{f_{\mathrm{Cs}}}{f^0_{\mathrm{Cs}}} \tag{3.8}$$

Thereby in practice we need to measure four quantities: f_{rep}, f_{L}, f_{bridge} with respect to the H maser, and f_{M} with respect to the Cs atoms.

3.1.2 Expression of optical frequency ratios

Since only ratios can accurately describe the result of a measurement in physics, clock comparisons are always expressed in terms of frequency ratios, also in the case of optical

to optical comparisons. The uncertainties of optical frequency standards have already surpassed the best realizations of the SI second. Thanks to the ratios and the OFCs, it is possible to compare directly OCs without using Cs clocks in between, what would limit both the stability and accuracy of the measurement.

To compare two optical clocks OC1 and OC2, with atomic frequencies ν_{at1} and ν_{at2}, from equations 3.1 and 3.2 we first derive the corresponding beatnotes f_L in the OFC, and next we account for the frequency differences f_{bridge} between their clock lasers and their clock transitions:

$$\begin{aligned} \nu_{at1} &= \nu_{L1} + f_{bridge1} = N_{L1} \cdot f_{rep} + \text{sign}_{L1} \cdot f_{L1} + f_{bridge1} \\ \nu_{at2} &= \nu_{L2} + f_{bridge2} = N_{L2} \cdot f_{rep} + \text{sign}_{L2} \cdot f_{L2} + f_{bridge2} \end{aligned} \tag{3.9}$$

In order to form the ratio only between the two clock lasers, ν_{L1}/ν_{L2}, we eliminate f_{rep}, which is in fact equivalent to apply the transfer oscillator method [107] by post-processing. The ratio therefore yields:

$$\frac{\nu_{L1}}{\nu_{L2}} = \frac{N_{L1}}{N_{L2}} + \frac{1}{\nu_{L2}} \left(\text{sign}_{L1} \cdot f_{L1} - \frac{N_{L1}}{N_{L2}} \cdot \text{sign}_{L2} \cdot f_{L2} \right) \tag{3.10}$$

where the beatnotes must be simultaneously recorded and the channels of the counter synchronized, otherwise f_{rep} would not be exactly the same in the two frequencies of equation 3.9. Note that for the particular case where the OFC is locked to one of the lasers involved, e.g. $\nu_{L2} = \nu_{IRef}$, measuring f_{L1} is sufficient since from equation 2.4 we know that the beatnote f_{L2} is at a constant frequency (see subsection 2.1.2). If we now incorporate the atomic bridge frequencies, the ratio is given by:

$$\frac{\nu_{at1}}{\nu_{at2}} = \frac{N_{L1}}{N_{L2}} + \frac{1}{\nu_{at2}} \underbrace{\left[\text{sign}_{L1} \cdot f_{L1} + f_{bridge1} - \frac{N_{L1}}{N_{L2}} \left(\text{sign}_{L2} \cdot f_{L2} + f_{bridge2} \right) \right]}_{\beta} \tag{3.11}$$

The transfer oscillator means that the term N_{L1}/N_{L2} usually provides at least the first 6 digits because β is typically around 100 MHz and ν_{at2} is a few 100 THz, so the second term of equation 3.11 is 10^{-6} or lower. It is important to remark that, in practice, each frequency is measured against the maser and the frequencies from equation 3.9 are multiplied by f_M/f_M^0 (denoted by the subscript M, as we did previously in equation 3.4). Hence, the frequency value really measured is:

$$\frac{\nu_{at1}}{\nu_{at2}} = \frac{\nu_{at1,M}}{\nu_{at2,M}} = \frac{N_{L1}}{N_{L2}} + \frac{1}{\nu_{at2,M}} \cdot \beta \tag{3.12}$$

To standardize the format of the data provided, we publish reduced ratios. From equation 3.8, if we transpose $\eta_{x,y}$ for $x = \nu_{at1}$ and $y = \nu_{at2}$, we obtain:

$$\eta_{at1,at2} \approx \frac{\nu_{at1}}{\nu_{at1}^0} - \frac{\nu_{at2}}{\nu_{at2}^0} = \frac{\nu_{at2}}{\nu_{at1}^0} \left(\frac{\nu_{at1}}{\nu_{at2}} - \frac{\nu_{at1}^0}{\nu_{at2}^0} \right) \approx \left(\frac{\nu_{at1}}{\nu_{at2}} - \frac{\nu_{at1}^0}{\nu_{at2}^0} \right) \Big/ \frac{\nu_{at1}^0}{\nu_{at2}^0} \tag{3.13}$$

which leads to:

$$\eta_{\mathrm{at1,at2}} = \left[\left(\frac{\nu_{\mathrm{L1}}}{\nu_{\mathrm{L2}}} - \frac{\nu^0_{\mathrm{at1}}}{\nu^0_{\mathrm{at2}}} \right) + \frac{1}{\nu_{\mathrm{at2,M}}} \cdot \beta \right] \Big/ \frac{\nu^0_{\mathrm{at1}}}{\nu^0_{\mathrm{at2}}} \tag{3.14}$$

where ν^0_{at1} and ν^0_{at2} will be taken from [106] for current atomic/molecular transitions. The ratio derivation is equivalent to measure $\beta/\nu_{\mathrm{at2,M}}$ since the rest of the quantities are fixed. A further simplification on the former term, often implemented, is to substitute the measured $\nu_{\mathrm{at2,M}}$ by ν^0_{at2}. To evaluate the impact in terms on the ratio accuracy we make the derivative of the time-dependent quantities involved, i.e. $\eta'_{\mathrm{at1,at2}} = \beta/\nu^0_{\mathrm{at2}}$, which yields:

$$\delta\eta'_{\mathrm{at1,at2}} = \frac{\delta\nu_{\mathrm{at2}}}{\left(\nu^0_{\mathrm{at2}}\right)^2} \cdot \beta = \frac{\delta\nu_{\mathrm{at2}}}{\nu^0_{\mathrm{at2}}} \frac{\beta}{\nu^0_{\mathrm{at2}}} \tag{3.15}$$

where $\frac{\beta}{\nu^0_{\mathrm{at2}}} \approx 10^{-6}$ as explained before, and the first term can be rewritten as:

$$\frac{\delta\nu_{\mathrm{at2}}}{\nu_{\mathrm{at2}}} = \frac{\nu_{\mathrm{at2,M}} - \nu_{\mathrm{at2}}}{\nu_{\mathrm{at2}}} \approx \frac{\nu_{\mathrm{at2}}(1+\varepsilon_{\mathrm{M}}) - \nu_{\mathrm{at2}}}{\nu_{\mathrm{at2}}} = \varepsilon_{\mathrm{M}} \tag{3.16}$$

being $\varepsilon_{\mathrm{M}} < 5 \cdot 10^{-13}$ the fractional offset of the H maser at SYRTE, whose fractional drift is negligible (10^{-16}/day). Therefore, replacing $\nu_{\mathrm{at2,M}}$ by ν^0_{at2} in equation 3.14 would make a change smaller than $5 \cdot 10^{-19}$ which is an order of magnitude below the accuracy's ratio considerations currently agreed to validate the measurement and fulfill the CIPM requirements for the redefinition of the SI second [106].

In Fig. 3.1 an example of the same SrB OLC at SYRTE is shown, where the accuracy of its absolute frequency against the Cs fountain FO2 is $1.6 \cdot 10^{-16}$ and its fractional ratio versus the Hg OLC is $1.1 \cdot 10^{-17}$.

3.1.3 Examples of comparisons in the microwave domain

In our frequency chain any optical, microwave or RF frequency is measured against a common reference that is the master H maser of SYRTE, whose offset is continuously measured by the three atomic fountains (FOx[2]). The H maser is kept free running due to its very predictable long-term behavior, which is precisely measured by the FOx. The result of the comparison is used to steer a micro-phase stepper to generate the timescale UTC(OP), i.e. the local realization of UTC in France. The relative offset can be as high as a few 10^{-13}, but this value does not matter since the role of the FOx is precisely to accurately measure it.

In the course of the fountains development at SYRTE, since 1995 with the FO1 [108], a CSO was developed in order to reduce their Dick effect sufficiently to reach the atomic

[2]FO stands for *fontaine* and "x" refers indistinctly for 1 (based on ^{133}Cs), 2 (dual, based on ^{133}Cs and ^{87}Rb) or M (mobile, based on ^{133}Cs).

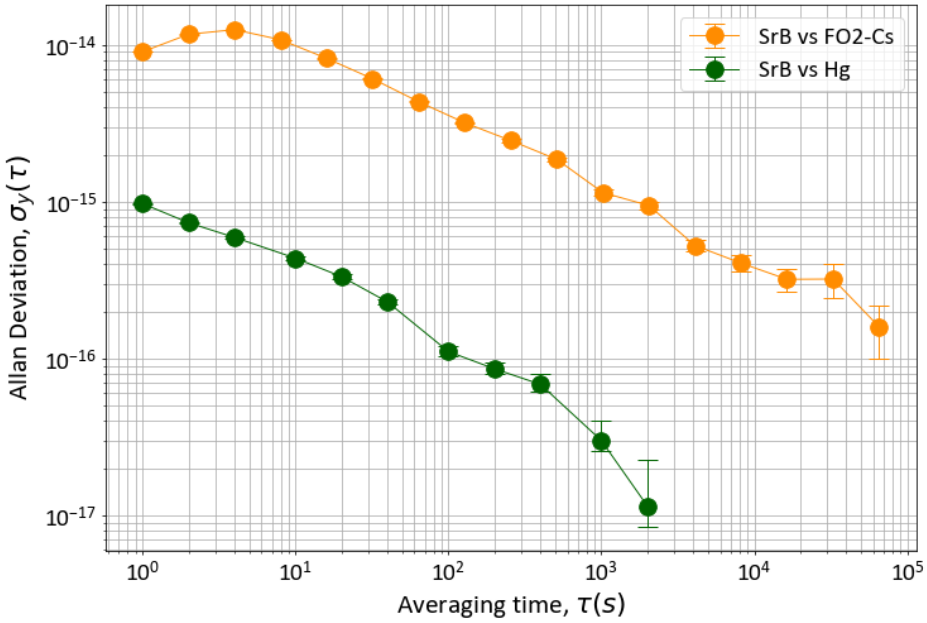

Figure 3.1: Fractional frequency stability of the frequency ratio between the SrB OLC and the atomic fountain FO2-Cs (orange), and the Hg OLC (green). Error bars smaller than markers when not shown. Stabilities in Pi mode.

QPN, allowing to set the theoretical accuracy limits of these clocks. This was possible thanks to the fractional frequency stability of the CSO of $1-2\cdot10^{-15}$ at 1 s that, after a set of high-performance synthesizers, is able to drive the FOx with stabilities down to $1-2\cdot10^{-14}/\sqrt{\tau}$ [109].

Despite its excellent short-term stability, the free-running CSO drifts in the long-term at a rate of 10^{-13} per day while the H maser does it at 10^{-16} per day. To take advantage of both oscillators, we phase lock the CSO to the maser with a long time constant of $\tau_{\mathrm{PLL}} = 1000\,\mathrm{s}$ where their respective curve's stabilities meet as shown in Fig. 3.2. The result is the UMR signal featuring a fractional stability of $1-2\cdot10^{-15}$ up to 1000 s, way better than the H maser (around $1-2\cdot10^{-13}$ at 1 s), or than the best quartz oscillators BVA[3] available (in the high 10^{-14} at 1 s), while benefiting from the long run behavior of the maser.

Thereby, the UMR is required at SYRTE to probe Cs atoms at the QPN limit in the three FOx and to characterize low noise microwave signals generated by the OFCs or from another CSO as in [110]. We will see next other benefits of counting with such a low-noise oscillator as the characterization of a laser in the microwave domain or its

[3]BVA stands for *boîtier à vieillissement amélioré*, enclosure with improved aging in English. It represents the state-of-the-art oven controlled crystal oscillators (OCXO).

drift removal via an offset lock.

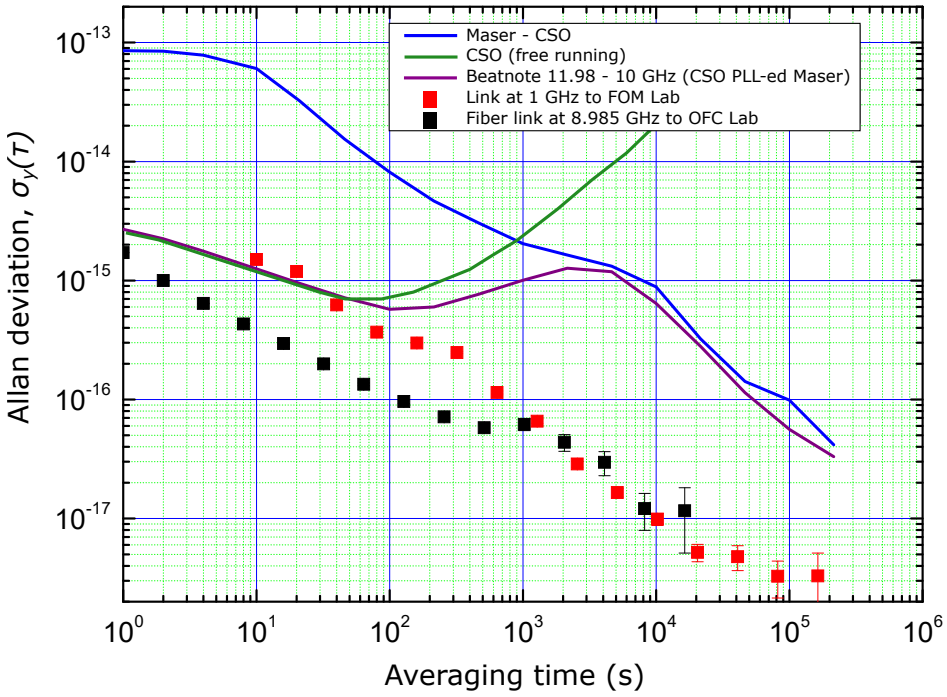

Figure 3.2: Ultrastable microwave reference: cryogenic sapphire oscillator (green line curve) phase locked to the H maser (purple line curve) at $\tau_{\mathrm{PLL}} = 1000\,\mathrm{s}$. The black square markers curve shows the stability of the fiber link (AM) used to bring the microwave reference to the OFC laboratory (operational optical frequency chain). The H maser fractional stability (blue line curve) starts at $8 - 9 \cdot 10^{-14}$ because it has been additionally filtered with a BVA quartz. Data taken from SYRTE Fountains laboratory [110].

Microwave stability limit

Signals derived from the UMR by rescaling are dispatched towards the OFC laboratory at 8.985 GHz and 1 GHz. Another 1 GHz signal, derived from the unfiltered maser, is used as back-up. Since we want to characterize their stability, we will compare each of these three signals to the photonic microwave ones generated by the OFC: the 4^{th} ($\approx 1\,\mathrm{GHz}$) or the 36^{th} ($\approx 9\,\mathrm{GHz}$) harmonic of the repetition rate.

In order to overcome the resolution of the counter, the different pairs of signals are

mixed and multiplied by 200, as described in section 2.2.2, before being sent to the counter, according to Fig. 3.3.

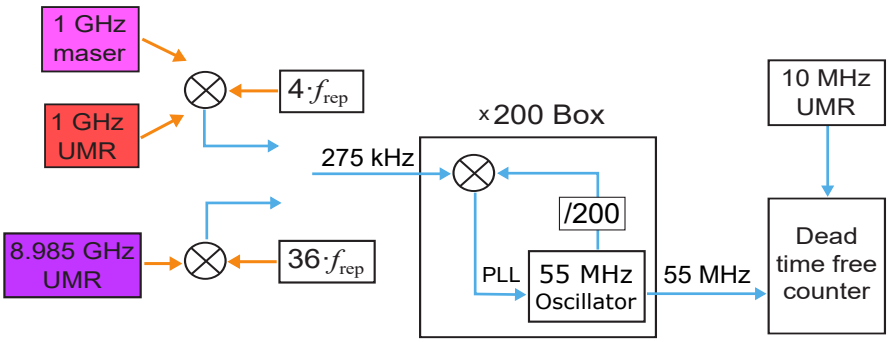

Figure 3.3: Principle of work of the 200-multiplier box and the scheme used to characterize the different microwave references arriving to the laboratory. The 8.985 GHz and 1 GHz from the UMR and 1 GHz from the H maser are compared to the closest comb's repetition rate harmonics. The respective fractional stabilities are shown in Fig. 3.5.

The stability of the 1 GHz UMR against the 4$^{\text{th}}$ harmonic of the OFC is given by:

$$\sigma^2(\text{Ch}) = \sigma^2(\times 200) + 200^2\left[\sigma^2(4\cdot f_{\text{rep}}) + \sigma^2(1\,\text{GHz})\right] + \sigma^2(\varepsilon_C) \tag{3.17}$$

where $\sigma^2(\times 200) = \left[(275\,\text{kHz})^2\cdot\sigma^2(\varepsilon_M) + \sigma^2(\varepsilon_A)\right]$.

The predominant noise of 5.6 mHz at 1 s (red curve on Fig. 3.4) is due to $\sigma(1\,\text{GHz})$, since $\sigma(\times 200) \approx 50\,\mu\text{Hz}$ as seen in equation 2.16, and $\sigma(4\cdot f_{\text{rep}})$ and $\sigma(\varepsilon_C)$ are about one order of magnitude below (see green and black curves in Fig. 3.4). The way the noise of $4\cdot f_{\text{rep}}$ has been derived will be justified later in subsection 3.2.1. The final fractional stability at 1 s for the 1 GHz UMR signal is $\sigma_y(1\,\text{GHz}) = 5.6\,\text{mHz}/(200\cdot 1\,\text{GHz}) = 2.8\cdot 10^{-14}$.

Applying the same equation 3.17 to the 1 GHz maser and normalizing we get a relative (absolute) stability of $1.2\cdot 10^{-13}$ (0.12 mHz) at 1 s, while the corresponding one for the 8.985 GHz UMR, which is compared to the 36$^{\text{th}}$, is $6-7\cdot 10^{-15}$ ($54-63\,\mu$Hz) at 1 s (see magenta and purple curves in Fig. 3.5, respectively). The stability degradation of the 1 GHz UMR, with respect to the 8.985 GHz, is explained by the independent and uncompensated microwave link disseminating the signal to the OFC laboratory.

The comparison of USLs vs the UMR at 8.985 GHz (CSO + maser) is limited by the microwave part of the setup when measuring USLs with short-term stabilities lower than $6-7\cdot 10^{-15}$. The 1 GHz UMR does the same in all devices using directly the 1 GHz, e.g. DDSs, or the down-converted 10 MHz used to reference frequency counters and synthesizers. However, most of the time, all these devices are in charge of producing frequencies that are only offsets of optical carriers, or of counting optical beatnotes.

These quantities are always on the order of 100 MHz at most and therefore their absolute stabilities ($2.8 \cdot 10^{-14} \cdot 100\,\text{MHz} = 2.8\,\mu\text{Hz}$) once rescaled to an optical frequency (around 10^{-20}) are negligible.

A laser vs the ultrastable microwave reference

There are two methods to consider when measuring the frequency of a laser ν_L versus the UMR, which depend on the linewidth $\delta\nu_L$ of the laser itself.

- When $\delta\nu_L$ is large, e.g. more than 1 kHz, it is necessary to use filters with a larger bandwidth (at least a factor 100 wider than the linewidth) before counting the frequency of the optical beatnote f_L between the laser and the OFC. Unavoidably, this results in a reduction of the SNR of the f_L that can potentially become too small to be counted by the frequency counter. The solution is to lock the OFC directly to the ν_L, with a sufficient bandwidth and gain to avoid lock-related cycle slips (as we do for ν_{IRef} in equation 2.4), and to compare the resulting f_{rep} against

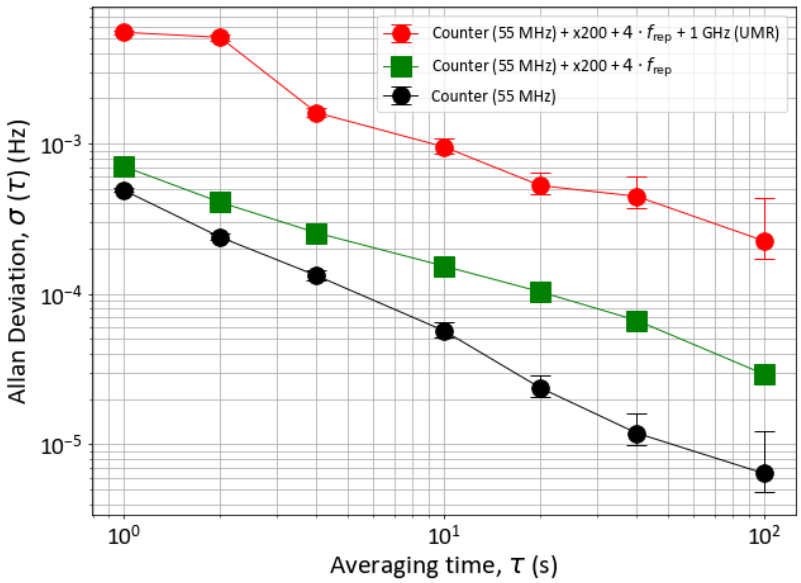

Figure 3.4: Noise of the 1 GHz microwave reference signal compared against the comb (4^{th} harmonic of its repetition rate) where the $\times 200$ multiplier is at play (red curve). The $4 \cdot f_{rep}$ (green curve) has been measured against another IR ultrastable laser, ν_{IRefB1}. The black curve shows the noise floor of the phase/frequency counter at 55 MHz. All stabilities shown are in Pi mode.

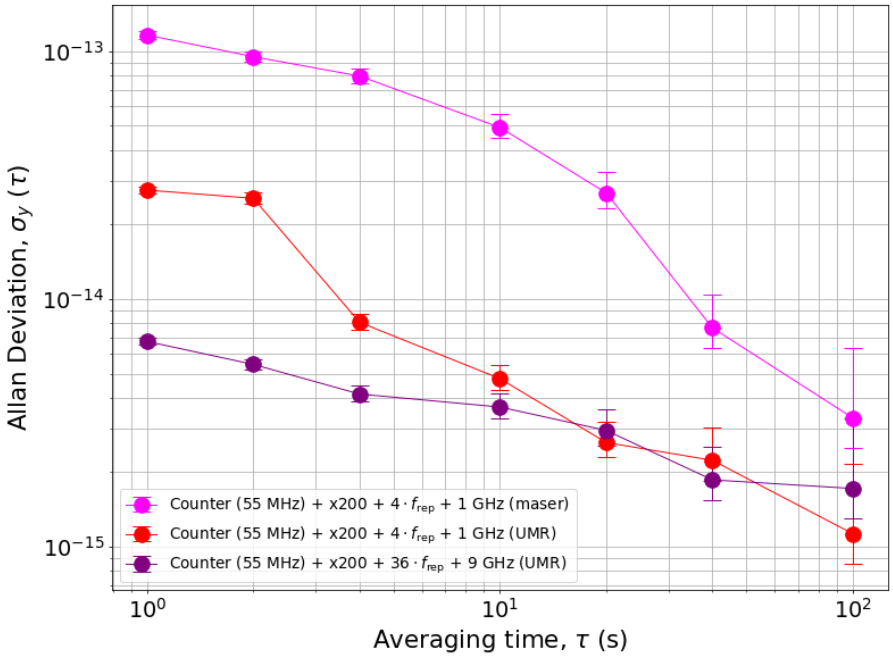

Figure 3.5: Stabilities in Pi mode of all microwave references used in the OFC laboratory.

the UMR at 8.985 GHz (equation 2.8). Doing this, we transfer the stability from the optical domain to the microwave frequencies generated by the comb (harmonics of the repetition rate, $f_\mu = n \cdot f_{\text{rep}}$) so: $\delta\nu_L/\nu_L = \delta f_{\text{rep}}/f_{\text{rep}} \approx \delta f_\mu/f_\mu$[4], with $\nu_L \approx N_L \cdot f_{\text{rep}}$ since $f_L \ll \nu_L$. For instance, for $\nu_L = 194$ THz and $f_\mu = 9$ GHz, with $f_{\text{rep}} = 250$ MHz, we divide the carrier frequency by $M = \nu_L/f_\mu = N/n \approx 2 \cdot 10^4$, reducing the phase fluctuations accordingly and therefore resulting in an enhancement of the SNR sufficiently good to be measured in a typical measurement bandwidth.

This case applies for lasers that can be beaten directly in the spectrum of the OFC main oscillator (1515 – 1595 nm). Nevertheless, this could be applied in an indirect way for lasers out of this range but still covered by one of the EDFAs outputs. In this particular case a second PLL doing the fine-tuning of the stabilization of the beatnote between ν_L and the EDFA output should be implemented on top of the one locking the OFC main oscillator to a laser in the band 1515 – 1595 nm to reach the narrow linewidth regime.

- For a narrow linewidth laser, usually $\delta\nu_L < 1$ kHz, the optical beatnote between

[4] In the stability transfer to the microwave domain we must take into account the (predominating) noise introduced by the photodetection and amplification of the repetition rate harmonics.

the laser and the comb is narrow enough to be measured in a filter that allows for a reasonable SNR to have the counter functioning nominally. The absolute frequency is then reconstructed by taking into account the simultaneous measurement of f_{rep} (equation 2.8) in equation 2.18. In the case where ν_{L} is within reach of the OFC main output, one can also lock the comb to the laser although this requires to adapt the PLL parameters and chain RF filters, while the optical approach is straightforward and simpler.

Application: dedrift of the ultrastable 1542 nm IR reference

Thanks to the optical to microwave measurements where we connect and compare optical frequencies (within the OFC spectral range) to the UMR, we are able to characterize the drift of the USL, ν_{IRef}, where the OFC is locked to.

This is possible because the short-term stability of the UMR is around $2 \cdot 10^{-15}$ until 1000 s that it averages down, with a negligible drift of around 10^{-18} per second. In contrast, the natural drift of the IRef laser is of a few 10^{-14} per second due to the lack of temperature regulation. This means that once the IRef laser curve stability crosses the UMR one, we can see the laser's drift and quantify it. The initial drift can therefore be resolved in a few seconds. The change of drift is then visible after 15 – 30 s, so we base the residual drift detection on an integration time of 30 s. We take advantage of this fact to induce a counter drift or "dedrift" in a computer-controlled DDS (Ettus USRP N200), df_{Ettus}/dt, that is in charge of the offset lock between the master ($\nu_{\text{IR,master}}$) and slave (ν_{IRef}) lasers, where $\nu_{\text{IRef}} = \nu_{\text{IR,master}} + f_{\text{Ettus}}$ (see bottom left plot, dashed line, in Fig. 2.1). Replacing f_{rep} from equation 2.8 into 2.4, the IRef optical frequency is given by:

$$\nu_{\text{IRef}}(t) = N^{(0)}_{\text{IRef}} \frac{f_{\text{UMR}} + f_{\text{DDS2}} - \frac{\text{Ch1}(t)}{200}}{36} + 8 \cdot \text{sign}^{(0)}_{\text{IRef}} \cdot f_{\text{DDS1}} \tag{3.18}$$

with $\nu_{\text{IRef}} = \nu^{(0)}_{\text{IRef}} - f^{0}_{\text{s,IRef}}$. If we differentiate equation 2.4 we can express the drift of the IR reference laser, $d\nu_{\text{IRef}}/dt$, in terms of the repetition rate as $N_{\text{IRef}} \cdot df_{\text{rep}}/dt$, where we do a linear fit by $\nu_m + \alpha_m \cdot t$ on a 30-s segment number m.

The first approach we performed was based on an update of the dedrift (from the previous segment m slope) and it is given by the following equation:

$$\left(\frac{df_{\text{Ettus}}}{dt}\right)_{m+1} = \left(\frac{df_{\text{Ettus}}}{dt}\right)_{m} - \alpha_m \tag{3.19}$$

Note that the dedrifting of ν_{IRef} can be also performed in the optical domain against another, more stable optical reference, as far as this latter is locked to an atomic reference in order to fight against its tendency to suffer from the temperature fluctuations induced phenomenon due to the tight connection between the cavity mounting and the mechanical mount. This option, in fact, is implemented in our control software with the

clock laser ν_{HgL} and performed when the Hg OLC is operational. However, its current uptime does not allow us to fully rely on it while the microwave reference does.

This dedrift technique, whether it is implemented with a microwave or an optical reference, is applied to a laser previously locked on an ultrastable Fabry-Perot resonator. Even if the drift is removed, the absolute frequency is free running and this becomes relevant when the dedrifted laser, ν_{IRef}, is also used as the seed signal for the French part of the European fiber link for time and frequency metrology purposes since, on the long run, SYRTE has the goal to distribute accuracy, on top of stability, in the French fiber network REFIMEVE+. The disseminated frequency at 194.4 THz must not get away by more than a few 100 MHz from the source nominal value in order to stay in the range covered by the diode lasers (RIO Planex) used and all the optical/electro-optical components deployed all along the link, e.g. filters, detectors, PPLs, tracking oscillator filters, and so on.

The lock performed in equation 3.19 is only proportional to $d\nu_{\mathrm{IRef}}/dt$ and the walk of the integral ν_{IRef} is not stopped. The typical fluctuations are around several hundreds of Hz per day and f_{DDS2} has to be monitored and adjusted manually in order to stay in the range of the filters. To overcome this limitation, an additional correction was added at the end of 2019 to the correction of equation 3.19, which became operational last March 2020 coinciding with the annual optical clock's international calibration campaign. The new approach consists in adding a term corresponding to the integral of the drift, i.e. to the frequency itself to which the frequency target ν_{target} is subtracted. The updated dedrift now reads:

$$\left(\frac{df_{\mathrm{Ettus}}}{dt}\right)_{m+1} = \left(\frac{df_{\mathrm{Ettus}}}{dt}\right)_{m}\left(-\alpha_m - \frac{\nu_{\mathrm{IRef}} - \nu_{\mathrm{target}}}{T}\right) \tag{3.20}$$

where T is the time constant set to 100 s. The resulting data provides us now with a slope and also with an offset to the (arbitrarily chosen) ν_{target} value of 194.400 121 THz that is quantified in terms of maser Hertz. Note that, in the end, the final accuracy must be refined later by comparison of the maser against the atomic fountains.

In Fig. 3.6 the result of the dedrifted ν_{IRef} can be observed when the IRef laser is compared to the UMR. The green data points show the former loosely locked to the latter, it is therefore an in-loop measurement: when locked to the UMR, the frequency of the IRef laser is counted via a K+K counter, which is referenced to the UMR. The oscillator's comparison is first dominated by the less stable oscillator, the UMR at $1-2\cdot10^{-15}$ at 1 s, which averages down at short time scales (see purple curve in Fig. 3.2) until it meets the IRef laser that is dominated by its drift around $\tau = 5$ s. From this time on the drift is measured by the UMR for the next 100 s after which the correction is applied. After $\tau = 100$ s, when only the proportional term was used (equation 3.19), the red curve shows the residual IRef laser noise instability (combined random walk noise and remaining laser drift). In contrast, when the integrator term was added (equation 3.20), we observe an inflection point at $\tau = 100$ s where the IRef laser tries to follow

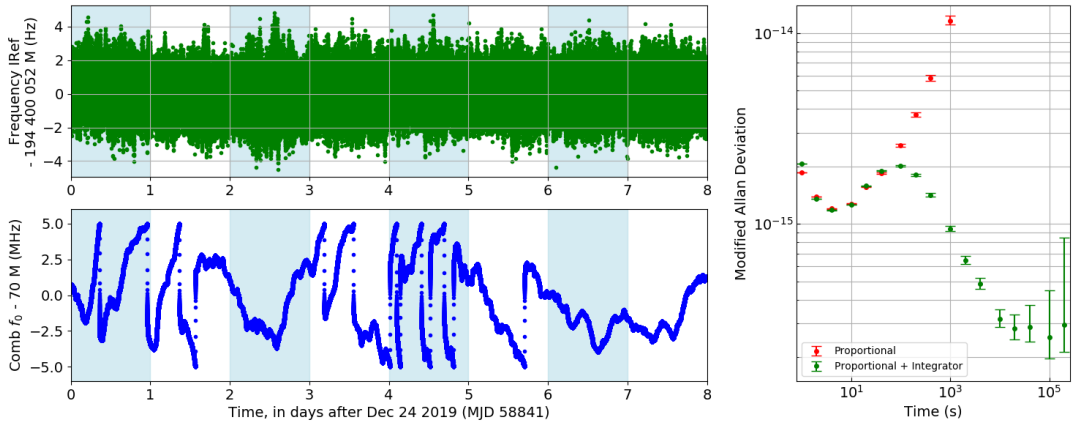

Figure 3.6: Comparison of the SYRTE ultrastable microwave reference (UMR) at 8.985 GHz against the IRef laser. Top left plot: the IRef laser is dedrifted every 100 s by the UMR (green). Bottom left plot: Offset frequency of the comb during the measurement (blue). Right plot: long-term instability of the IRef laser after being dedrifted using a proportional correction (red), and after adding an integrator term for the dedrift (green), where the laser follows to some extent the UMR due to the improved proportional lock performed. Counter set in Lambda mode.

the UMR (green curve) and averages down with it, as the computer imposes a slow proportional in frequency lock (as we integrate the drift) in order to keep its frequency constant in average. It is important to remark that it is neither a frequency lock nor a phase lock. At this stage there is no guaranty that we don't loose any cycle, so it is not yet ready to make a timescale based on an optical vector.

On the one hand, one would expect the former in-loop stability curve (green curve in Fig. 3.6) to be well below the absolute stability of the UMR itself (purple curve in Fig. 3.2 up to $10^4 - 10^5$ seconds) at all timescales but this is not the case between $10 - 10^3$ s. On the other hand, the in-loop stability stops averaging down, remaining at $3 \cdot 10^{-16}$ after 10^5 s. We have thought about it from two different (and possibly associated) points of views, although further investigations are needed for a detailed justification. The first argument we give is a delayed drift correction: the measurement of the residual drift takes place over 100 s, the dedrift's value is updated accordingly, and this new value stays applied during the next 100 s interval, and so on. Besides, we know that there is still a second order drift that is not negligible and that is not taken into account in the feedback correction, which would affect the stability. The second argument is related to the proportional (frequency) lock, i.e. integration of the drift with a very low time constant of 100 s. The correction is always proportional to the frequency difference between the actual laser's frequency and the target frequency. Thereby, there is always a small offset (due to the lack of integration) that might fluctuate and set a stability floor

limit around $3 \cdot 10^{-16}$ after 10^4 seconds.

3.1.4 Examples of comparisons in the optical domain

We can divide our two optical oscillators' comparisons in two groups. On the one hand, the oscillators that are frequency close enough so once they are combined, the resulting beatnote comes directly within the PD's bandwidth, up to 100 GHz ($\Delta\lambda = 0.8$ nm for a 1542 nm laser) for the fastest existing detectors. In this case, the instabilities at play will be the ones from the oscillators themselves, assuming that the fiber links along the setup, if any, are well compensated. On the other hand, we have the oscillators that are far away in frequency from each other, and the very powerful method yielded by an OFC is precisely to be able to compare them as long as they are within reach of the spectrum provided at the OFC outputs.

In the case where two ultranarrow lasers (< 1 Hz large spectrally) are compared, e.g. the IRef used to lock the OFC and another USL under study, it is very important that the optical path from the USLs respective reference points (usually the input mirrors of their reference ultrastable cavities) are well compensated to avoid any extra noise transferred to the beatnotes between the lasers and the comb. Note that an uncompensated fiber can broaden the spectrum up to a few 10 Hz.

Two ultrastable lasers comparison

Since our OFC is locked to an optical reference, ν_{IRef}, we can compare any USL ν_{L} against IRef since all the comb's teeth will have the same stability as ν_{IRef} due to the narrow linewidth regime.

When deriving the stability of an optical beatnote formed in an OFC, as explained in subsection 2.3, we also have to take into account the noise $\varepsilon^{(z,i)}(\nu_{\mathrm{L}})$ added by the locking of the comb and uncompensated paths. Thus, equations 2.4 and 2.5 become:

$$n^{(z)} \cdot f_{\mathrm{DDS1}}^{(z)} = \mathrm{sign}_{\mathrm{L}}^{(z,0)} \left(\nu_{\mathrm{L}} + f_{\mathrm{s,L}}^{(z,0)} - N_{\mathrm{L}}^{(z,0)} \cdot f_{\mathrm{rep}}^{(z)} + \varepsilon^{(z,0)}(\nu_{\mathrm{L}}) \right) \Bigg(\tag{3.21}$$

where $i = 0$ only applies to the fiber combs ($z = 1, 2$), and $n = 8$ ($n = 16$) and $\mathrm{L} = \mathrm{IRef}$ ($\mathrm{L} = \mathrm{HgL}$) for the fiber combs (for the Ti:sa comb ($z = 3$)), and $f_{\mathrm{s,L}}^{(z,0)}$ is the applied frequency shift (see values in table 3.2). In the same way, equation 2.18 now reads:

$$f_{\mathrm{L}}^{(z,i)} = \mathrm{sign}_{\mathrm{L}}^{(z,i)} \left(\nu_{\mathrm{L}} + f_{\mathrm{s,L}}^{(z,i)} - N_{\mathrm{L}}^{(z,i)} \cdot f_{\mathrm{rep}}^{(z)} + \varepsilon^{(z,i)}(\nu_{\mathrm{L}}) \right) \Bigg(\tag{3.22}$$

where the term $\varepsilon^{(z,i)}(\nu_{\mathrm{L}})$ scales with the frequency measured and i indicates the OFC output used ($i = 0$ for main, $i = 1$ for EDFA 1, and $i = 2$ for EDFA 2 in the case of our Er:fiber combs), as we will show in the next section. Based on equations 3.21 and

3.22, the fractional variance of the optical beatnote depends on three independent noise sources:

$$\left(\frac{\sigma(f_{\mathrm{L}}^{(z,i)})}{\nu_{\mathrm{L}}}\right)^2 = \left(\frac{\sigma(\nu_{\mathrm{IRef}})}{\nu_{\mathrm{IRef}}}\right)^2 + \left(\frac{\sigma(\nu_{\mathrm{L}})}{\nu_{\mathrm{L}}}\right)^2 + \left(\frac{\sigma(\varepsilon_{\mathrm{tot}}^{(z,i)})}{\nu_{\mathrm{L}}}\right)^2 \tag{3.23}$$

where on top of the noise of the two lasers at play we also have the noise added by $\varepsilon_{\mathrm{tot}}^{(z,i)} = \varepsilon^{(z,i)}(\nu_{\mathrm{L}}) - \frac{N_{\mathrm{L}}^{(z,i)}}{N_{\mathrm{IRef}}^{(z,0)}} \cdot \varepsilon^{(z,0)}(\nu_{\mathrm{IRef}})$.

Since we are considering ultrastable oscillators we must also take into account their respective frequency drifts to make sure they do not hinder the stability characterization. Furthermore, when using narrow band-pass filters to count the optical beatnotes as we do, we must make sure that the USL fractional drifts stay below $2 \cdot 10^{-15}$ per second to avoid significant frequency shifts (see subsection 2.2.3). Additionally, when measuring an atomic clock, due to the difference between its cycle time (typically 0.6 – 0.8 ms) and the gate time of the counter (usually set at 1 s), having non linear drifts can lead to an underestimation of the frequency averaged value given by the counter. Thereby, we differentiate and combine equations 3.21 and 3.22, to be able to see both laser's drifts:

$$\frac{df_{\mathrm{L}}^{(z,i)}}{dt} = \frac{d\nu_{\mathrm{L}}}{dt} + \frac{N_{\mathrm{L}}^{(z,i)}}{N_{\mathrm{IRef}}^{(z,0)}} \cdot \frac{d\nu_{\mathrm{IRef}}}{dt} \tag{3.24}$$

At SYRTE the USLs drifts are constantly removed either by comparison with the UMR (as we previously described for the ν_{IRef}) or by comparison with an atomic reference as it is done for ν_{HgL} or ν_{SrL}, for instance. So equation 3.24 provide us with the residual drift of one laser against the other.

For the general case where we want to compare, in terms of stability, two distant optical frequencies oscillators, ν_{L1} and ν_{L2}, via the comb, we form the beatnotes of equation 3.22. Once we combine them and normalize by ν_{L1}, having into account that $\nu_{\mathrm{L}} \approx N_{\mathrm{L}} \cdot f_{\mathrm{rep}}$, the final fractional variance yields:

$$\begin{aligned}\left(\frac{1}{\nu_{\mathrm{L1}}}\right)^2 \sigma^2 \left(f_{\mathrm{L1}}^{(z,i)} - \frac{N_{\mathrm{L1}}^{(z,i)}}{N_{\mathrm{L2}}^{(z,j)}} \cdot f_{\mathrm{L2}}^{(z,j)}\right) = &\left(\frac{\sigma(\nu_{\mathrm{L1}})}{\nu_{\mathrm{L1}}}\right)^2 + \left(\frac{\sigma(\varepsilon^{(z,i)}(\nu_{\mathrm{L1}}))}{\nu_{\mathrm{L1}}}\right)^2 \\ &+ \left(\frac{\sigma(\nu_{\mathrm{L2}})}{\nu_{\mathrm{L2}}}\right)^2 + \left(\frac{\sigma(\varepsilon^{(z,j)}(\nu_{\mathrm{L2}}))}{\nu_{\mathrm{L2}}}\right)^2\end{aligned} \tag{3.25}$$

being j a different comb output used for the second laser than the one used for the first laser (i).

In Fig. 3.7 the different stabilities of the main USLs at SYRTE are shown. The three IR cavities at 1542 nm (ITU channel 44) are compared directly without the need

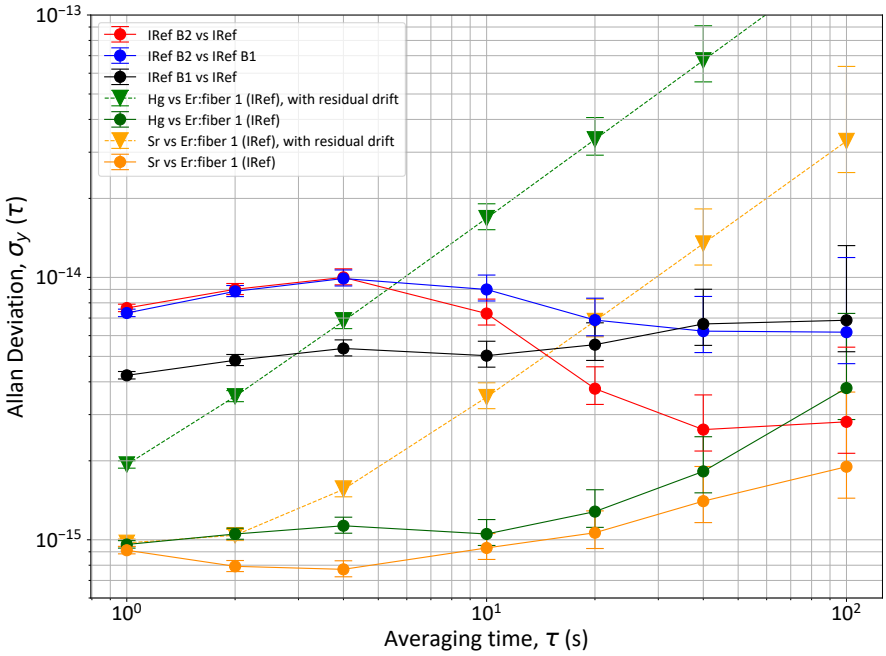

Figure 3.7: Optical ultrastable oscillators comparison (Pi mode). The three upper curves (red, blue and black) show the USLs at 1542 nm compared directly by pairs. In contrast, the two bottom curves, USLs IRef (1542 nm) and Hg (1062.5 nm), and IRef and Sr (698 nm) are compared via the OFC (green and orange curves). All data sets corresponding to circular markers curves have been dedrifted (order 1) by post-processing. No post-process drift removal was applied on the curves with triangular markers, where a real-time dedrift was performed in IRef laser with a proportional correction (green and orange).

of the comb. We can see that the fractional frequencies' stabilities at 1 s of ν_{IRefB1} and ν_{IRefB2} are $4 \cdot 10^{-15}$ (black curve) and $7 - 8 \cdot 10^{-15}$ (red and blue curves), respectively. When we compare the Hg or Sr clock lasers, ν_{HgL} and ν_{SrL}, against the comb via equation 3.23, i.e. ν_{IRef}, both are limited by their respective $\varepsilon^{(z,i)}(\nu_{\mathrm{L}})$ since $\sigma(\nu_{\mathrm{IRef}}) \approx 6 \cdot 10^{-16}$ at 1 s. This is shown in Fig. 3.8 where we measured simultaneously ν_{HgL} and ν_{SrL} (red and blue curves) in the Er:fiber 1 comb. After applying equation 3.25 to remove ν_{IRef} (green curve), the short-term stability did not change, meaning that is limited by $\sqrt{\sigma_y^2(\varepsilon^{(z,1)}(\nu_{\mathrm{HgL}})) + \sigma_y^2(\varepsilon^{(z,2)}(\nu_{\mathrm{SrL}}))}$. Additionally, the same comparison was performed in the Ti:sa comb (purple curve) where only a measurement of the Sr laser is required since this comb is locked to ν_{HgL}. In this case the limit is imposed by $\sigma_y^2(\varepsilon(\nu_{\mathrm{HgL}}))$ that accounts only for the noise comb and residual compensated paths in the lock since there are not any optical amplifiers involved.

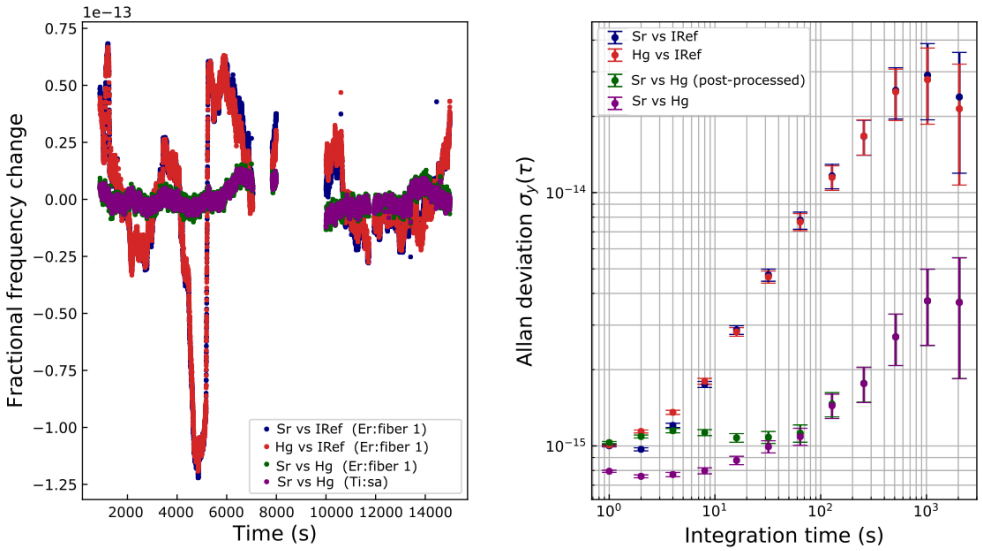

Figure 3.8: Hg and Sr USLs comparison (Pi mode) in Er:fiber 1 and Ti:sa combs. Red and blue curves show the stability of each laser against the fiber comb locked to IRef where the outputs of EDFAs 1 and 2 where used, respectively. Green curve shows its post-processed comparison when removing IRef. Purple curve accounts for a direct comparison between the lasers in Ti:sa comb (no different comb outputs involved).

3.2 Comparison setups

One of the first issues that one needs to tackle when doing an optical measurement, i.e. a comparison, is to be sure that the tool used, the OFC, not only provides the right quantity but also a sufficient resolution for the experiment. In order to check the accuracy of our system we need to measure the same frequency synchronously with another independent measurement system and verify that the result does not depend on the device used.

In the following we will focus on the frequencies of the clock lasers used to interrogate the atoms of the Sr and Hg OLCs, and the IRef laser feeding the optical fiber link. For our purpose it is sufficient to compare oscillators since it is only the parts that are not common (links, combs and counters essentially) that we want to assess. In this context, connecting oscillators to clocks is not necessary since they would correct oscillators from the same (fractional) quantity referred to as "frequency bridges" in this manuscript. Hence, to measure absolute frequencies ($\nu_{\mathrm{at,Cs}}$) and ratios ($\nu_{\mathrm{at1}}/\nu_{\mathrm{at2}}$), since the correction brought by the atoms is in common mode, it is sufficient to measure the ratio between the oscillators ($\nu_{\mathrm{L,M}}$) and ($\nu_{\mathrm{L1}}/\nu_{\mathrm{L2}}$). Note that several steps can lead to instabilities or inaccuracies and special attention must be taken when referencing and

synchronizing all the devices involved, compensating non-common optical paths, and with the offsets added by AOMs or possible delays introduced by the filters.

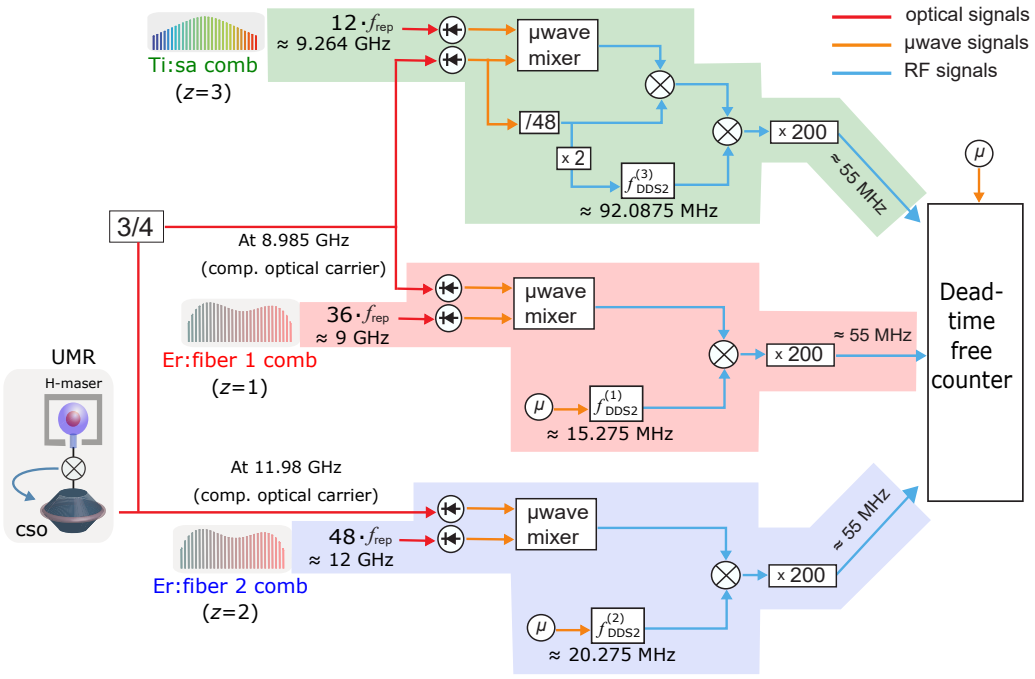

Figure 3.9: Simplified scheme of the three independent RF chains adapted to their respective combs for the measurement capacity evaluation of the SYRTE operational frequency chain.

For this purpose, we have built the three almost completely independent frequency chains depicted in Fig. 3.9, which are attached to three different OFCs: two of them of similar technology (Erbium fiber doped laser), complemented by a Titanium:sapphire comb, as described in more details in section 2.1. To assess the accuracy and stability of the metrological chain we will compare the systems by pairs in both the microwave and the optical domain. The first comparison will be between the two fiber based combs, Er:fiber 1 ($z = 1$) and Er:fiber 2 ($z = 2$), both locked to the same USL, in multi- and single-branch configurations, to check the consistency of the results. The second comparison will be between the Er:fiber 1 and the Ti:sa ($z = 3$) combs, locked to different USLs and in a multi-branch scheme, according to Fig. 3.10.

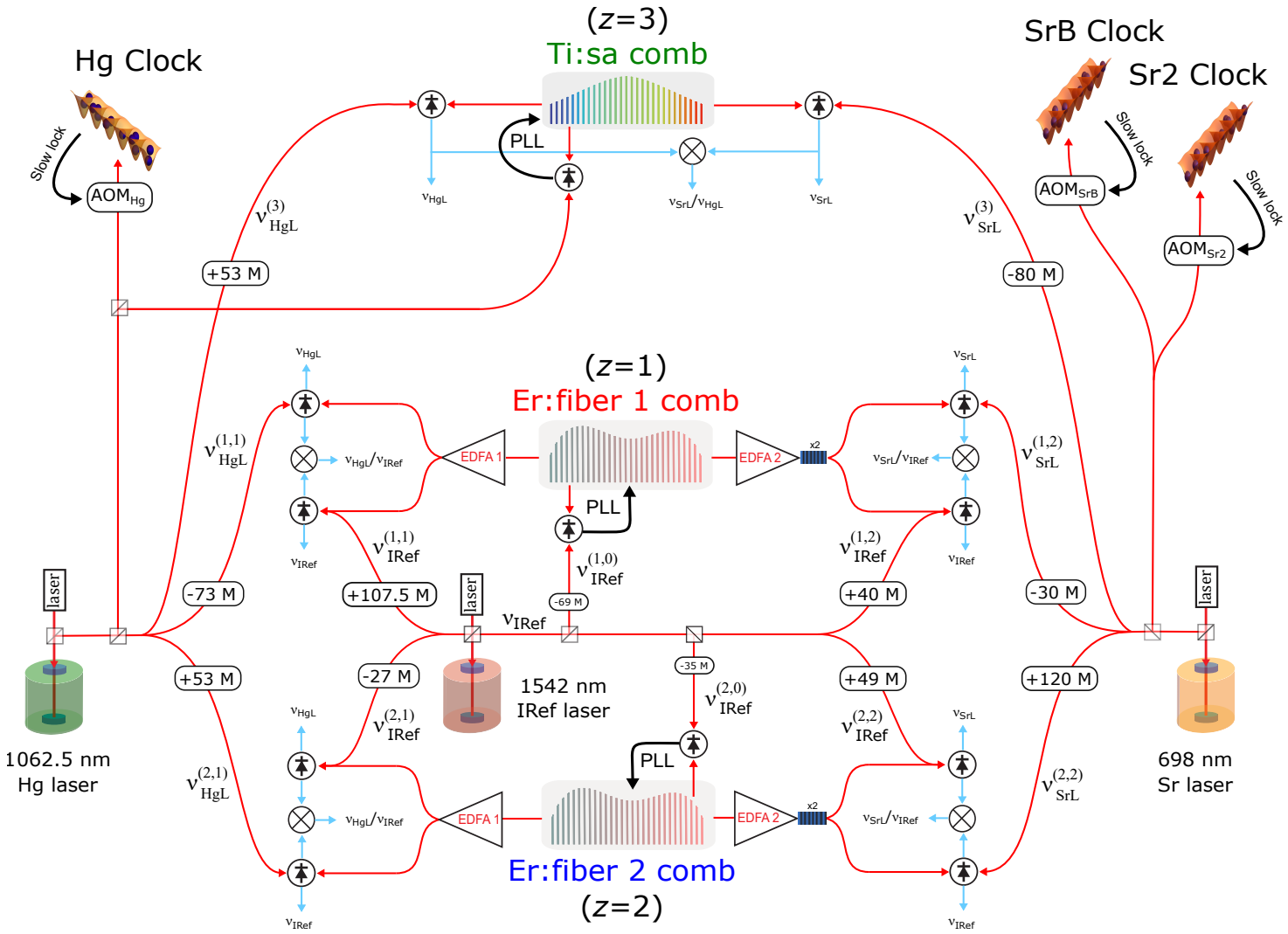

Figure 3.10: Optical to optical frequency chain evaluation. The three OFCs are currently set in a free-space and single-branch configuration (the Ti:sa one is single-branch by nature). Note that at the time of the Er:fiber 1 vs Ti:sa comparison the uncompensated paths for the Er:fiber 1 were in fiber and the Er:fiber 1 was in a multi-branch configuration. Frequency shifts, in MHz units, are applied by AOMs to allow propagation noise compensation of the USLs used, and are summarized in table 3.2.

	Type of comb (z)		
	Er:fiber 1 ($z=1$)	**Er:fiber 2** ($z=2$)	**Ti:sa** ($z=3$)
$f_{\text{rep,fixed}}$	$=250$	$=250$	$=772$
n	36	48	12
f_{UMR}	$3/4\cdot f_{\text{UMR}}$	f_{UMR}	$3/4\,[f_{\text{UMR}}\,(1+1/48)]$
f_{offset}	15	20	91.812 5
Ch1	≈ 55		
f_{DDS1}	110		18.75
f_{DDS2}	≈ 15.275	≈ 20.275	$\approx 92.087\,5$

Table 3.1: Corresponding values for repetition rates (f_{rep}) and their harmonics (n), offset frequencies (f_{offset}) and DDS frequencies (f_{DDS}) used for the OFCs accuracy and noise assessment. All units in MHz, except for n that are integer numbers. Reference value for the UMR frequency is $f_{\text{UMR}} = 11.98\,\text{MHz}$. Note that $f^{(z)}_{\text{DDS2}} = f^{(z)}_{\text{offset}} + 275\,\text{kHz}$ within $\pm 1\,\text{Hz}$ margin, with $f^{(z)}_{\text{offset}} = n^{(z)}\cdot f^{(z)}_{\text{rep,fixed}} - f^{(z)}_{\text{UMR}}$.

	Type of comb (z)					
	Er:fiber 1 ($z=1$)		**Er:fiber 2** ($z=2$)		**Ti:sa** ($z=3$)	
USL	N num., sign	$f_{\text{s,L}}$	N num., sign	$f_{\text{s,L}}$	N num., sign	$f_{\text{s,L}}$
$\nu_{\text{IRef}}(i=0)$	777 598, +1	-69	777 286, +1	-35		
$\nu_{\text{IRef}}(i=1)$	777 602, +1	+107.5	777 289, +1	-27		
$\nu_{\text{IRef}}(i=2)$	777 602, -1	+40	777 290, -1	+49		
$\nu_{\text{HgL}}(i=1)$	1 128 576, +1	-73	1 128 124, +1	+53	365 471, -1	+52
$\nu_{\text{SrL}}(i=2)$	1 716 916, +1	-30	1 716 228, +1	+120	555 995, -1	-80

Table 3.2: Comb mode N numbers with their signs and frequency shifts f_{s}, in MHz units, present in the optical setups used for the OFCs accuracy and noise assessment. Frequency shifts are applied on the reference oscillator, this is, $\nu_{\text{L}} + f^{(z,i)}_{\text{L}} = \nu^{(z,i)}_{\text{L}}$ where L = IRef, HgL or SrL, and $i = 0,\ 1$ or 2 applies only for the fiber comb outputs, e.g. $\nu_{\text{IRef}} + f^{(1,0)}_{\text{IRef}} = \nu_{\text{IRef}} - 69\,\text{MHz} = \nu^{(1,0)}_{\text{IRef}}$.

3.2.1 Optical to microwave comparisons

Equations

The operational frequency chain is based on the measurement Er:fiber 1 comb whose 36$^{\text{th}}$ harmonic of f_{rep} is compared to the UMR at 8.985 GHz coming on a compensated fiber link. A very similar configuration is implemented for the backup measurement combs as we shown in Fig. 3.9. The Ti:sa comb shares the same f_{UMR} signal (as it is placed in the same laboratory) and since its repetition rate is approximately three times higher than the Er:fiber 1 we compare its 12$^{\text{th}}$ harmonic instead. For the Er:fiber 2 comb (in a different laboratory) we compare its 48$^{\text{th}}$ harmonic of f_{rep} because the UMR comes on a different compensated fiber link at 11.98 GHz. In order to carry out the comparison in the microwave domain we need to measure f_{rep}, f_{L} and N_{L} of the two OFCs to have all the information.

The repetition rate is measured through equation 2.8, adopted here for any of the combs (z):

$$\text{Ch1}^{(z)} = -200\left[n^{(z)}\cdot f_{\text{rep}}^{(z)} - f_{\text{UMR}}^{(z)} - f_{\text{DDS2}}^{(z)}\right] \tag{3.26}$$

where the corresponding values are displayed in table 3.1. This is equivalent to a comparison of $f_{\text{rep}}^{(z)}$ with the UMR, thereby the combined fractional stability of the two oscillators involved is:

$$\frac{\sigma\left(\text{Ch1}^{(z)}\right)}{200\cdot f_{\text{UMR}}^{(z)}} = \sqrt{\left(\frac{\sigma\left(f_{\text{rep}}^{(z)}\right)}{f_{\text{rep}}^{(z)}}\right)^2 + \left(\frac{\sigma\left(f_{\text{UMR}}^{(z)}\right)}{f_{\text{UMR}}^{(z)}}\right)^2} \tag{3.27}$$

given that the instability of $f_{\text{DDS2}}^{(z)}$ is negligible. Note that the fractional stability of $f_{\text{rep}}^{(z)}$ is not necessarily the same as the USL where the OFC is locked to (ν_{IRef} for $z = 1,2$ or ν_{HgL} for $z = 3$), since the photodetection of the f_{rep} harmonics and the microwave chain to recombine the signal to $f_{\text{UMR}}^{(z)}$ is also adding noise, and therefore degrading the stability.

The beatnote $f_{\text{L}}^{(z,i)}$ between the laser ν_{L} and the OFC is measured by another channel of the counter after demodulation by another DDS and shaping by a 10 kHz filter. The optical frequency in terms of the UMR is given by equation 3.22. The measurement of the laser frequency where the comb is locked to, it is simply a particular case where $f_{\text{L}}^{(z,i)}$ does not need to be measured but it is assumed to be equal to $8\cdot f_{\text{DDS1}}^{(1,2)}$ or $16\cdot f_{\text{DDS1}}^{(3)}$.

As we know, both the EDFA noise (if any is present) and the residual uncompensated fiber noise are negligible with respect to the noise of the UMR, so the term $\varepsilon^{(z,i)}(\nu_{\text{L}})$ is not taken into account in this presentation of the quantity to measure. Thus, the combined fractional stability of $f_{\text{L}}^{(z,i)}$ is given by:

$$\frac{\sigma\left(f_{\mathrm{L}}^{(z,i)}\right)}{\nu_{\mathrm{L}}} = \sqrt{\left(\frac{\sigma\left(f_{\mathrm{rep}}^{(z)}\right)}{f_{\mathrm{rep}}^{(z)}}\right)^2 + \left(\frac{\sigma\left(\nu_{\mathrm{L}}\right)}{\nu_{\mathrm{L}}}\right)^2} \tag{3.28}$$

It is important to be aware of computer representation of floating point numbers [111] when processing high frequencies, so as not to be limited by the precision of bits. The higher is the floating point value the lower is the floating point precision. For example, double precision which has 53 bits (about 16 decimal digits) is not enough when targeting fractional values in the order of 10^{-16} or lower. Therefore, we express all optical quantities down to the GHz level (as they do not change above that) and we remove the first 6 significant digits. In practice, this operation is applied to the $f_{\mathrm{rep}}^{(z)}$ measured value and we report instead $\delta f_{\mathrm{rep}}^{(z)} = f_{\mathrm{rep}}^{(z)} - f_{\mathrm{rep,fixed}}^{(z)}$, which is kept below the kHz level (once the 6-digit offset is removed). Combining equations 3.26 and 3.22, the real quantity measured is given by:

$$\begin{aligned} \nu_{\mathrm{L}} + f_{\mathrm{s,L}}^{(z,i)} &= N_{\mathrm{L}}^{(z,i)} \left(f_{\mathrm{rep,fixed}}^{(z)} + \delta f_{\mathrm{rep}}^{(z)} \right) + \mathrm{sign}_{\mathrm{L}}^{(z,i)} \cdot f_{\mathrm{L}}^{(z,i)} \\ &= N_{\mathrm{L}}^{(z,i)} \left(f_{\mathrm{rep,fixed}}^{(z)} + \frac{f_{\mathrm{DDS2}}^{(z)} - \frac{\mathrm{Ch1}^{(z)}}{200} - f_{\mathrm{offset}}^{(z)}}{n^{(z)}} \right) + \mathrm{sign}_{\mathrm{L}}^{(z,i)} \cdot f_{\mathrm{L}}^{(z,i)} \end{aligned} \tag{3.29}$$

being $f_{\mathrm{offset}}^{(z)} = n^{(z)} \cdot f_{\mathrm{rep,fixed}}^{(z)} - f_{\mathrm{UMR}}^{(z)}$, see values displayed in table 3.1.

The goal of the comparison discussed here is to measure $\Delta\nu_{\mathrm{L}}$ for the various pairs of combs. Notice that if the combs involved in the comparison were not only locked to the same cavity but also performing the same $f_{\mathrm{rep}}^{(z)}$, it would additionally allow a direct comparison of the quantities $f_{\mathrm{rep}}^{(z)}$ and $f_{\mathrm{L}}^{(z,i)}$ (after correction of the well control frequency shifts due to fiber propagation and offset locks).

Results and interpretation

We have measured three different frequencies: ν_{HgL} and ν_{SrL} with the three combs, and ν_{IRef} from the three different outputs of the two fiber combs. In table 3.3 we show the different comb agreements expressed as the averaged frequency differences, and their statistical resolutions for given measurement times.

In Fig. 3.11 the corresponding fractional stabilities in terms of the Allan deviation are plotted. All the curves average down with τ^{-1} and are therefore dominated by white phase noise since we performed the same measurements with the counter set in Lambda mode, computing the Modified Allan deviation, to be able to differentiate it from flicker phase noise. The fiber comb based comparisons were integrated for at least double than the ones involving the Ti:sa comb measurements but these lasts show a better short-term stability what led us to a similar agreement, between $1-5\cdot10^{-17}$, in both pairs of

combs. We must therefore focus our analysis on the short-term stabilities that is in fact setting the limit of our optical to microwave comparison.

The fractional stability between the Ti:sa and the Er:fiber 1 combs ($\Delta\nu_{\mathrm{HgL}}^{(1-3)}$ and $\Delta\nu_{\mathrm{SrL}}^{(1-3)}$) is limited at $5\cdot10^{-15}$ at 1 s, being lower than the other stability curves between the two fiber combs. This is because of the photodetection noise in the HLPDs used to detect the high f_{rep} harmonics and its posterior amplification, since both measurements are above the UMR noise ($1-2\cdot10^{-15}$ at 1 s) and the f_{rep} noises transferred from the IRef ($8\cdot10^{-16}$ at 1 s) and Hg ($4\cdot10^{-16}$ at 1 s) USLs in the optical domain, i.e. where no microwave photodetection is involved. The noise of the corresponding EDFA outputs (EDFAs 1 for $\Delta\nu_{\mathrm{HgL}}^{(1-3)}$ and EDFAs 2 for $\Delta\nu_{\mathrm{SrL}}^{(1-3)}$), shown in red and blue curves of Fig. 3.11, are well below the stabilities under study. We discard any residual noise from uncompensated fibers as even deliberately uncompensated ones never surpass the 10^{-15} level in a well-controlled environment (see appendix C) or any electronic noise or cycle slips from the PLLs of the combs which have an instability of $10^{-18}/\tau$ with τ the integration time.

On the contrary, the fiber comb comparison stabilities (circular markers) are degraded around a factor 4. This can be explained attributing the main contribution of the Ti:sa and Er:fiber 1 short-term stabilities (square markers) at $5\cdot10^{-15}$ to the photodetection in the HLPD and amplification of the microwave photonic signals (f_{rep} harmonics) in the Er:fiber 1 comb. This is inferred from the stabilities between the two fiber combs: if we assume the same contribution on the Er:fiber 2 comb we get a combined stability of $\sqrt{2}\cdot5\cdot10^{-15}\approx7\cdot10^{-15}$ as the stability's curves indicate. Additionally, there could also be a combined residual noise of the two different compensated fiber links used to bring the microwave signal via AM, in particular the one carrying the 11.98 GHz (as the link for the UMR at 8.985 GHz is below the signal itself, as shown in Fig. 3.2). In any case, the residual instabilities in both systems lie below the instabilities (of a few $10^{-14}/\sqrt{\tau}$) of the three AFs over all time scales.

In Fig. 3.12 we summarize the results displayed in table 3.3. All measurements are compatible with zero and their resolutions are smaller than the systematic uncertainties of the best Cs fountains, currently $1-2\cdot10^{-16}$ [19, 20]. Thereby, the OFCs themselves do not present any stability limitation and guarantee the reliability of SYRTE frequency chain for absolute optical frequency measurements.

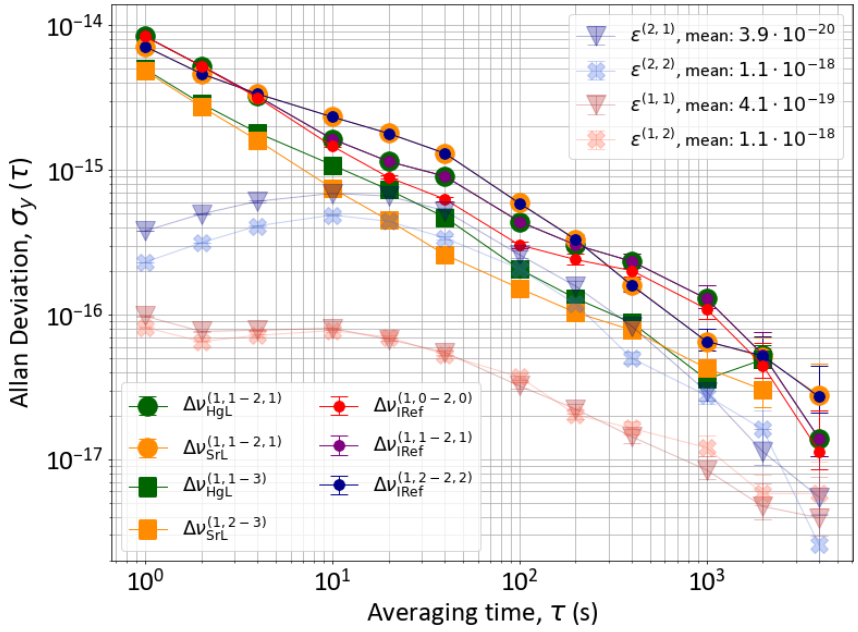

Figure 3.11: Optical to microwave stability comparison. Fractional stability in terms of the Allan deviation, ν_{HgL} and ν_{SrL} frequencies have been normalized by their respective Hg and Sr CIPM recommended frequency standard values [106] and the ν_{IRef} by ITU channel 44 [112]. Dead-time-free frequency counter set in Pi mode.

Marker	Quantity	OFCs	Result
●	$\left(\nu_{HgL}^{(1,1)} - \nu_{HgL}^{(2,1)}\right) / \nu_{Hg}^{0}$	1–2	$7.4 \cdot 10^{-19} \pm 1.4 \cdot 10^{-17}$ (a)
●	$\left(\nu_{SrL}^{(1,2)} - \nu_{SrL}^{(2,2)}\right) / \nu_{Sr}^{0}$	1–2	$(1.8 \pm 2.8) 10^{-17}$ (b)
■	$\left(\nu_{HgL}^{(1,1)} - \nu_{HgL}^{(3)}\right) / \nu_{Hg}^{0}$	1–3	$8.2 \cdot 10^{-18} \pm 4.9 \cdot 10^{-17}$ (c)
■	$\left(\nu_{SrL}^{(1,2)} - \nu_{SrL}^{(3)}\right) / \nu_{Sr}^{0}$	1–3	$(1.1 \pm 3.0) 10^{-17}$ (d)
●	$\left(\nu_{IRef}^{(1,0)} - \nu_{IRef}^{(2,0)}\right) / \nu_{Ch4}^{ITU}$	1–2	$1.2 \cdot 10^{-18} \pm 1.1 \cdot 10^{-17}$ (a)
●	$\left(\nu_{IRef}^{(1,1)} - \nu_{IRef}^{(2,1)}\right) / \nu_{Ch4}^{ITU}$	1–2	$7.7 \cdot 10^{-19} \pm 1.4 \cdot 10^{-17}$ (a)
●	$\left(\nu_{IRef}^{(1,2)} - \nu_{IRef}^{(2,2)}\right) / \nu_{Ch4}^{ITU}$	1–2	$(1.3 \pm 2.7) 10^{-17}$ (b)

Table 3.3: Averaged frequency differences and measurement resolutions in relative units of the data sets from Fig. 3.11. (a), (b), (c) and (d) for measurement times of 23 925 s (6 h 38 m 45 s), 29 957 s (8 h 19 m 17 s), 11 517 s (3 h 11 m 57 s) and 11 487 s (3 h 11 m 27 s), respectively.

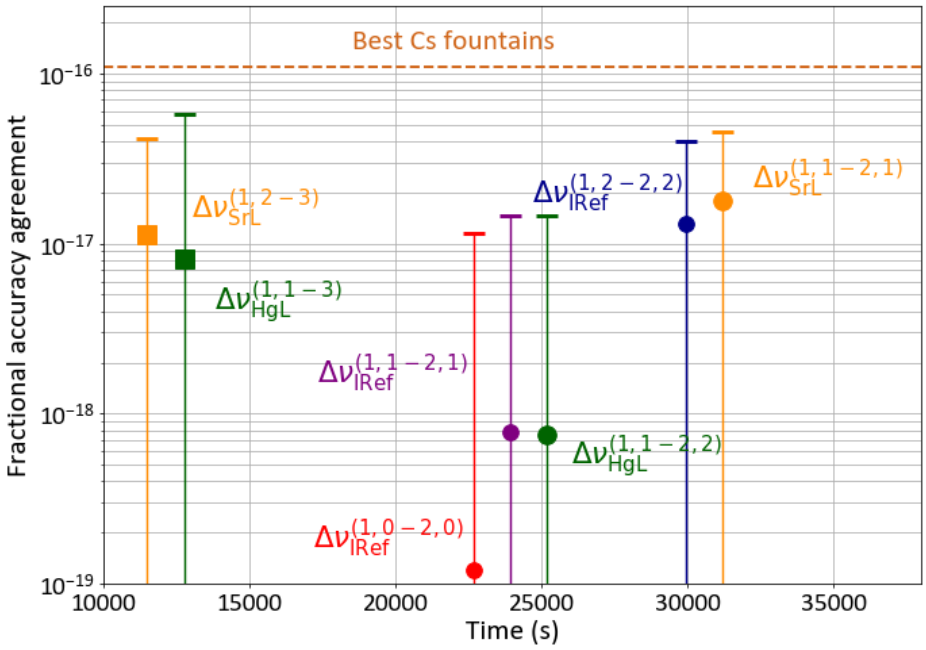

Figure 3.12: Overall comb's comparison agreements from the optical to the microwave domain. Circular markers refer to Er:fiber 1 vs Er:fiber 2 $(1-2)$ while square markers refer to Er:fiber 1 vs Ti:sa $(1-3)$. Error bars are based on the statistical resolution given by the Allan deviation. Horizontal time axis is approximated (see real integration times in table 3.3).

3.2.2 Optical to optical comparisons

Equations

To compare two optical frequencies the only quantities we need to determine with the combs are the two optical beatnotes f_L (since f_{rep} will be eliminated via de transfer oscillator method), although one might need a microwave measurement for each of the lasers to determine their N numbers. In our case, this is not a requirement because we already know their frequencies (and their N numbers) and the very low drift rate of the lasers makes negligible the N value change with respect to the previous estimation (see case 2 of appendix B).

We form the ratio between two optical frequencies from equation 3.22, after eliminating f_{rep} by post-processing, the ratio in any of the combs is given by:

$$\frac{\nu_{\mathrm{L1}}^{(z,i)}}{\nu_{\mathrm{L2}}^{(z,j)}} = \frac{1}{\nu_{\mathrm{L2}}^{(z,j)}}\left[\left(\mathrm{sign}_{\mathrm{L1}}^{(z,i)}\cdot f_{\mathrm{L1}}^{(z,i)} - f_{\mathrm{s,L1}}^{(z,i)} + \alpha^{(z,i,j)}\left(f_{\mathrm{s,L2}}^{(z,j)} - \mathrm{sign}_{\mathrm{L2}}^{(z,j)}\cdot f_{\mathrm{L2}}^{(z,j)}\right)\right)\right]\left(\right. + \underbrace{\frac{1}{\nu_{\mathrm{L2}}^{(z,j)}}\left(\alpha^{(z,i,j)}\cdot\varepsilon^{(z,j)}(\nu_{\mathrm{L2}}) - \varepsilon^{(z,i)}(\nu_{\mathrm{L1}})\right) + \alpha^{(z,i,j)}}_{\beta^{(z,i,j)}(\nu_{\mathrm{L1}},\nu_{\mathrm{L2}})}\left(\right. \tag{3.30}$$

where $\alpha^{(z,i,j)} = \frac{N_{\mathrm{L1}}^{(z,i)}}{N_{\mathrm{L2}}^{(z,j)}}$ and L = SrL, HgL or IRef, except for $z = 3$ that L = SrL or HgL since the IRef frequency is not covered by the Ti:sa spectral range. The corresponding fractional variance of the ratio yields:

$$\frac{\sigma^2\left(\nu_{\mathrm{L1}}^{(z,i)}/\nu_{\mathrm{L2}}^{(z,i)}\right)}{\left(\nu_{\mathrm{L1}}/\nu_{\mathrm{L2}}\right)^2}\left(\approx \left(\frac{\sigma(f_{\mathrm{L1}}^{(z,i)})}{\nu_{\mathrm{L1}}}\right)^2 + \left(\frac{\sigma(f_{\mathrm{L2}}^{(z,j)})}{\nu_{\mathrm{L2}}}\right)^2 + \left(\frac{\nu_{\mathrm{L2}}}{\nu_{\mathrm{L1}}}\right)^2\sigma^2\left(\beta^{(z,i,j)}(\nu_{\mathrm{L1}},\nu_{\mathrm{L2}})\right)\right. \tag{3.31}$$

where the intrinsic noise of the optical beatnotes is dominated by the optical noise accompanying these beatnotes (uncompensated fibers and possible EDFA noise).

The IRef laser can be beaten against three different outputs ($i = 0$, 1 or 2) in the fiber combs ($z = 1, 2$) while the Hg and Sr lasers are always beaten in outputs $i = 1$ and $i = 2$, respectively, and in the same unique output of the Ti:sa comb ($z = 3$). Thus, we can compare the same optical ratios under a multi-branch ($i \neq j$) or a single-branch ($i = j$) configuration, what has a significant impact on the short term instability of $\left(\frac{\nu_{\mathrm{L1}}^{(z,i)}}{\nu_{\mathrm{L2}}^{(z,j)}} - \frac{\nu_{\mathrm{L1}}^{(z,k)}}{\nu_{\mathrm{L2}}^{(z,l)}}\right)\Big/\frac{\nu_{\mathrm{L1}}}{\nu_{\mathrm{L2}}}$. Therefore, the last term of equation 3.31 will be for the different comparisons performed:

- If $i \neq j$ for $z = 1$, and $k \neq l$ for $z = 2$:
  $\left(\frac{\nu_{\mathrm{L2}}}{\nu_{\mathrm{L1}}}\right)\sigma\left(\beta^{(z,i,j,k,l)}(\nu_{\mathrm{L1}},\nu_{\mathrm{L2}})\right) = \varepsilon_y^{(1,j)}(\nu_{\mathrm{L2}}) - \varepsilon_y^{(1,i)}(\nu_{\mathrm{L1}}) - \varepsilon_y^{(2,l)}(\nu_{\mathrm{L2}}) + \varepsilon_y^{(2,k)}(\nu_{\mathrm{L1}})$.
  In order to check if the output comb noise scales or not with the frequency, we have compared two different ratios, while keeping the same outputs and fixing one of the frequencies involved, this is, $\left(\frac{\nu_{\mathrm{L1}}^{(z,i)}}{\nu_{\mathrm{L2}}^{(z,j)}} - \frac{\nu_{\mathrm{L1}}^{(z,i)}}{\nu_{\mathrm{L2}}^{(z,j)}}\right)\Big/\frac{\nu_{\mathrm{L1}}}{\nu_{\mathrm{L2}}}$ and $\left(\frac{\nu_{\mathrm{L3}}^{(z,i)}}{\nu_{\mathrm{L2}}^{(z,j)}} - \frac{\nu_{\mathrm{L3}}^{(z,i)}}{\nu_{\mathrm{L2}}^{(z,j)}}\right)\Big/\frac{\nu_{\mathrm{L3}}}{\nu_{\mathrm{L2}}}$.
  In Fig. 3.13 the resulting stability of this comparison is shown for L1 = ν_{IRef} with $i = 2$ and L2 = ν_{IRef} with $i = 0$ (orange curve) and L3 = ν_{SrL} with $i = 2$ and L2 = ν_{IRef} with $i = 0$ (blue curve). Since the fractional instabilities are the same at first order we can make the approximation $\varepsilon_y^{(1,2)}(\nu_{\mathrm{IRef}}) - \varepsilon_y^{(2,2)}(\nu_{\mathrm{IRef}}) \approx \varepsilon_y^{(1,2)}(\nu_{\mathrm{SrL}}) - \varepsilon_y^{(2,2)}(\nu_{\mathrm{SrL}})$, and therefore $\varepsilon_y^{(z,i)}(\nu_{\mathrm{IRef}}) \approx \varepsilon_y^{(z,i)}(\nu_{\mathrm{SrL}})$.

- If $i \neq j$ for $z = 1$, and $z = 3$:
  $\left(\frac{\nu_{L2}}{\nu_{L1}}\right)\sigma\left(\beta^{(z,i,j)}(\nu_{L1},\nu_{L2})\right) = \varepsilon_y^{(1,j)}(\nu_{L2}) - \varepsilon_y^{(1,i)}(\nu_{L1})$, since $\varepsilon_y^{(3)}(\nu_{L2}) \approx \varepsilon_y^{(3)}(\nu_{L1})$.
- If $i = j$ for $z = 1$, and $k = l$ for $z = 2$:
  $\left(\frac{\nu_{L2}}{\nu_{L1}}\right)\sigma\left(\beta^{(z,i,j,k,l)}(\nu_{L1},\nu_{L2})\right) = 0$, as the terms $\varepsilon_y^{(1,i)}(\nu_{L2})$ and $\varepsilon_y^{(1,i)}(\nu_{L1})$ cancel each other in the first comb, and $\varepsilon_y^{(2,k)}(\nu_{L2})$ and $\varepsilon_y^{(2,k)}(\nu_{L1})$ also cancel out in the second comb.

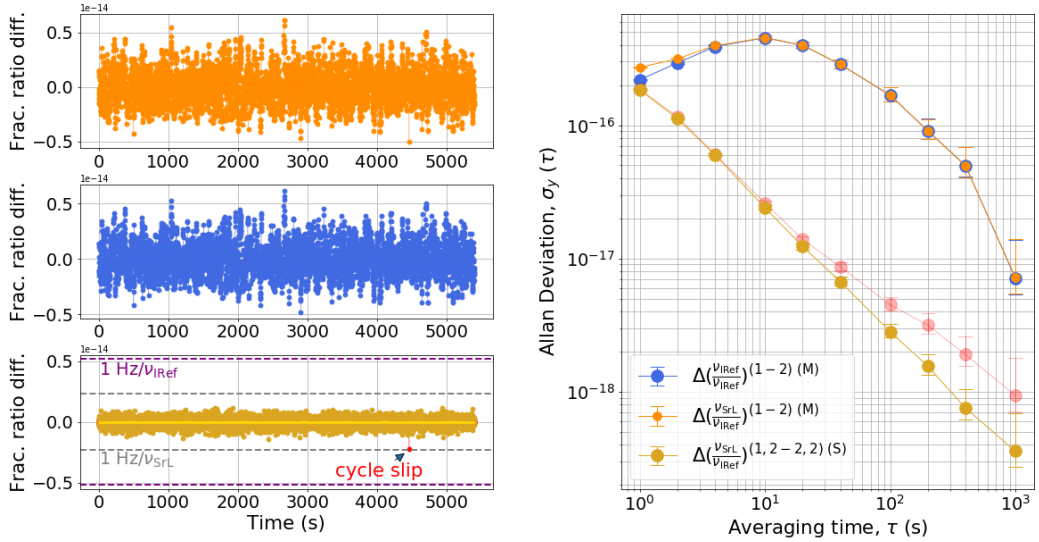

Figure 3.13: Multi-branch optical comparison (M: $i \neq j$) between the two fiber combs for $\nu_{SrL}^{(z,i)}/\nu_{IRef}^{(z,j)}$ (orange) and $\nu_{IRef}^{(z,i)}/\nu_{IRef}^{(z,j)}$ (blue). Bottom plot shows a direct detection of cycle slips on a single-branch optical comparison (S: $i = j$) for $\nu_{SrL}^{(z,i)}/\nu_{IRef}^{(z,j)}$ and its impact on the fractional stability (red curve).

The objective of this comparison is to evaluate the comb agreements for the different normalized optical ratios $\Delta\left(\nu_{L1}^{(z,i)}/\nu_{L2}^{(z,j)}\right)$ measured by each pair of combs for the three possible configurations: the two combs in multi-branch, in single-branch and only one of the combs in multi-branch.

Results and interpretation

In the optical domain we have compared three different optical ratios: $\frac{\nu_{SrL}}{\nu_{HgL}}$ between the Er:fiber 1 and the Ti:sa comb, and $\frac{\nu_{HgL}}{\nu_{IRef}}$ and $\frac{\nu_{SrL}}{\nu_{IRef}}$ with the fiber combs, both in multi and single-branch. The comb's agreements and statistical resolutions for the times of

measurement are presented in table 3.4, and the different comparison's stabilities are displayed in Fig. 3.14. Notice that in this all-optical comparison cycle slips can be directly detected as the short term instability of the residual differences between each pair of combs are below 1 Hz respect to the optical frequencies involved, e.g. $2.3 \cdot 10^{-15}$ for $\nu_{\mathrm{SrL}} = 429.2\,\mathrm{THz}$, shot to shot at 1 s. The former was used to filter the data when needed, we found only one jump in the measurements involving the Sr laser, as shown in Fig. 3.13.

When the frequency measurements $\Delta(\frac{\nu_{\mathrm{HgL}}}{\nu_{\mathrm{IRef}}})^{(1-2)}$ and $\Delta(\frac{\nu_{\mathrm{SrL}}}{\nu_{\mathrm{IRef}}})^{(1-2)}$ were performed in multi-branch the stability is limited by the combined noises of the two comb outputs involved $\varepsilon^{(z,i,j)}(\nu_{\mathrm{L}})$ (last two terms of equation 3.31, with $i = 1$ ($i = 2$) for $\mathrm{L} = \mathrm{HgL}$ ($\mathrm{L} = \mathrm{SrL}$). As we can see in Fig. 3.14, the curves (dark green and orange) follow respectively EDFA 1 and EDFA 2 outputs from Er:fiber 2 comb, both predominating over the ones from the Er:fiber 1 comb. These measurements show the overall noise added in the optical domain which confirm that the noise scales linearly with the N comb number, i.e. with the frequency, whose main contribution $\varepsilon^{(z,0)}(\nu_{\mathrm{IRef}})$ comes from the repetition rate (see equation 2.27).

In contrast, when the same ratios were formed in single-branch, the use of a unique comb output suppresses the effect of optically induced noise (residual uncompensated propagation noise, PLL noise and optical amplifiers noise) and the lasers are no longer limited by the comb outputs themselves, and the ratio difference averages down from the beginning. The measurements are dominated by white phase noise as we checked by repeating them in Lambda mode and computing the MDEV (note that in Fig. 3.14 the stabilities are in terms of ADEV as the counter was in Pi mode and white phase noise could not be distinguished from the flicker phase noise, both following a τ^{-1} slope). The fiber-comb based comparison surpass the 10^{-18} level after $90-400\,\mathrm{s}$ of averaging time, what reinforces the degree of confidence and reliability we have achieved with our two operational measurement OFCs when performing optical clocks comparisons. On the contrary, the ratio $\Delta(\frac{\nu_{\mathrm{SrL}}}{\nu_{\mathrm{HgL}}})^{(1-3)}$, shows an instability plateau at $7-9 \cdot 10^{-16}$ to about 10 s, after which averages down with τ^{-1} at longer time scales. This limit is imposed by the differential fiber-related noise of the two EDFAs since the Er:fiber 1 comb was in a multi-branch configuration [113].

The residual fractional stabilities of the optical to optical comparisons achievable lies significantly below the optical clocks at SYRTE over all time scales when the measurements are done in single-branch and after 30 minutes for multi-branch approaches. There is no noticeable offset between the two pairs of combs at the measurement resolutions given, and therefore the combs do not hinder any optical clocks comparison either in terms of accuracy or stability.

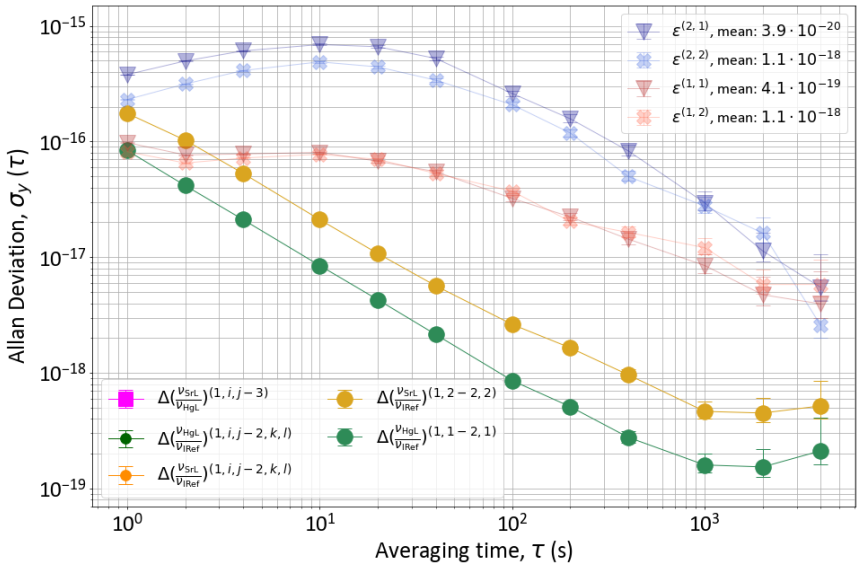

Figure 3.14: Optical to optical stability comparison. Fractional stability in terms of the Allan deviation. CIPM recommended frequency standard values for ν_{HgL} and ν_{SrL}, and ITU channel 44 for ν_{IRef} have been used to normalized where it corresponds. Dead-time-free frequency counter set in Pi mode.

Marker	Quantity	OFCs	Conf.	Result
■	$\left(\frac{\nu_{\mathrm{SrL}}^{(1,2)}}{\nu_{\mathrm{HgL}}^{(1,1)}} - \frac{\nu_{\mathrm{SrL}}^{(3)}}{\nu_{\mathrm{HgL}}^{(3)}}\right) \Big/ \frac{\nu_{\mathrm{Sr}}^{0}}{\nu_{\mathrm{Hg}}^{0}}$	1–3	M	$(1.2 \pm 2.0)10^{-17}$ (a)
●	$\left(\frac{\nu_{\mathrm{HgL}}^{(k,1)}}{\nu_{\mathrm{IRef}}^{(1,0)}} - \frac{\nu_{\mathrm{HgL}}^{(2,1)}}{\nu_{\mathrm{IRef}}^{(2,0)}}\right) \Big/ \frac{\nu_{\mathrm{Hg}}^{0}}{\nu_{\mathrm{Ch44}}^{\mathrm{ITU}}}$	1–2	M	$4.5 \cdot 10^{-19} \pm 3.6 \cdot 10^{-18}$ (b)
●	$\left(\frac{\nu_{\mathrm{SrL}}^{(1,2)}}{\nu_{\mathrm{IRef}}^{(1,0)}} - \frac{\nu_{\mathrm{HgL}}^{(2,2)}}{\nu_{\mathrm{IRef}}^{(2,0)}}\right) \Big/ \frac{\nu_{\mathrm{Sr}}^{0}}{\nu_{\mathrm{Ch44}}^{\mathrm{ITU}}}$	1–2	M	$(2.5 \pm 6.7)10^{-18}$ (c)
●	$\left(\frac{\nu_{\mathrm{SrL}}^{(1,2)}}{\nu_{\mathrm{IRef}}^{(1,2)}} - \frac{\nu_{\mathrm{SrL}}^{(2,2)}}{\nu_{\mathrm{IRef}}^{(2,2)}}\right) \Big/ \frac{\nu_{\mathrm{Sr}}^{0}}{\nu_{\mathrm{Ch44}}^{\mathrm{ITU}}}$	1–2	S	$(1.1 \pm 5.2)10^{-19}$ (c)
●	$\left(\frac{\nu_{\mathrm{HgL}}^{(1,1)}}{\nu_{\mathrm{IRef}}^{(1,1)}} - \frac{\nu_{\mathrm{HgL}}^{(2,1)}}{\nu_{\mathrm{IRef}}^{(2,1)}}\right) \Big/ \frac{\nu_{\mathrm{Hg}}^{0}}{\nu_{\mathrm{Ch44}}^{\mathrm{ITU}}}$	1–2	S	$2.6 \cdot 10^{-22} \pm 2.1 \cdot 10^{-19}$ (b)

Table 3.4: Averaged frequency differences and measurement resolutions in relative units of the data sets of Fig. 3.14. (a), (b) and (c) for measurement times of 11 501 s (3 h 11 m 41 s), 23 925 s (6 h 38 m 45 s) and 29 957 s (8 h 19 m 17 s), respectively.

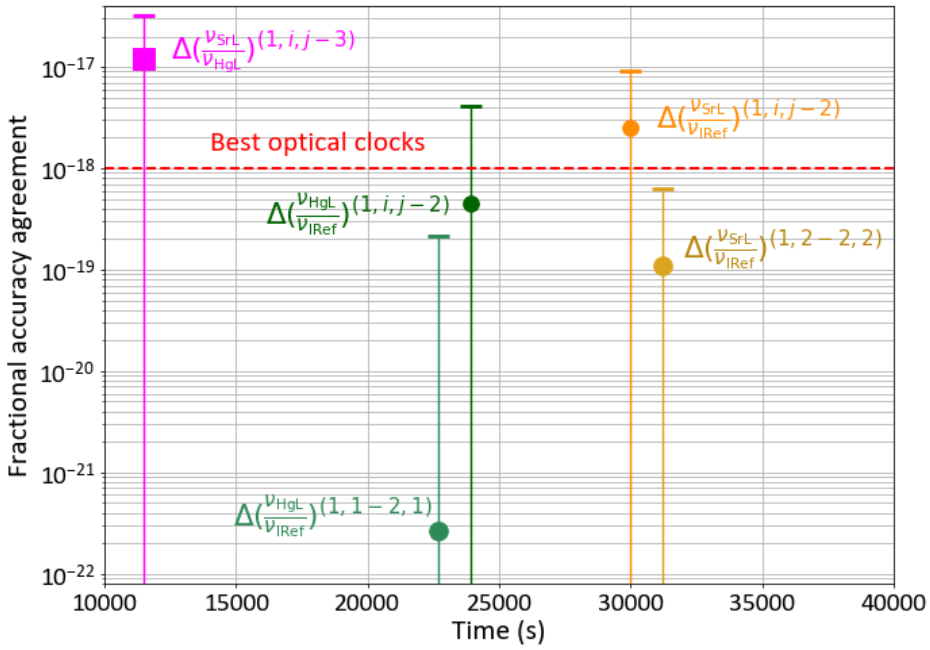

Figure 3.15: Overall comb's comparison agreements in the optical domain. Circular markers refer to Er:fiber 1 vs Er:fiber 2 $(1-2)$ while square markers refer to Er:fiber 1 vs Ti:sa $(1-3)$. Error bars are based on the statistical resolution given by the Allan deviation, if not shown they are smaller than the marker. Horizontal time axis is approximated (see real integration times in table 3.4).

3.3 Conclusion

The procedure followed to compare optical atomic clocks to other clocks, either in the microwave or in the optical domain via an OFC, can be simplified to compare their local oscillators, as the frequency corrections between the atomic samples and the clock lasers (applied a posteriori) are in common mode. In our case, at the time of expressing an absolute optical frequency the measurement is first expressed in maser Hertz units, by comparison with the UMR, and it is later transformed to SI Hertz by applying the correction between the H maser and the three atomic fountains available at SYRTE.

When local oscillators are compared directly, in terms of stability, in the microwave domain, we have verified that the detection and amplification of the photonic microwave signals generated by the combs, i.e. the repetition rate harmonics, result in instabilities larger than the UMR, which represents the ultimate stability limit of the frequency chain. The comparison of these two microwave signals sets a limit in the mid 10^{-15} range at 1 s, that is anyway negligible with respect to the stability of the atomic fountains (in the low 10^{-14} 1 s). From this comparison, we have taken advantage of the UMR constant

frequency value (with a predictable fractional frequency drift as low as 10^{-16} per day) to improve the dedrift of the IRef laser, as it is compared continuously to the UMR via de comb. The new approach of adding an integrator term in the loop features a slow proportional frequency lock of the laser to the maser, keeping the laser centered at 194.400 121 THz with shot to shot fluctuations of ± 3 Hz. As this IRef laser is seeding the French metrological fiber link REFIMEVE+, it simplifies the control and evaluation of the disseminated optical carrier for metrological comparisons and experiments.

In order to assess the stability and accuracy limits of the SYRTE operational optical frequency chain two additional chains have been built. These are based on two other independent OFCs (locked to independent USLs) of different technologies, with different mode-locking mechanisms and repetition rates. The two setups were implemented in parallel with the operational one, and we simultaneously measured three optical frequencies (ν_{IRef}, ν_{HgL} and ν_{SrL}). The comparison by pairs of these frequencies against the common UMR to derive their absolute values led us to a measurement resolution lower than 10^{-16} in less than one hour, standing behind the current state-of-the-art microwave clocks. Optical ratios with resolutions below the 10^{-18} level were achieved after $10-20$ minutes in the case of the fiber OFCs in single-branch configuration, being compatible with the best optical clocks' stabilities published to date. This comparison has allowed us to set permanently the second fiber comb and its chain as a back-up operational measurement system, which provides robustness to local and international clock comparisons campaigns.

Chapter 4

Spectral purity transfer

Ultrastable lasers together with optical frequency combs have contributed to the implementation of optical clocks permitting us the interrogation of optical weakly allowed transitions. These USLs are often built at wavelengths where components and spectrally pre-narrowed lasers are available, such as 1064 nm or the telecommunication C and L bands, in order to diminish the requirements on the servo loop system needed to reduce the linewidth. Additionally, the most common technique to achieve ultrastable frequencies is to lock a laser to an ultrastable cavity. Such cavities, when properly realized, mounted and hosted in a well controlled environment (isolated from vibrations, temperature stabilized, etc.) can reach a fundamental limit set by the thermal agitation of the atoms composing the cavity itself [45]. Operating ultrastable cavities at longer wavelength naturally leads to a larger size of the beams on the mirrors, which itself induces a better averaging of the thermal agitation of the atoms composing the mirror, reducing thereby the thermal-noise induced fundamental frequency fluctuations. Since optical clocks do not necessarily operate at wavelengths identical to that of the best realized or accessible ultrastable lasers, it is then necessary to transfer their spectral purity to target metrological wavelengths, such as 698 nm (^{87}Sr) and 1062.5 nm (^{199}Hg, after frequency quadrupling) in the case of LNE-SYRTE. Recently cutting-edge lasers based on ultrastable cavities (see subsection 1.2.1) have paved the way to clock stabilities in the $10^{-17}/\sqrt{\tau}$ level, stressing the need of transfer processes with noises below the USL noise itself, this is, at most in the 10^{-18} range.

The transfer of the spectral properties between two lasers is done via an OFC when their frequencies are distant enough so they can not be beaten and detected directly in a PD to subsequently phase lock one to the other. The OFC spectral bandwidth must cover the two lasers involved (either directly or after frequency conversion) and must be stabilized to a reference that can be a microwave oscillator such as a H maser or an optical one such as an USL. In the case where the OFC is tightly phase locked to an USL, whose properties are meant to be transmitted, phase locking the beatnote between the second laser and the comb itself would suffice to realize the transfer in the Fourier

frequencies range covered by the bandwidth of the feedback loop[1]. Even though the transfer would be limited by the optical noise introduced by the locking process of the comb, resulting in a f_{rep} slightly less stable than the master USL. In cases where this is not possible, e.g. the OFC is locked to a H maser, or where the OFC is simply locked to a more convenient but less stable optical reference, the transfer is performed via the transfer oscillator method [107].

In this chapter we present different transfer schemes and the results between various combinations of wavelengths transferred as well as all possible limitations regarding the final residual noise introduced by the process. We first implement a fibered multi-branch (different comb outputs) setup between the Hg and Sr clock lasers (ν_{HgL} and ν_{SrL}). Secondly, we perform two free-space single-branch (unique comb output) setups, to make transfers from the IRef laser (ν_{IRef}) to ν_{HgL} and ν_{SrL}. Lastly, we carry out a double single-branch approach between ν_{HgL} and ν_{SrL} for a direct local comparison between the two OLCs which has led to a significant stability improvement.

4.1 The transfer oscillator technique

The objective of this powerful method is to establish a direct phase relation between two lasers and to transfer the spectral purity of one to another via an intermediate oscillator, e.g. an OFC, whose parameters are eliminated. By the elimination of its two degrees of freedom, f_{rep} and f_0, the noise of the comb itself is eliminated, not having therefore any impact in the process. The most spectrally pure laser acts as the master laser (ν_M), and the "less good" laser, to which we want to transfer the ν_M spectral properties, is the slave laser (ν_S). Note that even if they have similar performances, phase linking them is very advantageous at the time of a clock comparison since the Dick effect (subsection 1.1.3) will be rejected when independent atomic clouds are probed synchronously by ν_M and ν_S respectively, as it will be shown at the end of this chapter.

4.1.1 Transfer and readout

The implementation of this technique is illustrated in Fig. 4.1. We initially form the beatnotes between ν_M and ν_S against the OFC ($z = 1$), respectively. Since we want to eliminate the comb parameters, after the beatnotes' detection (in the same or different PDs), we first proceed with f_0. To do this, the method we choose is to mix it out from the beatnotes using a double-balanced mixer. After applying equation 3.22, the two

[1]Note that, in practice, the finite SNR of the optical beatnote may imply a limited achievable locking bandwidth. Trying to lock a slave laser with a bandwidth larger than the maximum set by the SNR does not help and it can even be detrimental.

master and slave f_0-free beatnotes read as:

$$\begin{aligned} f_{\mathrm{M}}^{(1,i)} &= \mathrm{sign}_{\mathrm{M}}^{(1,i)} \left(\nu_{\mathrm{M}} - N_{\mathrm{M}}^{(1,i)} \cdot f_{\mathrm{rep}} + \varepsilon^{(1,i)}(\nu_{\mathrm{M}}) \right) \\ f_{\mathrm{S}}^{(1,j)} &= \mathrm{sign}_{\mathrm{S}}^{(1,j)} \left(\nu_{\mathrm{S}} - N_{\mathrm{S}}^{(1,j)} \cdot f_{\mathrm{rep}} + \varepsilon^{(1,j)}(\nu_{\mathrm{S}}) \right) \end{aligned} \tag{4.1}$$

where shifts $f_{\mathrm{s,L}}^{(z)}$, if any, have been omitted for the sake of simplification. Note that this step is no longer necessary if one uses one of the novel f_0-free OFCs that have appeared recently [114, 115]. Subsequently, to reject f_{rep} (and its corresponding instability) we rescale both beatnotes, dividing each of them by the division factors M_{M} and M_{S}, in such a way that when making the difference in a mixer:

$$\begin{aligned} f_{\mathrm{t}}^{(1)} &= \frac{\mathrm{sign}_{\mathrm{M}}^{(1,i)} \cdot f_{\mathrm{M}}^{(1,i)}}{M_{\mathrm{M}}^{(1,i)}} - \frac{\mathrm{sign}_{\mathrm{S}}^{(1,j)} \cdot f_{\mathrm{S}}^{(1,j)}}{M_{\mathrm{S}}^{(1,j)}} \\ &= \frac{\nu_{\mathrm{M}}}{M_{\mathrm{M}}^{(1,i)}} - \frac{\nu_{\mathrm{S}}}{M_{\mathrm{S}}^{(1,j)}} + \underbrace{\left(\frac{N_{\mathrm{S}}^{(1,j)}}{M_{\mathrm{S}}^{(1,j)}} - \frac{N_{\mathrm{M}}^{(1,i)}}{M_{\mathrm{M}}^{(1,i)}} \right)}_{\varepsilon_{\mathrm{rep}}^{(1,i,j)}} \left(f_{\mathrm{rep}} + \underbrace{\frac{\varepsilon^{(1,i)}(\nu_{\mathrm{M}})}{M_{\mathrm{M}}^{(1,i)}} - \frac{\varepsilon^{(1,j)}(\nu_{\mathrm{S}})}{M_{\mathrm{S}}^{(1,j)}}}_{\beta^{(1,i,j)}} \right) \end{aligned} \tag{4.2}$$

At the output of the mixer, the correct transfer beatnote frequency, f_{t}, is the one that is immune to a change of f_{rep} and, therefore, there is no need to know the respective beatnotes' signs in advance. It provides a direct relation between the two lasers in the same physical signal:

$$\Phi_{\mathrm{t}}^{(1)} = \frac{\Phi_{\mathrm{M}}}{M_{\mathrm{M}}^{(1,i)}} - \frac{\Phi_{\mathrm{S}}}{M_{\mathrm{S}}^{(1,j)}} + \varepsilon_{\mathrm{rep}}^{(1,i,j)} \cdot \Phi_{\mathrm{rep}} + \Phi_{\beta}^{(1,i,j)} \tag{4.3}$$

that for the sake of coherence with what was presented before, we will consider the relations on the derivatives, i.e. in terms of frequency.

The rescaling is typically performed with a DDS which acts as frequency divider, clocked by the signal to rescale, and whose output frequency is given by $f_{\mathrm{out}} = n\frac{f_{\mathrm{in}}}{2^k}$, where f_{in} is the frequency to be rescaled ($f_{\mathrm{M}}^{(1,i)}$ or $f_{\mathrm{S}}^{(1,j)}$), n is the tuning word, an integer within the range $[0, 2^{k-1}]$, and k the number of bits. The M factors are rational numbers given by $2^k/n$, it is therefore impossible to divide by less than 2 in the basic configuration (in fact, using aliasing, it is possible to have $f_{\mathrm{out}} > f_{\mathrm{in}}/2$, although a careful filtering is needed to extract the desired frequency). Note that equation 4.2 follows the general case where both beatnotes need to be rescaled such that $\frac{N_{\mathrm{S}}^{(1,j)}}{M_{\mathrm{S}}^{(1,j)}} = \frac{N_{\mathrm{M}}^{(1,i)}}{M_{\mathrm{M}}^{(1,i)}}$. However, for the particular case where the laser frequencies differ more than one octave, the corresponding comb modes $N_{\mathrm{M}}^{(1,i)}$ and $N_{\mathrm{S}}^{(1,j)}$ will differ by more than a factor 2,

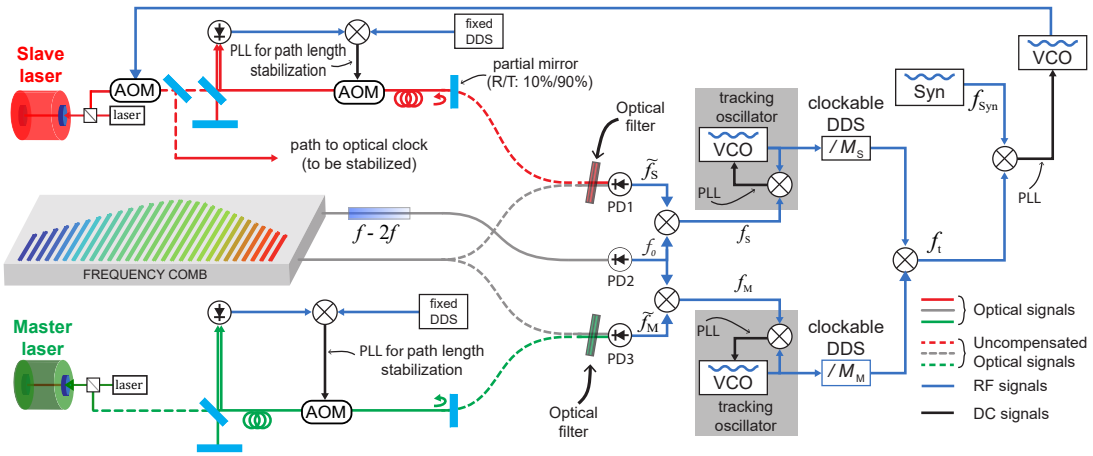

Figure 4.1: Principle of the transfer of spectral purity. The optical beatnotes $\tilde{f}_S$ and $\tilde{f}_M$ are detected respectively by the photodetectors PD1 and PD3. The carrier envelope offset frequency f_0 of the comb is detected by PD2 and mixed out of the optical beatnotes. These f_0-free beats are first regenerated by tracking oscillator filters before rescaling by division factors M and mixing them to form the transfer beatnote f_t. This latter carries all the information of the relative fluctuations of the master laser ν_M and slave laser ν_S, in the bandwidth chosen by the tracking oscillator filters. Finally, the f_t is locked to e.g. a synthesizer, and the feedback via a voltage controlled oscillator (VCO) to the acousto-optic modulator forces ν_S to follow the residual fractional fluctuations of ν_M. The propagation noise of some of the optical paths is not compensated, e.g. the comb light after being split (grey dashed lines), degrades the stability of the transfer, the strategy to tackle this issue is described in section 4.3.

and one can just rescale the beatnote with the highest N by a division factor given by $\max\left(N_M^{(1,i)}, N_S^{(1,j)}\right) / \min\left(N_M^{(1,i)}, N_S^{(1,j)}\right)$.

It is preferable to use RF tracking oscillator filters prior to the rescaling stage in order to clean and regenerate the signals in a given bandwidth, typically of a few kHz in our case. On the one hand, they filter spurious peaks from the beatnotes thus preventing mixers and amplifiers to suffer from saturation, providing enough RF power with sufficient SNR to the DDS input that otherwise would be hard to clock. On the other hand, filtering close to the central frequency of the RF beatnote effectively eliminates the white phase noise (typically due to the necessary RF amplifiers) that does not intrinsically correspond to the signal that we want to track.

A tracking oscillator filter consist of a VCO that is phase locked to the signal of interest, the beatnote, with an adjustable given bandwidth. This way, the signal at the output of the tracking oscillator filter is a copy of that applied at the input, for all Fourier frequencies within the locking bandwidth. On the contrary, the signal fluctuations and random noise at Fourier frequencies above this bandwidth is suppressed thanks to this process, hence the terminology of "filter". Compared to a passive RF filter, the advan-

tage is two-fold. First, the locking bandwidth can be set to a relatively low value, thereby realizing a very narrow filter which would be very difficult to realize with passive components at a carrier of typically several tens of MHz. Second, once phase locked, the tracking oscillator filter will follow the carrier frequency if it slowly drifts away, and thereby realize a narrow filter whose central band-pass frequency is always equal to that of the input signal to filter, a function extremely hard to realize with a passive and typically "fixed frequency" filter. It should be noted, nonetheless, that the narrow filtering effect means that, in the signal mixing that produces the removal of the effect from f_{rep} fluctuations, the effective removal of f_{rep} is only realized within the narrowest of the tracking oscillator bandwidth.

Once the comb parameters have been removed by using the OFC as an intermediate or "transfer" oscillator, the transfer beatnote signal from equation 4.2 is phase locked to a stable RF oscillator, f_{Syn}, that is a synthesizer external referenced to the UMR. The PLL itself is performed, in our case, by a feedback to the VCO feeding the first AOM placed after the slave laser (see Fig. 4.1). Thus, this correction is totally independent of any other pre-stabilization done on ν_{S} as is the case with the PDH cavity stabilization technique. An offset lock of a second laser to the ν_{S} can also be implemented to apply the former correction, in order to provide more flexibility in terms of optical power and frequency tunability. Once the servo loop is closed, the two lasers are related as:

$$\frac{\nu_{\mathrm{M}}}{M_{\mathrm{M}}^{(1,i)}} - \frac{\nu_{\mathrm{S}}}{M_{\mathrm{S}}^{(1,j)}} + \varepsilon_{\mathrm{rep}}^{(1,i,j)} \cdot f_{\mathrm{rep}} + \beta^{(1,i,j)} = f_{\mathrm{Syn}} \tag{4.4}$$

To analyze the noise of equation 4.4, on the one hand, we can neglect the term $\varepsilon_{\mathrm{rep}}^{(1,i,j)} = \left(\frac{N_{\mathrm{S}}^{(1,j)}}{M_{\mathrm{S}}^{(1,j)}} - \frac{N_{\mathrm{M}}^{(1,i)}}{M_{\mathrm{M}}^{(1,i)}} \right)$ as it is sufficiently small (typically 10^{-8}), which leads to a good enough rejection of the repetition rate noise. On the other hand, f_{Syn} is usually around tens of MHz (7 orders of magnitude smaller than ν_{M}), and $\sigma_y(\mathrm{UMR}_{1\mathrm{GHz}}) = 3 \cdot 10^{-14}$ at 1 s (red curve in Fig. 3.5), which also allows us to discard the noise added by the synthesizer ($\approx 10^{-21}$) since it is referenced to the UMR. We can derive the slave laser stability transferred with no degradation, neglecting the noise of the transfer itself, as:

$$\sigma(\nu_{\mathrm{S}}) = M_{\mathrm{S}}^{(1,j)} \sqrt{\left(\frac{\sigma(\nu_{\mathrm{M}})}{M_{\mathrm{M}}^{(1,i)}} \right)^2 + \sigma^2\left(\beta^{(1,i,j)}\right)} \tag{4.5}$$

If we assume that the two beatnotes signals are formed in the same comb output ($i = j$, which is the definition of the single-branch), $\beta^{(1,i,j)}$ vanishes as this noise is proportional to the frequency as demonstrated in subsection 3.2.2. Therefore, for the single-branch case, equation 4.5 now reads:

$$\sigma(\nu_{\mathrm{S}}) \approx \frac{M_{\mathrm{S}}^{(1,i)}}{M_{\mathrm{M}}^{(1,i)}} \sigma(\nu_{\mathrm{M}}) \approx \frac{\nu_{\mathrm{S}}}{\nu_{\mathrm{M}}} \sigma(\nu_{\mathrm{M}}) \tag{4.6}$$

where $\frac{M_S^{(1,j)}}{M_M^{(1,i)}} \approx \frac{\nu_S}{\nu_M}$. Thus, the noise of the master laser is imprinted in the slave one with the rescaling factor $\frac{\nu_S}{\nu_M}$.

Out-of-loop assessment

In order to assess the performance of the transfer we need to quantify the sources of noise that can not be eliminated, in particular, the residual effects of the transfer beatnote signal phase locking to the RF stable reference.

Since an in-loop measurement will constrain the noise of the locking signal only within the PLL bandwidth, it is necessary to do an out-of-loop measurement with a second independent OFC that accounts for the overall noise contained in the beatnote. On top of that, this readout comb does not suffer from the same possible (but unlikely) biases resulting from the transfer, allowing us to verify the accuracy of the transfer.

To this end, we duplicate the first setup carrying out the transfer itself as depicted in Fig. 4.2. The optical and RF setups corresponding to the second comb are very similar but completely independent of the setups necessary for the first comb. Additionally, the readout transfer beatnote is formed by post-processing as there is no need to form it physically considering it is not used for anything but numerical verification of the stability and the accuracy of the transfer process.

If we introduce an additive noise term $\varepsilon_{\mathrm{t}}^{(1)}$ in equation 4.4 that accounts for the different sources of noise involved, listed in table 4.1, the noise of the transfer process can be modeled as:

$$\nu_{\mathrm{S}} = M_{\mathrm{S}}^{(1,j)} \quad \frac{\nu_{\mathrm{M}}}{M_{\mathrm{M}}^{(1,i)}} - f_{\mathrm{Syn}} + \varepsilon_{\mathrm{rep}}^{(1,i,j)} \cdot f_{\mathrm{rep}} + \beta^{(1,i,j)} + \varepsilon_{\mathrm{t}}^{(1)} \Bigg) \Bigg(\tag{4.7}$$

For the second comb ($z = 2$) we derive the two f_0-free beatnotes in the same way as before, where $\varepsilon_{\mathrm{rep}}^{(2,k,l)} = \left(\frac{N_{\mathrm{S}}^{(2,l)}}{M_{\mathrm{S}}^{(2,l)}} - \frac{N_{\mathrm{M}}^{(2,k)}}{M_{\mathrm{M}}^{(2,k)}} \right) \Bigg(= 0$ as we rescale them by post-processing with $M = N$, and with k and l to denote its two possible outputs. The transfer beatnote, with an additive noise term $\varepsilon_{\mathrm{ro}}^{(2)}$ that accounts for the readout, now yields:

$$f_{\mathrm{t}}^{(2)} = \frac{\mathrm{sign}_{\mathrm{M}}^{(2,k)} \cdot f_{\mathrm{M}}^{(2,k)}}{N_{\mathrm{M}}^{(2,k)}} - \frac{\mathrm{sign}_{\mathrm{S}}^{(2,l)} \cdot f_{\mathrm{S}}^{(2,l)}}{N_{\mathrm{S}}^{(2,l)}} = \frac{\nu_{\mathrm{M}}}{N_{\mathrm{M}}^{(2,k)}} - \frac{\nu_{\mathrm{S}}}{N_{\mathrm{S}}^{(2,l)}} + \varepsilon_{\mathrm{ro}}^{(2)} + \beta^{(2,k,l)} \tag{4.8}$$

Inserting equation 4.7 into 4.8 we find the readout beatnote reads:

$$f_{\mathrm{t}}^{(2)} = \quad \frac{1}{N_{\mathrm{M}}^{(2,k)}} - \frac{M_{\mathrm{S}}^{(1,j)}}{N_{\mathrm{S}}^{(2,l)} M_{\mathrm{M}}^{(1,i)}} \Bigg) \Bigg(\nu_{\mathrm{M}} + \frac{M_{\mathrm{S}}^{(1,j)}}{N_{\mathrm{S}}^{(2,l)}} \left(f_{\mathrm{Syn}} - \varepsilon_{\mathrm{t}}^{(1)} - \varepsilon_{\mathrm{rep}}^{(1,i,j)} \cdot f_{\mathrm{rep}} - \beta^{(1,i,j)} \right) \Bigg(+ \varepsilon_{\mathrm{ro}}^{(2)} + \beta^{(2,k,l)} \tag{4.9}$$

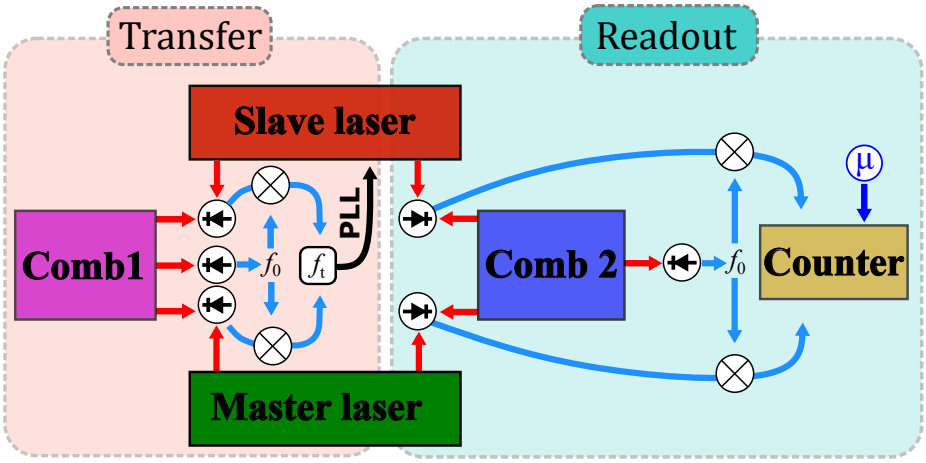

Figure 4.2: Out-of-loop assessment of the spectral purity transfer from the master laser to the slave laser via the first comb (transfer comb). The second comb (readout comb) measures the noise of the transfer process together with the added noise from the readout itself.

where the pre-factor of ν_M is typically 10^{-6} as the N number ratios between the transfer and readout OFCs are nearly identical $\frac{M_S^{(1,j)}}{M_M^{(1,i)}} \approx \frac{N_S^{(2,l)}}{N_M^{(2,k)}}$. This sets the fractional noise contribution of the first term to 10^{-6} times $4 \cdot 10^{-16}$, i.e. a quantity $< 10^{-21}$, which is completely negligible.

Finally, the stability of $f_t^{(2)}$ for a single branch approach (with $\beta^{(1,i,j)}$ and $\beta^{(2,k,l)}$ equal to zero) is then given by:

$$\sigma\left(f_t^{(2)}\right) = \sqrt{\left(\frac{M_S^{(1,j)}}{N_S^{(2,l)}}\right)^2 \left(\sigma^2\left(\varepsilon_t^{(1)}\right) + \sigma^2\left(\beta^{(1,i,j)}\right)\right) + \sigma^2\left(\varepsilon_{ro}^{(2)}\right) + \sigma^2\left(\beta^{(2,k,l)}\right)} \tag{4.10}$$

where we have neglected the noise terms due to $\varepsilon_{rep}^{(1,i,j)}$ and f_{Syn} as discussed before.

The formalism introduced in this section aims at quantifying the noise resulting from the entire transfer process. The resulting stability of ν_S, not accessible by this formalism, can be checked by a direct comparison with another independent USL with equal or better stability, by comparison by at least two other lasers even if they are less stable via cross-correlation [116], or by probing the atoms in an optical clock and inferring the stability of the laser from the Dick effect.

4.1.2 Limits of the implementation

At the time of performing the transfer oscillator method one should guarantee an adequate rescaling of the optical beatnotes to avoid an insufficient elimination of the repe-

tition rate of the OFC, and to consider all unavoidable different sources of noise arising from the diverse components used on the setup.

Beatnote rescaling

The division factors M used to rescale the two beatnotes involved play a fundamental role in the rejection of the $\varepsilon_{\mathrm{rep}} \cdot f_{\mathrm{rep}}$ term shown in equation 4.2. One must take into account, on the one hand, the number of bits k of the DDS since it provides the number of digital states it can work with, setting its resolution threshold, and on the other hand, the fractional stability of f_{rep}, which depends on the signal used to reference the comb. For instance, our comb modes N are in the order of 10^6 and $k = 48$, so it can be shown that the error on the rescaling of N can not be more than $N/2^{48}$, which is on the order of 10^{-8} or lower. Since, in our case, the comb is locked to ν_{IRef} featuring $\sigma_y(1\,\mathrm{s}) < 10^{-15}$, it means that the f_{rep} noise contribution in the optical domain during the transfer is lower than 10^{-29}. Additionally, it is best to keep the beatnotes at high frequencies because of the better performance of the RF components, so lower division factors are recommendable. In practice, we divide by $M = 2$ the laser with the smallest frequency and we adapt the other M factor to be between 2 and 4 if the lasers' frequencies are within an octave.

Unfortunately, it is not always possible to form the two beatnotes with the same OFC output, i.e. single-branch configuration (subsection 4.3), meaning that the f_{rep} noise is no longer in common mode due to path length fluctuations experienced along the new branch added. In this case the technique will ultimately be limited by some residual differential f_{rep} noise due to the use of different OFC outputs, known as multi-branch configuration (subsection 4.2).

Residual technical noise

We can split the setups (transfer and assessment), and therefore the noise sources, into two different parts as shown in table 4.1. On the one hand, an optical side where the lasers are combined with their respective OFC outputs and the optical paths are compensated on their way towards the PDs. On the other hand, an RF side that starts after the photodetection of the beatnotes to form $f_{\mathrm{t}}^{(1)}$ for the locking (transfer side) or the out-of-loop $f_{\mathrm{t}}^{(2)}$ for the characterization (readout side).

- In the RF domain non-linear components such as mixers, multipliers or amplifiers can contaminate the signals if they are not well filtered, are saturated or are lacking power at their input ports, degrading the SNR. One must check that the noise floor of the frequency chain is below the noise level targeted for the experiment.

  Ground loops can appear when dealing with signals from different setups which are power-supplied by different sources. Lock-related cycle slips can also happen

Noise sources and residual noises	
RF domain	**Optical domain**
Non linearities	Back reflections
Ground loops and cycle slips	Imperfect mode-matching
Tracking bandwidths	Path length fluctuations
Amplitude-phase conversion	Pointing instability

Table 4.1: Components to be considered when characterizing the noise floor of a transfer oscillator scheme at the 10^{-18} level.

both on the PLLs and on the counters due to the ambiguity in the number of elapsed cycles.

The bandwidth of the tracking oscillators used to track and filter the beatnotes has to be narrow enough both to reject spurious peaks around the beatnotes and to avoid collecting background noise that degrades the characterization of the inherent noise of the lasers under consideration.

- On the optical setup all the paths (fiber or free space) must be compensated when possible (see Fig. 4.1), paying special attention to deceiving parasitic reflections that might not come from the reflecting plane chosen, e.g. partial reflective mirror, to compensate the carrier for the optical path length fluctuations. These fluctuations arise from environmental variations (temperature and pressure) and external perturbations (mechanical or acoustic vibrations). It is the more important to isolate well the setup from the environment especially if uncompensated fibers are involved since the coupling between the propagation phase and the environment is considerably larger than it is in free space.

  There can also be noise due to the beatnote photodetection such an imperfect mode-matching between the beams resulting in photons detected by the PD but contributing only to the shot noise without contributing to the signal. Besides, any fluctuation of the beatnote at the detection point, induced by vibrations on the optical components (mirrors, lenses, etc.), will move the beam across the active area of the PD. Thus, these angular fluctuations of the laser beam will be converted into power ones, known as pointing instability. This effect can be minimized by a spatial filtering of the laser output (a short piece of single-mode optical fiber for instance) followed by a power control system (such an AOM) before the PD. Hence, the beam-pointing fluctuations are converted to power fluctuations at the input of the fiber that will be canceled by the AOM [117].

4.2 Multi-branch configuration

The optical setup is said to be multi-branch when the beatnotes f_M and f_S are formed in different comb outputs as depicted in Fig. 4.3 a). This can be because one single output does not cover the pair of wavelengths involved as it is the case for the Sr and Hg clock lasers (see Fig. 2.3) or simply because a more flexible approach is pursued. It can be the case where more than one simultaneous transfer from a master USL must be performed even if the slave lasers operating at different wavelengths are within the spectral range of the output of the comb. For this purpose, adding dedicated optical amplifiers followed by HNLFs for spectral shifting or broadening, and non-linear crystals if frequency conversions are needed, can be very advantageous since it allows specific SNR optimization of each of the several beatnotes that can be challenging to achieve in a single output. Thus, this approach is easy to implement and provides robustness at the cost of additional differential noise between the branches. Even though a transfer with an added noise as low as the mid 10^{-17} range has been demonstrated [118], this is already hardly sufficient to be compatible with the best existing USLs [49], which will keep improving. However, a novel technique has been implemented recently, permitting to detect and correct for the differential phase noise in the two branches which cover around $1-2.2\,\mu$m and $0.5-1.1\,\mu$m, with a stability as low as $3\cdot10^{-18}$ at 1 s [119].

With respect to the elimination of the comb's offset prior to the rescaling (except for f_0-free OFCs), even if the configuration is multi-branch, the differential noise introduced on f_0 does not contribute much. As we justified in the previous chapter the noise introduced after the EDFA outputs on the optical beatnotes is proportional to the N numbers. This is because f_0 is a small quantity (a few MHz) offsetting the beatnotes in the optical domain and whose differential noise is negligible, unlike the f_{rep} contribution which is multiplied by a large factor (the N numbers).

4.2.1 Optical setup

We have implemented a preliminary multi-branch transfer all-in-fiber setup between the Hg and Sr clock lasers ν_{HgL} at 1062.5 nm and ν_{SrL} at 1062.5 nm in the Er:fiber 1. The role of this comb is therefore to realize the transfer while operating in the narrow linewidth regime as described in subsection 2.1.2. The lasers are beaten with the OFC light coming from EDFA 1 and EDFA 2, respectively, and detected in two different fibered PDs as shown in Fig. 4.3 b). The fiber propagation noise of the incoming clock lasers is compensated as illustrated in C.1, where there is about 1 m of uncompensated fiber (fiber of the coupler output port + fiber of the mirror). There are also around 2 m of uncompensated and unshielded fiber between each of the noise cancellation and the photodetection. Polarization controllers are used to optimize the SNR of both beatnotes f_{HgL} and f_{SrL}, and beatnotes for the compensation simultaneously. All the SNRs are >35 dB in a 1 kHz bandwidth for all optical beatnotes.

After mixing f_0 out[2] we demodulate each of the f_0-free beatnotes to generate the corresponding error signals to lock them to the OFC via AOMs. Instead of forming a transfer beat, we phase lock the beatnotes from equation 4.1 for M = HgL (S = SrL) and $i = 1$ ($j = 2$) to two different synthesizers:

$$\begin{aligned} \text{sign}_{\text{HgL}}^{(1,1)} \left(\nu_{\text{HgL}} + f_{\text{s,HgL}}^{(1,1)} - N_{\text{HgL}}^{(1,1)} \cdot f_{\text{rep}}^{(1)} + \varepsilon^{(1,1)}(\nu_{\text{HgL}}) \right) &= f_{\text{SynHg}} \\ \text{sign}_{\text{SrL}}^{(1,2)} \left(\nu_{\text{SrL}} + f_{\text{s,SrL}}^{(1,2)} - N_{\text{SrL}}^{(1,2)} \cdot f_{\text{rep}}^{(1)} + \varepsilon^{(1,2)}(\nu_{\text{SrL}}) \right) &= f_{\text{SynSr}} \end{aligned} \tag{4.11}$$

so that the beatnotes share the transfer comb (Er:fiber 1) noise, that will be rejected at the time of evaluation.

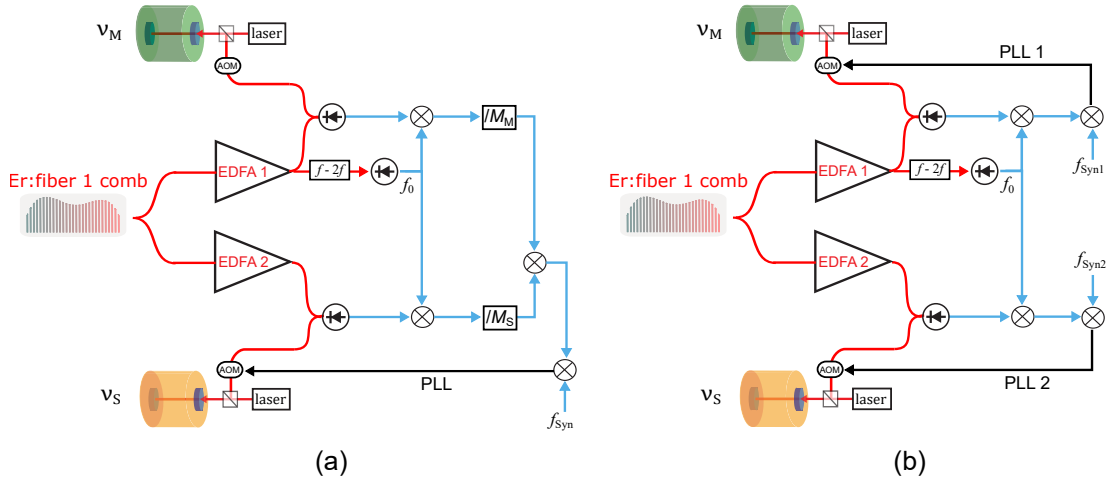

Figure 4.3: In (a) multi-branch transfer scheme. In (b) multi-branch assessment without a transfer beatnote.

4.2.2 Noise limit for 1062 nm - 698 nm transfer

The topology of our Ti:sa comb ($z = 3$), optically referenced to the ν_{HgL} (see Fig. 2.2) and spanning from $500 - 1100$ nm, allow us to use it directly for the transfer assessment from HgL to SrL or vice versa, without the need of implementing any equivalent setup on its side. To do so, we form and measure the Sr beatnote applying equation 3.22 with

[2] In the case of the Sr clock laser, the beatnote, f_{SrL}, is demodulated by $2 \cdot f_0$ since the comb's output after EDFA 2 is frequency doubled and hence it contains twice the frequency offset.

L = SrL:

$$\begin{aligned} f^{(3)}_{\mathrm{SrL}} &= \mathrm{sign}^{(3)}_{\mathrm{SrL}} \left(\nu_{\mathrm{SrL}} + f^{(3)}_{\mathrm{s,SrL}} + \varepsilon^{(3)}(\nu_{\mathrm{SrL}}) - N^{(3)}_{\mathrm{SrL}} \cdot f^{(3)}_{\mathrm{rep}} \right) \\ &= \mathrm{sign}^{(3)}_{\mathrm{SrL}} \left[\left(\nu_{\mathrm{SrL}} + f^{(3)}_{\mathrm{s,SrL}} + \varepsilon^{(3)}(\nu_{\mathrm{SrL}}) \right. \right. \\ &\quad \left. \left. - N^{(3)}_{\mathrm{SrL}} \left(\frac{\nu_{\mathrm{HgL}} + f^{(3)}_{\mathrm{s,HgL}} - 16 \cdot \mathrm{sign}^{(3)}_{\mathrm{HgL}} \cdot f^{(3)}_{\mathrm{DDS1}} + \varepsilon^{(3)}(\nu_{\mathrm{HgL}})}{N^{(3)}_{\mathrm{HgL}}} \right) \right) \right] \left(\right. \end{aligned} \tag{4.12}$$

where $f^{(3)}_{\mathrm{rep}}$ has been derived from equation 3.21 for $n = 16$ and L = HgL, and $\varepsilon^{(3)}(\nu_{\mathrm{L}})$ are the Ti:sa comb output noises. Replacing ν_{HgL} and ν_{SrL} from equation 4.11 the beatnote now yields:

$$\begin{aligned} \mathrm{sign}^{(1,2)}_{\mathrm{SrL}} \cdot f^{(3)}_{\mathrm{SrL}} = \mathrm{sign}^{(1,2)}_{\mathrm{SrL}} \cdot f_{\mathrm{SynSr}} &- \frac{N^{(3)}_{\mathrm{SrL}}}{N^{(3)}_{\mathrm{HgL}}} \left(\mathrm{sign}^{(1,1)}_{\mathrm{HgL}} \cdot f_{\mathrm{SynHg}} - 16 \cdot \mathrm{sign}^{(3)}_{\mathrm{HgL}} \cdot f^{(3)}_{\mathrm{DDS1}} \right) \\ &+ \frac{N^{(3)}_{\mathrm{SrL}}}{N^{(3)}_{\mathrm{HgL}}} \left(f^{(1,2)}_{\mathrm{s,HgL}} - f^{(3)}_{\mathrm{s,HgL}} \right) + f^{(3)}_{\mathrm{s,SrL}} - f^{(1,2)}_{\mathrm{s,SrL}} \\ &+ f^{(1)}_{\mathrm{rep}} \left(N^{(1,2)}_{\mathrm{SrL}} - \frac{N^{(3)}_{\mathrm{SrL}} \cdot N^{(1,1)}_{\mathrm{HgL}}}{N^{(3)}_{\mathrm{HgL}}} \right) + \varepsilon^{(3)}(\nu_{\mathrm{SrL}}) - \frac{N^{(3)}_{\mathrm{SrL}}}{N^{(3)}_{\mathrm{HgL}}} \cdot \varepsilon^{(3)}(\nu_{\mathrm{HgL}}) \\ &- \varepsilon^{(1,2)}(\nu_{\mathrm{SrL}}) + \frac{N^{(3)}_{\mathrm{SrL}}}{N^{(3)}_{\mathrm{HgL}}} \cdot \varepsilon^{(1,1)}(\nu_{\mathrm{HgL}}) \end{aligned} \tag{4.13}$$

where we can neglect the instabilities of all the fixed frequencies from the synthesizers and DDSs (first two lines) and the $f^{(1)}_{\mathrm{rep}}$ contribution since $\sigma(f^{(1)}_{\mathrm{rep}}) \approx f^{(1)}_{\mathrm{rep}} \cdot \sigma_y(\nu_{\mathrm{IRef}}) \approx 10^{-6}$, i.e. below the 10^{-20} level once it is rescaled. Besides, the two $\varepsilon^{(3)}(\nu_{\mathrm{L}})$ terms cancel each other out as they come from the same output. Therefore the final beatnote instability is given by:

$$\sigma\left(f^{(3)}_{\mathrm{SrL}} \right) = \sqrt{\sigma^2 \left(\varepsilon^{(1,2)}_{\mathrm{SrL}} + \frac{N^{(3)}_{\mathrm{SrL}}}{N^{(3)}_{\mathrm{HgL}}} \cdot \varepsilon^{(1,1)}_{\mathrm{HgL}} \right)} \tag{4.14}$$

The result of the transfer shows a fractional stability (blue curve in Fig. 4.4) of $2.2 \cdot 10^{-16}$ at 1 s, preventing the frequency comparison or transfer between the Hg and Sr clock lasers beyond this limit. This is mainly due to the uncompensated noise accumulated in the fibers along the setup, around 4 m in total. We have discarded other type of noise's sources at this level.

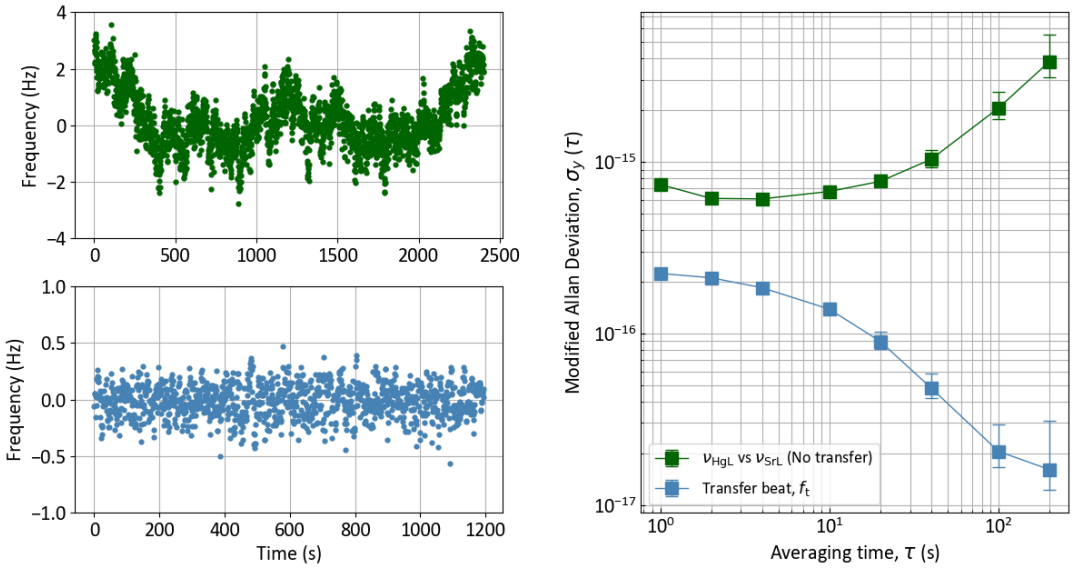

Figure 4.4: Multi-branch spectral purity transfer. Dark green: combined instability of lasers ν_{HgL} and ν_{SrL} without any transfer (uncorrelated noise). Light blue: transfer (correlated) noise between the two lasers. Dead-time-free frequency counter set in Lambda mode.

4.3 Single-branch configuration

In order to suppress the influence of path length fluctuations a unique OFC output must be used to form the pair of beatnotes f_M and f_S. A tradeoff in the optical spectrum optimization has to be done to have enough optical power at the wavelengths of interest. This makes this approach more challenging, especially when the transfer must be implemented for multiple slave lasers. But on the other hand, as we will demonstrate, it leads to residual instabilities in the 10^{-18} range [120, 121], making it suitable for the next generation of optical atomic clocks aiming stabilities at the 10^{-17} level at short time scales.

We have equipped the outputs of both EDFAs of the two Er:fiber combs. It consists of compensated fibers leading to free-space setups where the recombination of the cw beams with the comb light is structured so as to leave only a few centimeters of uncompensated propagation. This is done in contrast to the results reported in multi-branch where a preliminary setup, suffering from several meters of uncompensated fibers, was used. We perform the transfer oscillator technique described in section 4.1 and consider all type of noise sources that could be involved. We minimize the uncompensated optical paths and set the same path for ν_M and ν_S when possible as it will be explained for the two transfers carried out (subsections 4.3.1 and 4.3.2). In order to assess the results we have duplicated the two setups with a second Er:fiber 2 (readout) OFC, also locked

to ν_{IRef}, similar to the transfer OFC. We have tried to built the optical setups as identical as possible while their frequency chains are simpler since, in the case of the readout comb, the rescaling of the beatnotes is carried out by post-processing.

We have finally combined the former setups to implement a double single-branch scheme (shown in Fig. 4.5) to perform a transfer from the Hg clock laser to the Sr one, circumventing the noise of the two required EDFAs, as it will be explained in 4.3.3). The resulting stability was directly applied to a real local comparison of their clocks.

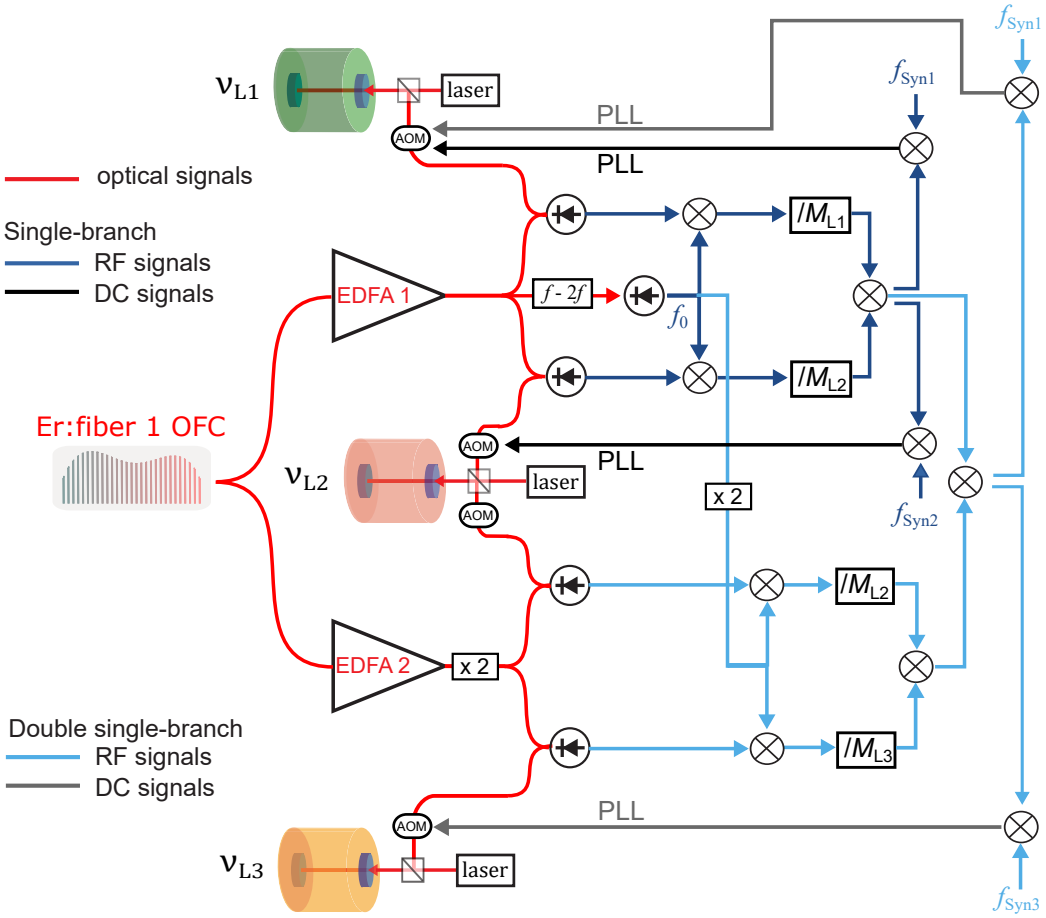

Figure 4.5: Single-branch (dark blue and black) and double single-branch (light blue and grey) schemes.

4.3.1 Transfer from 1542 nm to 1062 nm

The first transfer we have performed is in the IR domain from the ν_{IRef} at 1542 nm (master laser) to the ν_{HgL} at 1062.5 nm (slave laser). Since the two wavelengths in-

volved can be detected by a same InGaAs PD, we have based our noise compensation on the technique developed by the PTB team "Working group unit of length" [121], this is, overlapping the end paths of the lasers to have retro-reflected them in the same partial-reflector mirror (PRM), as shown in Fig. 4.6. Around 90 % of the lasers' power is transmitted and their beams are overlapped from the PRM on, propagating along the same path and suppressing differential phase fluctuations due to path length variations. To achieve this overlapping, once the beams to recombine (1062 nm, 1160 nm and 1542 nm) have exited the optical fibers bringing them to the experiment, we combine them with dichroic mirrors (first 1062 nm and 1160 nm, and then both of them with 1542 nm). Subsequently, we make them pass through a cat's eye where 10 % of their respective beams are reflected back for the noise compensation. Note that we have installed in the arm of each of the three wavelengths a second AOM in free space, before recombination, as a "marker" to be able to distinguish any parasitic reflection that might happen along the path before reaching the final feedback mirror, the PRM. The transmitted beams after the PRM are combined with the OFC's light from EDFA 1 in a 50/50 beam splitter (BS) and then focused by a 50 mm focal length lens. Thanks to the lens, we ensure that the waists of the beatnotes are within the active area (80 μm) of the unique photodetector used.

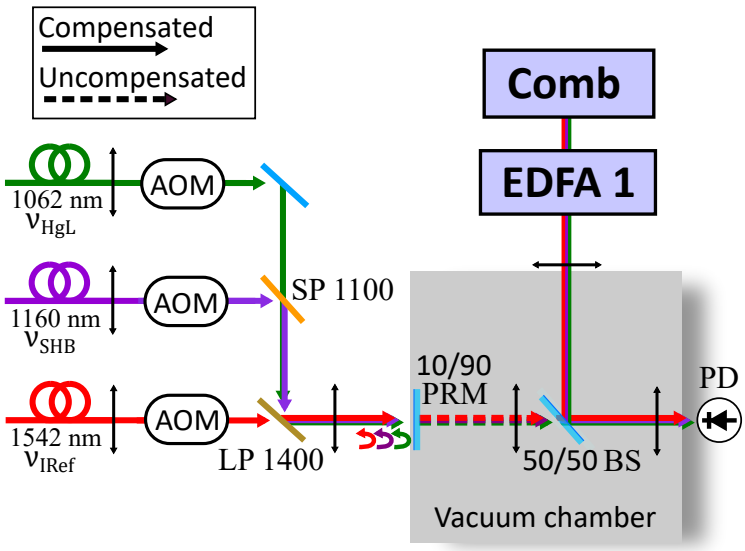

Figure 4.6: Optical setup for the ν_{IRef} at 1542 nm (master laser) spectral purity transfer to ν_{HgL} at 1062 nm (slave laser), with the possibility of being applied to ν_{SHB} at 1160 nm. The three lasers' paths are overlapped using short-pass (SP) and long-pass (LP) dichroic mirrors so they can be reflected back in the same 10/90 (R/T) partial retro-reflector mirror (PRM) for fiber noise compensation. Subsequently they are all combined on a 50/50 beam splitter (BS) with the comb's light for beatnote detection by the same photodetector (PD).

The comb light is brought by a 1-m long uncompensated fiber, and once the light goes into free space, reaches the BS after about 5 cm. The uncompensated path of the cw lasers goes from the PRM till the BS and it is less than 7 cm. After the BS, both the lasers and the OFC, are in common mode, sharing the same propagation noise, and being therefore canceled when forming the beatnotes. The possible differential dispersion effects between the lasers and their corresponding teeth N are negligible since they are separated at most $f_{\mathrm{rep}}/2$. The free-space uncompensated paths are placed in a 10×10 cm base plate in order to put it under vacuum if necessary one day. The same optical setup has been implemented in the Er:fiber 2 OFC for the readout.

Once the beatnotes are detected for M = IRef and S = HgL, we form and lock the transfer beatnote of equation 4.4 to f_{SynHg}, making the feedback on the Hg clock laser AOM.

Out-of-loop assessment

In order to assess the stability and the accuracy of the transfer, according to equation 4.8, we express the transfer beatnote as:

$$N_{\mathrm{IRef}}^{(2,1)} \cdot f_{\mathrm{t}}^{(2)} = \mathrm{sign}_{\mathrm{IRef}}^{(2,1)} \cdot f_{\mathrm{IRef}}^{(2,1)} - \frac{N_{\mathrm{IRef}}^{(2,1)}}{N_{\mathrm{HgL}}^{(2,1)}} \cdot \mathrm{sign}_{\mathrm{HgL}}^{(2,1)} \cdot f_{\mathrm{HgL}}^{(2,1)} \tag{4.15}$$

From the acquisition of the $f_{\mathrm{t}}^{(2)}$ we derive the noise and the accuracy of the transfer due to the combined contribution of the two combs, given by equation 4.10. The red and green curves in Fig. 4.7 correspond to the two optical beatnotes at play when the transfer feedback is on and therefore are correlated. In this case the limit is the same as it is in the multi-branch case, each beatnote suffers from its optical comb output noise ($\varepsilon^{(z,0)}$ and $\varepsilon^{(z,1)}$) but without an elimination of the common $\varepsilon^{(z,0)}$ in the readout comb. Most of this noise goes away when the beatnotes are recombined to form the transfer beatnotes, hence the blue curve. The blue data shows the difference between the value of $f_{\mathrm{t}}^{(2)}$ and its expected value, and the corresponding fractional instability around $8 \cdot 10^{-18}$ at 1 s. This is higher that the limit due to the SNR: a white phase noise floor 38 dB (in a 1 kHz bandwidth) below the signal (as it is the case for this measurement), corresponds to a stability limit of around $1.4 \cdot 10^{-18}/\tau[\mathrm{s}]$ at 1062 nm for one photodiode.

This result sets the upper bound of the measurement. If we assume equal noise contribution both on the transfer and on the readout side we can attribute a noise for the transfer around $5 - 6 \cdot 10^{-18}$ at 1 s. In any case, this value is well below the best laser stability demonstrated to date with a flicker floor of $4 \cdot 10^{-17}$. The limitation does not come from differential dispersion of the two wavelengths involved. The extension of the fiber in 10 m bringing the OFC light has not affected neither the SNR of the beatnotes nor the final stability below 10 s, then a flicker floor in the low 10^{-18} seems to appear, but more data must be accumulated to support this claim. Such a degradation would

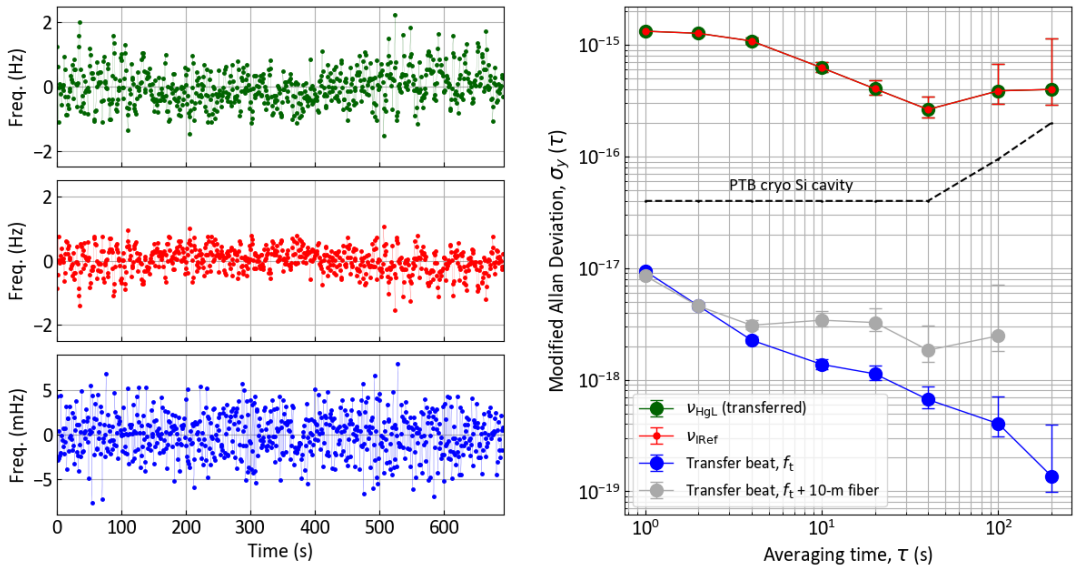

Figure 4.7: Single-branch spectral purity transfer from ν_{IRef} at 1542 nm to ν_{HgL} at 1062.5 nm (red and green curves). The resulting stability around $8 \cdot 10^{-18}$ at 1 s (blue curve), includes the contribution of the transfer by the first comb, and the contribution of the readout by the second comb. The impact of increasing the length of the fiber bringing the OFC light is negligible at a short-time scale (gray curve). The black dash lines indicates the best laser stability demonstrated to date [49]. Dead-time-free frequency counter set in Lambda mode.

be explained by dispersion effects on the comb light induced by the added fiber length. We also checked the contribution of the RF chain involved which resulted in a noise in the low 10^{-19}. The limitation is most likely due to some residual noise still present of the fibers and not to the few centimeters of uncompensated paths previous to the combination in the BS since they are correlated and will cancel out when mixing the beatnotes.

4.3.2 Transfer from 1542 nm to 698 nm

The second transfer we have realized is from the same ν_{IRef} in the IR domain to the ν_{SrL} in the visible one at 698 nm. This approach differs from the former in two ways: the beatnotes can not be detected by the same PD and the 698 nm light is not provided directly by the EDFA 2, what makes the implementation more challenging.

In this setup, the single branch, apart from comprising the optical amplifier and the HNLF, contains a PPLN crystal for the frequency doubling of the 1396 nm so as to obtain a 3-nm span comb spectrum centered at 698 nm to beat with the ν_{SrL} (see Fig. 2.3). The frequency doubling process depends strongly on the temperature so we use a spectrometer (USB2000 Ocean Optics) to optimize the doubling at 698.4 nm for

a temperature of 125 °C on the second comb (Er:fiber 2), since for the transfer comb (Er:fiber 1) was already optimized at a different temperature of 80 °C. As it is shown in Fig. 4.8, this wavelength tuning is not so critical in terms of temperature stabilization requirements.

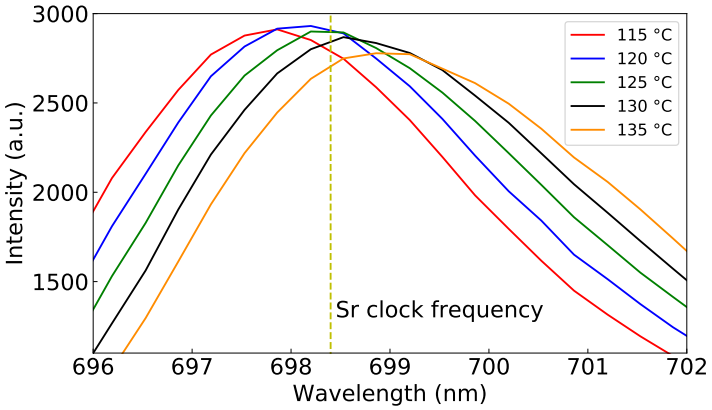

Figure 4.8: PPLN doubling crystal spectrum versus temperature for the EDFA 2 of Er:fiber 2. The yellow dash line shows an optimal temperature of 125 °C for the Sr clock wavelength. The optical resolution of the spectrometer is 1.5 nm approximately.

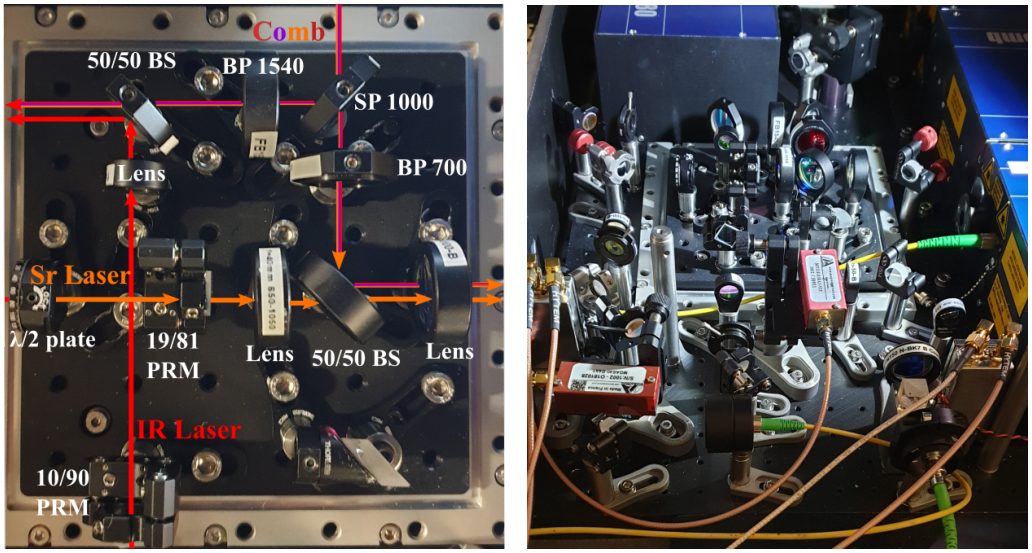

Figure 4.9: Optical setup picture for the ν_{IRef} to ν_{SrL} spectral purity transfer: Left: close-up view of the optical paths within the vacuum base. Right: overview of the whole setup.

We take advantage of the IR comb light that is still present after the doubling process so that we have the two frequencies we are interested in in the same beam (same comb output) to be recombined later with the two cw lasers. For a reason that has not been clearly identified yet, the IR and the visible parts of the comb spectrum behave in a very different way after the doubling stage in the readout comb: when one beam is collimated, the other one is strongly diverging. This is why we have chosen to not recombine the cw beams, and to split the IR light as soon as possible after the doubling crystal since anyway the detection would necessarily be performed by two detectors of different technologies due to the large frequency separation of the lasers involved. To do so, after splitting the comb light by using a dichroic mirror at 1000 nm, we recombine each component with the corresponding cw beam. In order to compensate the propagation noise we implement two separated cat's eyes to partly reflect the lasers as depicted in Fig. 4.10. The distances between splitting (on the comb side and on the cat's eyes for the cw side) and recombination are minimized since they can not be compensated.

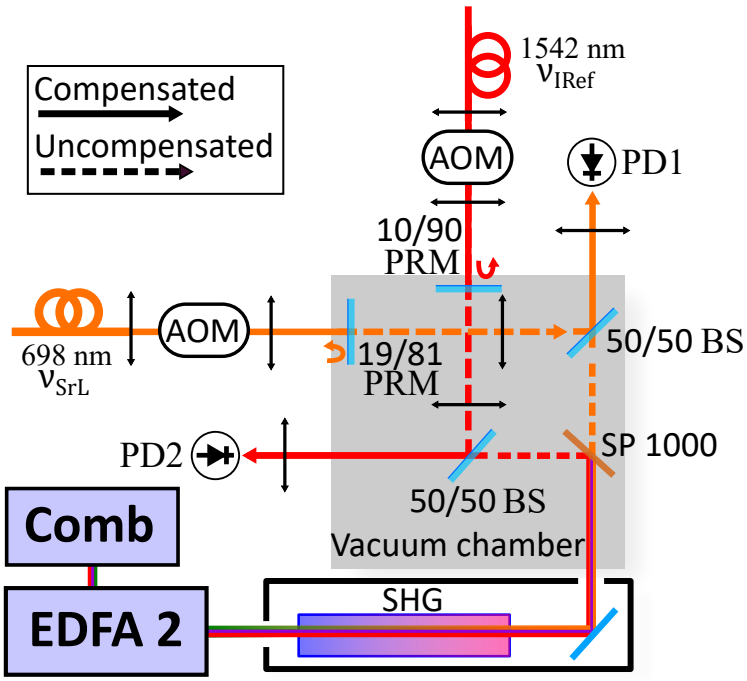

Figure 4.10: Optical setup for the ν_{IRef} at 1542 nm (master laser) spectral purity transfer to the ν_{SrL} at 698 nm (slave laser). The comb's light is split up in two with a short-pass (SP) dichroic mirror, separating the infrared and the visible light. Reflection for fiber noise compensation in partial retro-reflector mirrors (PRMs), combination with the lasers' lights for beatnote generation in beam splitters (BSs) and photodetection (PD1 and PD2) takes place individually.

As for the previous setup, we have placed the optics where the uncompensated paths are over a base plate so as to add a vacuum system in the future if necessary, as it can be seen in a real picture of the setup in Fig. 4.9. For this transfer, this implementation is even more critical due to the lack of mode-matching in the IR light and the different paths that account for a total of 15 cm of uncompensated paths in free space. Finally, after the beatnotes' detection (for M = IRef and S = SrL) and rescaling, we generate and lock the transfer beatnote according to equation 4.4, with f_{SynSr}, making the feedback to the Sr clock laser AOM.

Out-of-loop assessment

In the same way as before, we can evaluate the noise of the process via the transfer beatnote from equation 4.8 that we express as:

$$N_{\mathrm{IRef}}^{(2,2)} \cdot f_{\mathrm{t}}^{(2)} = \mathrm{sign}_{\mathrm{IRef}}^{(2,2)} \cdot f_{\mathrm{IRef}}^{(2,2)} - \frac{N_{\mathrm{IRef}}^{(2,2)}}{N_{\mathrm{SrL}}^{(2,2)}} \cdot \mathrm{sign}_{\mathrm{SrL}}^{(2,2)} \cdot f_{\mathrm{SrL}}^{(2,2)} \tag{4.16}$$

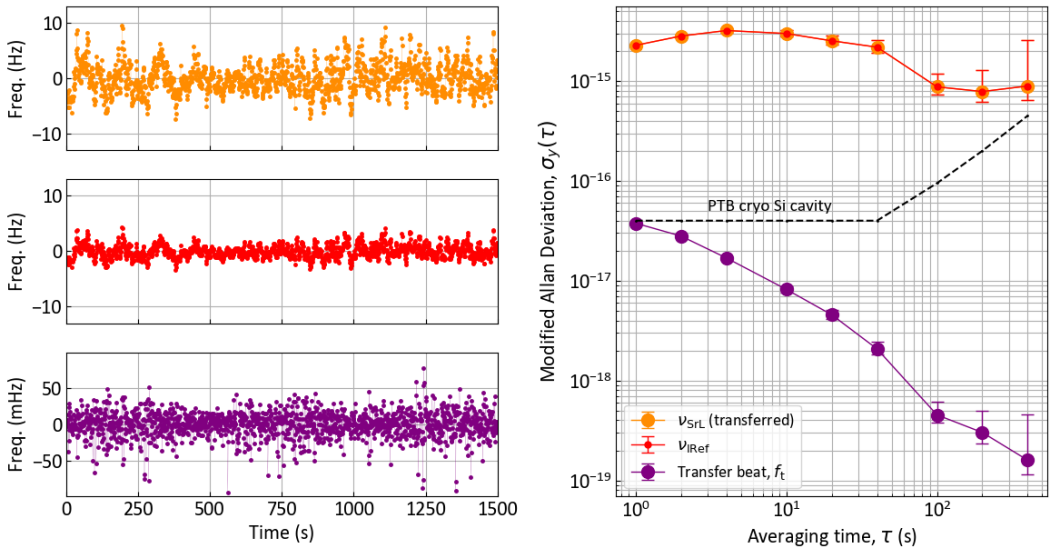

Figure 4.11: Single-branch spectral purity transfer from ν_{IRef} at 1542 nm to ν_{SrL} at 698 nm (red and orange curves). The resulting stability around $3 \cdot 10^{-17}$ at 1 s (purple curve), includes the contribution of the transfer by the first comb, and the contribution of the readout by the second comb. The black dash lines indices the best laser stability demonstrated to date [49]. Dead-time-free frequency counter set in Lambda mode.

The stability plot derived from the former equation is limited at $3 \cdot 10^{-17}$ at 1 s, averaging down rapidly, as shown in the purple curve of Fig. 4.11. Since the two combs are independent we could assume a $\sqrt{2}$ reduction instability but still there are some unidentified noises that prevent us for reaching the 10^{-18} level. Putting the vacuum chamber in place is a very good candidate to push the limit forward. This level of performance is sufficient for the current clock lasers operated at SYRTE but it must be improved to be compatible with the ongoing research on a new ultrastable cavity and on a source stabilized to spectral holes at SYRTE with an expected flicker floor noise in the low 10^{-17}.

4.3.3 Double single-branch: from 1062 nm to 698 nm

We want to transfer the stability from ν_{HgL} to ν_{SrL} directly not only to benefit from the better stability of the Hg ultrastable cavity at 1062.5 nm but also to correlate the frequency noise of both sources at Fourier frequencies < 100 Hz so as to enable Dick-free simultaneous interrogation of Sr and Hg optical lattice clocks as it will shown in the next section. We implement a transfer involving a recombination of the two single-branch transfer beatnotes, as shown in Fig. 4.5 for $\nu_{\mathrm{L1}} = \nu_{\mathrm{HgL}}$ (master) and $\nu_{\mathrm{L3}} = \nu_{\mathrm{SrL}}$ (slave). This approach simplifies the locking procedure with no intermediate lock to the IRef laser via de Er:fiber 1 OFC and eliminates the differential noise from the optical amplifiers, at the cost of using a third laser in the process ($\nu_{\mathrm{L2}} = \nu_{\mathrm{IRef}}$).

We generate the two transfer beatnotes from each of the single branches implemented (EDFA 1 and EDFA 2 outputs) following equation 4.2:

$$\begin{aligned} f_{\mathrm{t}}^{(1,1)} &= \frac{\mathrm{sign}_{\mathrm{IRef}}^{(1,1)} \cdot f_{\mathrm{IRef}}^{(1,1)}}{M_{\mathrm{IRef}}^{(1,1)}} - \frac{\mathrm{sign}_{\mathrm{HgL}}^{(1,1)} \cdot f_{\mathrm{HgL}}^{(1,1)}}{M_{\mathrm{HgL}}^{(1,1)}} = \frac{\nu_{\mathrm{IRef}}}{M_{\mathrm{IRef}}^{(1,1)}} - \frac{\nu_{\mathrm{HgL}}}{M_{\mathrm{HgL}}^{(1,1)}} + \varepsilon_{\mathrm{rep}}^{(1,1)} \cdot f_{\mathrm{rep}}^{(1)} + \beta^{(1,1)} \\ f_{\mathrm{t}}^{(1,2)} &= \frac{\mathrm{sign}_{\mathrm{IRef}}^{(1,2)} \cdot f_{\mathrm{IRef}}^{(1,2)}}{M_{\mathrm{IRef}}^{(1,2)}} - \frac{\mathrm{sign}_{\mathrm{SrL}}^{(1,2)} \cdot f_{\mathrm{SrL}}^{(1,2)}}{M_{\mathrm{HgL}}^{(1,2)}} = \frac{\nu_{\mathrm{IRef}}}{M_{\mathrm{IRef}}^{(1,2)}} - \frac{\nu_{\mathrm{SrL}}}{M_{\mathrm{SrL}}^{(1,2)}} + \varepsilon_{\mathrm{rep}}^{(1,2)} \cdot f_{\mathrm{rep}}^{(1)} + \beta^{(1,2)} \end{aligned} \tag{4.17}$$

Thereby, the transfer beatnote that is used to make the feedback and correct the ν_{SrL} (slave laser) is:

$$f_{\mathrm{t}}^{(1)} = f_{\mathrm{t}}^{(1,2)} - f_{\mathrm{t}}^{(1,1)} \frac{\nu_{\mathrm{HgL}}}{M_{\mathrm{HgL}}^{(1,1)}} - \frac{\nu_{\mathrm{SrL}}}{M_{\mathrm{SrL}}^{(1,2)}} + \beta_{\mathrm{tot}}^{(1)} = f_{\mathrm{SynSr}} \tag{4.18}$$

where we have neglected the $\varepsilon_{\mathrm{rep}}^{(1,1)}$ and $\varepsilon_{\mathrm{rep}}^{(1,2)}$ terms which reject the $f_{\mathrm{rep}}^{(1)}$ at the 10^{-6}, and $\beta_{\mathrm{tot}}^{(1)} = \beta^{(1,2)} - \beta^{(1,1)}$ accounts for the respective residual comb output noises. Note that is crucial to rescale ν_{IRef} by exactly the same or very close M_{IRef} so as to eliminate it as well as possible when mixing the two beatnotes.

Out-of-loop assessment

The final transfer beatnote in the readout comb is obtained in the same way as for the transfer comb (equation 4.18). Subtracting equation 4.15 from 4.16, the final beatnote is given by:

$$\frac{N_{\mathrm{HgL}}^{(2,1)}}{N_{\mathrm{IRef}}^{(2,1)}} \cdot f_{\mathrm{t}}^{(2)} = f_{\mathrm{HgL}}^{(2,1)} - \frac{N_{\mathrm{HgL}}^{(2,1)}}{N_{\mathrm{IRef}}^{(2,1)}} \cdot \frac{N_{\mathrm{IRef}}^{(2,2)}}{N_{\mathrm{SrL}}^{(2,2)}} f_{\mathrm{SrL}}^{(2,2)} \tag{4.19}$$

where again the rescaling is performed by post-process.

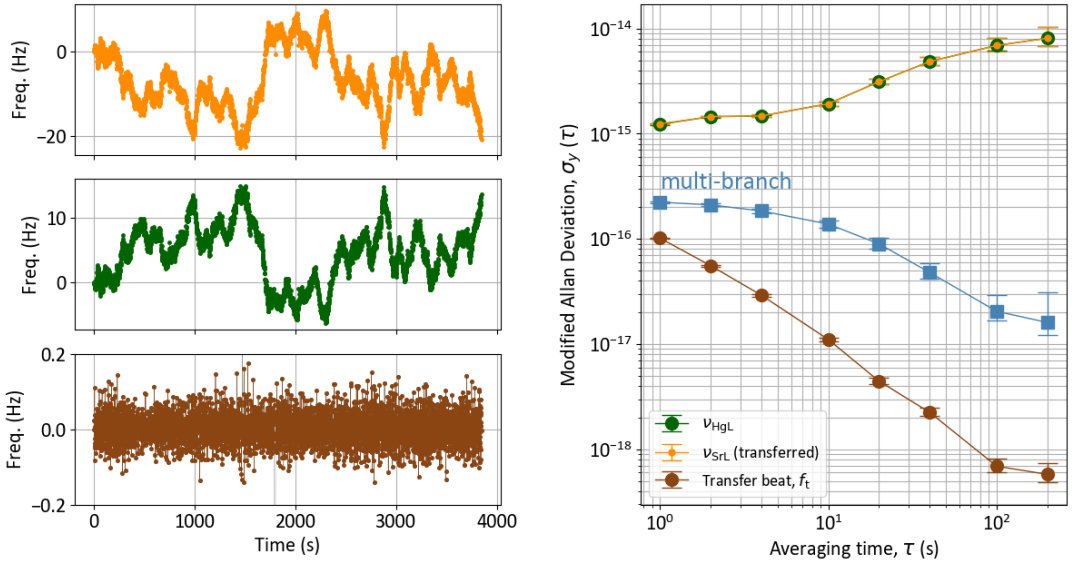

Figure 4.12: Dual single-branch spectral purity transfer from ν_{HgL} at 1062.5 nm to ν_{SrL} at 698 nm (green and orange curves). The transferred noise is of $1 \cdot 10^{-16}$ at 1 s (brown curve), a factor two lower than its multi-branch counterpart (blue curve). Dead-time-free frequency counter set in Lambda mode.

The green and orange curves in Fig. 4.12 are the Hg and Sr beatnotes on the readout comb when the transfer is performed, which show the same stability as they are now correlated. Once they are recombined and post-processed, the fractional stability obtained for the transfer beatnote (brown curve), is slightly below 10^{-16} at 1 s. There is a factor two improvement with respect to the former multi-branch approach (blue curve) especially during the first seconds where the transfer beatnote did not average due to the differential noise from path length fluctuations.

The result is expected to be limited by the worst of the two single-branch setups (the $\nu_{\mathrm{SrL}} \rightarrow \nu_{\mathrm{IRef}}$ with a relative instability of $3 \cdot 10^{-17}$ at 1 s) if the former ones would been carried out simultaneously. We attribute the stability degradation to a cross-talk in the

stabilization of the ten fibers, i.e. five per comb, necessary to yield enough beams to lock the two combs and form the eight out of-loop beatnotes (instead of four). The propagation noise is detected by a unique photodiode, with all beats in the range $0-150\,\mathrm{MHz}$, and despite splitting and filtering, there is a competition in some RF amplifiers between some of the beatnotes. Moreover, the ultrastable light to lock both fiber-based OFCs and to form the other four 1542 nm out-of-loop beatnotes is coming from the same master IR laser (ν_{IRef}), and the optical power becomes a limitation of the SNRs.

A new setup is under development where a second IR slave laser will be also locked to the master laser to distribute the light, increasing the optical power in each of the branches, and with dedicated PDs for each of the fiber noise in-loop beatnotes needed. Even though, the result obtained was still compatible with the ν_{HgL} (frequency floor at $4\cdot10^{-16}$) stability and the transfer to the Sr clock laser was achieved successfully.

4.4 Direct application to optical lattice clocks

Optical atomic clocks are limited by the sampling of the residual frequency noise of the USL probing the narrow atomic resonance, i.e. the Dick effect [35], due to its cyclic interrogation as described in subsection 1.1.3. This degradation of stability slows down the characterization of the systematic effects and complicates the accuracy evaluation of the clock. As a consequence the comparison between the Sr and Hg OLCs at SYRTE is limited by their clock lasers and their corresponding Dick effects at the $1\cdot10^{-15}/\sqrt{\tau}$ level.

Thanks to the double single-branch setup implemented between the two distant clock lasers, ν_{HgL} and ν_{SrL}, the OLCs experience the same Dick noise when the two atomic samples are probed synchronously and with the same type of pulses. Therefore the Dick effect is rejected when we form the ratio between the clocks.

On the pink curve of Fig. 4.13 we see a local comparison of the two clocks, limited at $1.1\cdot10^{-15}/\sqrt{\tau}$. When the transfer is performed (with a synchronized cycle operation) it is reduced to $4.6\cdot10^{-16}/\sqrt{\tau}$, and the resolution of the comparison improves by more than a factor 2.

The limit of this "virtual" elimination of the Dick effect is not only given by the instability of the transfer itself (at $1\cdot10^{-16}$ at 1 s) but also by the residual uncompensated phase noise on their way to the atom's interrogation such as propagation noise, and vibrational and thermal noise present in the two consecutive doubling cavities as it is the case of the Hg laser.

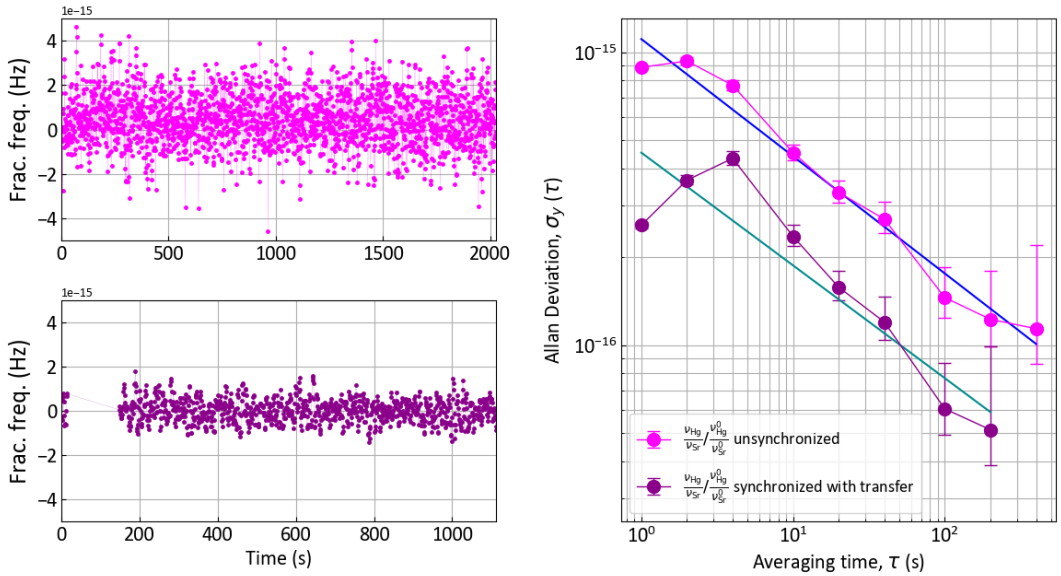

Figure 4.13: Normalized optical ratio $\nu_{\mathrm{Hg}}/\nu_{\mathrm{Sr}}$ between the Hg and Sr OLCs. The darker color shows the improvement when the ν_{HgL} is transferred to the ν_{SrL} and the measurement is synchronized.

4.5 Conclusion

Along this chapter different schemes have been implemented to carry out spectral purity transfers among four different wavelengths. We have focused on the lasers probing the Hg and Sr optical lattice clocks and the IRef laser required for the continental comparisons via an optical fiber link, leaving the setup ready for a future transfer to the 1160 nm used in the SHB experiment.

The multi-branch configuration is the easiest and most flexible approach when the transfer from the ultrastable laser (master) is meant to be provided to several lasers featuring very different frequencies. It allows independent optimization of the optical beatnotes' power, and therefore of their signal to noise ratios, by using dedicated optical amplifiers and high non-linear fibers (even followed by a frequency doubling stages in some cases). However, an exquisite propagation noise compensation of the lasers involved is required and inevitable uncompensated paths must be minimized at their best so as to surpass the 10^{-17} at 1 s stability level.

After evaluating the initial all-fibered and multi-branch setup, we implemented two separated single-branch ones, putting in free space the critical (uncompensated) paths, overlapping the cw laser fields with the comb light and using the same photodetector when possible. Doing this, the excess noise that mainly results from differential path length fluctuations between the pair of lasers at play (master and slave) and from the

beatnote detection was reduced. Hence, the preliminary multi-branch transfer in the low 10^{-16} ($\nu_{\mathrm{HgL}} \rightarrow \nu_{\mathrm{SrL}}$) was greatly improved to the mid 10^{-18} for the single-branch $\nu_{\mathrm{IRef}} \rightarrow \nu_{\mathrm{HgL}}$ transfer, where further improvement is expected when the setups are set under vacuum.

The single-branch transferred instabilities achieved are more than one order of magnitude below the best current optical atomic clocks published instabilities and still below the projected ones (in the low 10^{-17}) for next-generation optical clocks using clock lasers stabilized to cryogenic optical cavities.

Additionally, we have shown the potential of this technique at the time of comparing two synchronously-probed optical clocks, where the noise averages down faster due to the Dick effect noise rejection, reducing significantly the time needed for the characterization of their systematic effects. In our particular case, this was performed by the dual single-branch transfer, which simplifies the locking procedure as no intermediate lock to the IRef laser is needed. The stability of the Hg and Sr optical lattice clock's comparison reached $4.6 \cdot 10^{-16}/\sqrt{\tau}$, which improved by more than a factor two the comparison without any transfer.

Conclusion

Through this manuscript we have characterized the sources of noise involved in the process of measuring and comparing optical frequency standards and how they are connected to the rest of the microwave atomic clocks operated at SYRTE. Along with all these optical clocks are the necessary ultrastable local oscillators to interrogate their atomic or molecular metrological transitions (Sr, Hg, I_2 or Eu^{3+}), which are connected via the operational frequency chain with the OFCs at its heart.

A strong specificity of the frequency combs in operation at LNE-SYRTE, Er:fiber and Ti:sa, is the narrow linewidth regime achieved by phase locking them to ultranarrow optical infrared references. To do so, a control of the two degrees of freedom of the comb must be implemented. On the one hand, the offset frequency, f_0, is mixed out of all the beatnotes between the comb and the various cw sources involved, translating the comb to a virtual f_0-free comb. On the other hand, the repetition rate, f_{rep}, is directly locked to the cw optical source used as a reference and, therefore, features the same fractional stability. Considering the large bandwidth of these phase-lock loops ($> 800\,\mathrm{kHz}$), we transfer to all the longitudinal modes or teeth of the comb the spectral purity from the USL used (at 1542 nm for the Er:fiber comb and 1062 nm for the Ti:sa one). These tight phase locks ease other lasers' measurements and set the stability floor of the measurements performed with these OFCs, limited by their respective reference USLs (in the case of negligible optical and electronic noise sources). Moreover, and due to the increased demand on optical frequencies measurements, an auto-relocking system allows us to rearm the PLL of the comb automatically and to monitor and control the lock of the comb remotely.

Every component or device that is forming part of the frequency chain must be carefully evaluated to ensure that the stability of the signals under test is preserved. In the microwave domain, the measurement of absolute frequencies is based on the comparison between the harmonics of the repetition rate of the comb and the UMR. Given the very low noise of these signals (in the μHz range), the key element is the multiplication of the comparison result by 200 before counting by the frequency counter, in order to beat the resolution of this latter. We verified that no element is limiting the stability's chain and that the microwave noise floor is given by the combined photodetection and amplification noises of the microwave signals involved ($5 \cdot 10^{-15}$ at 1 s), the UMR it-

self ($1-2\cdot10^{-15}$ at 1 s, which is the state of the art in the microwave domain) and the microwave link bringing the UMR to our laboratory ($1-2\cdot10^{-15}$ at 1 s) that results in a total instability of $6-7\cdot10^{-15}$ at 1 s. Likewise, in the optical domain, the use of narrow band-pass filters rejects a large fraction of the white phase noise and are especially useful when running combs in the narrow linewidth regime. Nonetheless, filters introduce a frequency-dependent phase shift, which would turn into a frequency offset in case of drift of the frequency under measurement. The drift of the lasers being compared must thereby be considered, and we demonstrated that a maximum fractional drift of $2\cdot10^{-15}\,\mathrm{s}^{-1}$ is tolerable to ensure accuracy below the 10^{-18} level. Equally important is the noise added in the optical domain, before photodetection of the beatnotes. The noise of every single comb output must be characterized as well as the laser that is meant to be beaten and measured by the comb. We have carefully considered technical noise sources, such as 60-cm uncompensated piece of optical fiber (a few 10^{-16} at 1 s of residual instability), residual free-space propagation noise of less than 20 cm (a few 10^{-17} at 1 s), and the noise added by the optical amplifier of the comb itself (at most a few 10^{-17} at 1 s, from results obtained very recently).

We have measured the stability floors present in our chain when measuring and comparing the local oscillators. On the one hand, we demonstrated that in the microwave domain the stability is limited in the mid 10^{-15} at 1 s by either the photodetection of f_{rep} and its harmonics or the amplification of the microwave signals. This led to a good understanding of the behavior of the stability curves of the comparisons UMR versus repetition rate with one comb, where the stability at one second (typically $7\cdot10^{-15}$ in Pi mode) is not due to the oscillators being compared but rather to the aforementioned effects. On the other hand, the optical limit is due to the residual fiber noise or uncompensated optical paths between the laser source and the beatnote detection, and not by the source itself.

Additionally, we have assessed the accuracy of the measurements by building up two other frequency chains attached to independent combs of different technology and generation. We measured simultaneously the frequencies corresponding to the Sr and Hg clock lasers and the IRef laser, and compared them by pairs. In the microwave domain, a resolution below the 10^{-16} level was achieved in less than one hour while the 10^{-18} range was surpassed when performing optical ratios after $10-20$ minutes of integration time. As a result, the optical frequency chain attached to the second Er:fiber comb has become a permanent back-up frequency chain for operational measurements, making the system much more robust and reliable.

There is an ongoing development around the globe of next-generation lasers to be used as local oscillators for probing cold atoms in optical clocks with instabilities below 10^{-16} at short time scales. Since these ultrastable lasers are currently built in the infrared domain, far away from the optical atomic transitions targeted, spectral purity transfer with added noise below 10^{-17} is required. We have performed different trans-

fers among four different wavelengths by implementing the transfer oscillator method, which allows the elimination of the OFC parameters and therefore the comb noise. After a first evaluation in a multi-branch configuration, i.e. involving two distinct comb outputs, we were limited with a relative instability of $2.2 \cdot 10^{-16}$ at 1 s for a transfer between the Hg and Sr clock lasers (1062 nm and 698 nm). In multi-branch, differential effects of the comb can not, by definition, be eliminated: even though the noise of the optical amplifier is negligible, the propagation noise of the comb light until the recombination point with the cw lasers at play (master and slave(s)) can not be compensated, which leads to unavoidable noise. The natural next step was to implement single branch approaches. In spite of being less flexible as it does not allow independent optical power optimization of each comb wavelength, the single-branch approach suppresses the influence of differential path length fluctuations in the comb light since it comes from a unique output. However, one must be sure that none of the two SNRs of the beatnotes at play are limiting the transfer of stability. Thereby, all our beatnotes' SNRs were higher than 38 dB in a 1 kHz bandwidth since in the presence of white phase noise they set a limit around $1 \cdot 10^{-18}$ at 1 s.

Every noise source such as phase lock-related cycle slips, narrow tracking bandwidths, imperfect mode matching, etc., has to be warily considered when the goal is to reach transfer processes with fractional stabilities in the 10^{-18} level. To reduce noise sensitivity due to external perturbations, we implemented in free space the critical (uncompensated) part of the optical setup, leaving it ready to be put under vacuum if necessary. The uncompensated path, of only a few centimeters, is between the retro-reflection plane of the cw lasers, i.e. the reference plane of the interferometers compensating the propagation noise, and the recombination of the cw beam(s) with the comb light. Moreover, we overlap the cw laser beams' paths, retro-reflect them in the same partial reflective mirror (for Doppler cancellation), and even detect the beatnotes in the same photodiode when possible. Doing this we have demonstrated transfer stabilities of $8 \cdot 10^{-18}$ and $3 \cdot 10^{-17}$ at 1 s from the IRef laser (1542 nm) to the Hg and Sr clock lasers, respectively.

The last part of this PhD research work was devoted to a direct application of the spectral purity transfer between the Hg and Sr clock lasers with the design of a double single-branch scheme. The comparison's resolution of the two optical lattice clocks was preliminary improved by more than a factor two due to the Dick effect rejection, helping to characterize faster the systematic effects of the two clocks. Furthermore, a new ultrastable IR long cavity is currently under development, which aims at a flicker floor noise in the 10^{-17} range and whose main objective is to bring the optical clocks at the QPN limit. With this coming master oscillator, that will also seed the French fiber link REFIMEVE+, when only one of the OLCs is probed (for instance to connect it to the other European clocks), then the stability will be considerably improved. It will be expected to be in the low 10^{-16} at 1 s (one order of magnitude lower) since its

local oscillator will benefit from the spectral properties of the new USL at 1542 nm. The long-term goal is to reference all SYRTE atomic frequency standards to this unique oscillator, and start developing the first prototypes of optical timescales.

Conclusion

Dans ce manuscrit, nous avons caractérisé les sources de bruits impliquées dans le processus de mesure et de comparaison d'étalons de fréquence optique, et leur connexion avec les horloges atomiques micro-ondes en opération au SYRTE. Toutes ces horloges optiques sont nécessairement accompagnées de leur oscillateur local respectif, afin d'interroger leur transition atomique ou moléculaire de référence (Sr, Hg, I_2 ou Eu^{3+}). Ces oscillateurs sont connectés via la chaîne de fréquence opérationnelle, au cœur de laquelle se situe les OFCs.

Une spécificité importante des peignes de fréquence optiques en opération au LNE-SYRTE, qu'il soient basé sur un laser titane-Saphir ou un laser erbium, réside dans le fait qu'ils sont amenés dans un régime de raie étroite en les asservissant en phase sur une référence optique ou infrarouge ultrastable. Pour ce faire, le contrôle des deux degrés de liberté du peigne doit être mis en œuvre. D'une part, le décalage de fréquence, f_0, est déduit des battement de fréquences entre le peigne et les sources entretenues impliquées, translatant le peigne vers un peigne virtuel, libre de f_0. D'autre part, le taux de répétition, f_{rep}, est directement vérrouillé sur la source optique continue utilisée comme référence, et ainsi, dispose d'une même stabilité fractionnelle identique. De cette manière, nous transférons la pureté spectrale de l'USL utilisé à tous les modes longitudinaux, ou dents du peigne (à 1542 nm pour le peigne Er:fibre et à 1062 nm pour le Ti:Sa). Ces verrouillages de phase serrés rendent aisées les mesures des autres lasers et fixent le plancher de stabilité des mesures par peigne de fréquence, limité par leur USLs de référence respectifs dans le cas où les bruits optiques/électroniques sont négligeables. De plus, du fait de la demande croissante des mesures de fréquences optiques, un système automatique de reverrouillage permet de réarmer les PLL du peigne automatiquement et de surveiller et contrôler le verrouillage du peigne à distance.

Chacun des composants ou appareils inclus dans la chaîne de fréquences doit être soigneusement évaluée pour s'assurer que la stabilité des signaux testés est préservée. Dans le domaine des micro-ondes, la mesure absolue de fréquences repose sur la comparaison entre les harmoniques du taux de répétition du peigne et l'UMR. Étant donné le niveau de bruit très bas de ces signaux (de l'ordre du μHz), l'élément clé est la multiplication du résultat de la comparaison d'un facteur 200 avant mesure par le compteur de fréquence, afin de surpasser le plancher de résolution de celui-ci. Nous avons vérifié

qu'aucun élément ne limitait la chaîne de fréquences, et que le plancher de bruit micro-ondes était donné par la combinaison des bruits de photodétection et d'amplification des signaux micro-ondes en présence ($5 \cdot 10^{-15}$ à 1 s), de l'UMR lui-même ($1 - 2 \cdot 10^{-15}$ à 1 s, ce qui est l'état de l'art dans le domaine des micro-ondes) et du lien micro-ondes entre l'UMR et notre laboratoire ($1 - 2 \cdot 10^{-15}$ à 1 s). Il en résulte une instabilité totale de $6 - 7 \cdot 10^{-15}$ à 1 s. De la même manière, dans le domaine optique, l'utilisation d'un filtre passe bande étroit permet de rejeter une large partie du bruit blanc de phase, ce qui est particulièrement légitime d'implémenter pour les peignes opérant dans le régime de bande étroite. En revanche, ces filtres introduisent un déphasage dépendant de la fréquence, qui lors de la mesure d'une fréquence présentant une dérive induirait un décalage de fréquence. La dérive des lasers comparés doit ainsi être considérée, et nous avons démontré qu'une dérive fractionnelle maximale de $2 \cdot 10^{-15}\,\mathrm{s}^{-1}$ était tolérable pour assurer une précision en deça du 10^{-18}. Le bruit ajouté dans le domaine optique, avant photodetection et amplification, est d'importance égale. Le bruit de chacune des sorties des peignes doit être caractérisé aussi bien que le laser destiné à produire le battement mesuré par le peigne. Nous avons soigneusement considéré les sources de bruits techniques, tel qu'une partie de fibre optique non-compensée de 60 cm (quelque 10^{-16} à 1 s d'instabilité résiduelle), le bruit résiduel de propagation en espace libre de moins de 20 cm (quelque 10^{-17} à 1 s), et le bruit ajouté par les amplificateurs optiques du peigne lui-même (au plus quelque 10^{-17} à 1 s, d'après les résultats les plus récents).

Nous avons mesuré les planchers de stabilité présents dans nos chaîne lors de la mesure et de la comparaison des oscillateurs locaux. D'une part, nous avons démontré que dans le domaine micro-onde, la stabilité est limitée dans le mi 10^{-15} à 1 s, aussi bien par la photodétection de f_{rep} et de ses harmonique, que par l'amplification des signaux micro-onde. Cela mène à une bonne compréhension des tendances observées sur les courbes de stabilité des comparaisons d'UMR contre le taux de répétition d'un peigne, où la stabilité à une seconde (typiquement $7 \cdot 10^{-15}$ en mode Pi) n'es pas due à l'UMR lui-même mais plutôt aux 2 effets mentionnés ci-dessus. D'autre part, la limite optique est due au bruit résiduel des fibres, ou à la non-compensation des chemins optiques entre la source laser et la détection du battement, et non par la source elle-même.

De plus, afin d'être exhaustif, nous avons évalué la précision du système entier, en mettant en place deux autres chaînes de fréquences chacune associé à son propre peigne, de différentes technologies et générations. Les fréquences correspondant aux lasers des horloges Sr et Hg et au laser IRef ont été mesurées simultanément, et nous les avons comparées en les appairant. Dans le domaine micro-onde, une résolution sous le 10^{-16} est atteinte en moins d'une heure d'intégration, contre 10^{-18} en $10 - 20$ minutes pour la réalisation de ratios optiques. En conséquence, la chaîne de fréquence optique attachée au second peigne Er:fibre est devenue une solution de secours permanente lors des mesures opérationnelles, rendant le système plus robuste et plus fiable.

La prochaine génération de lasers utilisés en tant qu'oscillateurs locaux pour son-

der les atomes piégés des horloges optiques est actuellement en développement dans le monde, et présentent des instabilités au dessous du 10^{-16} à court terme. Puisque ces lasers ultrastables sont actuellement conçus dans le domaine infrarouge, loin des transitions optiques visées, des techniques de transfert de pureté spectrale avec des instabilités inférieures à 10^{-17} à toutes les échelles de temps sont requises. Nous avons menés différents transferts impliquant quatre longueurs d'onde différentes, en mettant en place la methode de l'oscillateur de transfert, qui permet l'élimination de tous les paramètres du peigne et par conséquence, son bruit. Une première évaluation en configuration multibranche, c'est à dire impliquant deux sorties de peigne distinctes, nous a limité à l'instabilité relative de $2.2 \cdot 10^{-16}$ à 1 s pour un transfert entre les lasers d'horloges Hg et Sr (1062 nm et 698 nm). En configuration multi-branche, les effets différentiels des peignes ne peuvent, par définition être éliminés : même lorsque le bruit de l'amplificateur optique est négligeable, la propagation de la lumière du peigne jusqu'au point de recombinaison avec les lasers entretenus en jeu (maître et esclave(s)) ne peut être compensée, ce qui induit inévitablement du bruit. Naturellement, l'étape suivante était la mise en place d'un système à une seule branche. Malgré la moindre flexibilité d'un tel système, qui ne permet pas d'optimiser les puissances optiques de chaque longueur d'onde du peigne indépendamment, l'approche à une seule branche supprime l'influence des fluctuations différentielles des longueurs de chemin optique du peigne puisqu'une seule sortie est en jeu. En revanche, il est nécessaire de s'assurer que le rapport signal sur bruit de chaque battement en présence ne limitent pas le transfert de stabilité (38 dB dans une bande de 1 kHz permet de s'assurer que le bruit blanc de phase ne limite pas les mesure au delà de quelques $1 \cdot 10^{-18}$ à 1 s).

Chaque source de bruit, tels que que ceux associés aux glissement de cycle du verrouillage de fréquence, à la bande étroite suivie, ou encore aux désaccords de mode doivent être considérés prudemment lorsque l'objectif est de parvenir à un transfert démontrant des des stabilités de l'ordre de 10^{-18}. Pour réduire la sensibilité aux bruits due aux perturbations extérieures, la partie critique (non compensée) du système a été mise en place en espace libre, prête à être mises sous vide si nécessaire. Cette partie non compensée, seulement quelques cm, se situe entre le plan de rétro-réflexion des lasers entretenus, c'est-à-dire le plan de référence du ou des interféromètres compensant le bruit de propagation, et la recombinaison du ou des faisceaux continus avec la lumière du peigne. De plus, nous avons superposées les trajectoires des faisceaux entretenus, en les rétro-réfléchissant sur le même miroir partiellement réfléchissant (afin d'annuler l'effet Doppler) et aussi, lorsque cela est possible réalisé la détection de leurs battements sur une même photodiode. Ce faisant, nous avons démontré des instabilités de transfert du laser IRef (1542 nm) vers les lasers d'horloge Hg et Sr de $8 \cdot 10^{-18}$ et de $3 \cdot 10^{-17}$ à 1 s respectivement.

La dernière partie de ce manuscrit de thèse nous a permis de présenter une application directe de la méthode de transfert de pureté spectrale entre les lasers d'horloge

Hg et Sr via un double schéma à branche unique. La résolution de la comparaison entre les deux horloges à réseau optique a été préalablement améliorées de plus d'un facteur deux en raison du rejet de l'effet Dick, ce qui permet d'accélérer la caractérisation de leurs effets systématiques. En outre, une nouvelle cavité longue ultrastable infrarouge est actuellement en cours de développement, et vise à obtenir un bruit de l'ordre de 10^{-17}, et dont l'objectif principal est d'amener les horloges optiques à la limite du bruit de projection quantique. Avec ce futur oscillateur maître, qui servira de référence au réseau fibré ultrastable français REFIMEVE+, lorsqu'une seule des OLC sera sondé (par exemple pour la connecter aux autres horloges européennes), la stabilité sera considérablement améliorée puisque l'oscillateur local de cette horloge bénéficiera des propriétés spectrales du nouveau laser 1542 nm. L'objectif à long terme est de référencer tous les étalons de fréquence atomique du SYRTE à cet oscillateur unique et commencer à développer les premiers prototypes d'échelles de temps optiques.

Conclusiones

A lo largo del presente manuscrito hemos caracterizado las fuentes de ruido involucradas en el proceso de medida y comparación de patrones ópticos de frecuencia, y cómo estos son conectados con el resto de relojes atómicos de microondas operados en el SYRTE. Todos estos relojes ópticos se encuentran necesariamente acompañados de sus osciladores locales ultra-estables respectivos, con el fin de interrogar sus transiciones atómicas o moleculares (Sr, Hg, I_2 or Eu^{3+}). Estos osciladores, a su vez, se encuentran interconectados a través de la cadena de frecuencias operacional que alberga en su núcleo a los OFCs.

Una particularidad importante de los peines de frecuencias ópticas operados en el LNE-SYRTE, Er:fiber y Ti:sa, reside en el hecho de que se encuentran en el llamado régimen de ancho de línea estrecha en donde son anclados en fase a referencias ópticas en el infrarrojo. Para ello, es imprescindible el control de los dos grados de libertad del peine. Por un lado, la frecuencia de desplazamiento, f_0, es eliminada en todo batido heterodino entre el peine y las diferentes fuentes láser de onda continua involucradas, convirtiéndole así en un peine virtual libre de desplazamiento. Por otro lado, la frecuencia de repetición, f_{rep}, es anclada en fase directamente a la fuente de onda continua usada como referencia y, por tanto, presentará una estabilidad relativa idéntica. Teniendo en consideración el alto ancho de banda del lazo de anclado en fase ($> 800\,\mathrm{kHz}$), somos capaces de transferir la pureza espectral del USL utilizado a todos los modos longitudinales o dientes del peine (en 1542 nm para el peine de Er:fiber y en 1062 nm para el de Ti:sa). Estos anclados en fase facilitan las medidas de otros láseres y establecen el suelo de estabilidad de los OFCs, limitados por sus respectivos USLs (en caso de fuentes de ruido ópticas y/o electrónicas despreciables). Además, y debido al aumento en la demanda de mediciones de frecuencias ópticas, un sistema de anclado automático ha sido implementado, el cual nos permite rearmar el lazo de seguimiento en fase del peine de manera automática, así como monitorizar y controlar el mismo de manera remota.

Todo componente o dispositivo que forma parte de la cadena de frecuencias debe ser cuidadosamente evaluado para asegurar que la estabilidad de las señales bajo evaluación sea preservada. En el dominio de las microondas, la medida de frecuencias absolutas se basa en la comparación entre los armónicos de la frecuencia de repetición del peine y la UMR. Dado el bajo ruido de ambas señales (en el rango de μHz), un paso clave es

la multiplicación por 200 del resultado de dicha comparación, de forma que el ruido de la señal resultante esté por encima de la resolución del contador de frecuencias. Hemos verificado que ningún elemento limita la estabilidad de cadena en sí y que el ruido límite de microondas está dado por el ruido combinado de foto-detección y amplificación de las señales de microondas involucradas ($5 \cdot 10^{-15}$ a 1 s), de la propia UMR ($1-2 \cdot 10^{-15}$ a 1 s, que representa el estado del arte en el dominio de las microondas) y del enlace de microondas entre la UMR y nuestro laboratorio ($1-2 \cdot 10^{-15}$ a 1 s), que resulta en una inestabilidad total de $6-7 \cdot 10^{-15}$ a 1 s. Asimismo, en el dominio óptico, el uso de filtros pasa banda estrechos elimina una buena parte del ruido blanco de fase y son especialmente útiles cuando se manejan peines en el régimen de ancho de línea estrecha. No obstante, estos filtros introducen un cambio en fase dependiente de la frecuencia, el cual se traduciría en un salto en frecuencia en caso de deriva de la frecuencia bajo medición. Es por ello que la deriva de los láseres comparados debe ser considerada, habiéndose demostrado que una deriva relativa máxima de $2 \cdot 10^{-15}\,\mathrm{s}^{-1}$ es tolerable para asegurar una exactitud por debajo de 10^{-18}. El ruido añadido en el dominio óptico, antes de la foto-detección y amplificación, es de igual importancia. El ruido de toda salida óptica del peine deber ser caracterizado así como el láser que será batido y medido por el peine. Hemos considerado cuidadosamente las fuentes de ruido técnico tales como las debidas a una porción de 60 cm de fibra óptica no compensada (con una inestabilidad residual en la parte baja de 10^{-16} a 1 s), ruido residual de propagación en aire en menos de 20 cm (en la parte baja de 10^{-17} a 1 s), e incluso posible ruido añadido por los amplificadores ópticos del propio peine (en partes bajas de 10^{-17} a 1 s, resultado obtenido recientemente).

Hemos medido los límites de estabilidad presentes en la cadena de frecuencias mediante mediciones y comparaciones de osciladores locales. Por una parte, hemos demostrado que en el dominio de las microondas la estabilidad está limitada en partes medias de 10^{-15} a 1 s, bien por la foto-detección de f_{rep} y sus armónicos o por la amplificación de las señales de microondas en juego. Lo anterior nos ha llevado a una mejor comprensión del comportamiento de las curvas de estabilidad de las comparaciones realizadas entre la UMR y la frecuencia de repetición con un peine, donde la estabilidad a un segundo (típicamente $7 \cdot 10^{-15}$ en modo Pi) no es debida a la inestabilidades de los osciladores bajo comparación sino a los efectos anteriormente citados. Por otra parte, el límite óptico es debido al ruido residual presente en la fibra o a caminos ópticos no compensados entre la fuente láser y su detección heterodina, y no por la fuente en sí.

De manera adicional hemos evaluado la exactitud de las medidas efectuadas mediante la construcción de dos nuevas cadenas de frecuencias ligadas a peines de frecuencia independientes, de diferentes tecnologías y generaciones. Hemos medido simultáneamente las frecuencias correspondientes a los láseres reloj de Sr y Hg y del láser IRef, y las hemos comparado por pares. En el dominio de las microondas, una resolución por debajo del nivel de 10^{-16} ha sido alcanzada en menos de una hora, mientras que el rango

de 10^{-18} fue sobrepasado al medir ratios ópticos tras $10-20$ minutos de tiempo de integración. Como resultado, la cadena de frecuencias ópticas correspondiente al segundo peine de Er:fiber se ha convertido en una cadena de frecuencias de respaldo permanente para medidas operacionales, aportando a todo el sistema una mayor robustez y fiabilidad.

La próxima generación de láseres utilizados como osciladores locales para la interrogación de átomos fríos en relojes ópticos está actualmente en desarrollo a nivel mundial, y estos presentan inestabilidades por debajo de 10^{-16} a corto plazo. Como estos láseres ultra-estables son en la actualidad construidos en el dominio infrarrojo, lejos de las transiciones atómicas ópticas perseguidas, técnicas de transferencia de pureza espectral con ruido añadido por debajo de 10^{-17} son requeridas. Hemos llevado a cabo transferencias distintas entre cuatro longitudes de onda diferentes mediante la implementación del método del oscilador de transferencia, el cual permite la eliminación de los parámetros del OFC y, por lo tanto, de su ruido. Tras una primera evaluación en configuración multi-rama, es decir, utilizando dos salidas ópticas diferentes del peine, nos vimos limitados por una inestabilidad relativa de $2.2 \cdot 10^{-16}$ a 1 s para una trasferencia entre los láseres reloj de Hg y Sr (1062 nm y 698 nm). En multi-rama, los efectos diferenciales del peine no pueden, por definición, ser eliminados: a pesar de que el ruido de los propios amplificadores ópticos sea despreciable, el ruido de propagación de la luz del peine hasta el punto de recombinación con los láseres de onda continua involucrados (máster y esclavo(s)) no puede ser compensado, constituyendo una fuente de ruido inevitable. El siguiente paso natural sugiere la implementación de montajes en configuración de rama-única. Estos, a pesar de ser menos flexibles, al no permitir la optimización de potencia óptica para cada longitud de onda de manera independiente, suprimen las fluctuaciones diferenciales de longitud de camino óptico de la luz del peine ya que esta proviene de una misma salida óptica. Sin embargo, uno debe de cerciorarse de que ninguno de los ratios de señal-ruido de las frecuencias batidas en cuestión limitan en estabilidad dicha transferencia. Es por ello que los SNRs de nuestros batidos superan los 38 dB, en un ancho de banda de 1 kHz, ya que en presencia de ruido blanco de fase estos niveles establecen un límite de estabilidad relativa en torno a $1 \cdot 10^{-18}$.

Todo tipo de fuentes de ruido tales como saltos de ciclos relacionados con el anclado en fase, anchos de banda estrechos en filtros mediante osciladores de seguimiento, ajuste de modos imperfecto, etc., tiene que ser escrupulosamente considerado cuando el objetivo es alcanzar procesos de transferencia con estabilidades fraccionales del orden de 10^{-18}. Para reducir al máximo la sensibilidad al ruido debido a perturbaciones externas, hemos implementado en aire la zona crítica (sin compensar) del montaje óptico, dejándolo preparado para ponerlo bajo condiciones de vacío en caso necesario. Esta parte no compensada comprende desde el plano de reflexión de los láseres de onda continua, es decir, el plano de referencia de los interferómetros usados para la compensación del ruido de propagación, y la recombinación del láser (o los láseres) con la

luz pulsada del peine. Además, superponemos los caminos ópticos de los láseres en juego, los reflejamos en el mismo espejo parcialmente reflectante, e incluso detectamos los batidos heterodinos en el mismo foto-detector siempre que es posible. Así, hemos demostrado transferencias con estabilidades de $8 \cdot 10^{-18}$ y $3 \cdot 10^{-17}$ a 1 s desde el láser IRef (1542 nm) a los láseres reloj de Hg y Sr, respectivamente.

La última parte de este trabajo de investigación doctoral ha sido consagrada a una aplicación directa de la técnica de transferencia espectral entre los láseres reloj de Hg y Sr, a través del diseño de un esquema de doble rama-única. La resolución de la comparación de los dos relojes de red óptica ha sido preliminarmente mejorada en más del doble debido a la supresión del efecto Dick, ayudando así a una caracterización más rápida de los efectos sistemáticos de ambos relojes. Además, una nueva cavidad larga ultra-estable en el IR se encuentra actualmente bajo desarrollo, la cual se espera que alcance un ruido flicker en el rango de 10^{-17}, y cuyo objetivo principal es llevar a los relojes ópticos al límite impuesto por el ruido de proyección cuántica. Con este venidero oscilador maestro, que también alimentará el enlace de fibra óptica francés REFIMEVE+, cuando uno de los OLCs sea interrogado (por ejemplo, cuando se quiera comparar con los otros relojes ópticos en Europa), su estabilidad será considerablemente mejorada. Se esperan estabilidades en partes bajas de 10^{-16} a 1 s (un orden de magnitud inferior) ya que su oscilador local se beneficiará de las propiedades espectrales del nuevo USL a 1542 nm. El objetivo a largo plazo es la referenciación de todos los patrones atómicos de frecuencia en el SYRTE a este único oscilador, y el comienzo del desarrollo de los primeros prototipos de escalas de tiempo ópticas.

Appendix A

Photodetection of an optical beatnote

Since electronics are not fast enough to follow optical cycles we must down-convert our laser frequencies into RF frequencies where the zero crossings of their cycles can be detected and counted. The only way to measure an optical frequency is to form an heterodyne beatnote between the two optical oscillators. These two can be as far as the bandwidth of the PD used allows us to detect the frequency difference. Then, we will add or subtract that difference to or from the laser we have as a reference.

The aim of this appendix is to explain where the optical beatnote comes from once is detected. First, between two very frequency-close lasers and, second, between a laser and the spectrum of an OFC.

Beatnote between two lasers

Let us express the electric field of an optical frequency from a laser as:

$$E_{\mathrm{L}}(t) = |E_{\mathrm{L}}| \exp(j\Phi_{\mathrm{L}}) \tag{A.1}$$

where $\Phi_{\mathrm{L}} = \omega_{\mathrm{L}} t - k_{\mathrm{L}} z - \phi_{\mathrm{L}}$, with E_{L} the amplitude of the field and ω_{L} its angular frequency.

At a given photodetection point, the interference, $E_{\mathrm{int}}(t)$, of two lasers of angular frequencies ω_{L1} and ω_{L2}, with E_{L1} and E_{L2} propagating in the same direction, can be formulated as:

$$E_{\mathrm{int}}(t) = E_{\mathrm{L1}}(t) + E_{\mathrm{L2}}(t) = |E_{\mathrm{L1}}| \exp(j\Phi_{\mathrm{L1}}) + |E_{\mathrm{L2}}| \exp(j\Phi_{\mathrm{L2}}) \tag{A.2}$$

Assuming $|\omega_{\mathrm{L1}} - \omega_{\mathrm{L2}}| \ll \omega_{\mathrm{L1}}, \omega_{\mathrm{L2}}$, we know that the bandwidth of the detector is inversely proportional to its time constant τ_{det}:

$$|\omega_1 - \omega_2| \ll 1/\tau_{\mathrm{det}} \ll \omega_1, \omega_2 \tag{A.3}$$

The averaged current on the photodiode over τ_{det} yields:

$$\begin{aligned} I_{\text{PD}}(t) \propto |E_{\text{int}}(t)|^2 &= ||E_{\text{L1}}|\exp(j\Phi_{\text{L1}}) + |E_{\text{L2}}|\exp(j\Phi_{\text{L2}})|^2 \\ &= E_{\text{L1}}^2 + E_{\text{L2}}^2 + 2|E_{\text{L1}}||E_{\text{L2}}|\text{Re}\{\underbrace{\exp(j(\Phi_{\text{L1}} - \Phi_{\text{L2}}))}_{\text{beatnote}}\} \end{aligned} \tag{A.4}$$

where the last term accounts for the heterodyne beatnote we were interested in.

Beatnote between one laser and an optical frequency comb

The electric field of an OFC can be written as:

$$E_{\text{OFC}}(t) = \sum_n |E_n|\exp(j\Phi_n) \tag{A.5}$$

where $\Phi_n = (n \cdot \omega_{\text{rep}} + \omega_0)t - k_n z - \phi_n$, and being ω_{rep} the angular repetition frequency of the OFC and ω_0 its CEO angular frequency.

When we beat a laser in an OFC, the combined electric fields, from equations A.1 and A.5, detected in the PD, yield:

$$\begin{aligned} I_{\text{PD}}(t) \propto |E_{\text{int}}(t)|^2 &= \left[\sum_n |E_n|\exp(j\Phi_n) + |E_{\text{L}}|\exp(j\Phi_{\text{L}})\right]^2 \\ &= \left[\sum_n |E_n|\exp(j\Phi_n) + |E_{\text{L}}|\exp(j\Phi_{\text{L}})\right] \\ &\quad \left[\sum_m |E_m|\exp(j\Phi_m) + |E_{\text{L}}|\exp(j\Phi_{\text{L}})\right]^* \end{aligned} \tag{A.6}$$

where we have changed the index of the conjugate term to m, to make sure we do not forget any term. After a bit of algebra, we get the expression:

$$\begin{aligned} I_{\text{PD}}(t) \propto &\sum_n |E_n|\exp(j\Phi_n)\sum_m |E_m^*|\exp(-j\Phi_m) + |E_{\text{L}}|\exp(j\Phi_{\text{L}})|E_{\text{L}}^*|\exp(-j\Phi_{\text{L}}) \\ &- \sum_n |E_n|\exp(j\Phi_n)|E_{\text{L}}^*|\exp(-j\Phi_{\text{L}}) - |E_{\text{L}}|\exp(j\Phi_{\text{L}})\sum_m |E_m^*|\exp(-j\Phi_m) \\ &= \sum_n E_n^2 + E_{\text{L}}^2 + \sum_{n\neq m} 2E_nE_m^*\text{Re}\{\underbrace{\exp(j(\Phi_n - \Phi_m))}_{\text{comb harmonics}}\} \\ &+ \sum_{n=m} 2E_nE_{\text{L}}^*\text{Re}\{\underbrace{\exp(j(\Phi_n - \Phi_{\text{L}}))}_{\text{beatnotes}}\} \end{aligned} \tag{A.7}$$

In this last equation we can clearly see the term that accounts for the possible beatnotes between the laser and the OFC and term that provides all the beating modes among all

the longitudinal modes of comb itself (see Fig. 1.2). This gives access to the common beatnote expression:

$$f_{\mathrm{L}} = \nu_{\mathrm{L}} - \nu_{\mathrm{OFC}} \tag{A.8}$$

with $\nu_{\mathrm{OFC}} = N \cdot f_{\mathrm{rep}} + f_0$.

Appendix B

Deriving the comb mode index and its uncertainty

The aim of this appendix is to complement, with a more detailed description, the four techniques already mentioned in subsection 2.2.3. The related equations to obtain the N comb number will be developed, together with some considerations to take into account. We will proceed from the easiest to the most technology-demanding particular cases and we will conclude with a general case with no additional tools or techniques required.

Cases 1 and 2: Wavemeter or a well-known optical reference

The best wavemeters (WMs) nowadays have a resolution around 1 MHz even though the bias, depending on the wavelength range, can be up to $20-30\,\mathrm{MHz}$ from the nominal value. However, this bias can be calibrated with an accurate optical source, e.g. a laser referenced to a narrow atomic transition. So, if we have one of these WMs, after measuring the frequency of the laser we are interested in, ν_L, we simply insert this value in equation 2.18 and we find two possible N_L values depending on the beatnote sign:

$$N_\mathrm{L} = \frac{\nu_\mathrm{L} - \mathrm{sign}_\mathrm{L} \cdot f_\mathrm{L}}{f_\mathrm{rep}} \tag{B.1}$$

As we can see in equation B.1, if the operator is lucky, only one of the two options ($\mathrm{sign}_\mathrm{L} = +1$ or $\mathrm{sign}_\mathrm{L} = -1$) will lead to a value close enough to an integer number. But it could be also the case where f_L is close to $f_\mathrm{rep}/2$ and then the operator can not conclude with this method. Additionally, one must pay attention to the uncertainty in the determination of the wavelength or optical frequency by the WM, $\sigma(\mathrm{WM})$, since we need $\sigma(\mathrm{WM}) \ll f_\mathrm{rep}/2$ to have no indetermination. In our case, the WM provides an accuracy of a few tens of MHz while our $f_\mathrm{rep} = 250\,\mathrm{MHz}$, meaning that there is one order of magnitude margin (even if the WM is not calibrated) that translates to a index

mode uncertainty. Another possibility is that we have a priori knowledge on ν_L and whose frequency drift, $d\nu_L/dt$, is small enough, i.e. $\sigma(\nu_L)/f_{rep} < 1$.

For these two first methods, let us calculate the final N_L uncertainty, $\sigma(N_L)$, with propagation of uncertainties[1] of the quantities involved:

$$\begin{aligned}\sigma^2(N_L) &= \left(\frac{1}{f_{rep}}\right)^2 \sigma^2(\nu_L - \text{sign}_L \cdot f_L) + \quad -\frac{\nu_L - \text{sign}_L \cdot f_L}{f_{rep}^2}\right)^2 \sigma^2(f_{rep}) \\ &\simeq \left(\frac{\nu_L}{f_{rep}}\right)^2 \quad \frac{\sigma^2(\nu_L)}{\nu_L^2} + \frac{\sigma^2(f_{rep})}{f_{rep}^2}\right)\Bigg(\end{aligned} \tag{B.2}$$

where $\sigma(\nu_L)$ is either $\sigma(\text{WM})$ or $\frac{d\nu_L}{dt} \cdot T$, with T the time necessary to perform the measurement.

In equation B.2, since f_L is small in value and uncertainty, we have neglected the two corresponding cross terms. Due to the resolution provided by the UMR, the knowledge on the repetition rate is limited to $\sigma_y(f_{rep}) < 2 \cdot 10^{-15}$ at 1 s (section 3.1.4). Thus, for an optical frequency $\nu_L = 282.1\,\text{THz}$ with a negligible drift and a WM inaccuracy $\sigma(\text{WM}) = 25\,\text{MHz}$, we get a final uncertainty for the N number $\sigma(N_L) = 0.1$, which is a priori sufficient to identify unambiguously the integer N_L. Some of the SYRTE's Sr and Hg ultrastable clock lasers do not drift more than 200 kHz per year, resulting in a negligible ($\sigma(N_L) = 8.3 \cdot 10^{-4}$) ambiguity of the N_L number estimated from a previously measured value. In short, looking at B.1, if we want to determine the N_L number (in the order of 10^6, for our relevant frequencies) with at least two significant decimal digits after the comma, we must know the ν_L at the MHz level, and f_{rep} at the Hz level.

Case 3: OFC phase-locked to an optical reference

In the case of a comb locked to an ultrastable optical reference, as it is at SYRTE, one can act directly on the PLL described by the equation 2.4. For clarity, this equation is rewritten as:

$$\nu_{IRef} - N_{IRef} \cdot f_{rep} = 8 \cdot \text{sign}_{IRef} \cdot f_{DDS1} \tag{B.3}$$

where we have omitted the superscript 0 (standing for the main comb output) and eliminate $f_{s,IRef}$ as it is a fixed frequency shift that does not affect the loop.

To this end, we shift the reference frequency imposed to DDS1 for the phase lock, f_{DDS1}, to $110\,\text{MHz} + \delta_{DDS1}$, with $\delta_{DDS1} = 2\,\text{MHz}$. This shift has to be done by ramping the DDS tuning word continuously, in a few seconds, in order to avoid a change rate higher than what the feedback loop can accommodate and preventing the PLL from

[1] For $z(x,y) = \frac{x}{y}$, $\quad \sigma^2(z) = \left(\frac{\partial z}{\partial x}\right)^2 \sigma^2(x) + \left(\frac{\partial z}{\partial y}\right)^2 \sigma^2(y)$.

failing. Once the ramp has reached the imposed shift, we average for 40 s the new value yielded by the repetition rate $f_{\mathrm{rep1}} = f_{\mathrm{rep}} + \delta f_{\mathrm{rep1}}$. Consequently, we proceed in the same way for a second change in the opposite direction ($110\,\mathrm{MHz} - \delta_{\mathrm{DDS1}}$) to get $f_{\mathrm{rep2}} = f_{\mathrm{rep}} + \delta f_{\mathrm{rep2}}$. The direction of δf_{rep} will depend on the sign of the locking beatnote. For instance, for $\mathrm{sign}_{\mathrm{IRef}} = +1$, for a positive increment of δ_{DDS1} we will have a negative one on δf_{rep1}, and vice versa.

The drift of the IRef laser, and therefore the drift of the repetition rate, $\beta = df_{\mathrm{rep}}/dt$, is previously calibrated during a time segment of $T = 40\,\mathrm{s}$, and subsequently subtracted from the measurements of f_{rep1} and f_{rep2}. If we take increments in equation B.3 that account for the two respective frequency shifts imposed to DDS1, we have:

$$\nu_{\mathrm{IRef}} - N_{\mathrm{IRef}} \cdot f_{\mathrm{rep1}} = 8 \cdot \mathrm{sign}_{\mathrm{IRef}} \left(f_{\mathrm{DDS1}} + \delta_{\mathrm{DDS1}} \right) \tag{B.4}$$

$$\nu_{\mathrm{IRef}} - N_{\mathrm{IRef}} \cdot f_{\mathrm{rep2}} = 8 \cdot \mathrm{sign}_{\mathrm{IRef}} \left(f_{\mathrm{DDS1}} - \delta_{\mathrm{DDS1}} \right) \tag{B.5}$$

Combining equations B.4 and B.5, and assuming the drift β is linear, we finally get:

$$N_{\mathrm{IRef}} = \frac{16 \cdot \mathrm{sign}_{\mathrm{IRef}} \cdot \delta_{\mathrm{DDS1}}}{\langle \delta f_{\mathrm{rep2}}(t) - \delta f_{\mathrm{rep1}}(t) \rangle + \beta \cdot T} \tag{B.6}$$

where $\beta \cdot T$ leads to an offset frequency in the total f_{rep} variation. The shifts of DDS1 and the corresponding acquisitions of f_{rep1} and f_{rep2} are totally automatized, as well as the computation of the result. Only the sign leading to a positive N is the correct one.

The corresponding N_{IRef} uncertainty[2] yields:

$$\begin{aligned} \sigma^2(N_{\mathrm{IRef}}) &= \left(\frac{\alpha}{(\delta f_{\mathrm{rep}})^2} \right)^2 \sigma^2(\delta f_{\mathrm{rep2}}) + \left(\frac{-\alpha}{(\delta f_{\mathrm{rep}})^2} \right)^2 \sigma^2(\delta f_{\mathrm{rep1}}) \\ &= 2 \cdot N_{\mathrm{IRef}}^2 \cdot \frac{\sigma^2(f_{\mathrm{rep}})}{(\delta f_{\mathrm{rep}})^2} \end{aligned} \tag{B.7}$$

where $\alpha = 16 \cdot \mathrm{sign}_{\mathrm{IRef}} \cdot \delta_{\mathrm{DDS1}}$ and $\delta f_{\mathrm{rep}} = \delta f_{\mathrm{rep2}} - \delta f_{\mathrm{rep1}} \approx 40\,\mathrm{Hz}$ (for $\delta_{\mathrm{DDS1}} = 2\,\mathrm{MHz}$, $N_{\mathrm{IRef}} = 8 \cdot 10^5$ and $\beta = 0$ in equation B.6). Since $\sigma_y(f_{\mathrm{rep}}) = 2 \cdot 10^{-15}$, the final $\sigma(N_{\mathrm{IRef}})$ we have is $1.4 \cdot 10^{-2}$.

Case 4: General method

When none of the options described above can be performed, a measurement with two very different repetition rates is needed. In this situation, we lock the comb on two distant N_{L} and we measure the corresponding f_{rep} change. To this end, we perform two

[2] For $z(x,y) = \frac{\alpha}{x-y}$.

successive comparisons between the laser to measure, ν_L, and the microwave reference, by measuring their respective repetition rates f_{rep1} and f_{rep2} (once the OFC is locked back after each change). Applying equation B.3 to the two comparisons, we get:

$$\nu_L - N_L \cdot f_{rep1} = 8 \cdot \text{sign}_L \cdot f_{DDS1} \tag{B.8}$$

$$\nu_L - (N_L + \delta N_L) \cdot f_{rep2} = 8 \cdot \text{sign}_L \cdot f_{DDS1} \tag{B.9}$$

Since we lock at 880 MHz the f_0-free beatnote, we can omit the signs in the above equations as we always lock to the same family of beatnotes (the offset-free ones). Moreover, we change quickly to the second measurement to avoid a significant drift of ν_L and that the quantity $N_L \cdot f_{rep}$ is conserved. One must notice that, when scrolling the different modes passing by, only the f_0-free ones must be counted (omitting the intermediate modes that will contain f_0). Therefore, combining equations B.8 and B.9, we obtain:

$$N_L = \frac{\delta N_L \cdot f_{rep2}}{\delta f_{rep}} \tag{B.10}$$

where $\delta f_{rep} = f_{rep1} - f_{rep2}$ and δN_L is evaluated "manually" by counting the beatnotes passing by when moving across the comb spectral lines from f_{rep1} to f_{rep2}.

In this case, the propagation of uncertainties leads to:

$$\begin{aligned} \sigma^2(N_L) = &\left(\frac{\delta N_L \cdot \delta f_{rep} + \delta N_L \cdot f_{rep2}}{(\delta f_{rep})^2} \right)^2 \sigma^2(f_{rep2}) \\ &+ \left(\frac{\delta N_L \cdot f_{rep2}}{(\delta f_{rep})^2} \right)^2 \sigma^2(f_{rep1}) \simeq 2 \left(\frac{N_L^2}{\delta N_L} \right)^2 \left(\frac{\sigma(f_{rep})}{f_{rep}} \right)^2 \end{aligned} \tag{B.11}$$

with $\delta f_{rep} = f_{rep1} - f_{rep2}$.

If the laser, which we are locking the OFC to, has a fractional short-term stability of $1 \cdot 10^{-11}$ (like a cutting-edge commercial telecommunication one), that is transferred to f_{rep} by the PLL. In order to have $\sigma(N_L) < 0.1$, the minimum change δN_L needed will be 91 units, assuming $N_L = 8 \cdot 10^5$. The term $\sigma_y(f_{rep})$ is, in fact, dominated either by the stability of the laser or by the drift rate of the laser multiplied by the time it takes to sweep from one N to the other. In equation B.11, since $\sigma_y(f_{rep}) \approx \sigma_y(\nu_L)$, we can take $\sigma(\nu_L)$ as the total uncertainty of the laser that accounts for stability and drift combined.

Appendix C

Fiber noise characterization

Optical fiber links are very convenient and are part of many optical setups when light needs to be sent from one zone of the optical setup to another or even between remote places that are thousands of kilometers away from each other. In the case of laser light with a linewidth smaller than 1 kHz, propagation in optical fibers is likely to degrade the spectrum (because of fiber core sensitivity to vibrations and temperature), therefore it is necessary to compensate the propagation noise.

A good understanding of phase noise contribution is required in order to account for it and compensate it when needed. This becomes essential when using fiber links to distribute USLs, compare oscillators or transfer their spectral purity from one to another. As we are going to show in the next paragraphs, just a few centimeters of an uncompensated fiber link can easily limit the performance of the whole link at the low 10^{-17} level.

The aim is to actively compensate the phase noise imposed on the USL radiation that travels along the fiber, between a point x, located as close to the source itself as possible, to point y, after which the light will be used in the experiment, as shown in the Doppler cancellation scheme of Fig. C.1.

We built a Michelson AC interferometer with a short reference arm and a long arm corresponding to the necessary propagation where an AOM is used as a frequency shifter. The phase difference between the two arms gives access to the phase noise accumulated in the course of the propagation. The USL is split up (point x) into path C (reference arm) and path E (arm to be compensated) in a 2×2 fiber coupler. Path C is retro-reflected back in a fiber mirror and path E follows the fiber that will carry the light to the experiment. At the end of this fiber (point y) another 2×2 fiber coupler is placed, splitting the light into G and F. Path F is also retro-reflected back and, thanks to the AOM (around tens of MHz frequency shift) placed in path E, will interfere (at twice that shifting frequency) with the light reflected from C when they hit the PD. Note that this AOM, where the feedback is applied to, must stay physically close to the photodiode to avoid long cables carrying RF or DC signals. It is preferable for long fibers ($> 10\,$m)

to put this "feedback AOM" before the input of the fiber and add a "marker AOM" (not represented in the scheme) at the output of the fiber and before the feed-back mirror. This last allows to unambiguously identify the correct beatnote, removing the effects of parasitic reflections along the fiber propagation.

According to Fig. C.1, the different phase shifts accumulated by the radiation for two reflected paths C and F are respectively:

$$\begin{aligned}\phi_1 &= \phi_{USL} + \phi_A + 2\phi_B + 2\phi_C + \phi_D \\ \phi_2 &= \phi_{USL} + \phi_A + 2\phi_B + 2\phi_{AOM} + 2\phi_E + 2\phi_F + \phi_D\end{aligned} \tag{C.1}$$

The interference of the two optical frequencies, whose phase shifts are written in the above equation, are detected in a PD. From appendix A, we know that the phase of the beatnote can be formulated as:

$$\phi_{PD} = \phi_2 - \phi_1 = 2\phi_{AOM} + 2\phi_E + 2\phi_F - 2\phi_C \tag{C.2}$$

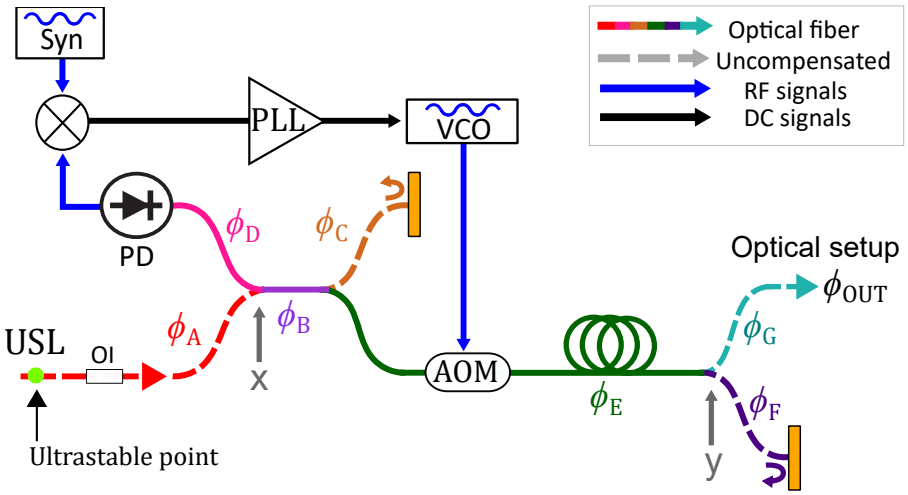

Figure C.1: Typical optical setup for fiber noise compensation from point x to point y. The different stretches where the light accumulates phase noise (ϕ) along fiber path are colored. Paths represented by dashed lines are never compensated. An error signal is generated, after demodulation of the beatnote detected in the PD, and sent via a PLL to a VCO for compensation. OI: optical isolator, PD: photodetector, and VCO: voltage-controlled oscillator.

The optical beatnote detected by the PD is demodulated in a mixer by an RF ultrastable source, in our case, a synthesizer externally referenced to the UMR. The frequency of the AOM is tuned close to half of the frequency set in the synthesizer until the error signal is inside the PLL's bandwidth to allow a feedback to the VCO feeding the AOM, which is the actuator compensating the setup. Thus, once the PLL is closed, equation C.2 becomes:

$$2\phi_{AOM} + 2\phi_E + 2\phi_F - 2\phi_C = \phi_{Syn} \tag{C.3}$$

The equation that accounts for the out phase (ϕ_{OUT}) going to the experiment when implementing the PLL yields:

$$\begin{aligned}\phi_{OUT} &= \phi_{USL} + \phi_A + \phi_B + \phi_{AOM} + \phi_E + \phi_G \\ &= \phi_{USL} + \phi_A + \phi_B + \left(\frac{1}{2}\phi_{Syn} - \phi_E - \phi_F + \phi_C\right) + \phi_E + \phi_G \\ &= \phi_{USL} + \phi_A + \phi_B + \frac{1}{2}\phi_{Syn} - \phi_F + \phi_C + \phi_G\end{aligned} \tag{C.4}$$

The path we want to compensate is A→B→E→G, but ϕ_A, ϕ_F, ϕ_C and ϕ_G are physically impossible to correct in the present setup. $\phi_{OUT} \approx \phi_{USL}$ provided that the instabilities of ϕ_A, ϕ_B, ϕ_F, ϕ_C, ϕ_G and ϕ_{Syn} are negligible. The instability of ϕ_{Syn} is very small since the fractional stability of the UMR is $2-3\cdot10^{-15}$ at 1 s, which gives a sub-μHz stability for its working frequency around 100 MHz. The other path instabilities are also negligible provided the corresponding pieces of fiber are short enough (typically around 20 cm or less) and well isolated from environmental fluctuations. High demanding applications ($\approx 10^{-17}$ at 1 s or below) require very careful designs on that account [91].

In the end, the predominant noise due to ϕ_E is compensated but due to the topology of the interferometer, we do not compensate the "ends", at least not the right ones, hence still a few tens of centimeters of uncompensated fiber. Note that ϕ_B, since it is in common mode, is not impacted by the AOM correction, what paradoxically plays against us. In any case, the length of B is just the fiber coupler itself and it is well protected by the manufacturer's casing. The lengths of C and F are about 20 cm each, what makes it very small in comparison with the length of path E (typically tens of meters) and permitting this scheme to be efficient and easy to implement. But, again, this over/uncompensated paths must meet the application stability requirements. We can avoid this over compensated paths C and F in free space by using 10/90 (R/T) partial reflective mirrors at 0 ° incidence angle as we did for the spectral purity transfer schemes (see subsection 4.3) and it is being implemented in the new ultrastable long cavity setup.

In order to characterize the fiber noise present in the setup and to measure the ultimate stability reachable, we added a second branch to circumvent some of the uncompensated paths, as depicted in Fig. C.2. Doing so, we are now able to make an out-of-loop measurement of the interference of branches 1 (Br1) and 2 (Br) on a second photodiode (PD2). As before, in the first one (PD1), the respective beatnotes are formed, which contain the phase information to feedback and to compensate the optical paths.

To start with the setup characterization under different conditions, we compensated the phase noise from the fiber propagation in both branches (Br1 and Br2) at our best in order to see the current stability limit and have a reference value. It is important to notice that the paths that normally would be considered as uncompensated (dash lines in Fig. C.1) are no longer at play since they are now in common mode and, therefore,

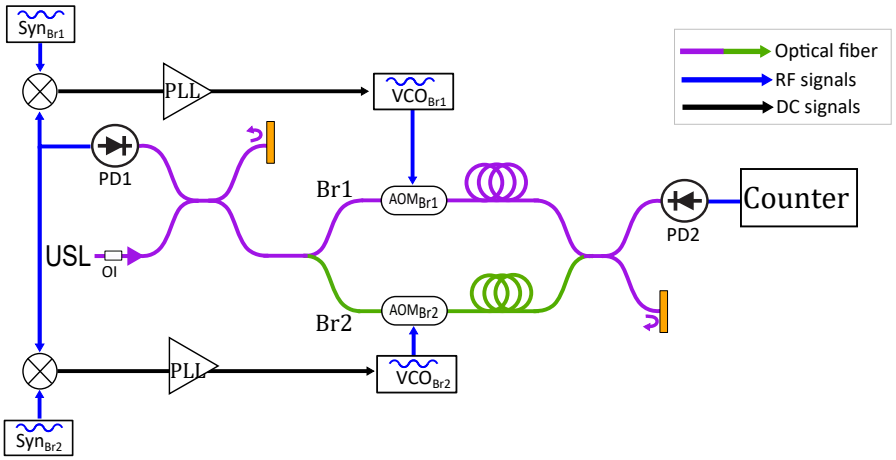

Figure C.2: Fiber noise characterization optical setup.

they share the same uncompensated added noise which cancels out when they interfere. We got a result of $9 \cdot 10^{-18}$ at 1 s (green curve of Fig. C.3). This limit can be explained by possible unwanted reflections after the AOMs along the branches Br1 and Br2 that eventually reach PD1 as well. These unavoidable stray reflections might occur between the fiber tips interfaces when connected with an adapter (as we did not splice the fiber components) or when additional fiber components/devices are placed in between.

To see the impact of having a fiber link uncompensated, we opened the PLL of branch B while keeping the AOM on to see the phase fluctuations due to the heating of the AOM crystal together with the fiber noise due to the 60 cm of fiber. In this case, the AOM was driven by an RF ultrastable source (DDS) locked to the UMR, as the VCO that is used as an actuator for the PLL would have been way too noisy if kept for this setup (with the phase lock loop opened). As expected, the stability was degraded to $7 \cdot 10^{-16}$ at 1 s. Subsequently, we removed the AOM from the setup, changing the expected frequency of the beatnote signal formed by PD2, and the stability remained practically the same, which means that the AOM's thermal effect is negligible (red and black curves of Fig. C.3). It is shown that the fractional frequency instability of the transfer becomes much higher, almost two orders of magnitude for a 60-cm length, when no fiber compensation is implemented.

Finally, we added and extra fiber of 20 m after the AOM in the uncompensated branch. This fiber was intentionally exposed to air conditioning air currents and the measurement was taken under laboratory's activity, what explains its noisy behavior. Even though a quiet stretch was chosen for its assessment (see pink time trace and its stability curve in Fig. C.3), it shown a stability of $2 \cdot 10^{-15}$ at 1 s.

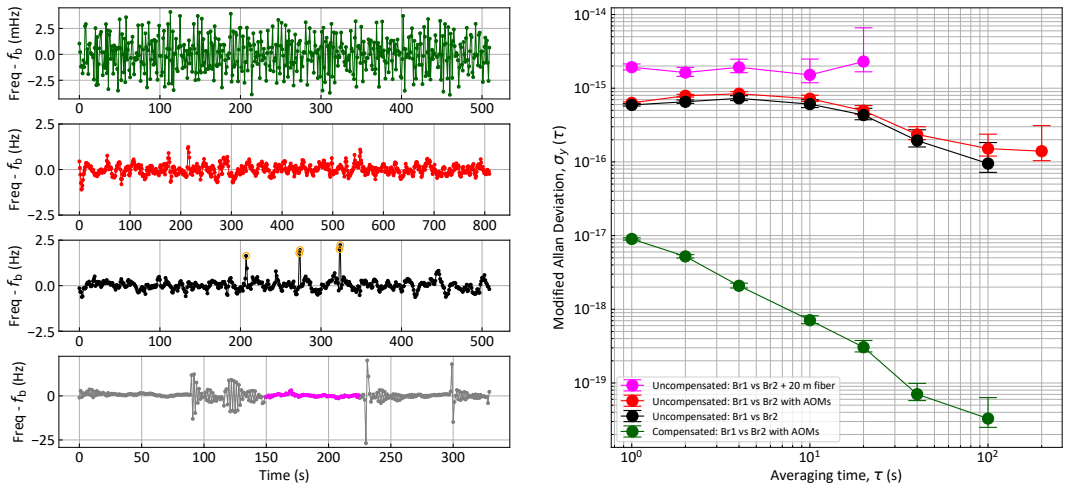

Figure C.3: Fiber noise results. Left plots show the respective frequencies minus the expected beatnote's frequencies (f_b) traces over time. Yellow circular markers indicate outlayers that have been removed for the MDEV computation. They correspond either to mechanical perturbations of the system while acquiring the data, or to cycle slips (around 2 Hz). Dead-time-free frequency counter set in Lambda mode.

Appendix D

OFC auto-relock implementation

Fiber based OFCs are nowadays a very reliable technology thanks to their robust mode-lock mechanisms that phase coherently couple the longitudinal modes, allowed by the broad gain medium of the fs oscillator, during months with no human intervention. In order to perform extended and efficient measurements, the SYRTE comb must be (quasi) continuously locked to a stable reference that in our case is the IRef ultrastable laser at 1542 nm. It is then necessary to fine control the comb parameters via its intra-cavity elements and actuators (see table 2.1), where a servo loop with one proportional and three integrator controllers applies the feedback corrections on the EOM and PZT actuators as explained in subsection 2.1.2. The other intra-cavity actuators such as the cavity end mirror translation stage or the motorized pair of wedges are used for coarse adjustment in order to ease the task of the servo loop.

The PLL described by equation 2.4 has a given dynamics, beyond which the control is no longer feasible. Ways to reach the end of the dynamics are: the quantity to lock naturally drifting too far away from the reference (meaning that the quantity to lock must be "recentered", what is performed with the coarse adjustment of the comb degrees of freedom), or a sudden, hard to predict, shock. Out of this range the PLL will be unable to track any error signal from a phase detector. Additionally, optical components such as optical fibers are very sensitive to vibrations, so any shock into the optical table can suddenly affect the mode-matching phase of the optical signals or the SNR of the optical beatnote meant to be locked and lead the loop to failure.

In the present case we are referring to the lock of the operational frequency comb that is used on a daily basis and is in charge of all optical metrological measurements at SYRTE. This includes the international optical clock calibration campaigns, where the OFC must run continuously with uptimes as high as possible. In consequence, we not only want to reference it to the optical cavity but also to keep the same comb mode N for which it was previously calibrated, so that it maintains the same repetition rate. For this reason we have implemented an "auto-relock" that enables to rearm the PLL when it fails or simply when it is close to the limit of its finite dynamics.

The offset frequency, f_0, is loosely locked to 70 MHz with the following condition: if more than 1 MHz away from target, we modify the current driving the pump diode laser of the fs-laser in order to set f_0 back to 70 MHz. Note that f_0 is eliminated, but still it needs to stay reasonably in the filter to be efficiently mixed out, therefore we keep it centered at all times. The repetition rate, f_{rep}, is locked to IRef laser, ν_{IRef}. As explained in subsection 2.2.2, we use the 275 kHz signal as an out-of-loop comparison of $36 \cdot f_{\text{rep}}$ and the UMR (always available) to derive f_{rep}. In case of a failing of the lock, the 275 kHz signal will move, and based on the former change we will be able to recenter f_{rep} close enough to target and re-engage the PLL successfully.

We have programmed a computer with a data acquisition device (DAQ) that access different information (frequencies measured by a frequency counter, error signal voltage and applied correction signal voltages) and acts on different actuators (mean pump diode laser current control, mean comb PZT voltage control and electronic relays controlling the PLL circuit). The detailed operation is described in the following.

Principle of work

The DAQ from National Instruments is driven by a Python software via a USB connection (NI USB-6002) where we use four digital output (DO) channels, three analog input (AI) channels and its two analog output (AO) channels. On the one hand, the software monitors the acquired AIs in conjunction with f_0 at 70 MHz from the interferometric unit (see Fig. 1.3), and the 275 kHz control reference signal from the frequency chain, which are both directly counted on the K+K frequency counter as the AIs are limited to maximum sample rates of 50 kS/s. On the other hand, it first controls the relays attached to the "lock box" (PLL circuit composed of PI2 + I) via the DOs ($0 - 3.3$ v) and, second, it acts together with the forth integrator on the PZT actuator and also on the pump diode of the fs oscillator via the AOs (± 10 v) when necessary. Fig D.1 gives an overview of the system.

The software takes control of the two degrees of freedom of the comb independently by running two scripts in parallel. Hence, we avoid any interference of f_0 with the f_{rep} relock, i.e. the comb relock, preventing f_{rep} to drift any further.

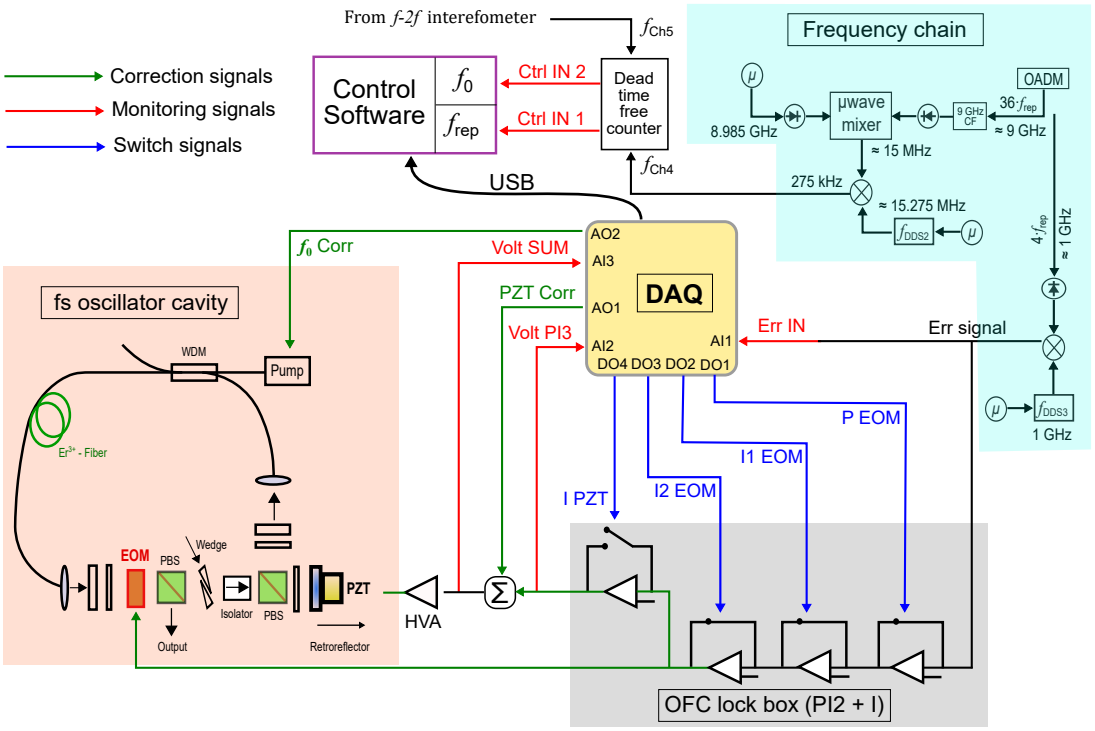

Figure D.1: Auto-relocking system design and main connections. Left: simplified and approximated scheme (similar to the one depicted on [122]) of the fs oscillator cavity showing the three actuators where the corrections are applied: the electro-optical modulator (EOM), end mirror piezo ceramic (PZT) and the pump diode laser. Top right: part of frequency chain used to derive the f_{rep} value by comparison of its 36th harmonic against the UMR at 8.985 GHz. It shows how the reference signal at 275 kHz is obtained to be employed as frequency discriminator. Bottom right: schematic of the PLL circuit based on four operational amplifiers configured as one proportional and three integrators which will be governed by the DAQ. AI: analog input, AO: analog output, DO: digital output, and HVA: high voltage amplifier.

Offset frequency soft lock to 70 MHz

There is an algorithm in charge of a recentering of f_0 so that it is always centered at 70 MHz, "Ctrl IN 2" (f_{Ch5}), continuously measured by the K+K counter), even if the system unlocks (see f_0 decision tree on the right in Fig. D.2).

To do so, every time $|f_0 - 70\,\text{MHz}| > 1\,\text{MHz}$, we apply a voltage correction, V_{f_0}, "f_0 Corr" (AO2), with steps $\Delta v_{f_0} = sign \cdot \beta/10$ of 1 mv to the controller of the pump diode current driver, whose voltage-to-frequency β coefficient has been previously cali-

brated (around 0.125 v/MHz). These steps do not affect the f_{rep}, which is independently locked regardless of the current value, especially because of the low pass filter (fraction of a Hz bandwidth) that makes the change of correction as smooth as possible.

In typical operation, the controller "f_0 Corr" acts roughly every $4-5$ hours to keep the offset frequency within the $69-71$ MHz range. When the AO2 voltage output reaches 8 v the software sends a warning message meaning that the DAQ is getting close to its maximum driving voltage of ± 10 v. Before this last is reached, when $\text{V}_{f_0} > 9.9$ v the software stops the loop iteration and it waits for a coarse tuning with the pair of motorized glass wedges.

Repetition rate PLL surveillance and control

There are several comb modes N that can fulfill the locking equation B.3 ($\nu_{\text{IRef}} - N_{\text{IRef}} \cdot f_{\text{rep}} = 8 \cdot \text{sign}_{\text{IRef}} \cdot f_{\text{DDS1}}$) when tuning the f_{rep} via the PZT ceramic, in such a way that they provide us with identical error signals for each of them when the loop is closed. We set a value of 194 400 121 MHz for the IRef laser's frequency, to which the comb will be locked to, that fulfills several operational requirements, such as the value of the beatnotes between the various reference lasers at the interconnections between European fiber links. Consequently we adjust the DDS frequency, f_{DDS2}, in order to have a target at exactly 275 kHz (within the resolution of the DDS, a few μHz). This means that if the OFC unlocks, after opening the PLL relays, we can use the 275 kHz signal as a frequency discriminator since it will move to a higher or lower value measured in the frequency counter, f_{Ch4}. Depending on the new frequency of the locking beatnote (higher or lower respect to the locking point at 880 MHz), we are able to recenter towards the reference value of 275 kHz exactly.

We continuously monitor four signals that we can divide in two categories: evaluative and preventive. The evaluation signals allow us to assess the regime (locked or unlocked) of the loop. First, by checking, on the DAQ card "Err IN" (AI1), the peak-to-peak amplitude of the voltage (V_{pp}) error signal that it is sent to the input of the lock box (PI2 + I). Second, by measuring and evaluating continuously, on the K+K counter, the frequency value of the 275 kHz control signal "Ctrl IN 1" (f_{Ch4}) used to compare the f_{rep} against the UMR in order to derive the f_{rep} value.

In contrast, the prevention signals allow us to predict and anticipate for avoidable technical failures due to the limited operational voltage range of both the lock box (± 15 v) and the DAQ card (± 10 v). They set up a convenient time to recenter the system, especially useful during international calibration campaigns, by sending warning messages when the current voltage's corrections exceed the threshold's values established (2 v before their maximum driving voltages). These are the monitored voltage applied by the lock box, V_{PZT}, "Volt PI3" (AI2), and the one applied by the DAQ, $\text{V}_{\text{PZT Corr}}$, "PZT Corr" (AO1). The sum of these two voltages "Volt SUM" (AI3), also monitored, is the total PZT voltage correction that, after a high-voltage amplifier (HVA), is finally

sent to the end mirror PZT.

When the OFC is locked, first, the measured signal f_{Ch4} stays centered at 275 kHz although a threshold frequency $f_{\text{thr}} = \pm 500\,\text{Hz}$ has been set. The reason for this is that the IRef laser can drift when the comb is unlocked, and since it can not be monitored by the comb it can not be dedrifted either. This can happen when a step PZT tuning is required[1] or due to some maintenance for example. Nevertheless, even if it has been several days unattended, this would lead to a laser frequency change of at most 10 MHz, resulting in a change smaller than 500 Hz on f_{Ch4}. On the the other hand, if the comb unlocks, it leads to a change $f_{\text{Ch4}} > 700\,\text{Hz}$. Thereby we set a threshold in between to tolerate drift but still detect unlocking events. Second, the averaged peak-to-peak voltage of the error signal is about ten times lower than when the OFC is not locked. We compute its standard deviation, s_{Err}, and establish a mean voltage threshold on the deviation $s_{\text{thr}} = 10\,\text{mv}$ that will detect a sudden unlock. The left's decision tree in Fig. D.2 illustrates all possible cases for the f_{rep} relocking procedure.

For instance, if a sudden unlock occurs, the relocking sequence can be summarized in three steps:

1. If $|f_{\text{Ch4}} - 275\,\text{kHz}| > f_{\text{thr}}$ and $s_{\text{Err}} > s_{\text{thr}}$, the DAQ opens "I PZT" (DO4). Note that the three other PLL controllers, "I2 EOM" (DO3), "I1 EOM" (DO2) and "P EOM" (DO1), stay closed. In other words, the feedback to the EOM is not reset, as it proved to be unnecessary experimentally.

2. The frequency difference $f_{\text{Ch4}} - 275\,\text{kHz}$ is used as an error signal to recenter the locking beatnote at 880 MHz in order to relock it by applying voltage corrections via "PZT Corr" (AO1). As in the case of f_0 corrections, the corresponding voltage-to-frequency coefficient α has been calibrated (around 1 v/kHz). We first apply a PZT fast voltage correction to bring the beatnote towards the threshold when $|f_{\text{Ch4}} - 275\,\text{kHz}| > f_{\text{thr}}$ with steps of $\Delta v_{\text{PZT fast}} = (f_{\text{Ch4}} - 275\,\text{kHz})sign \cdot \alpha$, where we use the *sign* function to discriminate the direction. Once it is within the threshold, a PZT slow voltage correction with $\Delta v_{\text{PZT slow}} = sign \cdot \alpha/10$ is applied. A voltage ramp is performed in one direction until the error signal "Err IN" (AI1) finds zero, fulfilling the locking condition for s_{thr}.

3. When $s_{\text{Err}} < s_{\text{thr}}$, the PZT relay "I PZT" (DO4) is closed and the $V_{\text{PZT Corr}}$ "PZT Corr" holds the last voltage value applied. The PLL circuit is in charge now of the feedback applying small voltage corrections V_{PZT} on the PI2 and on the last I, which act on the intra-cavity EOM and PZT, respectively. Note that since the

[1] This operation usually takes a couple of minutes and it can be done remotely (with a VPN) via the same control software which acts on the translation stage where the cavity end mirror (attached to the PZT) is mounted.

laser drifted, it can be that f_{Ch4} is not exactly 275 kHz when the lock is back, hence the f_{thr} margin. The decision to lock or not lock is made by monitoring the $\mathrm{V_{pp}}$ of the error signal, f_{Ch4} only says in which direction to go towards 275 kHz, and therefore seek for an opportunity to have the s_{Err} lower than s_{thr} and uses this criterion to attempt to close the loop. An independent script will subsequently bring the laser back to its target frequency, and therefore f_{Ch4} back to 275 kHz.

This auto-relock system was integrated into the laboratory control software and was satisfactory tested during the one-month international calibration campaign in June 2018.

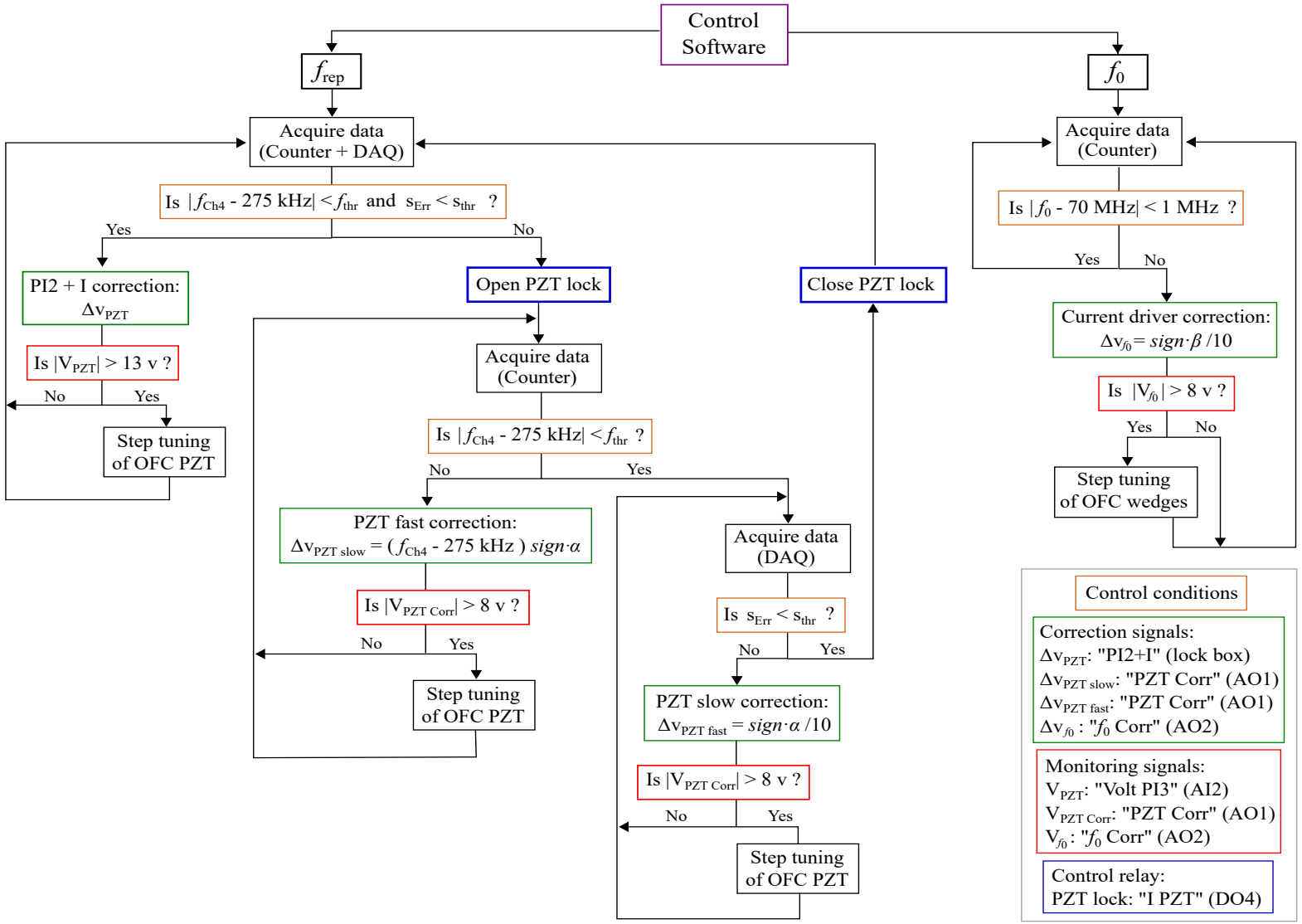

Figure D.2: Auto-relocking software's decision tree for the two comb's degrees of freedom. The "step tuning of OFC PZT" is performed by acting on the translation stage, to which the cavity end mirror (attached to the PZT) is mounted. The "step tuning of OFC wedges" it is performed via the pair of motorized glass wedges. These coarse adjustments, if needed, are implemented on the software.

Bibliography

[1] L. Essen, J. V. L. Parry, and T. W. Hänsch. "The caesium resonator as a standard of frequency and time". In: *Phil. Trans. Roy. Soc.* 250 (A 1957), pp. 45–69. DOI: https://doi.org/10.1098/rsta.1957.0010 (cit. on pp. 3, 7, 8).

[2] In: *Comptes rendus de la* 26^{e} *CGPM* (2018). URL: https://www.bipm.org/utils/common/pdf/CGPM-2018/26th-CGPM-Resolutions.pdf (cit. on p. 4).

[3] In: *Comptes rendus de la* 13^{e} *CGPM (1967)* 103 (1969). URL: https://www.bipm.org/utils/common/pdf/CGPM/CGPM13.pdf#page=103 (cit. on p. 4).

[4] T. H. Maiman. "Stimulated Optical Radiation in Ruby". In: *Nature* 187 (4736 1960), pp. 493–494. URL: https://doi.org/10.1038/187493a0 (cit. on p. 4).

[5] A. L. Schawlow and C. H. Townes. "Infrared and Optical Masers". In: *Phys. Rev.* 112 (6 1958), pp. 1940–1949 (cit. on p. 4).

[6] S. M. Brewer et al. "$^{27}Al^{+}$ Quantum-Logic Clock with a Systematic Uncertainty below 10^{-18}". In: *Phys. Rev. Lett.* 123 (3 2019), p. 033201. URL: https://link.aps.org/doi/10.1103/PhysRevLett.123.033201 (cit. on pp. 4, 10).

[7] D. B. Sullivan. "Time and frequency measurement at NIST: the first 100 years". In: *Proceedings of the 2001 IEEE International Frequncy Control Symposium and PDA Exhibition (Cat. No.01CH37218)*. 2001, pp. 4–17. DOI: 10.1109/FREQ.2001.956152 (cit. on p. 7).

[8] Harry M. Davis. "Radio Waves and Matter". In: *Scientific American* 179.3 (1948), pp. 16–23. URL: http://www.jstor.org/stable/24945880 (cit. on p. 7).

[9] Jean-Louis Picqué. "Hyperfine Optical Pumping of a Cesium Atomic Beam, and Applications". In: *Metrologia* 13.3 (1977), pp. 115–119. URL: https://doi.org/10.1088%2F0026-1394%2F13%2F3%2F006 (cit. on p. 8).

[10] Mark A. Kasevich et al. "rf spectroscopy in an atomic fountain". In: *Phys. Rev. Lett.* 63 (6 1989), pp. 612–615. URL: https://link.aps.org/doi/10.1103/PhysRevLett.63.612 (cit. on p. 8).

[11] A Clairon et al. “Ramsey Resonance in a Zacharias Fountain”. In: *Europhysics Letters (EPL)* 16.2 (1991), pp. 165–170. URL: https://doi.org/10.1209%2F0295-5075%2F16%2F2%2F008 (cit. on p. 8).

[12] A. N. Luiten et al. “Power stabilized cryogenic sapphire oscillator”. In: *IEEE Transactions on Instrumentation and Measurement* 44.2 (1995), pp. 132–135 (cit. on p. 8).

[13] V. Giordano et al. “Cryogenic sapphire microwave oscillators for space, metrology and scientific applications”. In: *2011 XXXth URSI General Assembly and Scientific Symposium*. 2011, pp. 1–4. DOI: 10.1109/URSIGASS.2011.6050311 (cit. on p. 8).

[14] G. Dick. “Local Oscillator Induced Instabilities in Trapped Ion Frequency Standards”. In: Proc. Precise Time and Time Interval. 1987 (cit. on pp. 8, 11).

[15] S. Grop et al. “ELISA: A cryocooled 10 GHz oscillator with 10-15 frequency stability”. In: *Review of Scientific Instruments* 81.2 (2010), p. 025102. URL: https://doi.org/10.1063/1.3290631 (cit. on p. 8).

[16] Nitin R. Nand et al. “Resonator power to frequency conversion in a cryogenic sapphire oscillator”. In: *Applied Physics Letters* 103.4 (2013), p. 043502. URL: https://doi.org/10.1063/1.4816284 (cit. on p. 8).

[17] URL: http://www.uliss-st.com/ (cit. on p. 8).

[18] A Jallageas et al. “First uncertainty evaluation of the FoCS-2 primary frequency standard”. In: 55.3 (2018), pp. 366–385. URL: https://doi.org/10.1088%2F1681-7575%2Faab3fa (cit. on p. 9).

[19] J. Guena et al. “Progress in atomic fountains at LNE-SYRTE”. In: *IEEE Transactions on Ultrasonics, Ferroelectrics, and Frequency Control* 59.3 (2012), pp. 391–409 (cit. on pp. 9, 77).

[20] Thomas P Heavner et al. “First accuracy evaluation of NIST-F2”. In: *Metrologia* 51.3 (2014), pp. 174–182. URL: https://doi.org/10.1088%2F0026-1394%2F51%2F3%2F174 (cit. on pp. 9, 77).

[21] D. J. Wineland, R. E. Drullinger, and F. L. Walls. “Radiation-Pressure Cooling of Bound Resonant Absorbers”. In: *Phys. Rev. Lett.* 40 (25 1978), pp. 1639–1642. URL: https://link.aps.org/doi/10.1103/PhysRevLett.40.1639 (cit. on p. 9).

[22] Hidetoshi Katori et al. “Ultrastable Optical Clock with Neutral Atoms in an Engineered Light Shift Trap”. In: *Phys. Rev. Lett.* 91 (17 2003), p. 173005. URL: https://link.aps.org/doi/10.1103/PhysRevLett.91.173005 (cit. on pp. 9, 10).

[23] F.M. Penning. “Die glimmentladung bei niedrigem druck zwischen koaxialen zylindern in einem axialen magnetfeld”. In: *Physica* 3.9 (1936), pp. 873–894. DOI: https://doi.org/10.1016/S0031-8914(36)80313-9 (cit. on p. 10).

[24] W. Paul and M. Raether. “Das elektrische Massenfilter”. In: *Zeitschrift für Physik* 140 (3 1955), pp. 262–273. ISSN: 0044-3328. URL: https://doi.org/10.1007/BF01328923 (cit. on p. 10).

[25] N. Huntemann et al. “Single-Ion Atomic Clock with 3×10^{-18} Systematic Uncertainty”. In: *Phys. Rev. Lett.* 116 (6 2016), p. 063001. URL: https://link.aps.org/doi/10.1103/PhysRevLett.116.063001 (cit. on p. 10).

[26] M. G. Raizen et al. “Ionic crystals in a linear Paul trap”. In: *Phys. Rev. A* 45 (9 1992), pp. 6493–6501. URL: https://link.aps.org/doi/10.1103/PhysRevA.45.6493 (cit. on p. 10).

[27] J. Keller et al. “Controlling systematic frequency uncertainties at the 10^{-19} level in linear Coulomb crystals”. In: *Phys. Rev. A* 99 (1 2019), p. 013405. URL: https://link.aps.org/doi/10.1103/PhysRevA.99.013405 (cit. on p. 10).

[28] C. W. Oates, E. A. Curtis, and L. Hollberg. “Improved short-term stability of optical frequency standards: approaching 1 Hz in 1 s with the Ca standard at 657 nm”. In: *Opt. Lett.* 25 (2000), pp. 1603–1605. URL: http://ol.osa.org/abstract.cfm?URI=ol-25-21-1603 (cit. on p. 10).

[29] G. Wilpers et al. “Optical Clock with Ultracold Neutral Atoms”. In: *Phys. Rev. Lett.* 89 (23 2002), p. 230801. URL: https://link.aps.org/doi/10.1103/PhysRevLett.89.230801 (cit. on p. 10).

[30] W. F. McGrew et al. “Atomic clock performance enabling geodesy below the centimetre level”. In: *Nature* 564 (7734 2018), pp. 87–90. URL: https://doi.org/10.1038/s41586-018-0738-2 (cit. on p. 11).

[31] Tobias Bothwell et al. “JILA SrI optical lattice clock with uncertainty of 2.0×10^{-18}”. In: *Metrologia* 56.6 (2019), p. 065004. URL: https://doi.org/10.1088/1681-7575/ab4089 (cit. on p. 11).

[32] I. Ushijima et al. “Cryogenic optical lattice clocks”. In: *Nature Photonics* 9 (2015), pp. 185–189. URL: https://doi.org/10.1038/nphoton.2015.5 (cit. on p. 11).

[33] Ekkehard Peik and Maxim Okhapkin. “Nuclear clocks based on resonant excitation of γ-transitions”. In: *Comptes Rendus Physique* 16.5 (2015), pp. 516–523. ISSN: 1631-0705. URL: http://www.sciencedirect.com/science/article/pii/S1631070515000213 (cit. on p. 11).

[34] Pavlo V Bilous, Ekkehard Peik, and Adriana Pálffy. "Laser-induced electronic bridge for characterization of the ^{229m}Th $\rightarrow$ ^{229g}Th nuclear transition with a tunable optical laser". In: *New Journal of Physics* 20.1 (2018), p. 013016. URL: https://doi.org/10.1088%2F1367-2630%2Faa9cd9 (cit. on p. 11).

[35] G. Santarelli et al. "Frequency stability degradation of an oscillator slaved to a periodically interrogated atomic resonator". In: *IEEE Transactions on Ultrasonics, Ferroelectrics, and Frequency Control* 45.4 (1998), pp. 887–894 (cit. on pp. 11, 109).

[36] P. G. Westergaard, J. Lodewyck, and P. Lemonde. "Minimizing the dick effect in an optical lattice clock". In: *IEEE Transactions on Ultrasonics, Ferroelectrics, and Frequency Control* 57.3 (2010), pp. 623–628 (cit. on p. 12).

[37] G Vallet et al. "A noise-immune cavity-assisted non-destructive detection for an optical lattice clock in the quantum regime". In: *New Journal of Physics* 19.8 (2017), p. 083002. URL: https://doi.org/10.1088%2F1367-2630%2Faa7c84 (cit. on p. 12).

[38] Richard Hobson et al. "Cavity-enhanced non-destructive detection of atoms for an optical lattice clock". In: *Opt. Express* 27.26 (2019), pp. 37099–37110. URL: http://www.opticsexpress.org/abstract.cfm?URI=oe-27-26-37099 (cit. on p. 12).

[39] M. Schioppo et al. "Ultrastable optical clock with two cold-atom ensembles". In: *Nature Photonics* 11 (2017), pp. 48–52. URL: https://doi.org/10.1038/nphoton.2016.231 (cit. on p. 12).

[40] E. Oelker et al. "Demonstration of 4.8×10^{-17} stability at 1 s for two independent optical clocks". In: *Nature Photonics* 13 (10 2019), pp. 714–719. URL: https://doi.org/10.1038/s41566-019-0493-4 (cit. on p. 13).

[41] B. Canuel et al. "MIGA: combining laser and matter wave interferometry for mass distribution monitoring and advanced geodesy". In: vol. 9900. International Society for Optics and Photonics. 2016. URL: https://doi.org/10.1117/12.2228825 (cit. on p. 13).

[42] Benjamin M Roberts et al. "Search for transient variations of the fine structure constant and dark matter using fiber-linked optical atomic clocks". In: *New Journal of Physics* (2020). URL: http://iopscience.iop.org/10.1088/1367-2630/abaace (cit. on p. 13).

[43] Ghelfi P. et al. "A fully photonics-based coherent radar system". In: *Nature* 507 (2014), pp. 341–345. URL: https://doi.org/10.1038/nature13078 (cit. on p. 13).

[44] Eric D. Black. "An introduction to Pound–Drever–Hall laser frequency stabilization". In: *American Journal of Physics* 69.1 (2001), pp. 79–87. URL: https://doi.org/10.1119/1.1286663 (cit. on p. 14).

[45] Kenji Numata, Amy Kemery, and Jordan Camp. "Thermal-Noise Limit in the Frequency Stabilization of Lasers with Rigid Cavities". In: *Phys. Rev. Lett.* 93 (25 2004), p. 250602. URL: https://link.aps.org/doi/10.1103/PhysRevLett.93.250602 (cit. on pp. 14, 87).

[46] S. Amairi et al. "Reducing the effect of thermal noise in optical cavities". In: *Applied Physics B* 113 (2 2013), pp. 1432–0649. URL: https://doi.org/10.1007/s00340-013-5464-8 (cit. on p. 14).

[47] H. Kogelnik and T. Li. "Laser Beams and Resonators". In: *Appl. Opt.* 5.10 (1966), pp. 1550–1567. URL: http://ao.osa.org/abstract.cfm?URI=ao-5-10-1550 (cit. on p. 14).

[48] S. Häfner et al. "8×10^{-17} fractional laser frequency instability with a long room-temperature cavity". In: *Opt. Lett.* 40.9 (2015), pp. 2112–2115. URL: https://doi.org/10.1364/OL.40.002112 (cit. on p. 15).

[49] D. G. Matei et al. "1.5 μm Lasers with Sub-10 mHz Linewidth". In: *Phys. Rev. Lett.* 118 (2017), p. 263202. URL: https://link.aps.org/doi/10.1103/PhysRevLett.118.263202 (cit. on pp. 15, 96, 103, 106).

[50] John M. Robinson et al. "Crystalline optical cavity at 4 K with thermal-noise-limited instability and ultralow drift". In: *Optica* 6.2 (2019), pp. 240–243. URL: http://www.osapublishing.org/optica/abstract.cfm?URI=optica-6-2-240 (cit. on p. 15).

[51] T. Kessler et al. "A sub-40-mHz-linewidth laser based on a silicon single-crystal optical cavity". In: *Nature Photonics* 6.10 (2012), pp. 687–692. URL: https://doi.org/10.1038/nphoton.2012.217 (cit. on p. 15).

[52] G. D. Cole et al. "Tenfold reduction of Brownian noise in high-reflectivity optical coatings". In: *Nature Photonics* 7 (8 2013). URL: https://doi.org/10.1038/nphoton.2013.174 (cit. on p. 15).

[53] Garrett D. Cole et al. "High-performance near- and mid-infrared crystalline coatings". In: *Optica* 3.6 (2016), pp. 647–656. URL: http://www.osapublishing.org/optica/abstract.cfm?URI=optica-3-6-647 (cit. on p. 15).

[54] B. Julsgaard et al. "Understanding laser stabilization using spectral hole burning". In: *Opt. Express* 15.18 (2007), pp. 11444–11465. URL: http://www.opticsexpress.org/abstract.cfm?URI=oe-15-18-11444 (cit. on p. 15).

[55] Shon Cook, Till Rosenband, and David R. Leibrandt. "Laser-Frequency Stabilization Based on Steady-State Spectral-Hole Burning in $Eu^{3+}:Y_2SiO_5$". In: *Phys. Rev. Lett.* 114 (25 2015), p. 253902. URL: https://link.aps.org/doi/10.1103/PhysRevLett.114.253902 (cit. on p. 15).

[56] O. Gobron et al. "Dispersive heterodyne probing method for laser frequency stabilization based on spectral hole burning in rare-earth doped crystals". In: *Opt. Express* 25.13 (2017), pp. 15539–15548. URL: http://www.opticsexpress.org/abstract.cfm?URI=oe-25-13-15539 (cit. on p. 16).

[57] N. Galland et al. "Double heterodyne probing for an ultra-stable laser based on spectral hole burning in a rare-earth-doped crystal". In: *Optics letters* 45.7 (2020), pp. 1930–1933. URL: https://doi.org/10.1364/OL.389833 (cit. on p. 16).

[58] M. Thorpe et al. "Frequency stabilization to 6×10^{-16} via spectral-hole burning". In: *Nature Photonics* 5 (11 2011), pp. 1749–4893. URL: https://doi.org/10.1038/nphoton.2011.215 (cit. on p. 16).

[59] Qun-Feng Chen et al. "Spectrally Narrow, Long-Term Stable Optical Frequency Reference Based on a $Eu^{3+}:Y_2SiO_5$ Crystal at Cryogenic Temperature". In: *Phys. Rev. Lett.* 107 (22 2011), p. 223202. URL: https://link.aps.org/doi/10.1103/PhysRevLett.107.223202 (cit. on p. 16).

[60] D. Meiser and M. J. Holland. "Steady-state superradiance with alkaline-earth-metal atoms". In: *Phys. Rev. A* 81 (2010), p. 033847. URL: https://link.aps.org/doi/10.1103/PhysRevA.81.033847 (cit. on p. 16).

[61] R. H. Dicke. "Coherence in Spontaneous Radiation Processes". In: *Phys. Rev.* 93 (1 1954), pp. 99–110. URL: https://link.aps.org/doi/10.1103/PhysRev.93.99 (cit. on p. 16).

[62] Matthew A. Norcia et al. "Frequency Measurements of Superradiance from the Strontium Clock Transition". In: *Phys. Rev. X* 8 (2 2018), p. 021036. URL: https://link.aps.org/doi/10.1103/PhysRevX.8.021036 (cit. on p. 16).

[63] Stefan A. Schäffer et al. "Lasing on a narrow transition in a cold thermal strontium ensemble". In: *Phys. Rev. A* 101 (2020), p. 013819. URL: https://link.aps.org/doi/10.1103/PhysRevA.101.013819 (cit. on p. 16).

[64] L. E. Hargrove, R. L. Fork, and M. A. Pollack. "LOCKING OF He–Ne LASER MODES INDUCED BY SYNCHRONOUS INTRACAVITY MODULATION". In: *Applied Physics Letters* 5.1 (1964), pp. 4–5. URL: https://doi.org/10.1063/1.1754025 (cit. on p. 16).

[65] J. N. Eckstein, A. I. Ferguson, and T. W. Hänsch. "High-Resolution Two-Photon Spectroscopy with Picosecond Light Pulses". In: *Phys. Rev. Lett.* 40 (13 1978), pp. 847–850. URL: https://link.aps.org/doi/10.1103/PhysRevLett.40.847 (cit. on p. 16).

[66] O. Acef et al. "A CO2 to visible optical frequency synthesis chain: accurate measurement of the 473 THz HeNe/I2 laser". In: *Optics Communications* 97.1 (1993), pp. 29–34. URL: http://www.sciencedirect.com/science/article/pii/0030401893906129 (cit. on p. 17).

[67] H. Schnatz et al. "First Phase-Coherent Frequency Measurement of Visible Radiation". In: *Phys. Rev. Lett.* 76 (1 1996), pp. 18–21. URL: https://link.aps.org/doi/10.1103/PhysRevLett.76.18 (cit. on p. 17).

[68] J. E. Bernard et al. "Cs-Based Frequency Measurement of a Single, Trapped Ion Transition in the Visible Region of the Spectrum". In: *Phys. Rev. Lett.* 82 (16 1999), pp. 3228–3231. URL: https://link.aps.org/doi/10.1103/PhysRevLett.82.3228 (cit. on p. 17).

[69] J. Reichert et al. "Measuring the frequency of light with mode-locked lasers". In: *Optics Communications* 172.1 (1999), pp. 59–68. ISSN: 0030–4018. URL: http://www.sciencedirect.com/science/article/pii/S0030401899004915 (cit. on pp. 17, 23).

[70] Theodor W. Hänsch. "Nobel Lecture: Passion for precision". In: *Rev. Mod. Phys.* 78 (4 2006), pp. 1297–1309. DOI: 10.1103/RevModPhys.78.1297 (cit. on p. 17).

[71] Scott A. Diddams. "The evolving optical frequency comb". In: *J. Opt. Soc. Am. B* 27.11 (2010), B51–B62. URL: http://josab.osa.org/abstract.cfm?URI=josab-27-11-B51 (cit. on pp. 17, 23).

[72] T. Brabec et al. "Kerr lens mode locking". In: *Opt. Lett.* 17.18 (1992), pp. 1292–1294. URL: http://ol.osa.org/abstract.cfm?URI=ol-17-18-1292 (cit. on pp. 18, 30).

[73] K. Tamura, H. A. Haus, and E. P. Ippen. "Self-starting additive pulse mode-locked erbium fibre ring laser". In: *Electronics Letters* 28.24 (1992), pp. 2226–2228. ISSN: 0013–5194. DOI: 10.1049/el:19921430 (cit. on pp. 18, 29).

[74] W. Hänsel et al. "All polarization-maintaining fiber laser architecture for robust femtosecond pulse generation". In: *Applied Physics B* 123 (1 2017), pp. 1432–0649. URL: https://doi.org/10.1007/s00340-016-6598-2 (cit. on p. 18).

[75] Jinendra K. Ranka, Robert S. Windeler, and Andrew J. Stentz. "Visible continuum generation in air–silica microstructure optical fibers with anomalous dispersion at 800 nm". In: *Opt. Lett.* 25.1 (2000), pp. 25–27. URL: http://ol.osa.org/abstract.cfm?URI=ol-25-1-25 (cit. on p. 19).

[76] David W. Kammler. *A First Course in Fourier Analysis*. 2nd Edition. Cambridge University Press, 2008. ISBN: 9780511619700. URL: https://doi.org/10.1017/CBO9780511619700 (cit. on p. 19).

[77] Thomas Brabec and Ferenc Krausz. "Intense few-cycle laser fields: Frontiers of nonlinear optics". In: *Rev. Mod. Phys.* 72 (2 2000), pp. 545–591. URL: https://link.aps.org/doi/10.1103/RevModPhys.72.545 (cit. on p. 21).

[78] S. T. Cundiff. "Phase stabilization of ultrashort pulses". In: *Journal of Physics D* 35.8 (2002), R43–R59 (cit. on p. 21).

[79] George A. Sefler. "Frequency Comb Generation by Four-Wave Mixing and the Role of Fiber Dispersion". In: *J. Lightwave Technol.* 16.9 (1998), p. 1596. URL: http://jlt.osa.org/abstract.cfm?URI=jlt-16-9-1596 (cit. on p. 22).

[80] Jay E. Sharping et al. "Four-wave mixing in microstructure fiber". In: *Opt. Lett.* 26.14 (2001), pp. 1048–1050. URL: http://ol.osa.org/abstract.cfm?URI=ol-26-14-1048 (cit. on p. 22).

[81] H. R. Telle et al. "Carrier-envelope offset phase control: A novel concept for absolute optical frequency measurement and ultrashort pulse generation". In: *Applied Physics B* 69 (1999), pp. 327–332. DOI: 10.1007/s003409900148 (cit. on pp. 22, 23).

[82] T. J. Kippenberg, S. M. Spillane, and K. J. Vahala. "Kerr-Nonlinearity Optical Parametric Oscillation in an Ultrahigh-Q Toroid Microcavity". In: *Phys. Rev. Lett.* 93 (8 2004), p. 083904. URL: https://link.aps.org/doi/10.1103/PhysRevLett.93.083904 (cit. on p. 23).

[83] E. Lucas et al. "Ultralow-noise photonic microwave synthesis using a soliton microcomb-based transfer oscillator". In: *Nature Communications* 11 (2020), p. 374. URL: https://doi.org/10.1038/s41467-019-14059-4 (cit. on p. 23).

[84] B. Corcoran et al. "Ultra-dense optical data transmission over standard fibre with a single chip source". In: *Nature Communications* 11 (1 2020), pp. 2041–1723. URL: https://doi.org/10.1038/s41467-020-16265-x (cit. on p. 23).

[85] Ryan P. Scott et al. "Amplitude and phase noise sensitivity of modelocked Ti:sapphire lasers in terms of a complex noise transfer function". In: *Opt. Express* 15.14 (2007), pp. 9090–9095. URL: http://www.opticsexpress.org/abstract.cfm?URI=oe-15-14-9090 (cit. on p. 23).

[86] A. Bartels, D. Heinecke, and S. A. Diddams. "Passively mode-locked 10 GHz femtosecond Ti:sapphire laser". In: *Opt. Lett.* 33.16 (2008), pp. 1905–1907. DOI: 10.1364/OL.33.001905 (cit. on p. 23).

[87] F. Tricot, S. Guerandel, and E. de Clercq. “Contributions to the mid-term frequency noise of the pulsed CPT clock at SYRTE”. In: *2018 European Frequency and Time Forum (EFTF)*. 2018, pp. 98–100 (cit. on p. 26).

[88] A. G. Mann, C. Sheng, and A. N. Luitenr. “Cryogenic sapphire oscillator with exceptionally high frequency stability”. In: *IEEE Trans. Instrum. Meas.* 50.2 (2001), pp. 519–521 (cit. on p. 26).

[89] E. Cantin et al. “Progress on the REFIMEVE+ project for optical frequency standard dissemination”. In: *2017 Joint Conference of the European Frequency and Time Forum and IEEE International Frequency Control Symposium*. 2017, pp. 378–380 (cit. on p. 27).

[90] F. Frank et al. “A Sub-ps Stability Time Transfer Method Based on Optical Modems”. In: *IEEE Transactions on Ultrasonics, Ferroelectrics, and Frequency Control* 65.6 (2018), pp. 1001–1006 (cit. on p. 27).

[91] D. Xu et al. “Two-Branch Fiber Link for International Clock Networks”. In: *IEEE Transactions on Instrumentation and Measurement* 68.6 (2019), pp. 2195–2200 (cit. on pp. 27, 135).

[92] X. Xie et al. “Photonic microwave signals with zeptosecond-level absolute timing noise”. In: *Nature Photonics* 11 (2017), pp. 1749–4893. URL: https://doi.org/10.1038/nphoton.2016.215 (cit. on p. 27).

[93] Franziska Riedel et al. “Direct comparisons of European primary and secondary frequency standards via satellite techniques”. In: *Metrologia* (2020). URL: http://iopscience.iop.org/10.1088/1681-7575/ab6745 (cit. on p. 28).

[94] L. Cacciapuoti, P. Laurent, and C. Salomon. “Atomic clock ensemble in space”. In: *52nd Rencontres de Moriond on Gravitation*. 2017, pp. 139–148 (cit. on p. 28).

[95] Philippe Laurent et al. “Qualification and frequency accuracy of the space based primary frequency standard PHARAO”. In: *Metrologia* (2020). URL: http://iopscience.iop.org/10.1088/1681-7575/ab948b (cit. on p. 28).

[96] Nathan R. Newbury and William C. Swann. “Low-noise fiber-laser frequency combs (Invited)”. In: *J. Opt. Soc. Am. B* 24.8 (2007), pp. 1756–1770. URL: http://josab.osa.org/abstract.cfm?URI=josab-24-8-1756 (cit. on p. 30).

[97] Richard Ell et al. “Carrier-envelope phase control by a composite plate”. In: 14 (2006). URL: http://www.opticsexpress.org/abstract.cfm?URI=oe-14-12-5829 (cit. on p. 31).

[98] W. Zhang et al. "Characterizing a fiber-based frequency comb with electro-optic modulator". In: *IEEE Transactions on Ultrasonics, Ferroelectrics, and Frequency Control* 59.3 (2012), pp. 432–438. ISSN: 1525–8955. DOI: 10.1109/TUFFC.2012.2212 (cit. on p. 34).

[99] C. Guo et al. "Accurate laser frequency locking to optical frequency combs under low-signal-to-noise-ratio conditions". In: *Review of Scientific Instruments* 91.3 (2020), p. 033202. URL: https://doi.org/10.1063/1.5140793 (cit. on p. 37).

[100] S. T. Dawkins, J. J. McFerran, and A. N. Luiten. "Considerations on the measurement of the stability of oscillators with frequency counters". In: *IEEE Transactions on Ultrasonics, Ferroelectrics, and Frequency Control* 54.5 (2007), pp. 918–925. DOI: 10.1109/TUFFC.2007.337 (cit. on p. 37).

[101] G. Kramer and W. Klische. "Extra high precision digital phase recorder". In: *2004 18th European Frequency and Time Forum (EFTF 2004)*. 2004, pp. 595–602 (cit. on p. 38).

[102] R. M. Godun et al. "Frequency Ratio of Two Optical Clock Transitions in $^{171}Yb^{+}$ and Constraints on the Time Variation of Fundamental Constants". In: *Phys. Rev. Lett.* 113 (21 2014), p. 210801. URL: https://link.aps.org/doi/10.1103/PhysRevLett.113.210801 (cit. on p. 56).

[103] Y. Huang et al. "Frequency Comparison of Two $^{40}Ca^{+}$ Optical Clocks with an Uncertainty at the 10^{-17} Level". In: *Phys. Rev. Lett.* 116 (1 2016), p. 013001. URL: https://link.aps.org/doi/10.1103/PhysRevLett.116.013001 (cit. on p. 56).

[104] Pierre Dubé, John E Bernard, and Marina Gertsvolf. "Absolute frequency measurement of the88Sr+clock transition using a GPS link to the SI second". In: *Metrologia* 54.3 (2017), pp. 290–298. URL: https://doi.org/10.1088%2F1681-7575%2Faa5e60 (cit. on p. 56).

[105] Hidekazu Hachisu et al. "SI-traceable measurement of an optical frequency at the low 10-16 level without a local primary standard". In: *Opt. Express* 25.8 (2017), pp. 8511–8523. URL: http://www.opticsexpress.org/abstract.cfm?URI=oe-25-8-8511 (cit. on p. 56).

[106] F. Riehle et al. "The CIPM list of recommended frequency standard values: guidelines and procedures". In: *Metrologia* 55 (2018), pp. 188–200. URL: https://doi.org/10.1088/1681-7575/aaa302 (cit. on pp. 57, 59, 78).

[107] H. R. Telle, B. Lipphardt, and J. Stenger. "Kerr-lens mode-locked lasers as transfer oscillators for optical frequency measurements". In: *Applied Physics B* 74 (2002), pp. 1–6 (cit. on pp. 58, 88).

[108] A. Clairon et al. “A cesium fountain frequency standard: preliminary results”. In: *IEEE Transactions on Instrumentation and Measurement* 44.2 (1995), pp. 128–131 (cit. on p. 59).

[109] D. Chambon et al. “Design and metrological features of microwave synthesizers for atomic fountain frequency standard”. In: *IEEE Transactions on Ultrasonics, Ferroelectrics, and Frequency Control* 54.4 (2007), pp. 729–735 (cit. on p. 60).

[110] M. Abgrall et al. “High stability comparison of atomic fountains using two different cryogenic oscillators”. In: *IEEE Transactions on Ultrasonics, Ferroelectrics and Frequency Control* 63.8 (2016), pp. 1198–1203. DOI: 10.1109/TUFFC.2016.2570898 (cit. on pp. 60, 61).

[111] “IEEE Standard for Floating-Point Arithmetic”. In: *IEEE Std 754-2019 (Revision of IEEE 754-2008)* (2019), pp. 1–84 (cit. on p. 76).

[112] ITU-T Recommendations. “Spectral grids for WDM applications: DWDM frequency grid”. In: *Series G: Transmission systems and media, digital systems and networks* G.694.1 (2012). URL: http://handle.itu.int/11.1002/1000/11482 (cit. on p. 78).

[113] Yoshiaki Nakajima et al. “A multi-branch, fiber-based frequency comb with millihertz-level relative linewidths using an intra-cavity electro-optic modulator”. In: *Opt. Express* 18.2 (2010), pp. 1667–1676. URL: http://www.opticsexpress.org/abstract.cfm?URI=oe-18-2-1667 (cit. on p. 82).

[114] Puppe T. et al. “Characterization of a DFG comb showing quadratic scaling of the phase noise with frequency”. In: *Opt. Lett.* 41.8 (2016), pp. 1877–1880. URL: http://ol.osa.org/abstract.cfm?URI=ol-41-8-1877 (cit. on p. 89).

[115] Kliese R. et al. “Difference-frequency combs in cold atom physics”. In: *The European Physical Journal Special Topics* 225.15 (2016), pp. 1951–6401. URL: https://doi.org/10.1140/epjst/e2016-60092-0 (cit. on p. 89).

[116] Xiaopeng Xie et al. “Phase noise characterization of sub-hertz linewidth lasers via digital cross correlation”. In: *Opt. Lett.* 42.7 (2017), pp. 1217–1220. URL: http://ol.osa.org/abstract.cfm?URI=ol-42-7-1217 (cit. on p. 93).

[117] E. N. Ivanov, S. A. Diddams, and L. Hollberg. “Analysis of noise mechanisms limiting the frequency stability of microwave signals generated with a femtosecond laser”. In: *IEEE Journal of Selected Topics in Quantum Electronics* 9.4 (2003), pp. 1059–1065. DOI: 10.1109/JSTQE.2003.819093 (cit. on p. 95).

[118] Piero Barbieri et al. “Spectral purity transfer with 5×10^{-17} instability at 1 s using a multibranch Er:fiber frequency comb”. In: *Metrologia* 56.4 (2019), p. 045008. URL: https://doi.org/10.1088%2F1681-7575%2Fab2b0f (cit. on p. 96).

[119] Antoine Rolland et al. “Ultra-broadband dual-branch optical frequency comb with 10^{-18} instability”. In: *Optica* 5.9 (2018), pp. 1070–1077. URL: http://www.osapublishing.org/optica/abstract.cfm?URI=optica-5-9-1070 (cit. on p. 96).

[120] D. Nicolodi et al. “Spectral purity transfer between optical wavelengths at the 10^{-18} level”. In: *Nature Photonics* 8 (3 2014), pp. 1749–4893. URL: https://doi.org/10.1038/nphoton.2013.361 (cit. on p. 99).

[121] Erik Benkler et al. “End-to-end topology for fiber comb based optical frequency transfer at the 10−21 level”. In: *Opt. Express* 27.25 (2019), pp. 36886–36902. URL: http://www.opticsexpress.org/abstract.cfm?URI=oe-27-25-36886 (cit. on pp. 99, 101).

[122] Darren D. Hudson et al. “Mode-locked fiber laser frequency-controlled with an intracavity electro-optic modulator”. In: *Opt. Lett.* 30.21 (2005), pp. 2948–2950. URL: http://ol.osa.org/abstract.cfm?URI=ol-30-21-2948 (cit. on p. 141).

Héctor ÁLVAREZ MARTÍNEZ **15 mars 2021**

Sujet : Caractérisation des mesures par peigne de fréquences optiques et transfert de pureté spectrale à des horloges atomiques optiques

Résumé : Cette thèse présente les avancées de la chaîne de fréquence opérationnelle du SYRTE, emsemble de différentes oscillateurs ultrastables et peignes de fréquence. Le travail de recherche porte sur l'analyse du bruit des éléments critiques, afin de déterminer les limites pratiques de stabilité et d'exactitude de cette architecture métrologique. Les performances sont mesurées par comparaisons simultanées de paires d'oscillateurs avec 3 chaînes entièrement indépendantes. Les résolutions relatives obtenues, en deçà de $1 \cdot 10^{-16}$ dans le domaine micro-onde et $1 \cdot 10^{-18}$ dans le domaine optique, démontrent que ces moyens de mesures ne sont pas limitants, même avec les horloges à l'état-de-l'art. Un élément clé des horloges optiques est la lumière sondant la transition métrologique. Si les meilleurs lasers ultrastables sont conçus dans l'infrarouge, la technique du transfert de pureté spectrale permet de transmettre leur niveau de performance aux longueurs d'onde visibles cibles (698 nm et 1062 nm) via un peigne de fréquence. Ce travail décrit ainsi un transfert hors boucle de résolution meilleure que $5 \cdot 10^{-18}$ à 1 s, utilisé pour l'interrogation synchronisées des horloges strontium et mercure du laboratoire lorsque leurs lasers d'horloge respectifs bénéficient du transfert d'un unique maître à 1542 nm. Ceci a déjà permis un gain d'un facteur 2 de la stabilité dans la mesure du rapport mercure/strontium.

Mots clés : chaîne de fréquences, horloges optiques, lasers ultrastables, métrologie de fréquence, peignes de fréquences optiques, transfert de pureté spectrale

Tema: Caracterización de medidas mediante peine de frecuencias ópticas y transferencia de pureza espectral para relojes atómicos ópticos

Resumen:
Esta tesis doctoral presenta los últimos avances de la cadena de frecuencias operacional del SYRTE, conjunto de diferentes osciladores ultra-estables y peines de frecuencia. Este trabajo de investigación se centra en el análisis del ruido de sus elementos más críticos con el fin de determinar los límites de estabilidad y exactitud de esta arquitectura metrológica. El rendimiento de estas capacidades fue medido mediante comparaciones simultáneas de pares de osciladores con 3 cadenas totalmente independientes. Las resoluciones relativas obtenidas, por debajo de 10^{-16} en el dominio de las microondas y de 10^{-18} en el óptico, demuestran que estos medios de medida no son un factor limitante, incluso con relojes de tecnología punta. Un elemento clave de los relojes ópticos es la luz que sondea la estrecha transición atómica. Mientras que en la práctica estos láseres son construidos en el rango infrarrojo, la técnica de transferencia de pureza espectral permite transmitir sus prestaciones hacia las longitudes de onda visibles de interés (698 nm y 1062 nm) por medio de un peine de frecuencias. Este trabajo demuestra una transferencia fuera de lazo mejor que $5 \cdot 10^{-18}$ a 1 s, utilizada para la interrogación sincronizada entre los relojes de estroncio y mercurio del laboratorio cuando sus respectivos láseres reloj se benefician de la transferencia de un único laser maestro a 1542 nm. Esto ha permitido la mejora en un factor de 2 de la estabilidad de la medida del ratio mercurio/estroncio.

Palabras clave: cadena de frecuencias, láseres ultra-estables, metrología de frecuencias, peines de frecuencias ópticas, relojes ópticos, transferencia de pureza espectral

Subject: Characterization of optical frequency comb based measurements and spectral purity transfer for optical atomic clocks

Abstract: This PhD thesis presents the latest advances in SYRTE operational frequency chain, based on ultrastable oscillators at different wavelengths and frequency comb technologies. After describing this metrological architecture, the work focuses on the noise analysis of its critical elements so as to determine its stability and accuracy limits. The performance of these capabilities was measured by performing simultaneous comparisons of oscillators pairs with 3 fully independent chains. The relative resolutions obtained, below 10^{-16} in the microwave and 10^{-18} in the optical domains, demonstrate that these means of measurement are not a limiting factor, even with state-of-the-art clocks. A key element of optical clocks is the light probing the narrow atomic transition. While in practice ultrahigh stability lasers are built in the infrared range, the technique known as transfer of spectral purity makes use of a frequency comb to transmit its level of performance to target visible wavelengths (698 nm and 1062 nm in the SYRTE case). This work demonstrates an out-of-loop transfer reaching a resolution better than $5 \cdot 10^{-18}$ at 1 s. This lead to the first synchronized interrogation between the SYRTE strontium and mercury clocks when their respective clock lasers benefit from the transfer of a single master at 1542 nm, resulting in a 2-fold improvement of their stability ratio measurement.

Keywords: frequency chain, frequency metrology, optical clocks, optical frequency combs, spectral purity transfer, ultrastable lasers